MOLECULAR MECHANISMS UNDERLYING OSTEOCYTE APOPTOSIS AND THE ASSOCIATED OSTEOCLASTOGENESIS IN CX43-DEFICIENCY AND AGING

Hannah Marie Davis

Submitted to the faculty of the University Graduate School
in partial fulfillment of the requirements
for the degree
Doctor of Philosophy
in the Department of Anatomy and Cell Biology,
Indiana University

June 2019

Accepted by the Graduate Faculty of Indiana University, in partial fulfillment of the requirements for the degree of Doctor of Philosophy.

Doctoral Committee

Lilian I. Plotkin, Ph.D., Chair

Joseph P. Bidwell, Ph.D.

April 26, 2019

Matthew R. Allen, Ph.D.

Angela Bruzzaniti, Ph.D.

DEDICATION

To my loved ones

Thank you for your endless support and for always reminding me of what truly matters.

ACKNOWLEDGEMENTS

I would like to thank the National Institutes of Health and the Cagiantas family for their funding, which allowed me to conduct these experiments and gave me the opportunity to present my work at numerous scientific conferences.

I would like to extend my thanks to my committee for their advice and support throughout my graduate training. Particularly, Dr. Bidwell, thank you for the countless hours of therapy sessions over the years.

Dr. Plotkin thank you for welcoming me into your lab and providing me with endless guidance and encouragement throughout my graduate training. You have been a wonderful mentor and I will always be thankful for the countless opportunities you have given me over the years.

I would like to thank the numerous individuals who helped contribute to these studies, as their efforts led to several publications. In particular, I thank all of the members of the Plotkin lab as well as the numerous other individuals in the Department of Anatomy and Cell Biology for all of their assistance and support with these studies.

I would like to thank the Department of Anatomy and Cell Biology, the IBMG program, and Indiana University School of Medicine for providing me with this opportunity.

Lastly and most important of all, I would like to thank my family and friends for their endless support and patience with me throughout my graduate studies.

Hannah Marie Davis

MOLECULAR MECHANISMS UNDERLYING OSTEOCYTE APOPTOSIS AND THE ASSOCIATED OSTEOCLASTOGENESIS IN CX43-DEFICIENCY AND AGING

Old age is associated with increased bone fragility and risk of fracture as a result of skeletal alterations, including low bone density and cortical thinning. Further, apoptotic osteocytes accumulate in old mice and humans. We have previously shown that mice lacking osteocytic connexin (Cx) 43 ($Cx43^{\Delta Ot}$) exhibit a phenotype similar to that of the aging skeleton, with elevated osteocyte apoptosis and an associated increase in osteoclastogenesis. These findings suggest that osteocyte apoptosis results in the release of factors that recruit osteoclasts to bone surfaces close to areas that contain apoptotic osteocytes. However, the specific chemotactic signals, the events mediating their release, and the mechanisms of their action remain unknown. Consistent with this notion, we also found that HMGB1 released by Cx43-deficient ($Cx43^{def}$) MLO-Y4 osteocytic cells enhances osteoclastogenesis in part by increasing osteocytic RANKL, which promotes osteoclastogenesis, and, at the same time, directly stimulating osteoclastogenesis. Further, expression of the pro-survival microRNA (miR), miR21, is low in $Cx43^{def}$ cells and bones from old female mice, and low miR21 levels increase osteocyte apoptosis. However, surprisingly, mice lacking miR21 ($miR21^{\Delta Ot}$) have decreased osteoclast number and activity even under conditions of elevated osteocyte apoptosis; suggesting that osteocytic miR21 may mediate osteoclast precursor recruitment/survival induced by apoptotic osteocytes. However, whether HMGB1/miR21 are released by osteocytes, and if the HMGB1 receptors, receptor for advanced glycation end products (RAGE) and/or toll-like receptor (TLR4) are involved in osteoclast recruitment in $Cx43^{\Delta Ot}$ and old mice is unknown. The overall objectives of this series of studies were to elucidate the mechanisms

underlying osteocyte apoptosis in Cx43-deficiency and aging and identify the signaling molecules that link osteocyte apoptosis and osteoclast recruitment. We hypothesize that enhanced extracellular release of the signaling factors HMGB1 and miR21 recruits osteoclasts to areas containing apoptotic osteocytes and promotes osteoclast activity, leading to targeted bone resorption. Overall, these studies will provide insights into the mechanisms governing osteocyte apoptosis and the associated targeted osteoclast resorption, allowing for the development of novel therapeutics for preserving the structure and strength of the aging skeleton.

Lilian I. Plotkin, Ph.D., Chair

TABLE OF CONTENTS

LIST OF TABLES

LIST OF FIGURES

Chapter 1

Introduction

Aging-related osteoporosis

Given to the considerable advancements in healthcare in recent decades, people are now living longer than ever before. Ironically, this has led us to face a new series of clinical challenges, i.e. chronic degenerative diseases, including heart disease, cancer, diabetes, and neurodegeneration, which are often associated with the development of additional debilitating conditions, including osteoporosis.[1-3] For example, the annual incidence of osteoporotic fractures, resulting from reduced bone mass and strength, is greater than that of heart attacks, strokes, and breast cancer combined [affecting ~1:2 women of all ages, and ~1:4 men over age 50 and costing the US ~$25.3 billion a year in healthcare expenses[4, 5]], and the incidence is forecasted to continue increasing.[6]

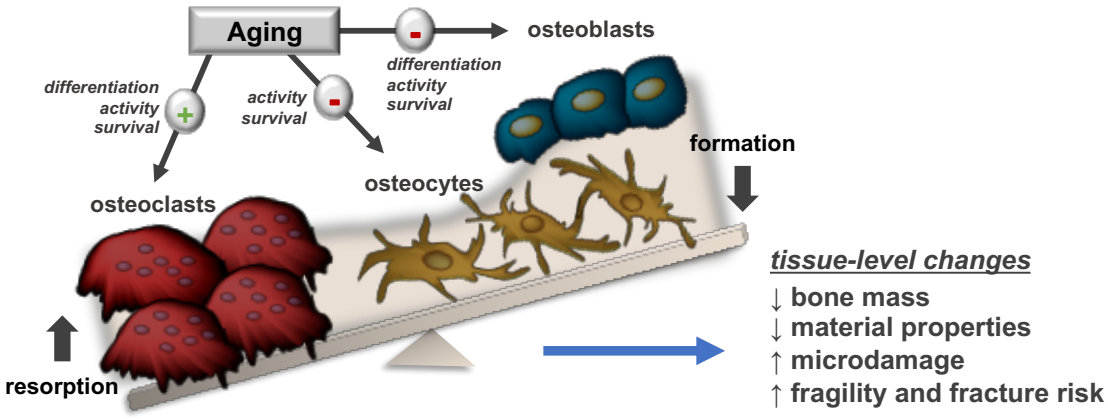

Figure 1-1. Illustration of the cellular and tissue-level skeletal alterations with aging.

Old age is a key risk factor underlying osteoporosis. Bone remodeling, a coordinated process critical for the maintenance of bone quality, occurs throughout life, but is significantly altered with advancing skeletal age, as illustrated in Fig. 1-1.[7, 8] In particular, aging leads to dysregulated bone turnover in which the amount of bone

resorbed by the osteoclasts outweighs the amount of new bone formed by the osteoblasts.[9] These alterations in bone turnover eventually result in the loss of trabecular and cortical bone mass, reduced thickness and increased porosity, all of which cause significant reductions in bone strength and greatly increase the risk of fractures.[10, 11]

In humans, studies have found that losses in bone mass are initially observed in the trabecular bone compartment and then later in the cortical bone compartment.[12] Interestingly, while aging in both mice and humans leads to reductions in osteoblast number and function in both the trabecular and cortical bone compartments,[8, 13-15] the effects on osteoclasts appear to be compartment specific, shown in Fig. 1-2. In particular, in cortical bone osteoclast activity is elevated with aging, which leads to cortical thinning and intracortical porosity; whereas, in trabecular bone osteoclast numbers are reduced with aging,[16-18] suggesting that aging has divergent effects on bone remodeling in the trabecular and cortical bone compartments.

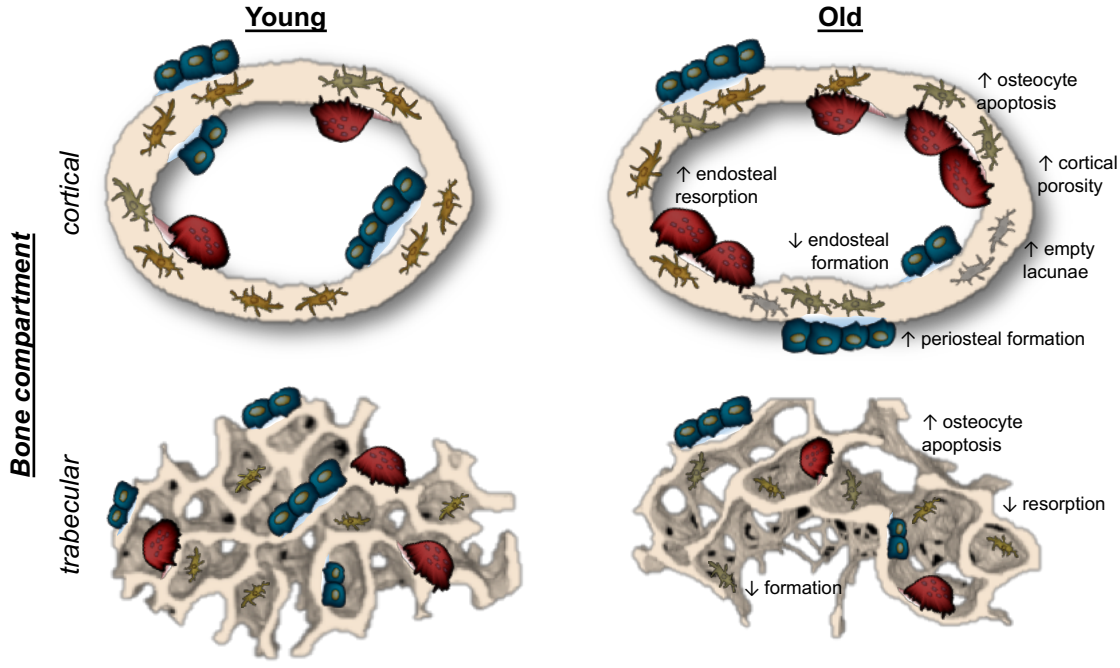

Figure 1-2. Graphic illustration of the bone compartment-specific cellular changes with aging.

In women, there is a rapid increase in bone loss after menopause, which is consistent with the numerous studies demonstrating the beneficial effects of estrogen on the skeleton.[19, 20] In particular, estrogen has been shown to promote osteoblast and osteocyte survival and induce osteoclast apoptosis. Conversely, aging has opposite effects, leading to reductions in osteoblast and osteocyte viability and increases in osteoclast activity.[9, 19] In addition, aging is also associated with defective bone material properties,[21] as changes in bone mineral matrix and collagen composition, as well as accumulation of microdamage further contribute to the increased skeletal fragility.[22] Notably, evidence suggests that the increases in osteocyte apoptosis directly contribute to the alterations in bone turnover and reductions in bone strength seen with aging.[7, 9, 23, 24] Thus, given the growing number of osteoporosis patients, there is an essential need to better understand the mechanisms leading to osteocyte apoptosis in aging and identify the contribution of this event to aging-related losses in bone mass and strength.

Cellular alterations associated with bone loss in aging

Impaired bone formation is one of the key mechanisms that result in bone loss in aging.[9] There are several factors thought to contribute to the reductions in bone formation observed with aging, including decreases in the number of mesenchymal stem cells, a reduced capacity of precursors to proliferation/differentiation into osteogenic lineage cells, and an increase in osteoblast apoptosis.[19, 25] In addition to the decreases in osteoblast function, aging is associated with increases in osteoclast recruitment and activity. In particular, the decreases in cortical thickness and increases in cortical porosity in aging are thought to primarily result from increases in bone resorption.[16-18] The processes of osteoblast and osteoclast differentiation and function are regulated by a variety of different factors and stimuli that control numerous signaling pathways.[9] Further, there are a number of factors thought to contribute to the alterations in bone turnover seen with aging, in

particular, increases in osteocyte apoptosis have been shown to directly stimulate osteoclast recruitment and function. For example, several models of increased osteocyte death, including ovariectomy, unloading, microdamage, and a transgenic model of osteocyte apoptosis induced by diphtheria toxin, exhibited co-localization of apoptotic osteocytes and osteoclasts, suggesting that signals released by dying osteocytes induce osteoclast recruitment.[26-29]

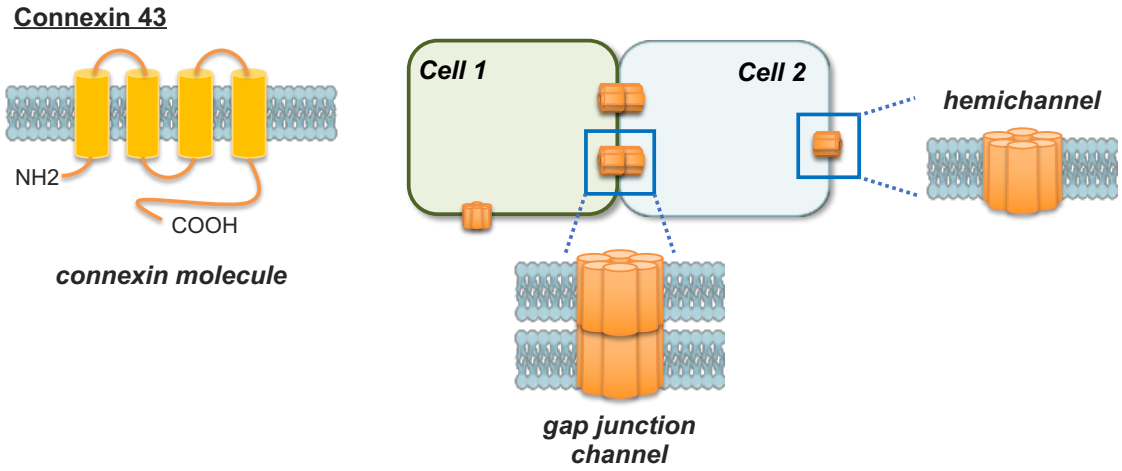

Figure 1-3. Schematic illustration of a Cx43 molecule, with one amino (NH_2) and carboxy (COOH) domains and 4 transmembrane domains. A connexon or hemichannel is made up of six Cx43 molecules, and 2 connexons on adjacent cells can align to form a gap junction channel.

Osteocytes, which are osteoblastic cells that become embedded in the bone mineral matrix, are the most abundant and long-lived type of bone cell, accounting for ~98% of the cells comprising the skeleton.[30, 31] Osteocytes have long dendritic processes that facilitate cell-signaling and allow for the exchange of nutrients between cells through the canaliculi network in the bone. Osteocytes are mechanosensitive cells embedded in the bone matrix and are key targets of bone acting stimuli.[26, 32-34] These cells allow for intercellular signaling with distant cells both through the extracellular release of molecules

and cytokines via hemichannels formed via connexins (Cx) and directly with adjacent cells through gap junction channels, formed by connexons present on the surface of neighboring cells (Fig. 1-3).[35, 36] Cx transmembrane proteins are expressed in osteoblasts, osteocytes and osteoclasts, with Cx43 being the most highly expressed connexin in bone.[37] The critical role of Cx43 in early and mature osteoblasts, as well as in osteocytes has been demonstrated in numerous studies (Fig. 1-4).[38-40]

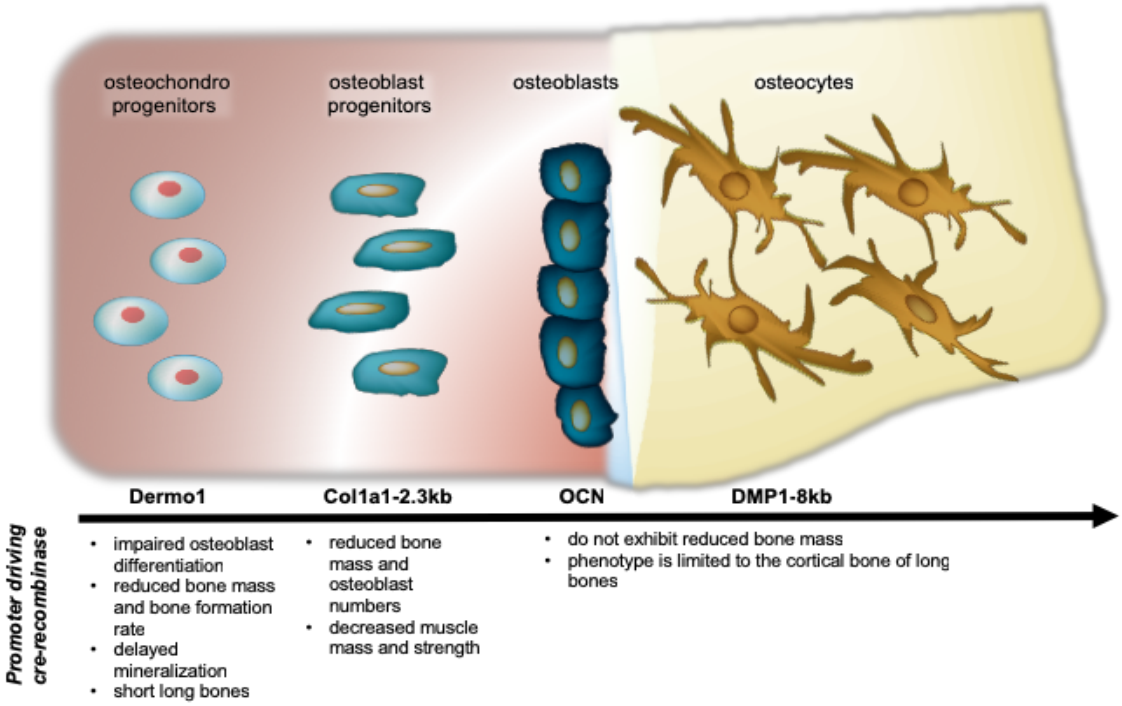

Figure 1-4. Skeletal effects of Cx43 deletion in osteoblastic lineage cells at different differentiation stages (adapted from Basic and Applied Bone Biology[41]). The Cre recombinase was targeted to the indicated cell populations using promoter for the Dermo1 gene (also known as Twist2); a 2.3kb fragment of the collagen 1a1 promoter (col1a12.3kb); the human osteocalcin promoter (OCN); or an 8kb fragment of the dentin matrix protein 1 promoter (DMP1).

Mounting evidence suggests that osteocytes play a critical role in regulating skeletal homeostasis and orchestrating bone turnover, and consistent with this, osteocytes

produce and release numerous factors that directly influence osteoblast and osteoclast activity. Consistent with this notion, mechanical loading induces fluid flow within the canalicularlacunar network and stimulates the release of antiapoptotic factors that can promote osteoblast survival. Additionally, several recent studies suggest that preservation of osteocyte viability contributes to maintaining bone strength,[32, 40, 42, 43] and that accumulation of apoptotic osteocytes results in targeted osteoclast recruitment.[26-29] Further, old age and conditions of increased skeletal fragility are associated with reductions in osteocyte viability and increased prevalence of empty lacunae; and disruptions in the osteocyte network alters osteocytic regulation of bone remodeling.[44] Moreover, skeletal aging is associated with an accumulation of apoptotic osteocytes, reduced osteoblast activity and enhanced osteoclast recruitment in both mice and humans.[8, 45] Taken together, these pieces of evidence suggest that osteocyte apoptosis results in the release of signaling factors that induce the dysregulations in osteoblast and osteoclast function in aging.

Our lab previously showed that removal of Cx43 from osteocytes results in a skeletal phenotype that resembles that of aged mice, shown in Fig. 1-5, with increased osteocyte apoptosis, marrow cavity widening, cortical thinning and defective bone material properties.[38, 46] In addition to the accumulation of apoptotic osteocytes and empty lacunae observed in aging and in the absence of osteocytic Cx43, osteoclast recruitment is also enhanced.[8, 45] In particular, osteoclasts localize along endocortical bone surfaces in both $Cx43^{\Delta Ot}$ mice and old wild type (WT) mice.[8, 46] In both models, the expression of the anti-osteoclastogenic cytokine osteoprogerin (OPG) is decreased in cells throughout the bone. In addition, osteoclasts only localize close to apoptotic osteocyte-containing regions, not those with empty lacunae.[8, 46] Further, the RANKL/OPG ratio is significantly increased in Cx43-deficient ($Cx43^{def}$) MLO-Y4 osteocytic cells. Consistently, Cx43 levels are significantly decreased in old mice and humans.[8, 46] However, the signaling events linking

osteocyte apoptosis to the subsequent osteoclast activation in old age and the absence of osteocytic Cx43 remain unknown.

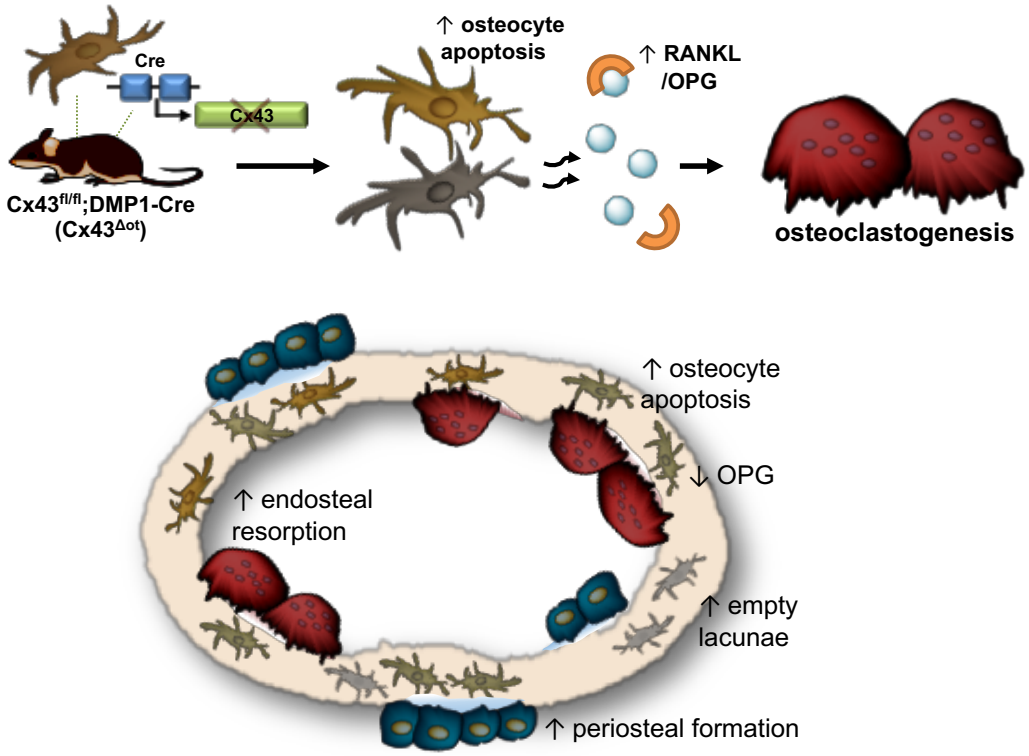

Figure 1-5. Illustration of the skeletal phenotype resulting from osteocytic Cx43 removal.

Interestingly, similar to the bone compartment-specific effects observed with aging, removal of osteocytic Cx43 also induces bone compartment specific effects. For example, removal of Cx43 from mature osteoblasts and osteocytes or exclusively from osteocytes results in cortical bone changes, but does not alter cancellous bone.[47] Further, other studies have shown that expression of a truncated Cx43 lacking the c-terminus domain can negatively affect cancellous bone, whereas heterozygous deletion of Cx43 attenuates cancellous bone loss.[48, 49] Overall, these findings demonstrate the essential role that Cx43 plays in maintaining osteocyte viability and bone homeostasis; thus underscoring the potential contribution of reduced levels of Cx43 in osteocytes to the decreased bone quality/strength in aging. However, the signaling pathway activated by Cx43 deficiency

involved in stimulating osteocyte apoptosis and the specific role that osteocytic Cx43 plays in controlling bone structure and strength in aging remain unknown.

In osteocytes and other cells, apoptotic cell death results in the release of the pro-inflammatory cytokine high-mobility group box-1 (HMGB1), a non-histone nuclear DNA-binding protein responsible of stabilization of nucleosomal structures facilitating gene transcription.[50, 51] Previous studies have shown that HMGB1 released from cells activates the receptor for advanced glycation end products (RAGE) and toll-like receptor 4 (TLR4).[52] In addition, HMGB1 is chemotactic for osteoclasts,[53] and induces osteoclastogenesis by activating RAGE,[54] and can regulate recruitment and differentiation of osteoclast precursors.[54, 55] However, whether HMGB1 mediates the increases in osteoclast recruitment and differentiation induced by apoptotic osteocytes in aging or in the absence of osteocytic Cx43, and whether activation of the HMGB1 receptors RAGE and/or TLR4 mediate the effects on osteoclasts are not known. Additionally, it is unclear if apoptotic osteocyte-derived HMGB1 regulates osteoclastogenesis by autocrine actions in osteocytes and/or through paracrine actions in osteoclasts, illustrated in Fig. 1-6.

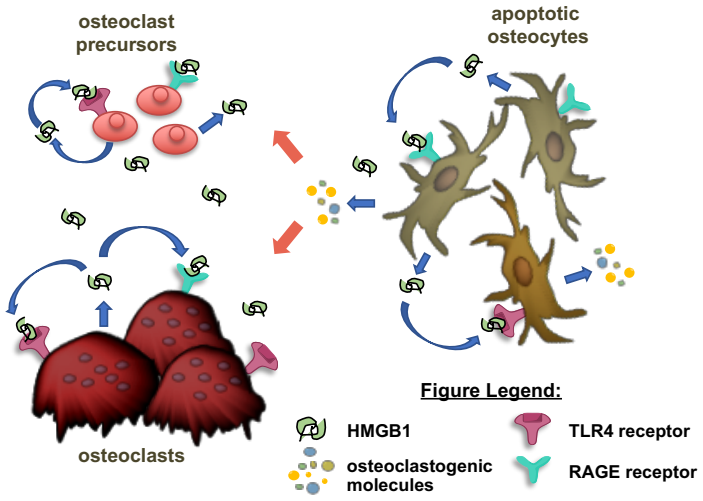

Figure 1-6. Schematic summary of the possible mechanisms of HMGB1 signaling in osteocytes and osteoclasts.

Aside from the alterations in bone turnover, osteocyte apoptosis is also thought to contribute to defects in bone mechanical properties in aging. For example, studies have shown that osteocyte apoptosis in aging leads to BMD-independent reductions in bone strength, due to increases in the prevalence of mineralized empty lacunae as well as decreases in microcrack repair resulting from disruptions in the canalicular system.[22, 56, 57] Further, studies have also shown that many of the factors that regulate cell function in bone remodeling, also regulate osteocyte and osteoblast apoptosis.[8] There are a variety of factors that may contribute to or be a consequence of the increased osteocyte apoptosis observed in aging. In particular, previous work by our lab found that reductions in osteocytic Cx43 expression levels alter several apoptosis-associated microRNAs (miRs), which are single-stranded non-coding RNAs that negatively regulate gene expression.[58] miRs are involved in cancer cell survival, and in particular, the expression of miR21 is upregulated in a variety of cancers, promoting cell survival through the direct inhibition of apoptotic genes including phosphatase and tensin homolog (PTEN).[59] In bone, miRs play an important role in controlling the function and lifespan of both osteoclasts and osteoblasts.[60] However, the role of miRs on osteocyte apoptosis has not been investigated. Thus, additional studies are needed to identify the specific mechanisms underlying increased osteocyte apoptosis in aging.

Current Osteoporosis Therapeutic Options

There a currently a number of osteoporosis treatments on the market including antiresorptive agents, monoclonal antibodies, and osteoanabolic agents, which function through different mechanisms to prevent bone loss or increase bone mass, and preserve bone strength.[61] The mostly commonly used class of therapeutics are antiresorptive agents, in particular bisphosphonates, which attenuate bone loss by inhibiting osteoclast activity.[61-63] In osteoporotic patients, bisphosphonate treatment has been shown to

increase bone mineral density and lower fracture risk.[62] However, despite the beneficial effects seen in the majority of patients treated with bisphosphonates, in some patients, suppression of osteoclast activity with antiresorptive agents has also been shown to have negative effects on bone. For example, the use of these agents has been shown to significantly suppress bone turnover, which decreases osteoblast activity and bone formation.[63] Moreover, in a small percentage of patients, extended treatment with bisphosphonates has also been linked to decreases in bone tissue toughness,[64, 65] and consistent with this, in some studies, bisphosphonate treatment has been found to be associated with higher fracture risk in elderly women.[63] Further, diminished bone turnover with prolonged suppression of osteoclast activity, has been shown to induce further microdamage and advanced glycation endproducts (AGEs) accumulation.[66-70] Thus, while these anti-resorptive agents prevent further bone loss, they also reduce the formation of new bone.

Interestingly, in addition to inhibiting osteoclast activity, bisphosphonates have been shown to have an antiapoptotic effects on osteoblasts and osteocytes, which are Cx43-dependent.[40, 43, 71, 72] For example, work by Plotkin et. al., found that bisphosphonate analogs without antiresorptive activity still prevent osteoblast and osteocyte apoptosis *in vitro*.[43, 73] Further, a bisphosphonate analog blocked osteoblast and osteocyte apoptosis and prevented glucocorticoid-induced loss of bone mass and strength in mice, despite having no effects on osteoclast activity.[74] Taken together, these osteoclast-independent beneficial effects of bisphosphonate treatment further highlight the relationship between osteocyte viability and bone mass/strength.

Thus, understanding the mechanisms underlying the increases in osteocyte apoptosis in aging and the absence of osteocytic Cx43, and identifying the events that link osteocyte apoptosis to the increases in osteoclast activity, are important steps needed to identify new therapeutic targets to prevent bone loss in aging. In particular, preventing

osteocyte apoptosis could potentially maintain bone mass and strength, without completely suppressing normal bone turnover. Additionally, identifying the molecules by which apoptotic osteocytes stimulate osteoclastogenesis could allow for the development of new treatment methods to reduce, rather than completely suppressing bone resorption. For example, using a small-molecule inhibitor of the signaling molecules that link osteocyte apoptosis and osteoclast activation, could allow for more opportunities to test different treatment regimens, durations and doses.

The purpose of the current series of studies, illustrated in Fig. 1-7, was to better understand the mechanisms underlying osteocyte apoptosis in aging and to identify the apoptotic osteocyte-derived signaling molecules responsible for the subsequent increases in osteoclast activation. Future studies will aim to improve the management of the adverse skeletal effects of aging by targeting osteocyte apoptosis and resorption.

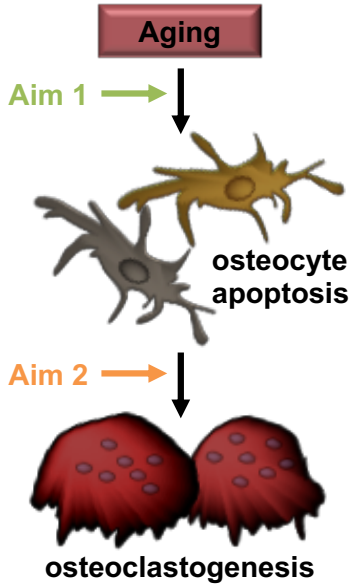

Figure 1-7. Aims of the current studies. Aim1: elucidate the mechanisms underlying osteocyte apoptosis in aging and in the absence of osteocytic Cx43. Aim 2: identify the signaling molecules that link osteocyte apoptosis and osteoclastogenesis.

Chapter 2

Reduced osteocyte apoptosis and preservation of cortical bone quality with advanced age in mice with osteocytic Cx43 overexpression

Rationale

Young, skeletally mature mice lacking Cx43 in osteocytes exhibit increased osteocyte apoptosis and decreased bone strength, resembling the phenotype of old mice. Further, the expression of Cx43 in bone decreases with age, suggesting a contribution of reduced Cx43 levels to the age-related changes in the skeleton. Here we sought to investigate whether expression of an osteocyte-targeted Cx43 transgene could preserve osteocyte viability and attenuate the skeletal phenotype in aged mice; using mice in which the DMP1-8kb promoter targeted Cx43 expression to osteocytes ($Cx43^{OT}$ mice).

Introduction

Advanced age is associated with skeletal fragility as a result of decreases in bone quantity and quality due to changes in the structural and material properties of bone.[22, 57] Bone remodeling, a coordinated process critical for the maintenance of bone quality, occurs throughout life, however the rate of bone turnover significantly decreases with advancing skeletal age.[7, 8] Alterations in bone turnover where resorption outweighs formation, eventually result in bone loss in old age. Initial age-induced bone loss is observed in trabecular bone due to decreased osteoblast activity; whereas cortical bone losses occur later.[17, 21] In addition to the alterations in bone structure, bone material is also affected in aging,[21] as changes in bone mineral matrix and collagen composition, as well as accumulation of microdamage further contribute to the increased skeletal fragility with aging.[22]

Numerous studies suggest that the extensive osteocyte network within the mineralized bone matrix plays an essential role in orchestrating bone remodeling through cell-cell communication among neighboring osteocytes and with cells on the bone surface.[30, 75] Consistent with this notion, old age and conditions of increased skeletal fragility are associated with reductions in osteocyte viability and increased prevalence of empty lacunae; and disruptions in the osteocyte network alters osteocytic regulation of bone remodeling.[44] Osteocytes participate in intercellular signaling with distant cells both through the extracellular release of small molecules via hemichannels formed via connexins (Cx) and directly with adjacent cells through gap junction channels, formed by connexons present on the surface of neighboring cells.[35, 36] Cx transmembrane proteins are expressed in osteoblasts, osteocytes and osteoclasts, with Cx43 being the most highly expressed connexin in bone.[37]

The critical role of Cx43 in early and mature osteoblasts, as well as in osteocytes has been demonstrated in numerous studies.[38-40] We previously showed that removal of Cx43 from osteocytes results in a skeletal phenotype that resembles that of aged mice with increased osteocyte apoptosis, enhanced osteoclast recruitment to bone surfaces, and defective bone material properties.[38, 46] Further, Cx43 is significantly decreased in old mice and humans.[8, 46] Overall, these findings demonstrate the essential role that Cx43 plays in maintaining osteocyte viability and bone homeostasis; thus underscoring the potential contribution of reduced levels of Cx43 in osteocytes to the bone weakness in aging. However, the specific role that osteocytic Cx43 plays in controlling bone structure and strength in aging has not been studied.

We investigated here whether expression of an osteocyte targeted Cx43 transgene could preserve osteocyte viability and attenuate the skeletal phenotype in aged mice; using mice in which the DMP1-8kb promoter targeted Cx43 expression to osteocytes ($Cx43^{OT}$ mice). Overall, the results of this study demonstrate that increased osteocytic

Cx43 expression partially preserves osteocyte viability and maintains cortical bone quality in aged mice. Because overexpression of Cx43 in osteocytes does not significantly affect cancellous bone, these findings also point to a site specific effect of Cx43 in osteocytes.

Materials and Methods

Mice. DMP1-8kb-Cx43/GFP mice (abbreviated as $Cx43^{OT}$) were generated at the Transgenic and KO Mouse Core (IUSM) with the Cx43 transgene, generated by S. and M. Harris (UTSHC, San Antonio), using the DMP1-8kb promoter[76] and a CMV-Cx43/GFP[77] constructs (Fig. 2-7A). The presence of the transgene was evaluated by PCR in genomic DNA extracted from ear notch samples using primer sets for Cx43 and GFP. DMP1-GFP mice were used as positive controls for GFP.[76] GFP expression in DNA from $Cx43^{OT}$ mice was detected by PCR but not by fluorescent microscopy, possibly due to low expression resulting from the transgene construct design in which GFP was after IRES. Mice lacking osteocytic Cx43, $Cx43^{\Delta Ot}$ mice, were generated by crossing $Cx43^{fl/fl}$ mice with DMP1-8kb-Cre mice, as previously published.[46, 78]

All mice were maintained on a C57BL/6Nhsd background (Envigo, Indianapolis, IN) and littermates were used as controls. Mice were fed a regular diet and water *ad libitum* and were maintained on a 12 h light/dark cycle. Mice were born at the expected Mendelian frequency, were fertile, and exhibited a similar size and weight to wild type (WT) littermate mice at birth. Female skeletally mature 6-month-old and aged 14-month-old mice were used. Based on published data our 6-month old mice are equivalent to 20-year old humans, whereas the 14-month-old mice correspond to middle aged female humans at the end of their reproductive stage of life (˜58-year-old).[79] For dynamic histomorphometric studies, mice received intraperitoneal injections of calcein (30 mg/kg) and alizarin red (50 mg/kg) (Sigma Chemical, St. Louis, MO, USA) 7 and 2 days before sacrificing, as published.[49] The protocols involving animal procedures were approved by the Institutional Animal Care and Use Committee of Indiana University School of Medicine.

Osteoblast and osteocyte isolation. Calvaria cells were isolated from $Cx43^{OT}$ mice bred to DMP1-8kb-GFP mice which have GFP-labeled osteocytes.[46, 78] Cells were

isolated by sequential 20-minute digestions using a trypsin/EDTA/collagenase P mixture as previously described.[80] The first digestion was discarded, and cells from all other digestions were pulled. GFP-expressing cells (osteocyte-enriched) were separated from GFP-negative cells (osteoblast-enriched) by sorting the cell suspension using a FACSAria flow cytometer (BD Biosciences, Sparks, MD) at the Indiana University Flow Cytometry Core Facility, as published.[81]

RNA extraction and real-time PCR (qPCR). Total RNA was isolated and purified using TRIzol (Invitrogen, Grand Island, NY). Reverse transcription was performed using a high-capacity cDNA kit (Applied Biosystems, Foster City, CA). qPCR was performed using the Gene Expression Assay Mix TaqMan Universal Master Mix containing 80 ng of each cDNA template using an ABI 7900HT real-time PCR system. The house-keeping gene glyceraldehyde 3-phosphate dehydrogenase (GAPDH) was used. Primers and probes were commercially available (Applied Biosystems, Foster City, CA) or were designed using the Assay Design Center (Roche Applied Science, Indianapolis, IN). Relative expression was calculated using the ΔCt method.[46]

Immunohistochemistry. Cx43 expression in osteocytes and osteoblasts was visualized in paraffin-embedded femora from 2-month-old mice, as described.[81, 82] Briefly, sections were deparaffinized, treated with 3% H_2O_2, blocked with rabbit serum, and incubated with 1:1000 anti-Cx43 (C6219) (Sigma-Aldrich, Saint Louis, MO, USA). Sections were incubated with the corresponding biotinylated secondary antibody followed by avidin conjugated peroxidase (Vectastain Elite ABC Kit; Vectora Laboratories). Color was developed with a diaminobenzidine substrate chromogen system (Dako Corp). Sections were counterstained with 2% methyl green.[46] Cells expressing the protein are

brown, whereas negative cells are green-blue. Non-immune IgGs were used as negative controls.

Western Blot analysis. Whole protein extracts from osteocyte-enriched long bones (cortical bone preparations), calvaria bones, and soft tissue samples were prepared as published.[46, 74] Protein levels were measured by western blot analysis. Membranes were probed with primary antibodies, rabbit anti-connexin43 (C6219) and mouse anti-β-actin (A5316) (Sigma Aldrich, Saint Louis, MO, USA) diluted 1:1000, overnight at 4ºC, followed by incubation with corresponding secondary antibodies conjugated with horseradish peroxidase (Santa Cruz Biotechnology, Santa Cruz, CA) for 4 hours at room temperature. Membranes were developed with an enhanced chemiluminescence Western blotting substrate kit (Pierce Biotechnology Inc., Rockford, IL, USA). Bands were quantified using ImageJ.

Bone mineral density (BMD) by dual energy x-ray absorptiometry (DXA). BMD was measured monthly by DXA using a PIXImus densitometer (G.E. Medical Systems, Lunar Division, Madison, WI, USA).[49] BMD measurements included total BMD (excluding the head and tail), entire femur (femoral BMD) and L1–L6 vertebra (spinal BMD).[81] Calibration was performed before scanning with a standard phantom, as recommended by the manufacturer.

Apoptosis. Osteocyte and osteoblast apoptosis was detected in undecalcified vertebral bone sections and paraffin embedded femur sections by TdT-mediated dUTP nick-end labeling (TUNEL) using a modified version of a commercial kit (EMD Millipore, Billerica, MA) in sections counterstained with 2% methyl green, as published.[46]

Serum biochemistry. Plasma collected 3 h after fasting by cheek bleeding was aliquoted and stored at − 80°C.[49] N-terminal propeptide of type I procollagen (P1NP) (Immunodiagnostic Systems Inc., Fountain Hill, AZ, USA, cat.#AC-33F1) and C-telopeptide fragments (CTX) (RatLaps, Immunodiagnostic Systems Inc., Fountain Hill, AZ, USA, cat.#AC-06F1) were measured as published.[46, 83]

Micro-computed tomography (μCT) analysis. Femora and L4 vertebrae were dissected, wrapped in saline-containing gauze and frozen at − 20°C.[83] Trabecular morphology of the L4 vertebral body was obtained using the Skyscan 1172 system with a 60kV source, 0.5mm Al filter, 0.7 degree rotation and two-image averaging with an isotropic voxel size of 6μm.[84] Femora were scanned using a 55kV source, 0.5mm Al filter, 0.7 degree rotation and two-image averaging with an isotropic voxel size of 9μm using a SkyScan 1176 system (SkyScan, Kontich, Belgium). Scans were reconstructed and analyzed using manufacturer software. Two different μCT systems were used due to constrained availability and only results within each system were captured. Nomenclature is reported in accordance with suggested guidelines for μCT.[85]

Bone histomorphometry. Femora and vertebrae were dissected, fixed in 10% neutral buffered formalin, and embedded in methyl methacrylate, as published.[83] Dynamic histomorphometric measurements were performed in unstained femoral mid-diaphysis and vertebrae sections.[83] Static histomorphometric analysis was performed on sequential plastic-embedded vertebra sections stained with von Kossa/McNeal for osteoblasts and TRAP/Toluidine blue for osteoclasts. Osteoclasts were also quantified on paraffin embedded femur sections. Analysis was performed by blinded investigators using the OsteoMeasure high-resolution digital video system (OsteoMetrics Inc., Decatur, GA,

USA).[74, 86] The terminology and units used are those recommended by the Histomorphometry Nomenclature Committee of the ASBMR.[85]

Biomechanical testing. Three-point bending testing of the femoral mid-diaphysis was performed following previously published protocols.[83] Axial compression of the L4 vertebrae was performed after removing the vertebral processes and endplates. A rate of 0.5 mm/min was used to load the vertebral bodies until failure, as previously described.[87] Structural mechanical properties were determined from the load-displacement curves using standard definitions, while material-level properties were derived from the load-displacement curves, cross-sectional moments of inertia, and the distances from the centroid to the tensile surface using geometrical data determined by μCT and standard beam-bending equations.[49]

Statistical analysis. Data were analyzed by using SigmaPlot (Systat Software Inc., San Jose, CA, USA). Differences were evaluated either by two-way ANOVA, with post-hoc analysis using Tukey Method or Student's t-test, as appropriate. Differences were considered significant when $p<0.05$.

Results

Effective expression of an osteocyte targeted Cx43 transgene in Cx43^{OT}mice.

To test the effect of Cx43 levels on osteocyte viability and bone homeostasis in aged mice, we generated a transgenic mouse model that expresses a DMP1-8kb-Cx43/GFP transgene primarily in osteocytes (Cx43^{OT} mice) (Fig. 2-7A). An amplified fragment of 297 bp corresponding to the Cx43 allele and of 525 bp to the GFP allele was used to generate transgenic Cx43^{OT}mice. Of the eleven potential transgenic founders generated, two mice were found to express the exogenous Cx43 and GFP genes. Due to higher Cx43 protein levels in the founder mouse #82 (data not shown), offspring generated from this mouse were used for the outlined studies. Expression of both exogenous Cx43 and GFP were transmitted to half of the offspring when crossed with a WT mouse, as expected (Fig. 2-7B). To confirm that our DMP1-8kb-Cx43/GFP transgene is primarily expressed in osteocytes and not in osteoblasts, Cx43^{OT} mice were crossed with DMP1-8kb-GFP mice.[46, 78] GFP positive osteocytes (Ot) isolated by FACS expressed high levels of the osteocyte markers SOST, DMP1, and FGF23, while the osteoblast marker keratocan was low (Fig. 2-1A). GFP negative osteoblasts (Ob) had undetectable levels of SOST and DMP1, while keratocan expression was higher, validating the identity of the cell populations. Cx43 expression was increased in the GFP positive osteocytes and decreased in the GFP negative osteoblasts isolated from Cx43^{OT} compared to WT littermate mice, demonstrating osteocyte-specific expression of the transgene. Moreover, the percentage of Cx43 positive osteocytes, detected by Cx43 immunostaining, was increased 2-fold in Cx43^{OT} mice compared to WT mice, whereas the percentage of Cx43 positive osteoblasts on the bone surface was similar, although it showed a tendency towards decrease (Fig. 2-1B), similar to the Cx43 mRNA levels in osteoblastic cells (Fig. 2-1A). Cx43 expression at the protein level, measured by western blotting analysis, was not increased in marrow-flushed cortical bone preparations or in calvaria lysates (Fig. 2-

1C), possibly due to the presence of other Cx43 expressing cells, such as osteoblasts.[46] Further, no changes in Cx43 protein were detected in the heart, kidney, brain or skeletal muscle of $Cx43^{OT}$ mice compared to WT mice.

Similar to mice lacking osteocytic Cx43,[46] overexpression of osteocytic Cx43 in $Cx43^{OT}$ mice did not result in major changes in BMD during growth in female (Fig. 2-1D) or male mice (data not shown), demonstrating that Cx43 in osteocytes is not involved in bone mass accrual. Total, femoral, and spinal BMD of the $Cx43^{OT}$ and WT mice by DXA were similar up to 5.5 months, except for a slight increase in total and femoral BMD in the female $Cx43^{OT}$ mice at 2 months of age, which was consistent with reduced BMD at this age in mice lacking osteocytic Cx43.[46] No decreases in total or femoral BMD were observed in either genotype up to 14 months compared to 5.5-month old mice. On the other hand, spinal BMD began to decline at 9.5 months in the WT mice and by 12 months decreases in spinal BMD were detected in both genotypes.

Increased Cx43 expression reduces osteocyte apoptosis in aged mice. To investigate the effects of aging on osteocyte viability, apoptosis was quantified in the different bone compartments of the lumbar vertebra and femur. No changes in the percentage of apoptotic osteocytes or osteoblasts were detected between the two genotypes at 6 months of age (young mice) (Fig. 2-2A). Aged WT mice exhibited a 6- and 5.5-fold increase in osteocyte apoptosis in the cortical and cancellous vertebral bone, respectively, and a 22-fold increase in cancellous osteoblast apoptosis compared to young WT mice.[7, 88] Cortical and cancellous osteocyte apoptosis was higher in aged compared to young animals even in $Cx43^{OT}$ mice; however, osteocyte apoptosis was 40% lower in the cortical bone and 24% lower in the cancellous bone of the vertebra in the aged transgenic mice compared to WT mice. Similar decreases were detected in the femoral cortical bone of aged transgenic mice compared to WT mice (Fig. 2-2B). In contrast, the

prevalence of apoptotic cancellous osteoblasts was increased approximately 40% with aging in both genotypes and no differences in osteoblast viability were detected between the two genotypes at 14 months of age (Fig. 2-2A). Thus, increased expression of Cx43 in osteocytes partially prevents the increase in osteocyte apoptosis induced by aging.

Endocortical bone formation is maintained in aged Cx43^{OT} mice. Aging led to alterations in the bone turnover markers in the WT mice, with a 42% decrease in the formation marker P1NP and a 34% increase in the resorption marker CTX in aged compared to young WT mice (Fig. 2-3A). On the other hand, P1NP levels were increased by 66% and CTX levels were decreased by 24% in aged compared to young Cx43^{OT} mice. Moreover, while no changes in P1NP were detected between the two genotypes in young mice, aged Cx43^{OT} mice exhibited 135% higher P1NP levels compared to WT mice of the same age. Further, at 6 months of age CTX levels were slightly increased in the Cx43^{OT} mice, whereas at 14 months CTX levels were 28% lower compared to aged WT mice.

No changes in periosteal bone formation parameters, mineralizing surface per bone surface (MS/BS), mineral apposition rate (MAR), or bone formation rate per bone surface (BFR/BS), were detected between the two genotypes at either age in the femoral mid-diaphysis (Fig. 2-3B). On the other hand, dynamic histomorphometric analysis revealed that all bone formation indexes (MS/BS, MAR, and BFR/BS) were increased on the endocortical surface in the Cx43^{OT} versus WT mice at 14 months, but not at 6 months (Fig. 2-3B), suggesting that increased osteoblast activity in this compartment contributes to the higher production of P1NP detected in the serum of 14-month-old Cx43^{OT} mice. As for MS/BS, the surfaces occupied by single and double labels on the periosteum were similarly increased by aging independently of the genotype of the mice, whereas Cx43 overexpression did not alter these parameters (Fig. 2-8A). On the other hand, the percent single labeled surface on the endocortex was increased by aging and decreased by the

transgene, whereas double labeled-covered surface was decreased in 14-month-old wild type mice but increased in $Cx43^{OT}$ mice compared to the corresponding 6-month-old mice (Fig. 2-8B).

Similar to the decreases in CTX observed in the $Cx43^{OT}$ mice at 14 months of age, static histomorphometric analysis of the endocortical surface of the femoral mid-diaphysis revealed a 2.5-fold reduction in the number of osteoclasts per bone surface (N.Oc/BS), a 1.9-fold decrease in bone surface occupied by osteoclasts (Oc.S/BS), and a 1.9-fold reduction in the eroded bone surface (ES/BS) in the 14-month-old $Cx43^{OT}$ compared to WT mice (Fig. 2-3C). Consistently, at the mRNA level RANKL and the RANKL/OPG ratio were decreased in cortical bone lysates from 14-month-old $Cx43^{OT}$ compared to WT mice at the same age (Fig. 2-9).

Cortical bone mechanical properties are preserved in aged $Cx43^{OT}$ mice. μCT analysis revealed that both WT and $Cx43^{OT}$ mice exhibited the expected age-related skeletal alterations in cortical bone geometry of the femoral mid-diaphysis, with increased marrow cavity area, as well as decreased cortical thickness (Ct.Th) and bone area/tissue area (BA/TA) in aged mice (Fig. 2-3D). Further, we did not detect changes in the cortical bone geometry of the femur between the genotypes at either age, aside from a slight increase in marrow cavity area of the aged $Cx43^{OT}$ mice.

In contrast, biomechanical studies of the femur by 3-point bending revealed that increased osteocytic Cx43 expression enhanced the structural and material bone properties in skeletally mature mice and prevented the loss of these properties in aged mice (Fig. 2-4). At 6-months of age $Cx43^{OT}$ mice exhibited enhanced femoral structural properties with increased yield force, ultimate force, stiffness, and work to yield (Fig. 2-4A), as well as increases in the material properties yield stress, modulus, and resilience (Fig. 2-4B). Moreover, aging in the WT mice resulted in decreases in both the structural

and material properties of the femoral bone, with decreases in ultimate force/stress, stiffness/modulus, postyield/total work, and toughness. Further, decreases were detected in the pre-yield properties with lower yield force/stress of WT bones from aged compared to young mice. In contrast, although decreases were detected in ultimate force/stress and stiffness/modulus of the femur from 14-month-old $Cx43^{OT}$ mice, displacement/strain to yield were significantly increased compared to 6-month-old transgenic mice. Aged $Cx43^{OT}$ mice also exhibited increases in the pre-yield properties, yield force/stress, displacement/strain to yield, and work to yield/resilience, compared to WT mice at the same age. In contrast to the effects of osteocytic Cx43 overexpression on pre-yield properties, osteocytic Cx43 deletion results in reductions in the pre-yield properties of the cortical bone at both the structural and material level (data not shown). Taken together, our data suggest that overexpression of osteocytic Cx43 in aging preserves certain cortical bone mechanical properties, maintaining the ability of the bone to absorb energy without damaging.

Increased osteocytic Cx43 does not prevent age-induced cancellous bone loss. Analysis of cancellous bone microarchitecture by μCT revealed that 6-month-old $Cx43^{OT}$ mice exhibited increased trabecular thickness (Tb.Th) in the lumbar vertebra, without changes in the other trabecular bone parameters (Fig. 2-5A). Consistent with the increases in vertebral cancellous bone detected by μCT, vertebral compression testing detected increases in ultimate load/stress in the $Cx43^{OT}$ compared to WT mice at 6 months of age (Fig. 2-5B). However, by 14 months of age, differences in cancellous bone between the two genotypes were no longer detected. Moreover, while aging led to a loss of vertebral cancellous bone BV/TV and Tb.N in both genotypes, decreases in vertebral Tb.Th were only detected in the 14-month-old $Cx43^{OT}$ mice (Fig. 2-5A). Further, stiffness/modulus of the vertebra were decreased in aged mice from both genotypes,

whereas decreases in ultimate load/stress were only detected in the 14-month-old $Cx43^{OT}$ mice (Fig. 2-5B).

Consistent with the decreases in vertebral cancellous bone observed with aging in both WT and trangenic mice, histomorphometric analysis revealed decreases in MS/BS and BFR/BS (Fig. 2-6A) along with reductions in osteoblast number (N.Ob/BS) and surface (Ob.S/BS) (Fig. 2-6B) in the aged compared to young mice of both genotypes. Further, osteoclast parameters, N.Oc/BS, Oc.S/BS, and ES/BS, were higher in both genotypes at 14 months compared to 6-month-old mice. At 6 months of age cancellous MAR and BFR/BS were reduced (Fig. 2-6A) and Ob.S/BS was decreased along with a tendency towards decrease in N.Ob/BS (Fig. 2-6B) in $Cx43^{OT}$ mice compared to WT mice. At 14 months of age, MAR was still decreased in $Cx43^{OT}$ compared to WT mice, while no differences in N.Ob/BS or Ob.S/BS were detected. On the other hand, no changes in osteoclasts were detected between the genotypes at either age (Fig. 2-6C). Taken together, these pieces of evidence suggest that increased osteocytic Cx43 does not prevent and may actually enhance cancellous bone loss induced with aging.

Discussion

Previous work from our laboratory demonstrated that Cx43 is critical for osteocyte survival and removal of osteocytic Cx43 leads a skeletal phenotype similar to that observed in aging with increases in osteocyte apoptosis and enhanced osteoclast recruitment, as well deficits in the material properties of the cortical bone.[38, 46] In this study, we examined the contribution of osteocytic Cx43 to the skeletal phenotype of aged mice, using $Cx43^{OT}$ mice expressing a Cx43 transgene targeted to DMP1-8kb-expressing cells. We show that the prevalence of apoptotic osteocytes was significantly reduced in the cortical and to a lesser extent in the cancellous bone of 14-month-old $Cx43^{OT}$ compared to WT mice, further demonstrating the critical role of Cx43 in maintaining osteocyte viability.

In addition, we found that in aged $Cx43^{OT}$ mice reductions in osteocyte apoptosis were accompanied by changes in bone remodeling with increased formation and decreased resorption along the endocortical bone surface. While this did not alter long bone geometrical changes induced with aging, improvements in the cortical mechanical properties were observed at the material level. It is possible that the aging process has just started in our 14-month-old animals and while changes were detected at the cellular levels, we did not allow enough time for these alterations to translate into structural changes. Consistent with this possibility, we did not detect increases in bone mass in the aged compared to the young $Cx43^{OT}$ mice by BMD or μCT analyses, even though the circulating markers suggest higher bone mass in the older animals. The reason for this discrepancy is not clear. However, it is possible that since the aging process may have just started in our animals and while changes were detected at the cellular levels, we did not allow enough time for these alterations to translate into structural changes. Furthermore, we cannot rule out the possibility that the moderate expression of the

transgene in osteocytes and a potential uneven expression in femoral versus vertebral bone may provide some explanation for the weak bone mass phenotype of $Cx43^{OT}$ mice.

In contrast, despite the increases in cancellous bone at 6 months of age in the $Cx43^{OT}$ compared to WT mice and maintenance of spinal BMD at 9.5 months, age-induced cancellous bone losses were not prevented in the $Cx43^{OT}$ mice by 14 months of age. These findings are consistent with previous reports demonstrating that removal of osteocytic Cx43 does not alter cancellous bone.[46] Altogether, our data demonstrates that Cx43 maintains osteocyte viability in both cortical and cancellous bone, and that preservation of osteocyte viability appears to be critical for the maintenance of cortical bone quality in aging, although cancellous bone is still lost. Furthermore, increased Cx43 expression in osteocytes partially ameliorates the age-induced skeletal changes, by preserving bone turnover which likely improves cortical bone mechanical properties but does not prevent against cancellous bone loss in old age.

Bone fragility in aging individuals results not only from the loss of bone mass, but also from deficits in bone quality.[21] The findings of the present study highlight the essential role of Cx43 in preserving osteocyte viability and maintaining the bone mechanical properties in aging. Age-related declines in bone material properties are accompanied by changes in the distribution and architecture of the cortical and trabecular bone.[17] We found that both aged WT and $Cx43^{OT}$ mice exhibited the expected age-related increases in long bone diameter accompanied by decreases in BA/TA and cortical thickness. These changes in microarchitecture led to a decrease in the biomechanical properties of the bone at both the structural and material level. On the other hand, while decreases in the material properties were detected in the aged compared to skeletally mature WT mice, aged $Cx43^{OT}$ mice partially maintained these biomechanical properties at both the structural and material level, when compared to the 6-month-old mice. Further, pre-yield mechanical measurements were all increased in aged $Cx43^{OT}$ compared aged WT mice. Interestingly,

the pre-yield properties of the cortical bone in mice lacking osteocytic Cx43 were also reduced at both the structural and material level, while deficits in bone post-yield properties were only detected at the material level.[38] Based on the fact that we did not detect differences in cortical bone mass or geometry between the two genotypes at 14 months of age, it is reasonable to speculate that the increases in the structural and material properties in the 14-month-old $Cx43^{OT}$ mice are not due to changes in bone architecture, but are likely due to other factors at the level of the collagen/mineral. Thus, it is possible that the enhanced capability of the cortical bone of aged $Cx43^{OT}$ mice to resist damage is due to changes in bone material as a result of increased osteocyte viability.

Bone quality depends not only on the geometry and microarchitecture of the bone, but also on its material composition.[22, 57] Bone material properties include mineral content, collagen composition, and micro-damage accumulation.[57] Numerous studies have demonstrated the critical role that osteocytes play in sensing mechanical stimuli and coordinating targeted bone remodeling to repair damaged areas.[30, 89] Decreases in osteocyte viability have been observed in many conditions underlying bone loss.[44] However, the specific mechanisms by which viable osteocytes prevent bone fragility in aging are not known. In the current study we found that maintenance of osteocyte viability in the 14-month-old $Cx43^{OT}$ mice is associated with preserved cortical bone elastic material properties and an improved resilience.

Preliminary gene expression measurements showed that increased expression of Cx43 in osteocytes results in higher levels of keratocan (a proteoglycan) in osteocytic cells (Fig. 2-1A) and, not shown, Chsy1 (a glucosaminoglycan) and Lox (lysil oxidase, an enzyme involved in collagen maturation) in bone preparations. Interestingly, deletion of Cx43 from osteocytic cells results in decreased levels of Lox,[38] suggesting that, as with the biomechanical properties, Cx43 deletion and overexpression leads to opposite effects on collagen-related genes. Further studies are needed to understand the mechanism for

the changes in the material properties of the bone of mice expressing DMP1-Cx43. In addition, whether the improved ability of the bone to resist damage is due to prevention of microdamage accumulation or direct preservation of the bone material by living osteocytes or a combination of both, remains to be determined.

Findings from numerous studies have consistently shown the differential role of osteocytic Cx43 in the cortical and cancellous bone compartments.[37] Removal of Cx43 from mature osteoblasts and osteocytes or exclusively from osteocytes results in cortical bone changes, but does not alter cancellous bone.[38, 46] Further, other studies have shown that expression of a truncated Cx43 lacking the c-terminus domain can negatively affect cancellous bone, whereas heterozygous deletion of Cx43 attenuates cancellous bone loss during hindlimb unloading.[48, 49] Our findings that osteocyte-targeted Cx43 transgene expression was sufficient to reduce osteocyte apoptosis in the cortical and to a lesser extent in the cancellous bone compartments, whereas changes in bone turnover and improvements in the mechanical properties of the bone were only observed in cortical bone, further demonstrate the differential actions of Cx43 in the two bone compartments.

In summary, the findings from the current study further highlight the critical role osteocytes play in the maintenance of cortical bone structure and mechanical properties in aging, and demonstrate the requirement of Cx43-mediated actions in osteocytes for the preservation of osteocyte viability and cortical bone quality in aging. On the other hand, osteocytic Cx43 does not appear to play a critical role in maintaining cancellous bone in aged mice.

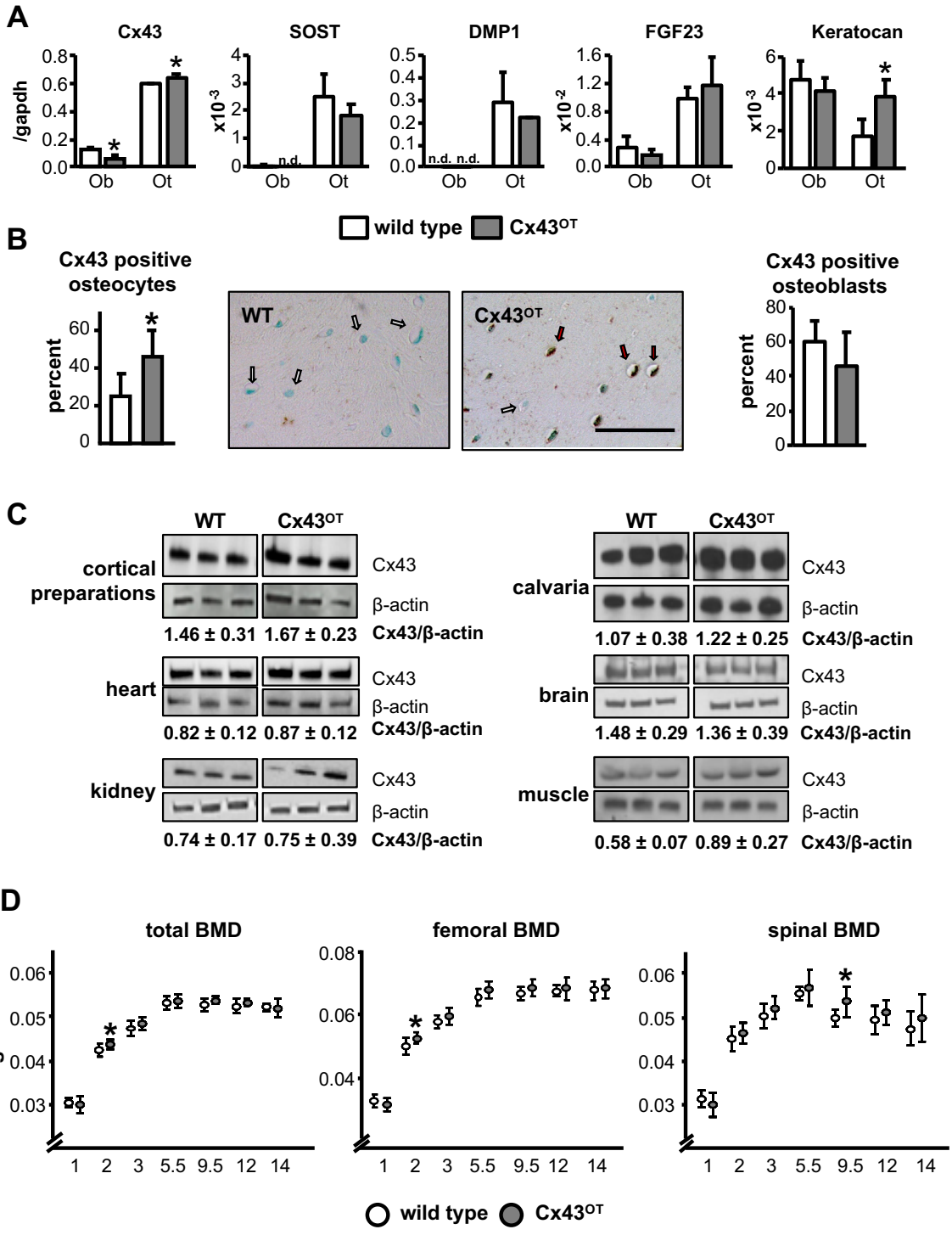
A
Cx43
SOST
DMP1
FGF23
Keratocan
/gapdh
x10-3
x10-2
n.d.
Ob
Ot
wild type
Cx43OT
B
Cx43 positive osteocytes
percent
WT
Cx43OT
Cx43 positive osteoblasts
C
WT
Cx43OT
cortical preparations
heart
kidney
calvaria
brain
muscle
Cx43
β-actin
1.46 ± 0.31 1.67 ± 0.23 Cx43/β-actin
0.82 ± 0.12 0.87 ± 0.12 Cx43/β-actin
0.74 ± 0.17 0.75 ± 0.39 Cx43/β-actin
1.07 ± 0.38 1.22 ± 0.25 Cx43/β-actin
1.48 ± 0.29 1.36 ± 0.39 Cx43/β-actin
0.58 ± 0.07 0.89 ± 0.27 Cx43/β-actin
D
total BMD
femoral BMD
spinal BMD
g/cm²
wild type
Cx43OT

Figure 2-1. Effective osteocyte targeted Cx43 transgene expression in DMP1-8kb-Cx43/GFP ($Cx43^{OT}$) mice. (A) mRNA expression in primary osteoblasts and osteocytes isolated from DMP1-8kb-GFP mice expressing GFP under the control of the 8kb fragment of the DMP1 promoter. Ob: osteoblastic cells; Ot: osteocytic cells; n.d.: non-detectable. Bars represent mean ± s.d. of triplicate measurements, *: $p<0.05$, t-test versus WT cells. (B) Cx43 expression in osteocytes and osteoblasts was evaluated in the femoral mid-diaphysis of $Cx43^{OT}$ and WT littermate mice stained with a non-immune IgG or anti-Cx43 polyclonal antibody, counterstained with 0.2% methyl green. Bars represent mean ± s.d., *: $p<0.05$, t-test versus WT mice, n=6 WT and n=4 $Cx43^{OT}$. Representative images of Cx43 negative (arrow, white) and Cx43 positive (arrow, red) osteocytes are shown. Scale bar indicates 25 μm. (C) Cx43 protein levels measured in marrow-flushed cortical bone preparations, calvarial bones, and in the soft tissues of $Cx43^{OT}$ and WT mice by western blot correct by β-actin levels, n=3. (D) Total body, spinal and femoral BMD were measured from 1 to 14 months of age by DXA in females, n=13 WT and n=11 $Cx43^{OT}$. Symbols represent ± s.d., *$p<0.05$ versus WT littermates by t-test.

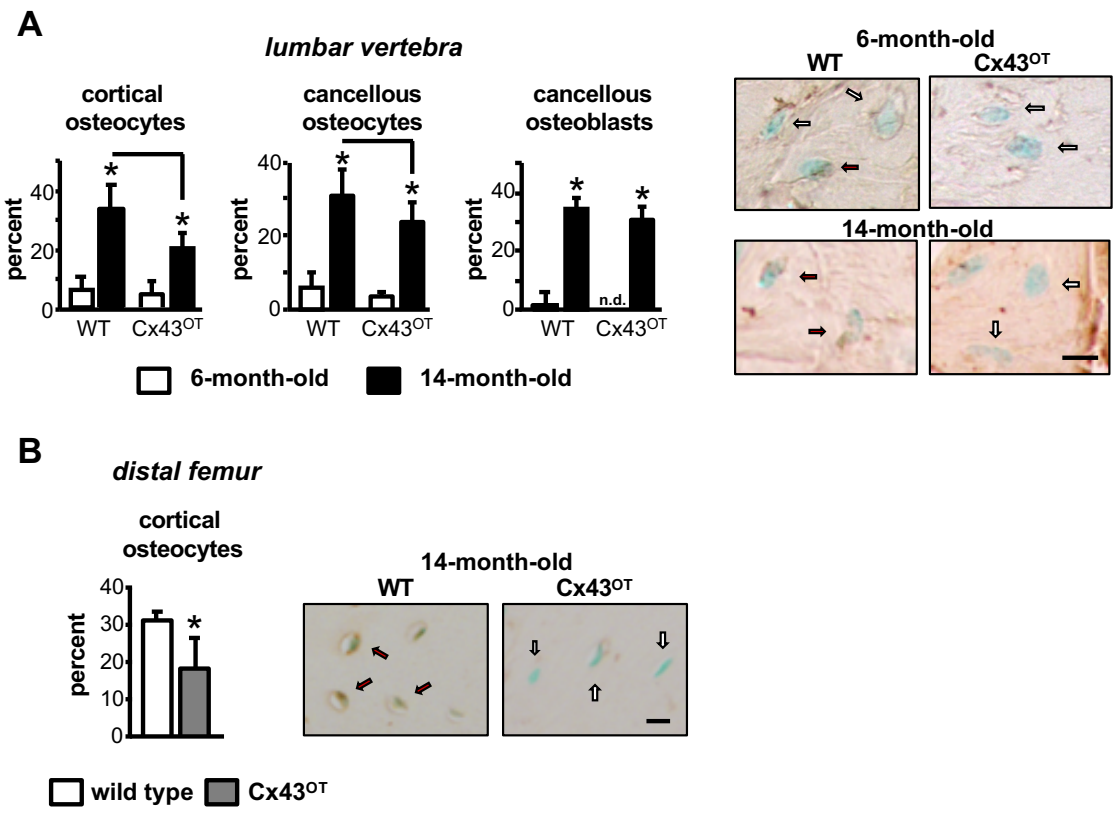

Figure 2-2. Expression of Cx43 in osteocytes reduces osteocyte apoptosis induced with aging. (A) Percentage of apoptotic (TUNEL positive) cortical and cancellous osteocytes, as well as, cancellous osteoblasts were scored in vertebral bone sections. Bars represent mean ± s.d., *: $p<0.05$, versus 6-month-old genotype-matched mice by two-way ANOVA, tukey, black line: $p<0.05$, versus old control mice by t.test. 6-month-old mice: n=9 WT and n=8 $Cx43^{OT}$, 14-month-old mice: n=8 WT and n=7 $Cx43^{OT}$. Representative images of TUNEL negative (arrow, white) and positive (arrow, red) osteocytes are shown. Scale bar indicates 2.5 μm. (B) Percentage of apoptotic cortical osteocytes were scored in longitudinal distal femur sections from 14-month old mice. Bars represent mean ± s.d., *: $p<0.05$ versus WT littermates by t-test, n=7 WT and n=9 $Cx43^{OT}$. Representative images of TUNEL negative (arrow, white) and positive (arrow, red) osteocytes are shown. Scale bar indicates 6.25 μm.

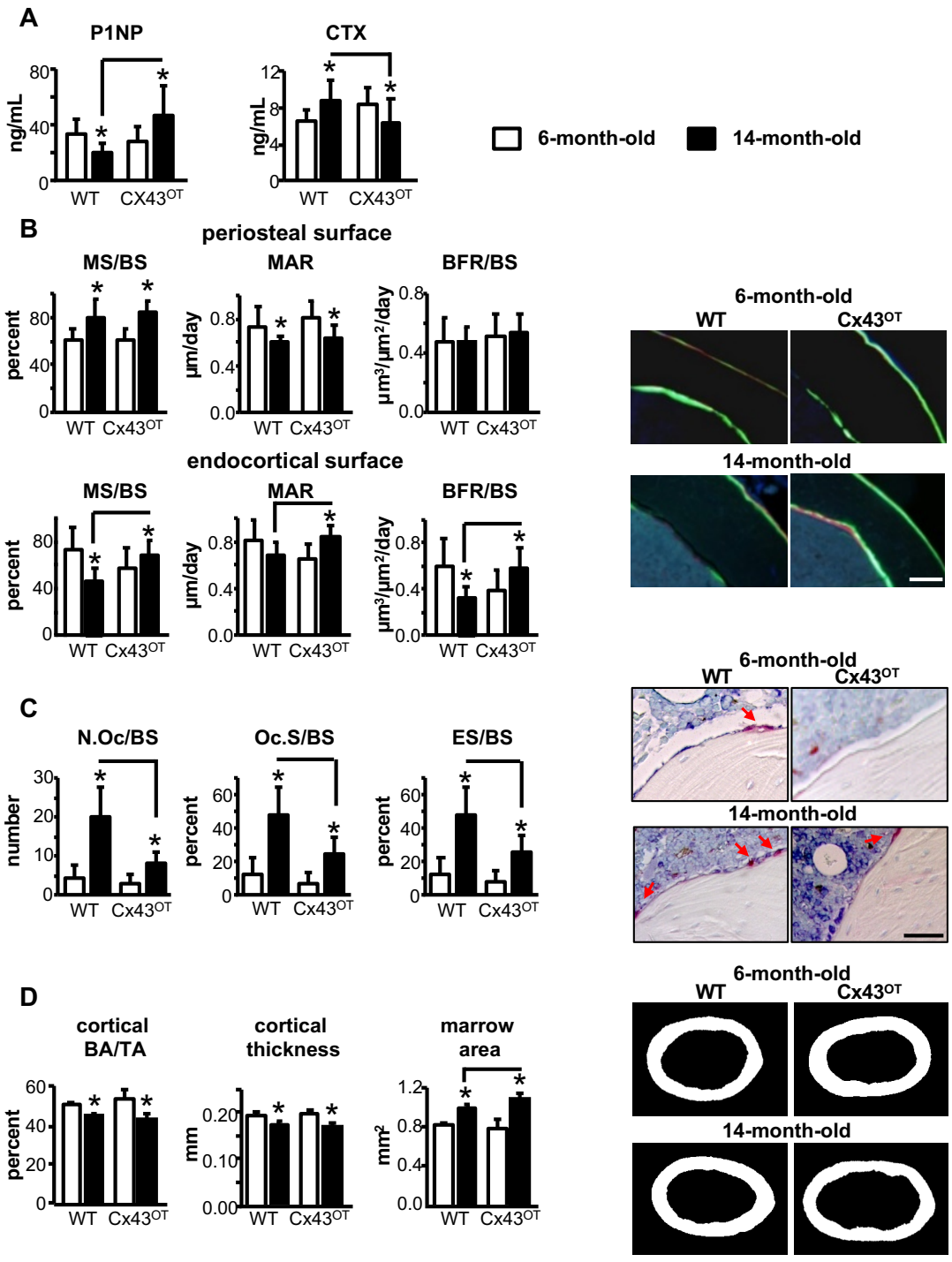

Figure 2-3. 14-month-old Cx43^{OT} mice exhibit enhanced endocortical bone formation and decreased resorption. (A) Circulating levels for P1NP and CTX were measured by ELISA in serum collected from 6- and 14-month-old mice. 6-month-old mice: n=10 WT and n=9

$Cx43^{OT}$, 14-month-old mice: n=11 WT and n=9 $Cx43^{OT}$. (B)Periosteal and endosteal MS/BS, MAR, and BFR/BS were measured in unstained sections from the femoral mid-diaphysis. 6-month-old mice: n=9 WT and n=9 $Cx43^{OT}$, 14-month-old mice: n=8 WT and n=7 $Cx43^{OT}$. Representative images are shown. Scale bars indicate 100μm. (C) N.Oc/BS, Oc.S/BS, ES/BS were scored in femoral cortical mid-diaphysis after staining for TRAP/Toluidine blue in $Cx43^{OT}$ and WT mice. 6-month-old mice: n=9 WT and n=9 $Cx43^{OT}$, 14-month-old mice: n=5 WT and n=7 $Cx43^{OT}$. Osteoclasts on the bone surface (arrow, red) are shown. (D) Cortical bone geometry was evaluated by μCT in the femoral mid-diaphysis. 6-month-old mice: n=8 WT and n=9 $Cx43^{OT}$, 14-month-old mice: n=8 WT and n=6 $Cx43^{OT}$. Representative reconstructed images of the femoral mid-diaphysis are shown. Bars represent mean ± s.d., *: $p<0.05$, versus 6-month-old genotype-matched mice by two-way ANOVA, tukey, black line: $p<0.05$, versus old control mice by t.test.

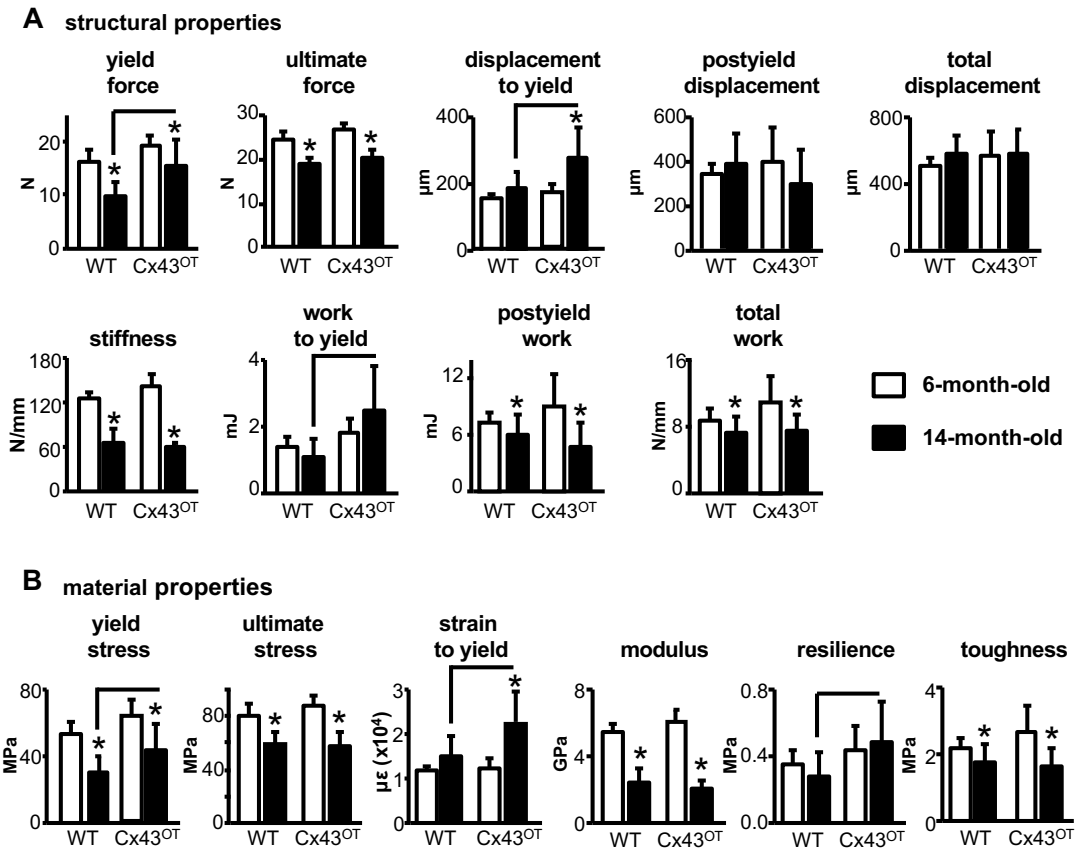

Figure 2-4. Cx43^{OT} mice exhibit increased cortical bone resilience to fracture that is maintained with advanced age. Cortical bone biomechanical properties structural (A) and material (B) were evaluated by femoral 3-point bending testing. 6-month-old mice: n=7 WT and n=5 Cx43^{OT}, 14-month-old mice: n=11 WT and n=8 Cx43^{OT}. Bars represent mean ± s.d., *: $p<0.05$, versus 6-month-old genotype-matched mice by two-way ANOVA, tukey, black line: $p<0.05$, versus old control mice by t.test.

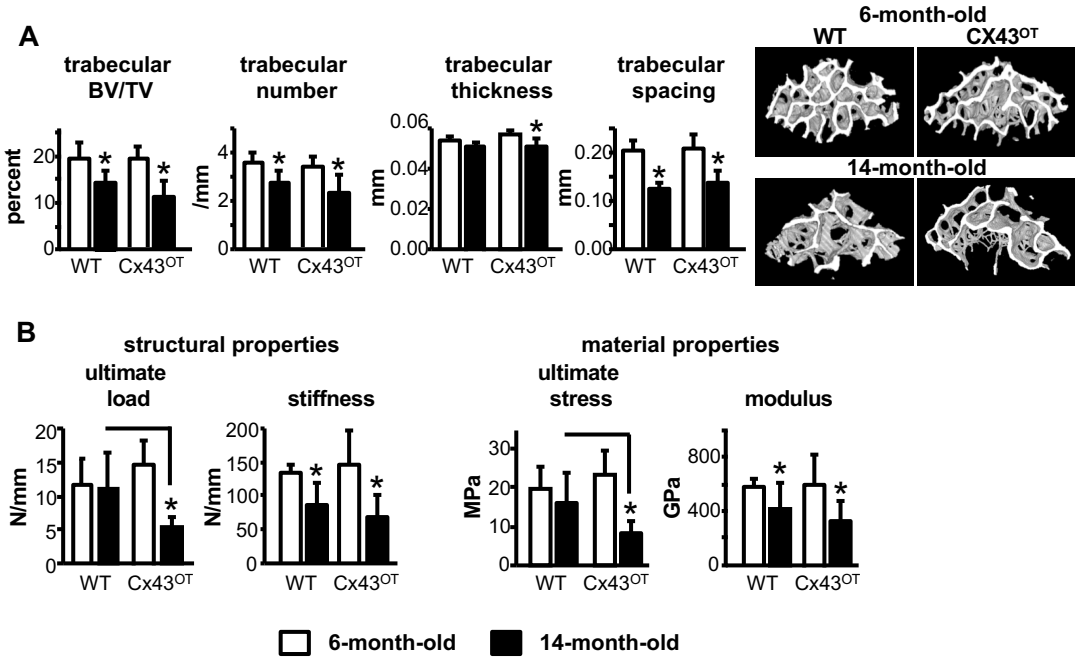

Figure 2-5. Cx43^{OT} mice are not protected against age-induced loss of cancellous bone mass. (A) Cancellous bone microarchitecture was evaluated by μCT in the distal femur L4 vertebra. 6-month-old mice: n=7 WT and n=5 Cx43^{OT}, 14-month-old mice: n=14 WT and n=11 Cx43^{OT}. Representative reconstructed 3D μCT images are shown. (B) Mechanical testing of the structural and material properties was evaluated by axial compression on the L4 vertebra. 6-month-old mice: n=7 WT and n=7 Cx43^{OT}, 14-month-old mice: n=13 WT and n=10 Cx43^{OT}. Bars represent mean ± s.d., *: $p<0.05$, versus 6-month-old genotype-matched mice by two-way ANOVA, tukey, black line: $p<0.05$, versus old control mice by t.test.

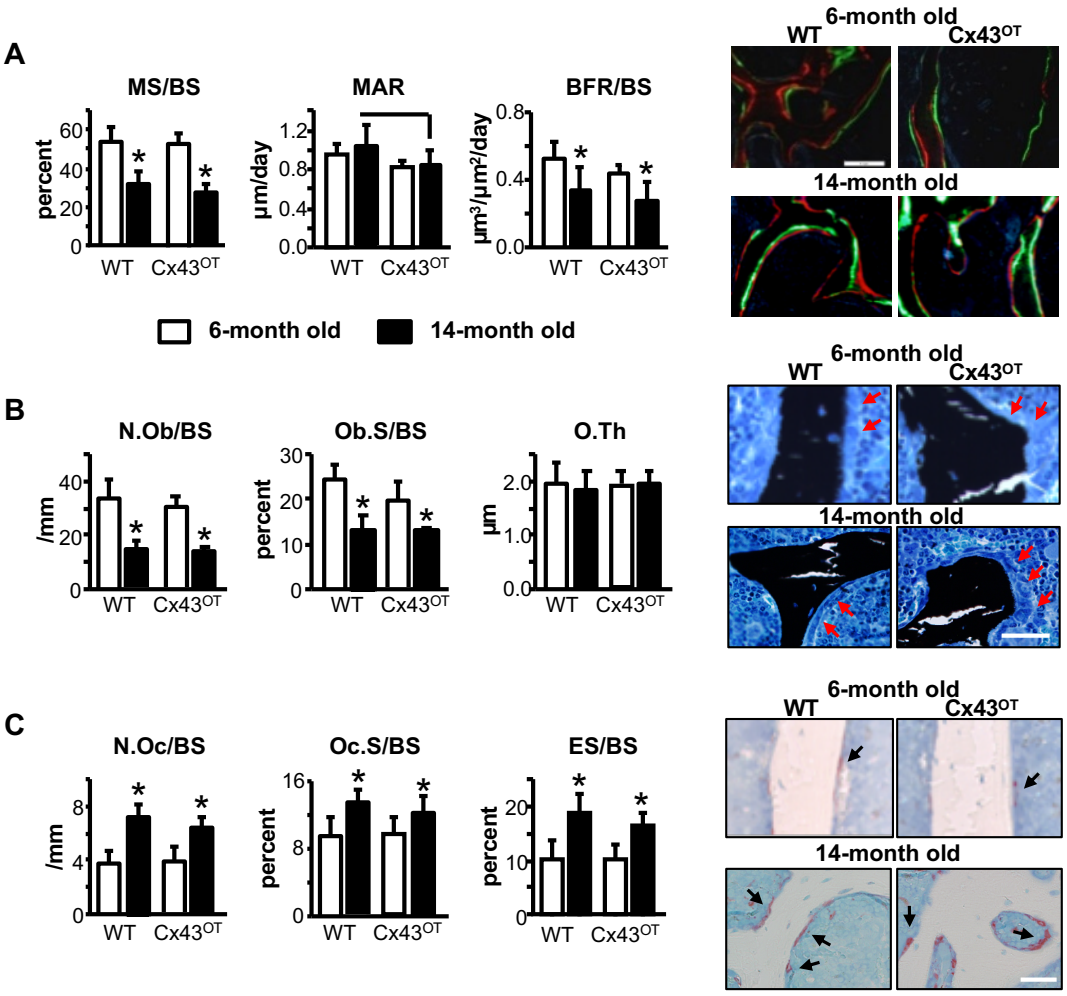

Figure 2-6. Expression of osteocytic Cx43 does not alter changes in cancellous osteoblast or osteoclast activity induced with aging. (A) Vertebral cancellous bone MS/BS, MAR, and BFR/BS were measured in unstained longitudinal vertebral sections. 6-month-old mice: n=9 WT and n=7 Cx43^{OT}, 14-month-old mice: n=8 WT and n=8 Cx43^{OT}. Representative images show green and red fluorochrome levels. (B) N.Ob/BS, Ob.S/BS and O.Th were scored in lumbar vertebra sections stained with von Kossa/McNeal. 6-month-old mice: n=9 WT and n=8 Cx43^{OT}, 14-month-old mice: n=7 WT and n=7 Cx43^{OT}. Representative osteoblast images are shown (arrow, red). (C)Cancellous osteoclasts were scored in TRAP/Toluidine blue stained vertebral bone sections. N.Oc/BS, Oc.S/BS, and ES/BS are

reported. 6-month-old mice: n=10 WT and n=8 $Cx43^{OT}$, 14-month-old mice: n=7 WT and n=8 $Cx43^{OT}$. Representative osteoclast images are shown (arrow, black). Bars represent mean ± s.d., *: $p<0.05$, versus 6-month-old genotype-matched mice by two-way ANOVA, tukey, black line: $p<0.05$, versus old control mice by t.test. Scale bars indicates 100μm.

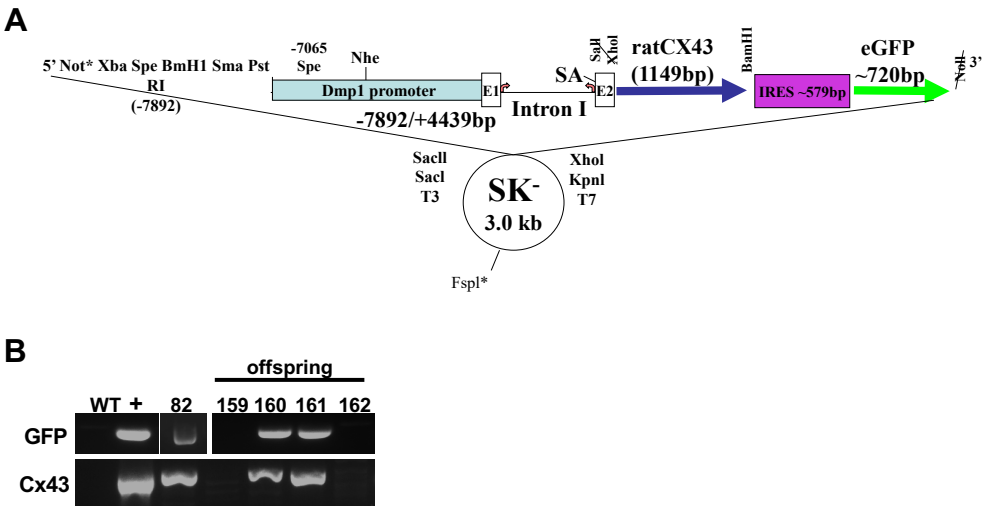

Figure 2-7. Osteocyte targeted Cx43 transgene expression in DMP1-8kbCx43/GFP (Cx43OT) mice. (A) DNA map of CMV-Cx43/GFP transgene construct. (B) Genotyping of mouse founder # 82 and its litter using primers to identify GFP and the transgene containing Cx43. +: DMP1-GFP mouse for GFP (upper line) and the construct injected in the mice for Cx43 (bottom line).

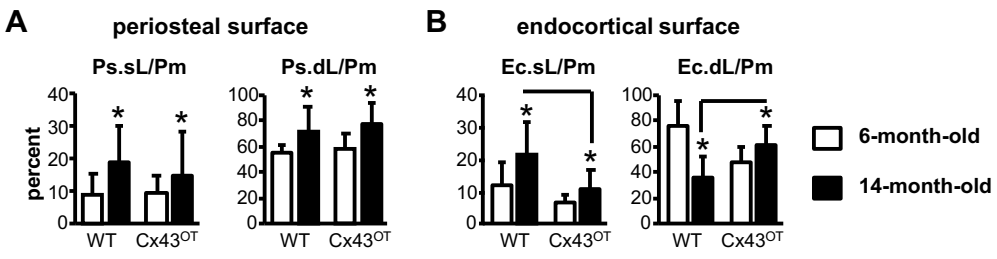

Figure 2-8. Cx43 overexpression alters the percent single- and double-labeled surfaces on the periosteum and endosteum of the femur mid-diaphysis. Percentage of single and double-labeled surfaces were measured on the periosteal (A) and endosteal (B) surfaces in unstained sections from the femoral mid-diaphysis. Bars represent mean ± s.d., *: $p<0.05$, versus 6-month-old genotype-matched mice by two-way ANOVA, tukey, black line: $p<0.05$, versus old control mice by t.test.

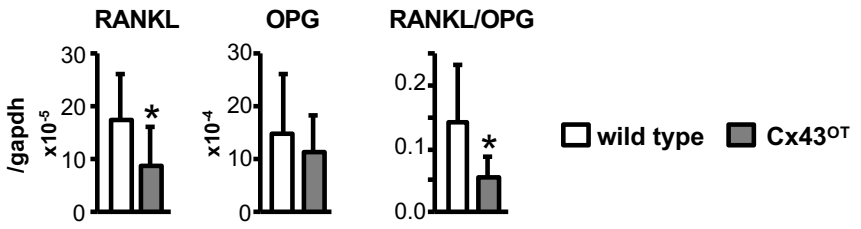

Figure 2-9. RANKL and the RANKL/OPG mRNA ratio in bone was decreased in old $Cx43^{OT}$ compared to WT mice at the same age. Bars represent mean ± s.d., *: $p<0.05$, versus old control mice by t.test.

Chapter 3

Disruption of the Cx43/miR21 pathway leads to osteocyte apoptosis and increased osteoclastogenesis with aging

Rationale

Skeletal aging results in apoptosis of osteocytes, cells embedded in bone that control the generation/function of bone forming and resorbing cells. Aging also decreases Cx43 expression in bone; and osteocytic Cx43 deletion partially mimics the skeletal phenotype of old mice. Particularly, aging and Cx43 deletion increase osteocyte apoptosis, and osteoclast number and bone resorption on endocortical bone surfaces. Based on these findings, we examined herein the molecular signaling events responsible for osteocyte apoptosis and osteoclast recruitment triggered by aging and Cx43 deficiency.

Introduction

Increasing evidence suggests that the viability of osteocytes embedded within the bone mineral matrix is essential for maintaining skeletal homeostasis, as supported by the increase in apoptotic osteocytes and prevalence of empty lacunae observed in conditions of elevated bone fragility and with old age.[75] Osteocytes have long dendritic processes that create an extensive network allowing for communication between adjacent osteocytes and with osteoblasts and osteoclasts on the bone surface; and disruption of this network impairs osteocytic regulation of bone formation and resorption.[30] Osteocyte interactions with other cells occur through the release of cytokines to the lacunar-canalicular system that surrounds osteocytes, as well as through cell-to-cell communication via gap junction channels.[37] Previous work from our group has demonstrated that the gap junction protein connexin 43 (Cx43) is a critical component of the signaling pathway controlling osteocyte

survival, as evidenced by the increased osteocyte apoptosis in mice lacking Cx43 in osteoblasts and osteocytes or only in osteocytes.[40, 46] In addition to increased osteocyte apoptosis, mice lacking osteocytic Cx43 ($Cx43^{\Delta Ot}$) exhibit enhanced endocortical resorption, partially mimicking the phenotype of old mice [8] and raising the possibility that decreased Cx43 contributes at least in part to the skeletal phenotype of aging. However, while it has been shown that Cx43 levels in osteocytes are decreased in old mice,[91] the signaling pathway activated by Cx43 deficiency involved in osteocyte apoptosis with aging is not known.

One of the potential molecules that could mediate osteocyte apoptosis are microRNAs (miRs), single-stranded non-coding RNAs that negatively regulate gene expression.[58] miRs are involved in cancer cell survival, and in particular, the expression of miR21 is upregulated in a variety of cancers, promoting cell survival through the direct inhibition of apoptotic genes including phosphatase and tensin homolog (PTEN).[59] In bone, miRs play an important role in controlling the function and lifespan of both osteoclasts and osteoblasts.[60] However, the role of miRs on osteocyte apoptosis has not been investigated.

Several models of increased osteocyte death, including ovariectomy, unloading, microdamage, and a transgenic model of osteocyte apoptosis induced by diphtheria toxin, exhibited co-localization of apoptotic osteocytes and osteoclasts, suggesting that signals released by dying osteocytes induce osteoclast recruitment.[26-29] However, the nature of these signals remains unknown. In osteocytes and other cells, apoptotic cell death results in the release of the pro-inflammatory cytokine high-mobility group box-1 (HMGB1), a non-histone nuclear DNA-binding protein responsible of stabilization of nucleosomal structures facilitating gene transcription.[50, 51] HMGB1 released from the cells activates the receptor for advanced glycation end products (RAGE) and toll-like receptor 4 (TLR4), and can regulate recruitment and differentiation of osteoclast precursors.[54, 55] However, whether

HMGB1 is involved in osteoclast recruitment and differentiation induced by apoptotic osteocytes is not known.

Based on the results of the current study, we propose that miR21 lies downstream of Cx43 in the control of osteocyte viability; and that increased osteocyte apoptosis in the absence of Cx43 and with aging is a consequence of disruptions in the PTEN/pAkt pathway and reduced response to the insulin like growth factor 1 (IGF-1). Further, the increased osteoclastogenic potential of Cx43-deficient osteocytes is a result of elevated release of the cytokines RANKL and HMGB1 during apoptosis, and the subsequent activation of RAGE on osteoclast progenitors. In conclusion, our data identifies a novel Cx43/miR21/HMGB1/RANKL pathway mediated by gap junction communication in osteocytes that could be targeted to treat bone fragility in aging.

Experimental procedures

Mice. C57BL/6 female mice were purchased from National Institute on Aging and sacrificed at 4, 12, 18, 21 and 24 months of age. To delete Cx43 specifically in osteocytes, mice were generated using the Cre/LoxP system.[46] $Cx43^{fl/fl}$ mice were crossed with mice harboring DMP1-8kb-Cre, which express Cre recombinase under control of a DNA fragment containing 8kb of the murine dentin matrix protein 1 promoter (abbreviated as $Cx43^{\Delta Ot}$). Mice harboring both 'floxed' miR21 alleles (abbreviated as $miR21^{fl/fl}$) were generated by M. Ivan and crossed amongst themselves. All mice used were maintained in a C57BL/6 background. The protocols involving mice were approved by the Institutional Animal Care and Use Committee of Indiana University School of Medicine.

Cell culture, silencing and transient transfections. MLO-Y4 osteocytic and Ob-6 osteoblastic cells were silenced using short hairpin (sh)RNA Lentiviral Particles (Sigma-Aldrich), as previously reported,[40, 92] and cultures as previously described. The efficiency of deletion was determined by quantifying Cx43 protein and mRNA levels by Western blotting and by qPCR, respectively. All samples from *in vitro* studies were collected 24h after seeding the cells or 48h after transfection, unless otherwise indicated. The plasmid encoding the full length rat Cx43 (abbreviated as Wt) was provided by R. Civitelli (Washington University, Saint Louis, MO).[93] The mutant Cx43 truncated at amino acid 245 (abbreviated as $Cx43^{\Delta 245}$)[94] and the Cx43 carboxy-terminal tail (abbreviated as $Cx43^{C\text{-}tail}$)[94] were provided by B. Nicholson (University of Texas, Santo Antonio, TX). Cx43 lacking seven residues from the internal loop at positions 130-136 (abbreviated as $Cx43^{\Delta 130}$) was provided by V.A. Krutovskikh (International Agency for Research on Cancer, Lyon, France).[95] $Cx43^{Cys\text{-}less}$, which has all cysteine sites on the two extracellular loops replaced by alanine (abbreviated as $Cx43^{Cys\text{-}less}$) was provided by G.M. Kidder (University of

Western Ontario, Ontario, Canada).[77] All of the constructs used in this study are of rat origin and have been shown to produce functional proteins. pcDNA3.1 empty vector was used as control (Invitrogen). MLO-Y4 osteocytic cells were transiently transfected with different DNA constructs together with nuclear GFP using Lipofectamine Plus (Invitrogen) reagent with 0.1μg/cm^2 as described previously.[92] Apoptosis was assessed 48h after trasnfection by quantification of cells exhibiting nuclear fragmentation and chromatin condensation under an EVOS fluorescence microscope system (Life Technologies, Carlsbad, CA). HeLa cells (2x10^{4}cells/cm^2) were transiently transfected with either empty vector or rat Cx43 together with IGFR1 and nuclear GFP using Lipofectamine Plus, as published,[96] and apoptosis was assessed as indicated below.

Western Blotting analysis. Whole protein extracts from MLO-Y4 osteocytic cells or from bone were prepared as published.[46, 74] To determine the levels of HMGB1 on culture supernatants, proteins concentrated 10x by precipitation using trichloroacetic acid (5:1). Protein lysates were separated on 10% SDS-PAGE gels and electrotransferred to polyvinylidene difluoride (PVDF) membranes (Millipore, Billerica, MA). These membranes were incubate in blocking solution (5% non-fat milk) for 30 minutes and probed with primary antibodies diluted 1:1000 in 5% non-fat milk against a monoclonal anti-PTEN (Sc-7974), polyclonal anti-GADD153 (Sc-575), anti-lamin B (Sc-6217) (Santa Cruz Biotechnology, Santa Cruz, CA), monoclonal anti-Akt (2920), anti-phosphorylated Akt at serine 473(4060) (Cell Signaling Technology, Danvers, MA), anti-caspase3 cleaved (Asp175) (Thermo Fisher Scientific, Rockford, IL, PA5-23921), anti-connexin43 (C6219) and anti-β-actin (A5316) (Sigma Aldrich), and anti-HMGB1 (ab18256) (Abcam, Cambridge, MA) overnight at 4ºC, followed by corresponding secondary antibodies conjugated with horseradish peroxidase in 5% non-fat milk (Santa Cruz Biotechnology, Santa Cruz, CA) for 4 hours at room temperature. After rinsing with TBS-T, the

membranes were developed with an enhanced chemiluminescence Western blotting substrate kit (Pierce Biotechnology Inc., Rockford, IL). Bands were detected and their intensity was quantified using the TotalLab TL 100 software (Durham, NC).

RNA extraction and real-time PCR (qPCR). Total RNA was isolated and purified using TRIzol (Invitrogen, Grand Island, NY), as published.[83] Reverse transcription was performed using a high-capacity cDNA kit (Applied Biosystems, Foster City, CA). qPCR was performed using the Gene Expression Assay Mix TaqMan Universal Master Mix with an ABI 7900HT real-time PCR system. The house-keeping gene glyceraldehyde 3-phosphate dehydrogenase (GAPDH) was used. Primers and probes were commercially available (Applied Biosystems, Foster City, CA) or were designed using the Assay Design Center (Roche Applied Science, Indianapolis, IN). To evaluate miR expression levels, total RNA was isolated and purified using TRIzol reagent and 10ng were reversely transcribed to cDNA using TaqMan microRNA reverse transcription kit (Applied Biosystems, Carlsbad, CA) to detect and quantify mature miR21 (assay ID: 000397), miR18 (assay ID: 000521), and miR135 (assay ID: 001230). The reaction mixtures were incubated at 16°C for 30 minutes, 42°C for 30 minutes, 85°C for 5 minutes, and 4°C for 30 seconds. The values were normalized for housekeeping miR135. Relative expression was calculated using the ΔCt method.

IGF-1, DEVD, and PTEN inhibitor treatment. MLO-Y4 osteocytic cells or HeLa cells were treated with vehicle or 5 ng/mL IGF-1 for 1h, followed by 6h treatment with vehicle or 10^{-6} M dexamethasone. In addition, in a parallel experiment, MLO-Y4 osteocytic cells were treated with vehicle or 1μM SF1670 (Abcam Biochemical, Cambridge, MA) for 30 min and then cultured for 24 hours. For apoptosis inhibition, cells were treated for 1 hour with 50nM Ac-DEVD-CHO (DEVD, Biotium, Inc., Hayward, CA), a caspase-3/7

inhibitor, which was then removed and cells were cultured in fresh media for 24 hours, or treated for 24h with 50nM DEVD. To determine the percentage of dead cells, supernatant was removed and cells were re-suspended in 25µL of 1x trypan blue. Ten microliters of the cell suspension were transferred to a hemocytometer and the number of viable cells (clear, transparent) and dead (blue) were counted. Data is reported as percentage of dead cells. Cells were transfected with the indicated constructs together with nuclear GFP to assess the nuclear morphology only in transfected cells. Forty-eight hours after transfection cells were washed to remove dead cells, and treated with 5 ng/mL IGF-1 for 1h, followed by 10^{-6} M dexamethasone. Cells were fixed 6h later and the prevalence of apoptotic cells exhibiting chromatin condensation and nuclear fragmentation was assessed under fluorescence microscopy. Data is reported as percentage of apoptotic cells.

miRNA micro array analysis. The effect of Cx43 silencing on miRNA levels in MLO-Y4 osteocytic cells was assessed using the Apoptosis-Associated miRNA Plate Array, as described by the manufacturer (Signosis Inc., Santa Clara, CA, cat. # MA-1002). The values were normalized for U6 RNA.

microRNA silencing and overexpression. MLO-Y4 osteocytic cells silenced or not for Cx43 were plated at the density of $2x10^4$ cells/cm^2 on 48-well plates coated with type I rat tail collagen overnight. Cells were transiently transfected using Lipofectamine RNAiMAX reagent (Invitrogen) containing miRIDIAN negative control inhibitor, miR21 inhibitor, negative control mimic or miR21 mimic (GE Healthcare Bio-Sciences, Pittsburgh, PA) at a final concentration of 0.1nM in medium without serum and penicillin/streptomycin for 6 hours. Next, medium 2x concentrated was added to each well and then cultured overnight**.** Medium was changed to a regular growing medium and cells were then cultured

for an additional 24 hours before measuring cell death by Trypan blue uptake. miR21 levels were decreased by 60% in MLO-Y4 scramble cells and by 91% in MLO-Y4 Cx43 shRNA cells treated with miR21 inhibitor, as measured by qPCR. miR21 levels were increased by 44% in MLO-Y4 scramble cells and 234% in MLO-Y4 Cx43 shRNA cells treated with the miR21 mimic.

Viral infection of calvaria bone ex vivo. Calvariae of miR21$^{fl/fl}$ mice were harvested at 5 days of age and two 5mm pieces of the bone were removed using a biopsy punch (Integra LifeSciences Corporation, New Jersey, USA). Samples were washed in PBS and incubated in a 96-well plate with α-minimal essential medium supplemented with 10% FBS and 1% penicillin/streptomycin for 6 hours. Bones were then treated with 2.5µl/well of control adenovirus (Adeno-GFP, cat.#1060) or Cre-recombinase virus (cat.#1700) (Vector BioLabs Malvern, PA, USA) diluted in serum-free α-minimal essential medium in a final volume of 45 µl overnight. Next, media was removed and samples were washed twice with PBS before adding α-minimal essential medium supplemented with 10% FBS and 1% penicillin/streptomycin and cultured for additional 48h at 37% and 5% CO_2. mRNA was quantified by qPCR and protein quantified by Western blotting.

Transmission electron microscopy (TEM). Calvaria bones from miR21$^{fl/fl}$ mice treated with adenovirus (Adeno-GFP, cat.#1060) or Cre-recombinase virus were processed for TEM as previously published.[46] Briefly, bones were decalcified and post-fixed in 2% paraformaldehyde/2% glutaraldehyde in 0.1M cacodylate buffer for 1h, followed by 1h-treatment with 1% osmium tetroxide in 0.1M cacodylate buffer. After standard dehydration and embedding in Embed 812 (Electron Microscopy Sciences, Hatfield PA) the blocks were sectioned at 85nm and placed on copper grids, stained with uranyl acetate, and viewed on a Tecnai G2 12 Bio Twin electron microscope (FEI,

Hillsboro, OR) at the Electron Microscopy Center of the Department of Anatomy and Cell Biology (Indiana University School of Medicine). Digital images were taken with an Advanced Microscope Techniques (Danvers, MA) CCD camera.

Osteoclastogenesis in co-cultures and with conditioned medium. Bone marrow cells were isolated from C57BL/6 mice by flushing the bone marrow out with α-minimal essential medium supplemented with 10% FBS and 1% penicillin/streptomycin and cultured for 25-48h. Next, non-adherent were collected and $2x10^5$ cells/cm^2 were seeded on top of MLO-Y4 osteocytic cells silenced or not for Cx43. Cells were cultured in the presence of 10 nM $1.25(OH)_2$ vitamin D3 and 1 μM PGE2. Medium was changed every 2 days for 5 days, as previously published.[97] The conditioned medium from MLO-Y4 osteocytic cells silenced or not for Cx43 was collected after 24 h and then concentrated 4x using centricon filters (10kD cut off) (EDM Millipore, Billerica, MA). Media was diluted 1:4 and added to 48-well plate containing $2x10^5$ non-adherent cells/cm^2 with 40 ng/ml RANKL and 20 ng/ml M-CSF.[83] Growing medium that had not been in contact with the cells was used as control. Osteoclasts exhibiting 3 or more nuclei were enumerated after staining for TRAPase using a commercial kit (Sigma-Aldrich). Images were acquired using a Zeiss Axiovert 35 microscope equipped with a digital camera.

Neutralization of HMGB1 in cell cultures. MLO-Y4 osteocytic cells silenced or not for Cx43 were plated at the density of $2x10^5$ cells/cm^2 on 6-well plates coated with type I rat tail collagen overnight. Cells were either treated with 1 mg/ml GA[98] or with 0.5μg/ml non-immune (ni) rabbit IgG (Abcam, Cambridge, MA, cat.# ab171870) or neutralizing rabbit anti-HMGB1 (Abcam, cat.# ab18256) antibodies for 24h and then concentrated 4x using centricon filters (10kD cut off) (EDM Millipore, Billerica, MA). For cultures with immunoglobulins, conditioned media was incubated with 10 μl/ml Protein A agarose

(Roche Applied Science, Indianapolis, IN, cat.# 11719408001) overnight at 4°C to remove the immunoglobulins. 1M HEPES was then added to IgG-depleted conditioning media, which was then aliquoted and stored at 80ºC until used.

Soluble RANKL, OPG and HMGB1 levels in conditioned media. Conditioned media from MLO-Y4 cells were collected, aliquoted, and stored at -80ºC until used. RANKL, OPG and HMGB1 protein levels in the supernatants were determined using Quantikine Mouse RANKL Immunoassay (R&D Systems, Inc., Minneapolis, MN, cat.# MTR00), Quantikine Osteoprotegerin Immusoassay (R&D Systems, Inc., Minneapolis, MN, cat.# MOP00) or HMGB1 Immunoassay (IBL International, Germany, cat.# ST51011), respectively.

Statistical analysis. Data were analyzed using SigmaPlot (Systat Software Inc., San Jose, CA). All values are reported as the mean ± standard deviation. Differences were evaluated either by one- or two-way ANOVA, with post-hoc analysis using Tukey Method or by Student's t-test, as appropriate. Differences were considered significant when $p<0.05$.

Results

Aging and Cx43 deficiency result in increased osteocyte apoptosis. Bones from 24-month-old mice exhibited a decrease in Cx43 mRNA levels compared to 4-month-old mice (Fig. 3-1A), and 21-month-old mice exhibited a 95% decrease in Cx43 protein levels, compared to young, 3.5-month-old mice (Fig. 3-1B). Consistent with the increased osteocyte apoptosis reported in old humans and mice,[8, 45] bones (without bone marrow) from 21-month-old mice exhibit increased expression of apoptosis-related genes (Fig. 3-1C). To further study the connection between reduced Cx43 levels and osteocyte apoptosis, we used an *in vitro* system in which Cx43 was silenced in osteocytic and osteoblastic cells. Silencing Cx43 in MLO-Y4 osteocytic and Ob-6 cells using shRNA resulted in a significant reduction in mRNA levels (Fig. 3-1D), and ~70% and 60% reduction at the protein level respectively, compared to cells treated with scramble shRNA (Fig. 3-1E). Decreased Cx43 expression led to increased cell death in culture over time in MLO-Y4 osteocytic cells, as previously shown.[46] Cx43 deficiency does not increase osteoblast apoptosis *in vivo*, and, similarly, silencing Cx43 in Ob-6 osteoblastic cells did not alter viability, compared to scramble shRNA-treated cells (Fig. 3-1F). Cell death in MLO-Y4 osteocytic cells lacking Cx43 was reversed by DEVD treatment, an irreversible active caspase-3 inhibitor, indicating cell death by apoptosis (Fig. 3-1G). Furthermore, mRNA levels of FoxO3, p27 and GADD153, genes involved with apoptosis[99] were increased in MLO-Y4 Cx43-silenced cells (Fig. 3-1H) but unaltered in Ob-6 cells (Fig. 3-7A). Consistent with this, protein levels for GADD153 and for the apoptosis marker active caspase-3 were increased in Cx43-deficient cells (Fig. 3-1I).

We next investigated the domain of Cx43 required to maintain cell viability. As expected, expression of full-length Cx43 decreased apoptosis in Cx43-silenced MLO-Y4 cells (Fig. 3-1J and Fig. 3-7B). Similarly, $Cx43^{\Delta 245}$, lacking the C-terminus scaffold domain, as well as simultaneous transfection with $Cx43^{\Delta 245}$ and the C-terminus domain (C-tail),

which reassemble to form a complete connexin molecule in the cell,[100] reversed the increase in apoptosis. On the other hand, this Cx43 mutant is not able to confer responsiveness to bisphosphonates or to PTH.[92, 96] Cx43-silenced cells expressing the Cx43 C-tail alone or $Cx43^{Cys\text{-}less}$, a mutant that due to the lack of Cysteine residues in the extracellular domain[101] only forms hemichannels and it is unable for form gap junctions,[77, 102] maintained an elevated percentage of apoptosis, similar to vector-transfected cells. This contrasts with the reversal of the effect of Cx43 silencing in osteoblastic cells by the same $Cx43^{Cys\text{-}less}$ mutant.[92] Furthermore, expression of $Cx43^{\Delta 130}$, a mutant that lacks channel permeability,[95] not only did not reverse the increase in cell death, but further increased apoptosis, compared to Cx43-silenced cells transfected by empty vector.

Decreased Cx43 expression reduces miR21, promoting osteocyte apoptosis. We next examined whether increased apoptosis was associated with dysregulation of miRs in Cx43-deficient osteocytic cells. Screening of apoptosis-associated miRNAs revealed a decrease in the levels of miR21, which promotes survival in various cell types[59] but is of unknown function in osteoblastic cells (Fig. 3-2A). On the contrary, miR218, a pro-apoptotic miR, was expressed at higher levels in Cx43-deficient MLO-Y4 cells, compared to cells treated with scramble-shRNA. Changes in the expression was confirmed by qPCR, which showed that miR21 is decreased by 50% whereas miR218 is increased by 500% in Cx43-deficient osteocytic cells (Fig. 3-2B). Consistent with increases in miR218, expression of its target IκB kinase B was reduced (not shown). On the other hand, silencing Cx43 did not alter the levels of miR21, miR218 (Fig. 3-2C) or IκB kinase B (not shown) in Ob-6 osteoblastic cells. In addition, 24-month-old mice exhibited a decrease in miR21 levels, compared to young mice, similar to $Cx43^{def}$ cells. The expression of miR218 was not significantly changed in the bones from aging mice,

although it showed a tendency towards increase in 18-month-old mice (Fig. 3-2D). Furthermore, $Cx43^{\Delta Ot}$ mice lacking Cx43 in osteocytes exhibit reduced miR21 levels; however, miR218 and IκB kinase B were not altered (Fig. 3-2E).

Reduced miR21 levels lead to osteocytic cell death and increased PTEN levels in bone. Similar to silencing Cx43 gene, reduction of miR21 expression by transfecting a specific oligonucleotide inhibitor induced apoptosis of control osteocytes, whereas transfection of a miR21-mimic oligonucleotide resulted in lower levels of dead cells in scramble-transfected cells (Fig. 3-3A). Further, miR21 mimic reversed the increased apoptosis of Cx43-deficient osteocytes. To further assess the role of miR21 on bone cell apoptosis, neonatal calvaria bone from $miR21^{fl/fl}$ mice were treated with adenovirus-Cre to delete the miR21 gene, and compared to bone treated with adenovirus-GFP as control (Fig. 3-3B-E). Addition of adenovirus-Cre resulted in a 91% reduction of miR21 levels (Fig. 3-3B). Ultrastructural analysis of osteocytes using transmission electron microscopy revealed that adenovirus-Cre-treated calvariae from $miR21^{fl/fl}$ mice exhibited abundant empty lacunae (Fig. 3-3C). Furthermore, osteocytes, when present, exhibited swollen endoplasmic reticulum, an indicator of cellular stress when compared to calvaria bones infected with adenovirus-GFP. Similar to Cx43-deficient cells, bones with deleted miR21 exhibited increased expression of the apoptosis-related genes FoxO3 and p27, and a tendency towards increased GADD153 levels (Fig. 3-3D). Moreover, protein levels of the miR21 target phosphatase PTEN were increased by ~ 2.7-fold (Fig. 3-3E).

Cx43 deficiency and aging result in disruptions in PTEN/pAkt pathway. Consistent with the decrease in miR21 expression, protein levels of PTEN were increased 2.4-fold in $Cx43^{\Delta Ot}$ compared to $Cx43^{fl/fl}$ mice (Fig. 3-4A). Further, reduction of Cx43

expression in MLO-Y4 osteocytic cells resulted in increased levels of the phosphatase PTEN and a decreased phosphorylated Akt, a known target of PTEN (Fig. 3-4B and C). Cell death was blocked by the PTEN inhibitor SF1670 (Fig. 3-4D and E), adding support for a role of the phosphatase on cell death induced by Cx43 deficiency.

We next examined whether the pro-survival effect of IGF-1, which is mediated by Akt phosphorylation in several cell types, requires Cx43 expression. Because IGF-1 does not decrease the low level of cell death in vehicle-treated control cells, we induced apoptosis with the synthetic glucocorticoid dexamethasone, as previously reported.[103] IGF-1 prevented dexamethasone-induced apoptosis in scramble-silenced MLO-Y4 osteocytic cells, and in HeLa cells [which lack endogenous $Cx43^{96}$] transfected with Cx43, but not in $Cx43^{def}$ cells or in vector-transfected HeLa cells (Fig. 3-4F). The levels of dead cells were quantified 7h after all detached cells were removed from the cultures, unlike the ones shown in previous figures, which were measured at least 24h after washing the cultures to remove dead cells. Nevertheless, we still detected an increase in the percentage of dead cell in vehicle-treated Cx43 silenced MLO-Y4 cells compared to vehicle-treated scramble-shRNA cells (~6% vs. ~4%).

Deletion of Cx43 increases the release of pro-osteoclastogenic cytokines by osteocytic cells. We next examined the molecular basis for osteoclast recruitment induced by Cx43 deficiency. As found before,[46] silencing Cx43 from MLO-Y4 cells results in increased RANKL and reduced OPG levels (Fig. 3-5A). Similar results were found in old mice.[104, 105] Inhibition of apoptosis with DEVD reversed the increase in RANKL mRNA levels, but did not change OPG mRNA levels in $Cx43^{def}$ cells. Furthermore, removal of miR21 from bones increased RANKL, but did not alter OPG mRNA levels (Fig. 3-5B). Taken together, these pieces of evidence suggest that the increase in RANKL but not the

reduction in OPG levels in the absence of Cx43 is due to increased osteocyte apoptosis downstream of miR21 downregulation.

HMGB1, a ubiquitously expressed molecule, has been shown to increase in the circulation in rats with aging,[106, 107] and to increase RANKL expression in osteocytic cells.[50] However, we did not find changes in HMGB1 levels in the serum of old mice (Fig. 3-8). Silencing of Cx43 in MLO-Y4 osteocytic cells resulted in a 77% decrease in the amount of intracellular HMGB1, and a 480% increase in the levels of the cytokine in the conditioned media, suggesting increased release of HMGB1 (Fig. 3-5C). We also detected a tendency towards HMGB1 increase in serum from $Cx43^{\Delta Ot}$ mice, although it did not reach significance (Fig. 3-8).

Inhibition of apoptosis with DEVD or blockage of HMGB1 activity with glycyrrhizic acid (GA) reversed the increase in RANKL mRNA levels, and the release of RANKL to the extracellular media (Fig. 3-5D). In addition, the levels of HMGB1 in conditioned media were reversed to control levels in cells treated with DEVD, and attenuated in cells treated with GA (Fig. 3-5E). GA binds to HMGB1 and blocks HMGB1 chemoattractant and mitogenic activities,[108] and, unlike its analog glycyrrhetinic acid, does not inhibit connexin channel activity in MLO-Y4 osteocytic cells.[96] Addtion of a neutralizing anti-HMGB1 antibody to Cx43-silenced MLO-Y4 cells partially reversed the increase in RANKL mRNA without affecting OPG levels, resulting in a significant decrease in RANKL/OPG ratio, compared to cells treated with non-immune IgG (Fig. 3-5F).

Increased osteoclastogenesis is inhibited by blocking apoptosis of Cx43-deficient MLO-Y4 osteocytic cells. We next investigated whether deletion of Cx43 in osteocytic cells resulted in enhanced osteoclastogenic potential. Increased number of multinucleated TRAP-positive osteoclasts were observed in co-cultures of non-adherent bone marrow cells (osteoclast precursors) with Cx43-silenced MLO-Y4 cells (Fig. 3-6A). In addition, conditioned media from cells silenced for Cx43 induced more osteoclasts than media from

control cells (Fig. 3-6B), indicating that factors secreted by the osteocytic cells are responsible for the increased osteoclast differentiation. Inhibition of apoptosis of $Cx43^{def}$ cells with DEVD reduced the osteoclastogenic potential of the conditioned media, which was now similar to conditioned media from scramble-shRNA-treated cells. Furthermore, the expression of osteoclast markers was increased in bone marrow cells treated with conditioned media from Cx43-deficient cells, whereas their levels were similar to controls when the conditioned media was obtained from cells treated with DEVD (Fig. 3-6C). Treatment with boxA, which antagonizes HMGB1 binding to its receptor RAGE,[109] decreased osteoclast formation induced by conditioned media from Cx43-deficient cells (Fig. 3-6D), suggesting the HMGB1 released by osteocytic cells is responsible for the increase in osteoclast differentiation via activating RAGE.

Discussion

In the current study, we dissected the molecular signaling pathway underlying osteocyte apoptosis triggered in the absence of osteocytic Cx43 and by aging (Fig. 3-6E). In addition, we unveiled the molecular link between osteocyte apoptosis and targeted osteoclastic bone resorption. Based on our evidence, we propose that old age and absence of osteocytic Cx43 cause decreased miR21 levels, and the associated increased PTEN protein levels and decreased Akt activation, resulting in osteocyte apoptosis. Apoptotic osteocytes release more HMGB1, which in turn activates RAGE in osteoclast precursors to induce osteoclast differentiation.

Similar to the current report, immunohistochemistry studies showed that Cx43 expression in osteocytes decreases in old mice.[91] On the other hand, the expression of Cx43 is not decreased in osteoblastic cells isolated from old rats.[110] This evidence suggests that Cx43 expression decreases in osteocytes but not in osteoblasts with aging.

Deletion of Cx43 from osteocytes in mice and stable silencing of Cx43 in MLO-Y4 osteocytic cells results in spontaneous cell death by a caspase3-dependent mechanism, demonstrating the requirement of Cx43 in the survival of osteocytes[46] and this report. The survival effect of Cx43 requires intact intercellular gap junction communications, but does not involve the scaffold or regulatory domains present in Cx43 C-terminus. This is consistent with our previous study showing that expression of a truncated Cx43 lacking the C-terminus domain restores osteocyte viability in mice lacking Cx43 in osteocytes.[49] Similarly, the altered bone material mechanical properties, with decreased stiffness, of mice lacking osteocytic Cx43 is reversed by the truncated Cx43. These findings suggest that the trans-membrane and cytoplasmic amino-terminal domains are sufficient to maintain osteocyte viability and preserve normal cortical bone geometry and material properties. Future studies using mice overexpressing Cx43 in osteocytes (currently under development in our laboratory) will allow us to determine whether maintenance of Cx43

levels reverses the increased osteocyte apoptosis and, at least partially, the skeletal phenotype of old mice.

The underlying molecular mechanisms that lead to increased osteocyte apoptosis in the absence of Cx43 and in old age remained unclear. We now propose the existence of a signaling cascade that maintains cell viability through the regulation of miR21 downstream of Cx43 (Fig. 3-6E). Although we also found that miR218 levels are increased in $Cx43^{def}$ cells, this increase was not reproduced in bones from old mice or mice lacking Cx43 in osteocytes, suggesting that whereas miR21 is regulated by Cx43, signals other than Cx43 are involved in miR218 regulation *in vivo*.

Several pieces of evidence support the role of miR21 on osteocyte apoptosis. First, both $Cx43^{\Delta Ot}$ mice and Cx43-deficient osteocytic cells exhibit accelerated cell death and express lower levels of miR21, a pro-survival miR.[59] Further, miR21 deletion by adenovirus-Cre in $miR21^{fl/fl}$ calvaria bones increases the expression of apoptosis related genes; and reducing miR21 expression using oligonucleotide inhibitors induces apoptosis of control osteocytic cells. Conversely, a miR21 oligonucleotide mimic attenuates Cx43-deficient osteocyte apoptosis, supporting the idea that miR21 reduction causes the increased osteocyte apoptosis in the absence of Cx43. Consistently, the expression of both Cx43 and miR21 are reduced in old bones, suggesting that the decreases in Cx43 and miR21 levels contribute to the decreased osteocyte viability in old age. Although the mechanism by which reduced Cx43 expression leads to decrease in miR21 levels is not known, these 2 genes are not located in the same gene locus,[111] excluding the possibility that a deletion of one gene removes the other one.

In addition to inducing apoptosis, miR21 deletion increases RANKL expression. The regulation of RANKL expression in Cx43-deficient osteocytes could be a consequence of increased apoptosis in the absence of miR21, or to the lack of direct

actions of miR21 on the RANKL gene. However, miR21 deletion reduces RANKL expression in multiple myeloma-exposed bone marrow cells,[112] suggesting that direct actions of the microRNA on gene expression are not the cause of increased RANKL levels in our study. It is therefore likely that the changes in RANKL expression in cells in which miR21 was deleted is a consequence of increased apoptosis. Future studies are needed to further support this conclusion.

The mechanism by which old age leads to increased osteocyte apoptosis is not completely understood. Previous studies showed that the survival effect of IGF-1 is reduced in osteoblastic cells isolated from old (24-month-old) compared to young (1.5-month-old) and adult (6-month-old) mice, even though the levels of the IGF-1 receptor is increased in the older mice.[113] The resistance of bone marrow cells from old mice to IGF-1 effect was associated with reduced activation of Akt, a known mediator of survival induced by the cytokine.[114] We now propose that reduced response to IGF-1 in old animals is due to decreased Cx43/miR21 levels, counteracting the effect of IGF-1 on the PTEN/pAkt pathway. Consistent with this notion, IGF-1 prevents apoptosis of osteoblastic cells[115, 116] and Cx43 is required for the survival effect of IGF-1 in cardiomyocyte precursors.[117]

Osteocyte apoptosis has been shown to precede and to be associated with increased targeted recruitment of osteoclasts along adjacent bone surfaces in several animal models [recently reviewed by us[24, 75]]. Consistently, we showed that osteocyte specific Cx43 deletion leads to accumulation of apoptotic osteocytes, and an associated increase in osteoclasts in some adjacent areas on endocortical bone surfaces.[46] Additionally, Cx43-deficient osteocytic cells exhibit an increase in the RANKL/OPG ratio, facilitating osteoclast formation. However, increased populations of osteocytes with reduced OPG levels are present even in areas lacking osteoclasts in $Cx43^{\Delta Ot}$ mice,

suggesting that apoptotic osteocytes release other signals that are required for osteoclast recruitment. The specific molecules underlying this increased osteoclast recruitment were heretofore unknown. We now show that Cx43-deficient osteocytes release elevated levels of the pro-inflammatory cytokine HMGB1. Similarly, induction of MLO-Y4 osteocytic cell apoptosis with TNFα/cycloheximide increases HMGB1 release.[50] However, in Yang's study, addition of HMGB1 to the cells increased Akt phosphorylation, rather than decreased it, as reported here. This evidence suggests that the changes in Akt activity in the Cx43-deficient cells is not a response to the released HMGB1, but the result of the increase in PTEN levels downstream of miR21 downregulation.

We also found that inhibition of osteocyte apoptosis with DEVD or treatment with a HMGB1 neutralizing antibody or GA, an inhibitor of HMGB1 action,[98] reduces RANKL expression in Cx43-deficient cells. This is consistent with previous work showing that apoptotic MLO-Y4 osteocytic cells release HMGB1.[51, 118] Further, HMGB1 is chemotactic for osteoclasts and triggers osteoclastogenesis by activating RAGE.[53-55] Consistently, inhibition of apoptosis prevents RANKL and HMGB1 release, and attenuates the enhanced osteoclastogenesis and osteoclast marker expression induced by conditioned media from Cx43-deficient osteocytes. In addition, the HMGB1-RAGE receptor antagonist boxA[109] blocks osteoclastogenesis induced by conditioned media from Cx43-deficient osteocytes. Thus, we propose that HMGB1 released by Cx43-deficient osteocytes enhances osteoclastogenesis by increasing RANKL in osteocytes and, at the same time, directly stimulating osteoclast precursor differentiation at least partially through activation of RAGE. Future studies will allow us to further elucidate the mechanisms by which apoptotic osteocytes in Cx43$^{\Delta Ot}$ and old mice release HMGB1 and the role of the RAGE and TLR4 receptors on the induction of osteoclast recruitment.

In summary, we propose that gap junction communications through Cx43 channels maintain osteocyte viability via downstream regulation of miR21, leading to the subsequent inhibition of PTEN activity and preservation of the Akt survival pathway (Fig. 3-6E). Additionally, our findings support a model where reduced Cx43 levels in osteocytes in old animals lead to apoptosis and the release of RANKL and HMGB1, which signal osteoclasts to increase resorption along associated bone surfaces. We therefore identified a novel Cx43/miR21/HMGB1/RANKL pathway mediated by gap junction communications in osteocytes that could be targeted to treat bone fragility with aging.

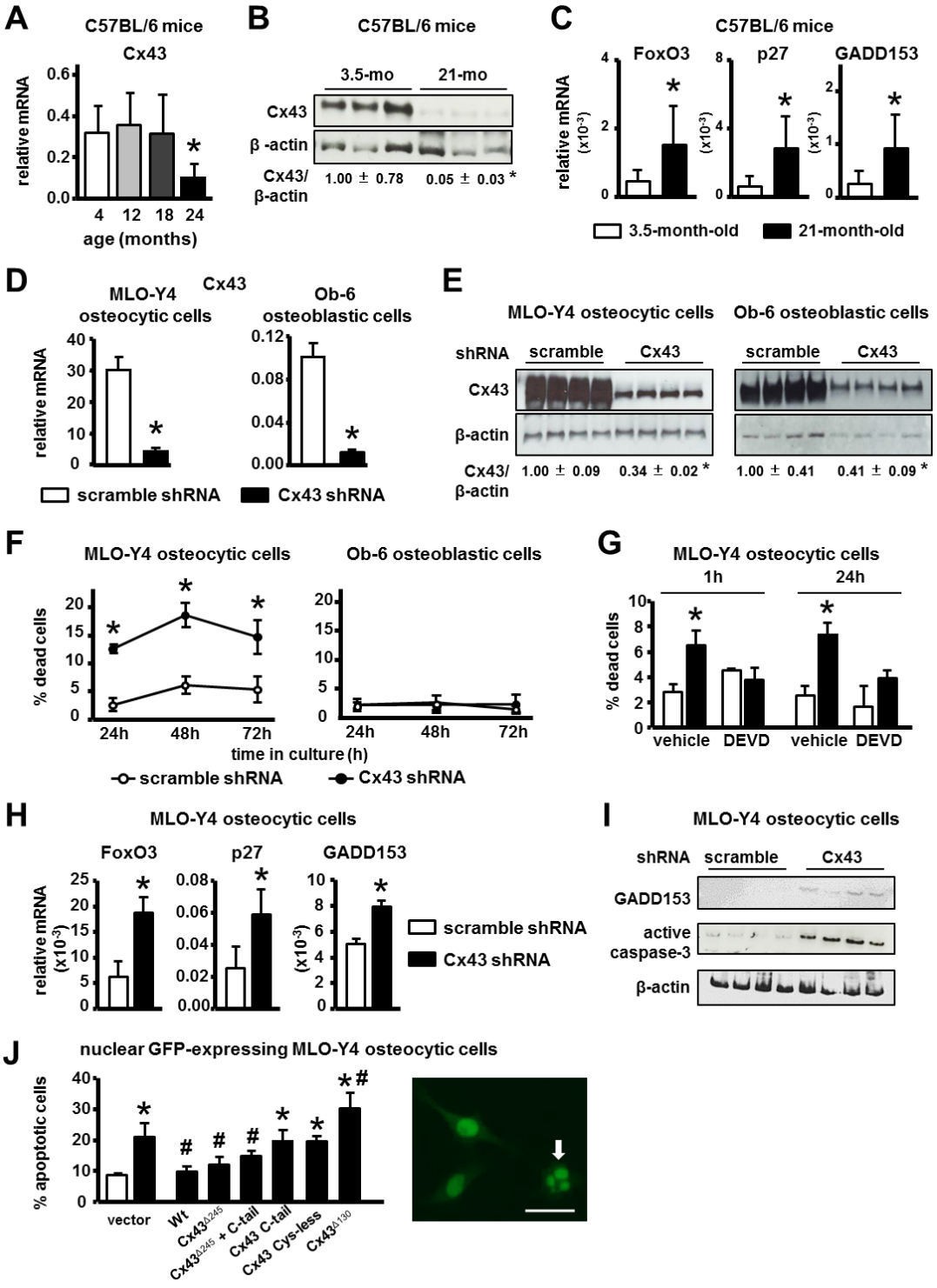

Figure 3-1. Aging and deletion of Cx43 in MLO-Y4 osteocytic cells leads to increased apoptosis. (A) Cx43 mRNA levels in calvaria from 4- to 24-month-old mice measured by

qPCR and corrected by GAPDH (Cx43 *n* = 5–9). (B) Cx43 protein levels in L5 vertebra from mice at 3.5 and 21 months of age were assessed by Western blotting and normalized by β-actin (*n* = 6–7). (C) mRNA levels for the indicated apoptosis-associated genes in tibia from young and old mice. (D) Cx43 protein expression was measured in MLO-Y4 osteocytic (*n* = 6–9) and Ob-6 (*n* = 3) expressing (scramble) or lacking (shRNA) Cx43 by qPCR and corrected by GAPDH. (E) Cx43 protein expression was measured in MLO-Y4 osteocytic and Ob-6 osteoblastic cells by Western blot analysis and normalized by β-actin (*n* = 4). (F) Cell death assessed in MLO-Y4 osteocytic cells (*n* = 3) and in Ob-6 cells (*n* = 6) expressing or not Cx43 by Trypan blue uptake after culturing them for the indicated times. (G) MLO-Y4 osteocytic cells silenced or not for Cx43 were treated for 1 or 24 h with DEVD and percentage of cells undergoing cell death were assessed by Trypan blue uptake (*n* = 6). (H) Gene expression was measured by qPCR and corrected by GAPDH (*n* = 6–9). (I) Protein expression for GADD153 and active caspase-3 assessed by Western blotting (*n* = 4). (J) MLO-Y4 osteocytic cells were transiently transfected with empty vector or the indicated Cx43 constructs together with nGFP. Apoptosis was determined by evaluating nuclear morphology of the transfected (green fluorescent) cells. A representative image of cells exhibiting nuclear fragmentation (arrow) compared to other cells with normal morphology is shown. Bars and dots represent mean ± SD. **P* < 0.05 vs. 4 months of age, by one-way ANOVA (A), **P* < 0.05 vs. young (B and C) or vs. scramble shRNA cells (D-I), by t-test. **P* < 0.05 vs. vector-transfected scramble shRNA cells, $^{\#}$ *P* < 0.05 vs. vector-transfected Cx43 shRNA cells by one-way ANOVA (J).

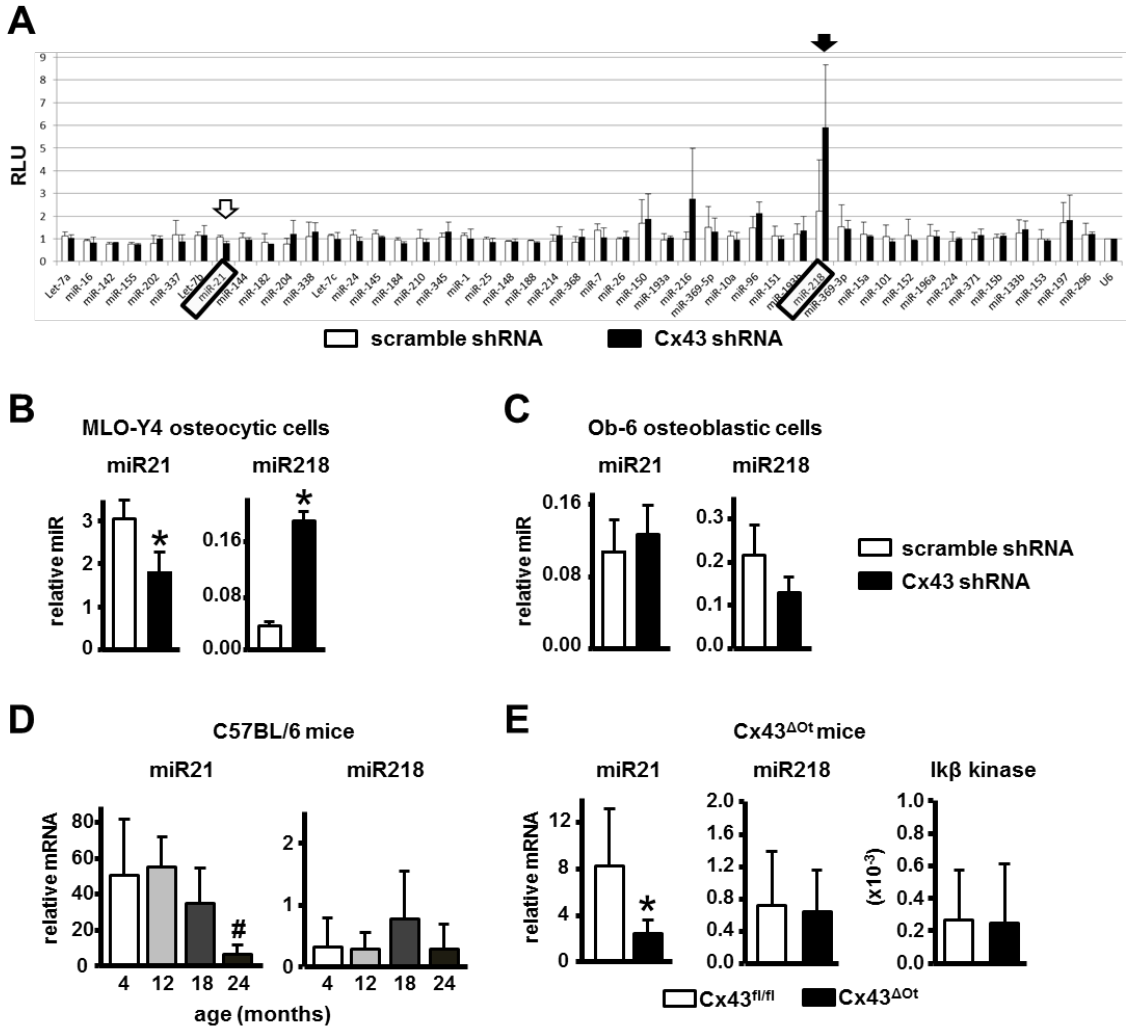

Figure 3-2. Cx43 deficiency and old age results in decreased miR21 expression. (A) Profile of 48 apoptosis-associated miRNA assessed in MLO-Y4 osteocytic cells expressing or not for Cx43 using an miRNA plate array and corrected by U6 RNA (*n* = 3). (B) Changes in the expression of miR21 and miR218 in MLO-Y4 osteocytic cells were validated by qPCR and corrected by miR135 (*n* = 3). (C) Expression of miR21 and miR218 corrected by miR135 in Ob-6 osteoblastic cells (*n* = 3). (D) miRNA expression in calvaria from 4- to 24-month-old mice measured by qPCR and corrected by miR135 (*n* = 5–9). Bars represent mean ± SD. $^{\#}$ $P < 0.05$ vs. 12 months of age, by one-

way ANOVA. (E) Gene and miRNA expression in calvaria from $Cx43^{fl/fl}$ and $Cx43^{\Delta Ot}$ mice measured by qPCR and corrected by miR135 (miR21 and miR218) or GAPDH (Ikβ kinase B). Bars represent mean ± SD (n = 5–8). *P < 0.05 vs. $Cx43^{fl/fl}$ mice, by t-test.

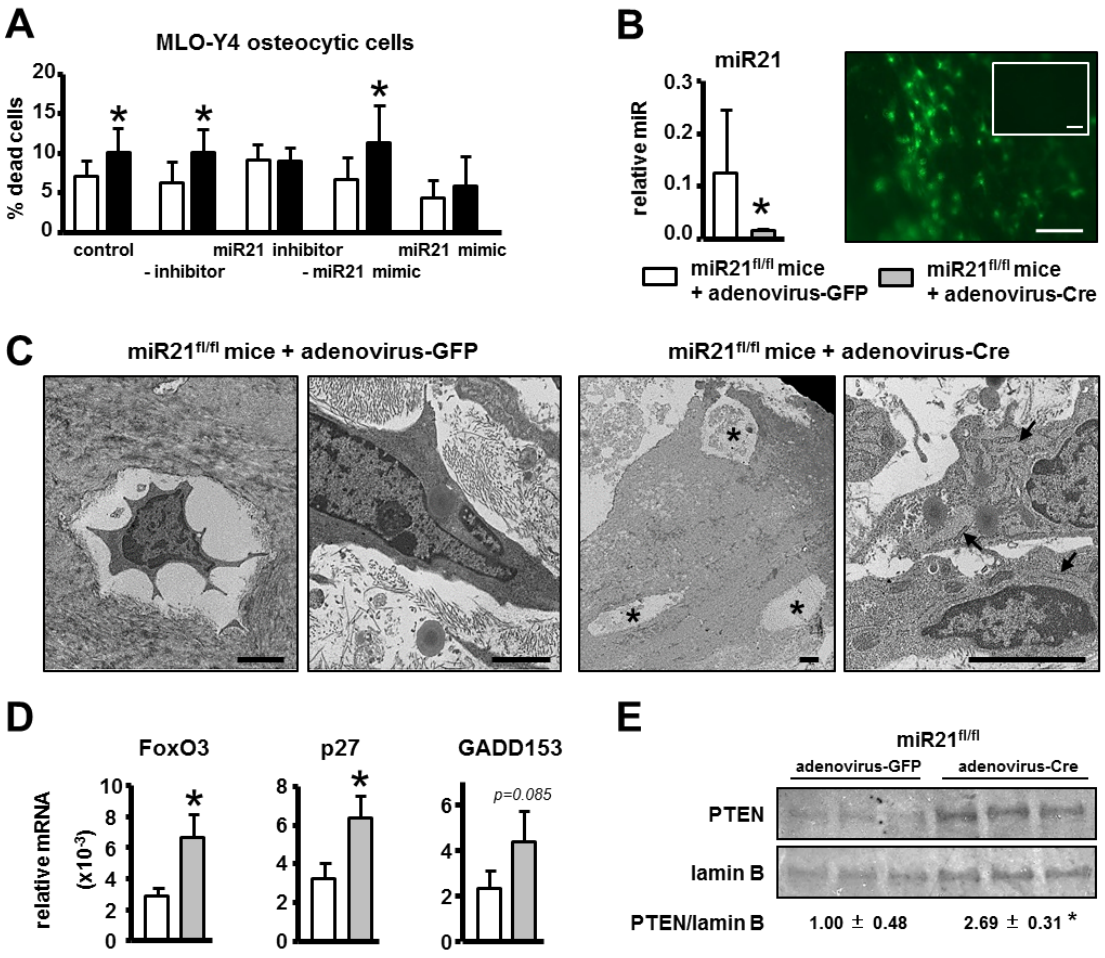

Figure 3-3. Deletion of miR21 is sufficient to induce osteocyte apoptosis and increase PTEN levels in bone. (A) MLO-Y4 osteocytic cells were transfected with the indicated oligonucleotides, and cell death was assessed by Trypan blue uptake (n = 6). *P < 0.05 vs. corresponding scramble shRNA cells, by t-test. (B) Neonatal calvariae from miR21$^{fl/fl}$ mice at 5 days of age were treated with adenovirus-Cre to delete miR21 gene. miR21 levels corrected by miR135 measured by qPCR. Representative images of viral infection efficiency under fluorescence microscope in adenovirus-GFP calvariae and adenovirus-Cre (without GFP expression) calvariae (inset) are shown. Scale bar indicates

100 μm. (C) TEM images of neonatal calvariae from miR21$^{fl/fl}$ mice treated with adenovirus-GFP (control) or adenovirus-Cre. Images are representative of three samples. Asterisks indicate empty lacunae, and arrows point at the endoplasmic reticulum. Scale bars indicate 2 μm. (D) Gene expression measured in calvaria by qPCR and corrected by GAPDH (n = 3). Bars represent mean ± SD. (E) PTEN expression in calvaria was assessed 48 h after miR21 deletion by Western blotting and normalized to lamin B levels (n = 3). (B–E) *P < 0.05 vs. corresponding cells infected with adenovirus-GFP, by t-test.

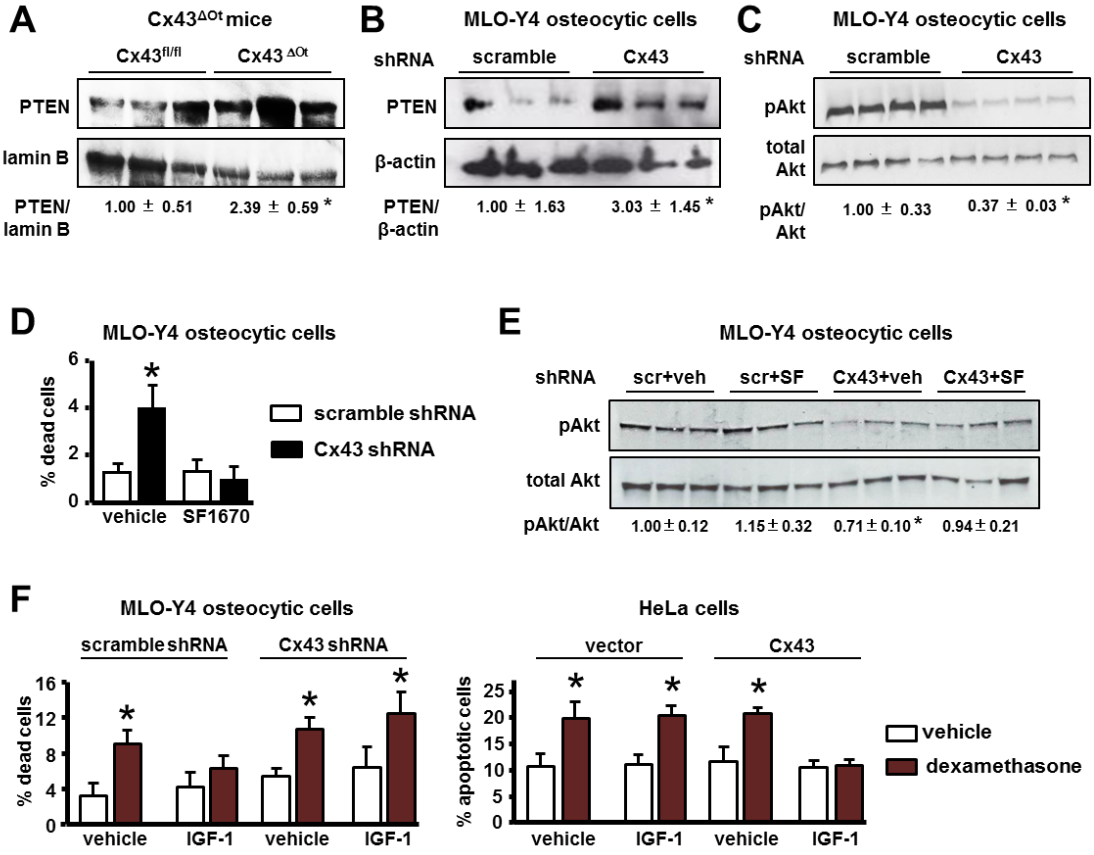

Figure 3-4. Cx43-deficiency and aging leads to disruptions in PTEN/pAkt pathway and abolishes the anti-apoptotic effect of IGF-1. (A) PTEN expression in ulna from $Cx43^{fl/fl}$ and $Cx43^{\Delta Ot}$ mice at 4.5 months of age assessed by Western blotting and normalized by lamin B (n = 3). *P < 0.05 vs. $Cx43^{fl/fl}$ mice, by t-test. Bars represent mean ± SD. (B,C) PTEN and phosphorylated Akt (pAkt) were analyzed in MLO-Y4 osteocytic cell lysates by Western blotting (n = 3–4). *P < 0.05 vs. corresponding scramble shRNA cells, by t-test. (D) MLO-Y4 osteocytic cells were treated with vehicle or the PTEN inhibitor SF1670 for 30 min, the media were changed, and the cells were cultured for additional 24 h. Percentage of dead cells was assessed by Trypan blue uptake (n = 3). *P < 0.05 vs. corresponding scramble shRNA cells by two-way ANOVA. (E) pAkt

and total Akt were analyzed by Western blotting (n = 3). *P < 0.05 vs. corresponding scramble shRNA cells, by t-test. (F) MLO-Y4 osteocytic cells expressing or not Cx43 and HeLA cells transfected with empty vector or Cx43 together with IGF receptor 1 and nGFP were treated with vehicle or IGF-1 for 1 h, followed by 6-h treatment with vehicle or dexamethasone. Cell death was assessed by Trypan blue uptake (for MLO-Y4 cells) or by nuclear morphology (for HeLa cells) (n = 3). *P < 0.05 vs. vehicle-treated cells for each condition, by two-way ANOVA.

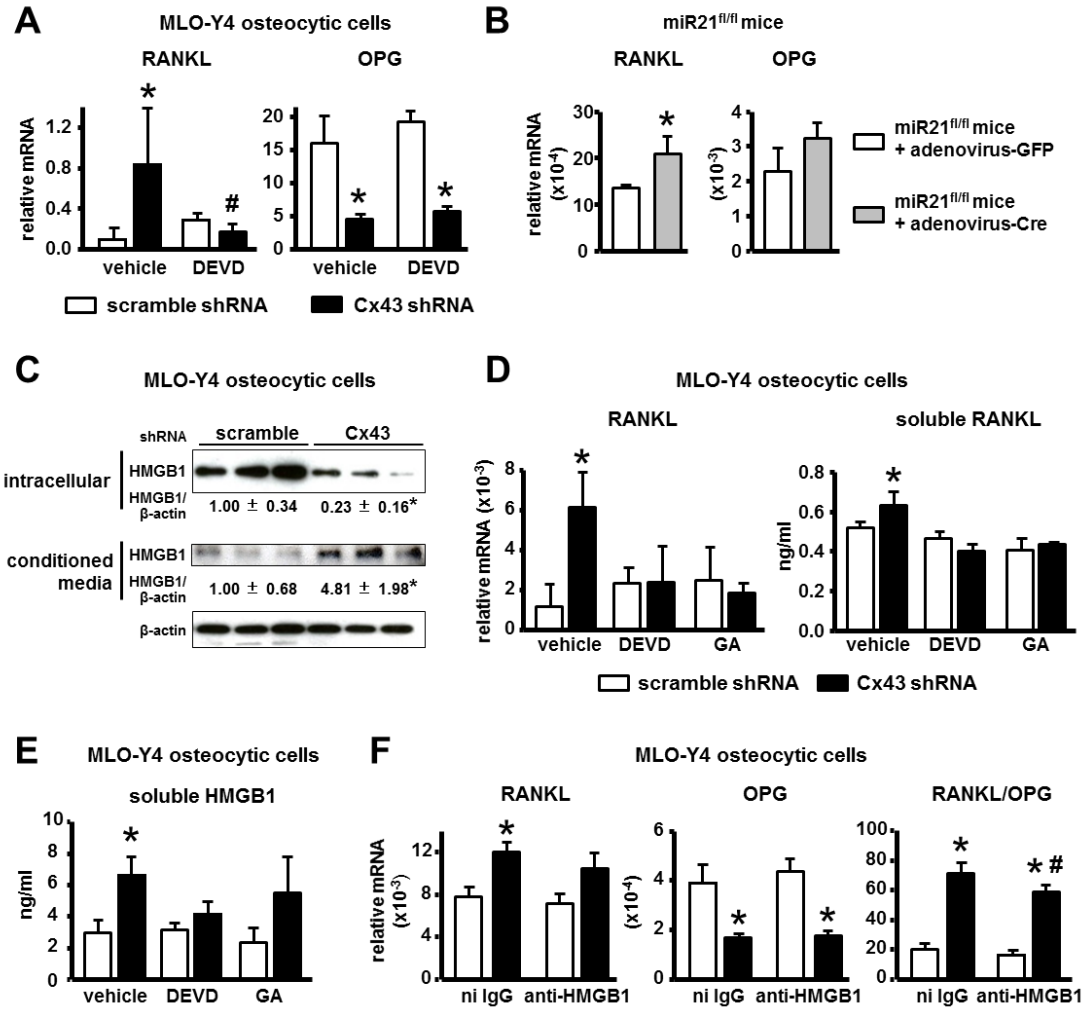

Figure 3-5. Increased osteocyte apoptosis with reduced Cx43 and miR21 leads to increased RANKL/OPG ratio. (A) Expression of the indicated genes and in MLO-Y4 cells expressing or lacking Cx43 treated with vehicle or DEVD for 1 h and measured 24 h later. Bars represent mean ± SD (n = 6). *P < 0.05 vs. corresponding shRNA scramble cells and $^{\#}P$ < 0.05 vs. vehicle-treated Cx43 shRNA cells by two-way ANOVA. (B) mRNA levels for the indicated genes in calvaria from miR21$^{fl/fl}$ mice treated with adenovirus-GFP or adenovirus-Cre (n = 3). Bars represent mean ± SD (n = 3). *P < 0.05 vs. adenovirus-GFP-treated bone, by t-test. (C) HMGB1 protein expression corrected by

β-actin measured in cell lysate and conditioned medium of MLO-Y4 osteocytic cells by Western blotting (n = 3). (D,E) mRNA levels for RANKL and concentration of sRANKL and HMGB1 in conditioned media from MLO-Y4 cells expressing or not Cx43, and treated with vehicle, DEVD or GA were measured by qPCR and ELISA, respectively (n = 3). (F) Expression of the indicated genes corrected by GAPDH in MLO-Y4 cells expressing or not Cx43 and treated with nonimmune (ni) IgG or neutralizing anti-HMGB1 antibodies for 24 h (n = 6). *P < 0.05 vs. corresponding shRNA scramble cells and $^{\#}$ P < 0.05 vs. ni IgG-treated Cx43 shRNA cells by two-way ANOVA.

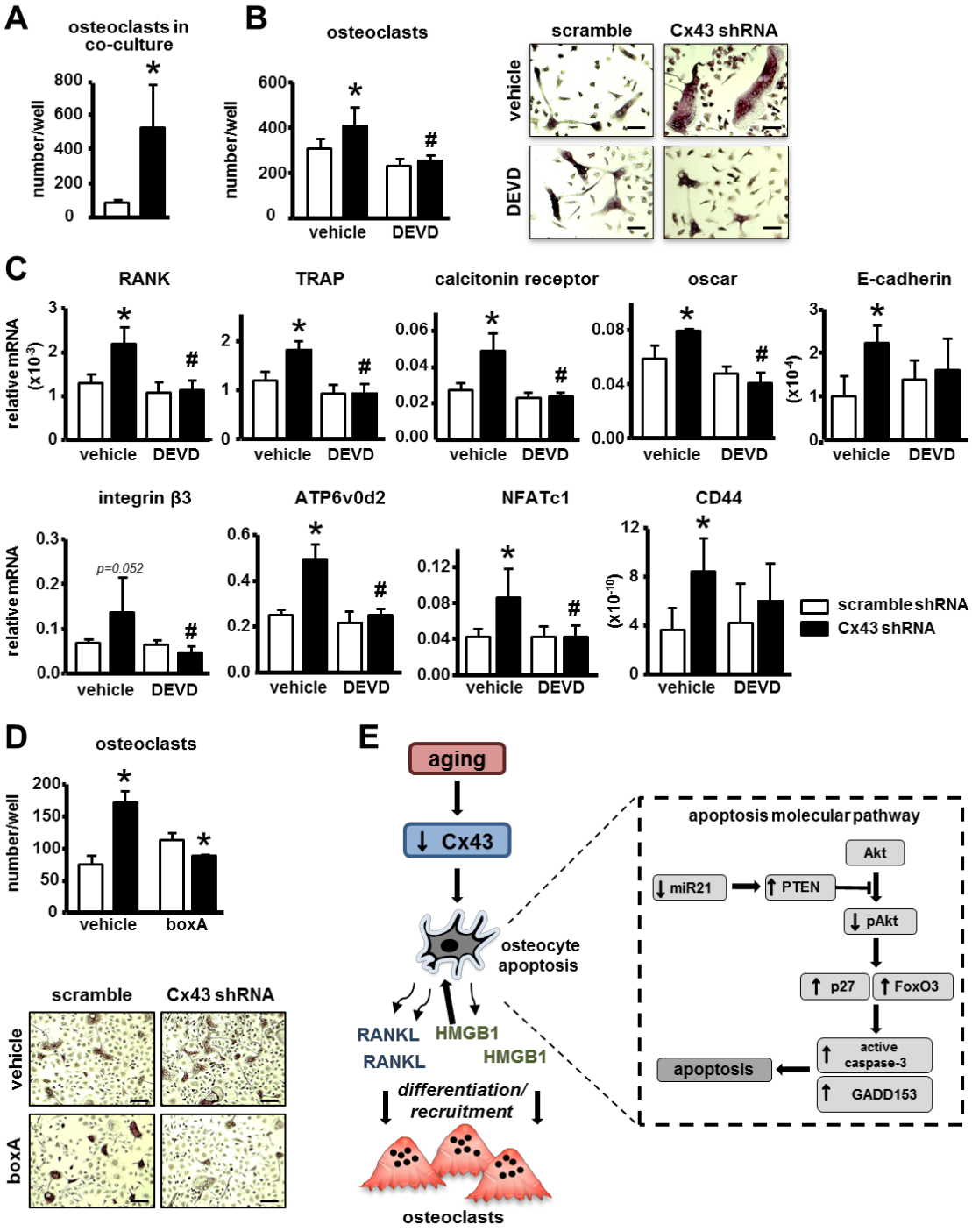

Figure 3-6. Blockage of apoptosis in Cx43-silenced MLO-Y4 osteocytic cells reduces their osteoclastogenic potential. (A) Bone marrow cells isolated from C57Bl/6 mice and co-cultured with MLO-Y4 osteocytic cells expressing or not Cx43 for 7 days. Multinucleated

(≥ 3 nuclei) osteoclasts were enumerated. Bars represent mean ± SD (n = 4). *P < 0.05 vs. shRNA scramble cells by t-test. (B,C) Bone marrow cells were cultured in the presence of conditioned media from MLO-Y4 osteocytic cells expressing or not Cx43 and treated for 1 h with vehicle or DEVD. (B) Multinucleated osteoclasts and representative images of cultured osteoclasts stained by TRAP and (C) mRNA expression for the indicated genes assessed by qPCR were measured after 7-day culture. Bars represent mean ± SD (n = 4). *P < 0.05 vs. vehicle-treated shRNA scramble cells, and $^{\#}P$ < 0.05 vs. vehicle-treated Cx43 shRNA cells, by two-way ANOVA. Scale bars indicate 200 μm. (D) Multinucleated osteoclasts were enumerated after treatment of nonadherent bone marrow cells with conditioned media from MLO-Y4 osteocytic cells expressing or not Cx43 in the presence of vehicle or boxA. Bars represent mean ± SD (n = 4). *P < 0.05 vs. corresponding shRNA scramble cells, by two-way ANOVA. Representative images of cultured osteoclasts stained by TRAP are shown. Scale bars indicate 100 μm. (E) Working model showing decreased osteocytic Cx43 leads to a reduction in miR21 levels which, in turn, leads to an increase in PTEN levels and consequently a reduction in Akt activation. Decreased Akt activity leads to increased expression of the apoptosis-related genes p27, FoxO3, and GADD153 resulting in caspase-3-mediated apoptosis. At the same time, apoptotic osteocytes release RANKL and HMGB1, which induce osteoclast differentiation and recruitment.

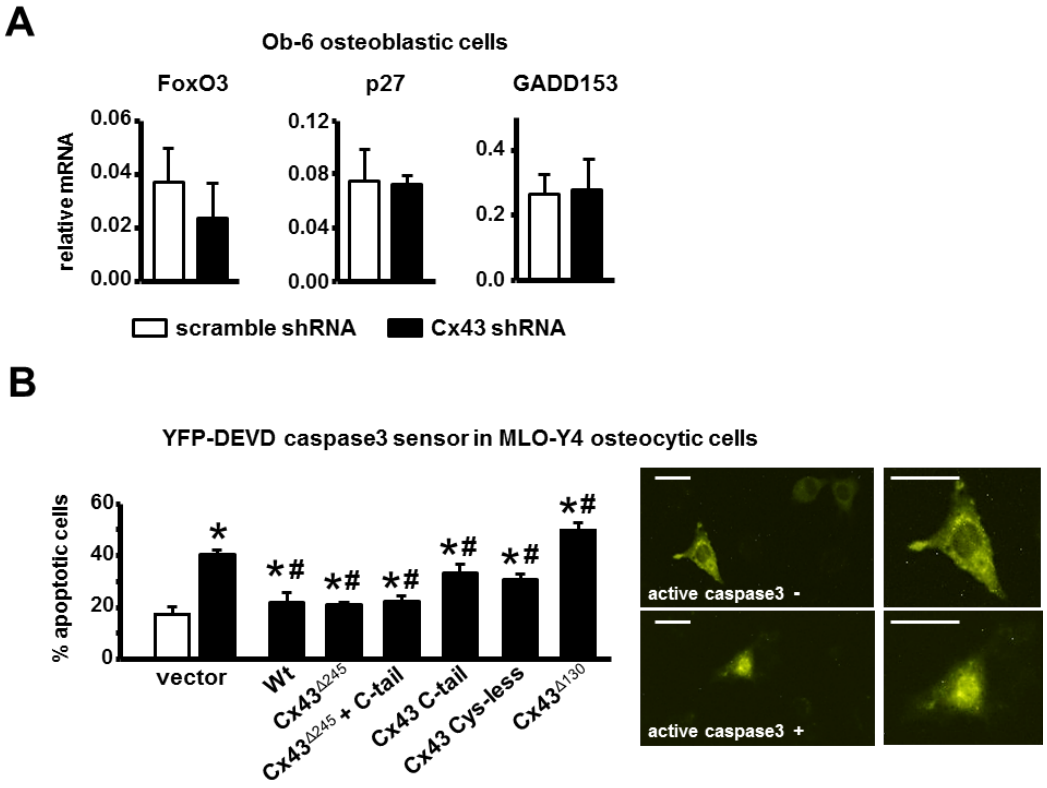

Figure 3-7. Deletion of Cx43 does not affect Ob-6 cells but leads to caspase3-mediated apoptosis in MLO-Y4 osteocytic cells. (A) mRNA levels were measured in Ob-6 cells expressing (scramble) or lacking (shRNA) cx43 by qPCR and corrected by GAPDH. Bars represent mean ± S.D. (n=3). *$p<0.05$ versus scramble cells, by t-test. (B) MLO-Y4 osteocytic cells were transiently transfected with empty vector or the indicated Cx43 constructs together with YFP-DEVD-caspase3 sensor. *$p<0.05$ versus vector-transfected scramble shRNA cells, $^{\#}p<0.05$ versus vector-transfected Cx43 shRNA cells by one-way ANOVA. Representative images of cells are shown. Scale bars indicate 50μm.

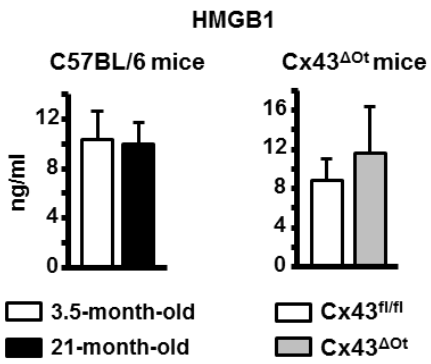

Figure 3-8. HMGB1 levels are not altered systemically with aging or in osteocytic Cx43-deficient mice. Serum HMGB1 levels were assessed in C57BL/6 mice (n=8-10) and in osteocytic Cx43-defient mice (n=6-7) by ELISA.

Chapter 4

Sex divergent role of osteocytic miR21 in the maintenance of osteocyte viability and regulation of bone turnover

Rationale

Osteocytes play a critical role in mediating cell-cell communication and regulating bone homeostasis, and osteocyte apoptosis is associated with increased bone resorption. miR21, an oncogenic microRNA, regulates bone metabolism by acting directly on osteoblasts and osteoclasts, but its role in osteocytes is not clear. Based on our previous findings and the notion that osteocyte apoptosis triggers osteoclast differentiation and recruitment, we proposed that induction of osteocyte apoptosis upon miR21 deletion would lead to subsequent increases in bone resorption and decreases bone strength. The purpose of this series of studies was to determine the skeletal effects of osteocytic miR21 deletion, and identify if miR21 has sex-divergent effects in bone.

Introduction

Osteocytes are the most prevalent and long-living type of cell in bone.[30] Extensive evidence suggests that osteocytes embedded in the bone matrix are targets of bone acting stimuli, and that osteocyte lifespan affects skeletal homeostasis.[32, 40, 42, 43] Osteocytes regulate bone remodeling by modulating osteoclasts and osteoblasts through direct cell-cell interactions and via extracellular signaling through the release of soluble factors.[30, 75] Additionally, osteocyte viability is reduced in conditions of increased bone fragility[26, 32-34] and conversely, agents that preserve bone strength prevent osteocyte apoptosis.[32, 40, 42, 43] Moreover, osteocyte apoptosis and the prevalence of empty lacunae are increased in old mice and humans.[8, 45] However, the molecular mechanisms that lead to increased

osteocyte apoptosis and the osteocyte-derived signaling factors that control bone metabolism in old age are not completely understood.

Recent work has identified microRNAs (miRs) as negative regulators of gene expression.[60] miRs are ~18-22-nucleotide long noncoding RNAs that regulate a plethora of cellular processes and dysregulation of particular miRs have been associated with numerous human diseases. Changes in miR expression can also contribute to the effects of aging in several organs.[120] In particular, alterations in miR21 abundance, a miR predominantly regarded as a pro-survival and oncogenic, have been detected in numerous pathologies. In bone, miR21 has been shown to directly regulate osteoblast and osteoclast differentiation and function.[121] However, the role of miR21 in osteocytes and its effects on bone turnover remain unclear.

We previously demonstrated several putative pro-survival miRs are dysregulated in MLO-Y4 osteocytic cells in the absence of Cx43. In particular, miR21 levels are significantly decreased in Cx43-deficient cells, which undergo spontaneous apoptosis in culture; and addition of a miR21 mimic sufficiently restores the viability of these cells.[119] Conversely, inhibition of miR21 induces osteocyte apoptosis in control MLO-Y4 osteocytic cells. Further, we found that bones from mice lacking osteocytic Cx43 and from old female mice express lower levels of miR21 compared to control $Cx43^{f/f}$ and young mice, respectively.[59] Based on these findings and the notion that osteocyte apoptosis triggers osteoclast differentiation and recruitment,[24] a simplistic model would predict apoptotic effects on osteocytes upon miR21 deletion, with subsequent increases in bone resorption and decreases bone strength. However, given the complex nature of miR regulation, both intra- and extracellular, in nearly every cell in the body, it should not have been surprising that this hypothesis was overly simplistic. Here, we provide experimental evidence that *in vivo* effects of the miR21 locus are more nuanced, and identify for the first time a sex-divergent impact of miR21 on osteocyte biology. We show that miR21 regulates osteocyte

viability in a sex-dependent manner, preserving osteocyte viability in females but reducing osteocyte viability in males. Further, we demonstrate that osteocytic miR21 regulates osteocyte cytokine production and bone turnover in a sex-specific manner. In particular, we found miR21 deletion differentially altered osteocyte cytokine production, as well as, several related signaling pathways in females and males. Despite these changes, miR21 deletion enhanced bone mechanical properties in both sexes, albeit to a greater extent in males. Taken together, these results suggest that miR21 exerts a sex-divergent role in osteocytes, regulating bone mass and architecture through non-cell autonomous effects on osteoblasts and osteoclasts, whereas, miR21 has sex-independent effects on bone mechanical properties.

Materials and Methods

Mice. The miR21 floxed mouse strain was engineered with lox cassettes on both sides of the mmu-miR-21 genomic locus (named miR21$^{f/f}$).[119] To generate mice lacking the miR21 gene preferentially in osteocytes miR21$^{f/f}$ mice were crossed with DMP1-8kb-Cre mice[46] to obtain female and male miR21$^{f/f}$ and miR21$^{f/f}$;DMP1-8kb-Cre (miR21$^{\Delta ot}$) mice. All mice were of the C57BL/6 background. Mice were fed a regular diet and water *ad libitum* and maintained on a 12h light/dark cycle. The protocols involving mice were approved by the Institutional Animal Care and Use Committee of Indiana University School of Medicine.

RNA extraction and qRT-PCR. Total RNA was isolated using TRIzol (Invitrogen, Grand Island, NY), as published.[83] Reverse transcription was performed using a high-capacity cDNA kit (Applied Biosystems, Foster City, CA). qPCR was performed using the Gene Expression Assay Mix TaqMan Universal Master Mix with an ABI 7900HT real-time PCR system, and gene expression was corrected by the levels of the house-keeping gene glyceraldehyde 3-phosphate dehydrogenase (GAPDH). Primers and probes were commercially available (Applied Biosystems, Foster City, CA) or were designed using the Assay Design Center (Roche Applied Science, Indianapolis, IN). miR21 (assay ID: 000397) and miR135 (assay ID: 001230) expression levels were evaluated as previously published.[119] miR21 levels were normalized to the housekeeping miR135. Relative expression was calculated using the ΔCt method.

Body weight and bone mineral density (BMD) by dual energy x-ray absorptiometry (DXA). BMD was measured monthly from 1 to 4 months of age by DXA PIXImus densitometry (G.E. Medical Systems, Lunar Division, Madison, WI).[83] Body weight was measured at the time of the DXA scan. BMD measurements included total

BMD (whole body BMD, excluding the head and tail), femoral BMD (entire femur) and spinal BMD (L1-L6 vertebrae). Calibration was performed using a standard control phantom before scanning, as recommended by the manufacturer.

μCT analysis. Femur and lumbar vertebra (L4) samples were harvested from 4-month-old female and male mice. The female bones were scanned using the Scanco μCT-35 system (Scanco Medical AG, Brüttisellen, Switzerland) using a 50kV source, 120 mA, 151 milliseconds integration time, and 10μm voxel resolution.[83] The male bones were scanned using a 65kV source, 0.5mm Al filter, 0.7 degree rotation and two-image averaging with an isotropic voxel size of 9μm using a SkyScan 1176 system (SkyScan, Kontich, Belgium).[90] Two different systems were used due to constrained availability of the instruments. The terminology and units used for μCT are those recommended by the American Society for Bone and Mineral Research (ASBMR).[84]

Bone histomorphometry. Femur and vertebra harvested from 4-month-old female and male mice were fixed in 10% neutral buffered formalin and embedded using previously established methods at the ICMH Histology and Histomorphometry Core.[90] To allow for dynamic histomorphometric analysis mice were injected intraperitoneally with calcein (20 mg/kg; Sigma) and alizarin red (20 mg/kg; Sigma) 7 and 2 days prior to sacrifice, respectively. Dynamic histomorphometry was performed on unstained methyl methacrylate-embedded L1-L3 vertebra (sagittal) and femur mid-diaphysis (transverse) sections using an epifluorescence microscope. Osteoclasts were quantified in TRAPase/Toluidine blue stained femur mid-diaphysis and vertebra sections and osteoblasts in von Kossa/McNeal stained-sections using static histomorphometric analysis. Histomorphometric analysis was performed using OsteoMeasure high resolution digital video system (OsteoMetrics Inc., Decatur, GA, USA). The terminology and units

used are those recommended by the ASBMR Histomorphometry Nomenclature Committee.[85]

Biomechanical testing. Three-point bending testing of the femoral mid-diaphysis was performed following previously published protocols.[49, 90] Briefly, bones were thawed to room temperature, hydrated in 0.9% saline, and loaded until failure at 2 mm/min with force versus displacement data collected at 10Hz using a servo-hydraulic test system (TestResources Inc., Shakopee, MN, USA). Femora were loaded until failure in an anterior–posterior direction with the upper contact area at the mid-diaphysis (50% total bone length) and the bottom contact points centered around this point and separated by 8mm. Cross-sectional moment of inertia and anterior–posterior diameter were determined by μCT and were used to calculate material-level properties, as previously described.[49]

Ex vivo bone organ cultures. Long bones were isolated from 2-month-old female and male miR21$^{f/f}$ and miR21$^{\Delta ot}$ mice. Bone-marrow cells (BMCs) were flushed out with α-minimal essential medium (MEM) and osteocyte-enriched long bones were cultured *ex vivo* in α-MEM supplemented with 10% FBS and 1% penicillin/streptomycin (P/S) for 48h. Conditioned media was collected and stored at -20°C until used for the osteoclastogenesis assays and cytokine arrays.

Osteoclast assays. BMCs were isolated from C57BL/6 mice by flushing the bone marrow out with α-MEM supplemented with 10% FBS and 1% P/S and cultured for 48h.[83, 119] Next, non-adherent cells were collected and 2x10^4 cells/cm^2 were seeded on 96-well plates and cultured with conditioned media collected from *ex vivo* cultures of osteocyte-enriched marrow-flushed long bones isolated from miR21$^{f/f}$ and miR21$^{\Delta ot}$ female and male mice. Additionally, BMCs isolated from the miR-21$^{f/f}$ and miR21$^{\Delta ot}$ female and male mice

were cultured in α-MEM supplemented with 10% FBS and 1% P/S for 48h. Next, non-adherent cells were collected and $2x10^4$ cells/cm^2 were seeded on 96-well plates. RANKL (80 ng/ml) and M-CSF (20 ng/ml) were added to induce osteoclast differentiation and media was changed every 3 days for 7 days. Cells were stained using a TRAPase kit (Sigma-Aldrich) and mature osteoclasts exhibiting 3 or more nuclei were quantified. Images were acquired using a Zeiss Axiovert 35 microscope equipped with a digital camera. Osteoclast size and number of nuclei were quantified using ImageJ.

Multiplex cytokine and cell-signaling assays. Cytokines in serum and conditioned media released from osteocyte enriched *ex vivo* bone organ cultures of female and male $miR21^{f/f}$ and $miR21^{\Delta ot}$ mice, were measured using the Bioplex protein array system at the Multiplex analysis core at IUSM. For the cytokine assay, premixed magnetic beads of the Milliplex mouse cytokine/chemokine 32 plex [Eotaxin/CCL11, G-CSF, GM-CSF, IFNγ, IL-1α, IL-1β, IL-2, IL-3, IL-4, IL-5, IL-6, IL-7, IL-9, IL-10, IL-12 (p40), IL-12 (p70), IL-13, IL-15, IL-17A/CTLA8, IP-10/CXCL10, KC/GROα/CXCL1, LIF, LIX, MCP-1/CCL2, M-CSF, MIG/CXCL9, MIP-1α/CCL3, MIP-1β/CCL4, MIP-2/CXCL2, RANTES/CCL5, TNFα, VEGF-A] kit was used (Milliplex, Burlington, MA). Cell-signaling pathway alterations induced by deletion of osteocytic miR21 were examined in female and male $miR21^{f/f}$ and $miR21^{\Delta ot}$ calvaria bone lysates. For cell-signaling assays, premixed magnetic beads of the Milliplex multi-pathway 9-plex [Akt/PKB, CREB, ERK/MAPK 1/2, JNK/SAPK1, NF-κβ, p38/ SAPK2A/B, p70S6 Kinase, STAT3, STAT5A/B] phosphoprotein and total kits were used.

Cell culture and lentiviral transfection. miR21-silenced MLO-Y4 osteocytic cells were generated using short hairpin (sh)RNA Lentiviral Particles (Sigma-Aldrich Chemical Co., St. Louis, MO, USA), as previously reported,[40, 46] and cultured as previously

described. MLO-Y4 osteocytic cells silenced or not for Cx43 were plated at the density of 2 x 10^4 cells cm^{-2} on 48-well plates coated with type I rat tail collagen and cultured overnight. Cells were transiently transfected using Lipofectamine RNAiMAX reagent (Invitrogen) containing miRIDIAN negative control inhibitor, miR21 inhibitor, negative control mimic, or miR21 mimic (GE Healthcare Bio-Sciences, Pittsburgh, PA, USA) at a final concentration of 0.1 nM in medium without serum and penicillin/ streptomycin for 6 h. Next, 2x concentrated medium was added to each well and then cultured overnight. Medium was changed to a regular growing medium, and cells were then cultured for an additional 24 h before isolating mRNA. miR21 levels were decreased by 60% in MLO-Y4 scramble cells and by 91% in MLO-Y4 Cx43 shRNA cells treated with miR21 inhibitor, as measured by qPCR. miR21 levels were increased by 44% in MLO-Y4 scramble cells and 234% in MLO-Y4 Cx43 shRNA cells treated with the miR21 mimic.

Whole-mount skeletal staining. Cartilage and mineralized tissue were analyzed in 6-day old newborn mice using alizarin red/alcian blue staining, as previously published.[122]

Circulating metabolites. Blood was collected by cheek bleeding after 6 hours of fasting. Plasma was separated, aliquoted, and stored at −80 °C until used. Plasma N-terminal propeptide of type I procollagen (P1NP) (Immunodiagnostic Systems Inc., Fountain Hill, AZ, USA, cat.#AC-33F1) and C-telopeptide fragments (CTX) (cat.#AC-06F1) were measured as described by the manufacturer. Alkaline phosphatase (ALP) activity was assessed by a standard automated method using a Randox Daytona chemical analyzer (Northern Ireland, United Kingdom).

Statistical analysis. Data were analyzed using SigmaPlot. All values are reported as the mean ± standard deviation. Data were evaluated by Student's t-test or two-way ANOVA and differences with $p<0.05$ were considered statistically significant.

Results

miR21 regulation of osteocyte viability and mitochondrial function is sex-dependent. To investigate the role of osteocytic miR21 locus *in vivo*, we generated a mouse model in which miR21 was deleted from osteocytes (Fig. 4-1A). Targeted-deletion of miR21 in osteocytes decreased miR21 levels ~50% in calvaria bone lysates of both female and male miR21$^{\Delta ot}$ compared to control miR21$^{f/f}$ mice (Fig. 4-1B). Interestingly, basal miR21 levels were higher in miR21$^{f/f}$ females than males, suggesting a sex-related difference in miR21 expression in bone. Additionally, we detected decreases in mRNA levels of vacuole membrane protein-1 (VMP1) in both female and male miR21$^{\Delta ot}$ compared to control miR21$^{f/f}$ mice, due to overlap between miR21 and the 3' UTR of VMP1 (Fig. 4-7). However, no sex-specific differences in VMP1 expression were detected in control mice.

Similar to our previous findings in Cx43-deficient osteocytic cells,[119] in females, the RANKL/OPG mRNA ratio was increased in bones from miR21$^{\Delta ot}$ compared to miR21$^{f/f}$ mice (Fig. 4-1C). Additionally, female miR21$^{\Delta ot}$ mice exhibited higher expression of the apoptosis-associated gene P27, as well as tendencies towards higher Gadd153 and Foxo3 (Fig. 4-1D).

Moreover, miR21 inhibition in control MLO-Y4 osteocytic cells, which are derived from a female mouse, increased the RANKL/OPG mRNA ratio and the expression of the apoptosis associated-genes (P27, Gadd153, and Foxo3) (Fig. 4-8A). Conversely, transfection of a miR21 mimic decreased the RANKL/OPG mRNA levels and apoptosis-related gene expression (Fig. 4-8B). Further, overexpression of miR21 in Cx43-deficient MLO-Y4 cells, which exhibit increased levels of apoptosis and express low levels of miR21 compared to scramble-silenced cells,[119] attenuated the increased RANKL/OPG mRNA ratio and apoptosis associated-gene expression (Fig. 4-9).

While no changes in RANKL or OPG gene expression were detected in the miR21$^{\Delta ot}$ compared to miR21$^{f/f}$ males (Fig. 4-1E), interestingly, our findings suggest that miR21 negatively regulates osteocyte viability. Specifically, miR21$^{\Delta ot}$ males exhibited lower levels of the apoptosis-associated genes (p27, Gadd153 and Foxo3) (Fig. 4-1F). Consistent with the sex-divergent effects of osteocytic miR21 deletion on the apoptosis-associated genes and RANKL/OPG mRNA levels, miR21 deletion differentially altered mitochondrial gene expression in females and males. Specifically, miR21$^{\Delta ot}$ females, but not males exhibited significantly lower levels of several mitochondria-associated genes, whereas in males, the expression of ND2 was increased (Fig. 4-1G,H).

Removal of osteocytic miR21 differentially regulates bone turnover in females and males. To determine whether removal of osteocytic miR21 also regulates bone mass and bone cell activity in a sex-dependent manner, we next examined the bone phenotype of miR21$^{\Delta ot}$ and miR21$^{f/f}$ mice of each sex. In females, deletion of miR21 from osteocytes did not alter the distribution of cartilage and mineralized bone in newborn mice (Fig. 4-10). Similarly, total, spinal and femoral BMD were not affected by miR21 deletion in females up to 4 months of age, although slight increases in body weight were detected between 3 and 4 months of age in miR21$^{\Delta ot}$ compared to miR21$^{f/f}$ mice (Fig. 4-2A). On the other hand, in males, total, spinal and femoral BMD were all significantly increased by 4 months of age in miR21$^{\Delta ot}$ compared to miR21$^{f/f}$ mice, while body weight was unaltered (Fig. 4-2B).

Osteocytic miR21 deletion led to sex-specific changes in bone cell activity and bone geometry in both cortical and cancellous bone compartments. In females, dynamic bone histomorphometry analysis of the femur mid-diaphysis showed that, while the bone formation parameters on the periosteal surface were not changed, MS/BS (the mineralized surface per total bone surface) and BFR/BS (bone formation rate per bone surface) were

significantly lower on the endocortical surface in miR21$^{\Delta ot}$ compared to miR21$^{f/f}$ mice (Fig. 4-3A). Conversely, in males, dynamic histomorphometry analysis of the femur mid-diaphysis showed that all bone formation measurements, MAR (mineral apposition rate), MS/BS, and BFR/BS, were increased on the periosteal surface, whereas no changes in bone formation were detected on the endocortical surface (Fig. 4-3B). Further, static histomorphometry analysis of the endocortical femur surface in females revealed a reduction in osteoclast number and surface per bone surface (N.Oc/BS and Oc.S/BS) in miR21$^{\Delta ot}$ compared to miR21$^{f/f}$ mice (Fig. 4-3C). Consistent with the histomorphometric findings in cortical bone, decreases in circulating serum levels of the bone turnover makers, CTX, P1NP, and ALP were also detected in the female miR21$^{\Delta ot}$ compared to miR21$^{f/f}$ mice (Fig. 4-11). In contrast to the reduced osteoclasts parameters in the miR21$^{\Delta ot}$ females, in males, N.Oc/BS and Oc.S/BS were higher in the miR21$^{\Delta ot}$ compared to miR21$^{f/f}$ mice (Fig. 4-3D).

Consistent with the sex-related alterations in bone cell activity induced by osteocytic miR21 deletion, sex-dependent changes in femur cortical bone geometry were also revealed by μCT analysis of the femur mid-diaphysis. In females, the suppressed endocortical bone turnover did not alter cortical bone geometry (Fig. 4-3E), whereas in males, the μCT parameters, tissue area (TA), bone area (BA), cortical thickness (C.Th), marrow cavity area, and moment of inertia were all increased in miR21$^{\Delta ot}$ compared to miR21$^{f/f}$ mice (Fig. 4-3F).

Sex-dependent alterations in bone turnover and architecture were also detected on cancellous surfaces within the vertebra. However, unlike the decrease in formation detected on the endocortical femur surface in females, removal of osteocytic miR21 did not alter cancellous osteoblast number or activity (Fig. 4-4A,B). On the other hand, reductions in Oc.S/BS were detected on the cancellous surface of miR21$^{\Delta ot}$ compared to miR21$^{f/f}$ female mice, while N.Oc/BS was unchanged (Fig. 4-4C). In males, no significant

changes in cancellous osteoblast number or surface per cancellous bone surface (N.Ob/BS and Ob.S/BS) were detected in miR21$^{\Delta ot}$ compared to miR21$^{f/f}$ mice (Fig. 4-4D). However, the dynamic histomorphometry bone formation parameter MS/BS was significantly higher in the male miR21$^{\Delta ot}$ mice, suggestive of higher amounts of bone forming surface (Fig. 4-4E). Similar to N.Ob/BS and Ob.S/BS, no significant differences in vertebral cancellous N.Oc/BS and Oc.S/BS were detected in the male miR21$^{\Delta ot}$ compared to the miR21$^{f/f}$ mice (Fig. 4-4F).

Despite the small changes in cancellous bone cell activity, μCT analysis detected significant alterations in cancellous bone architecture. In females, μCT of the vertebra revealed a slight increase in Tb.th (trabecular thickness) (Fig. 4-4G). On the other hand, in males μCT analysis detected significant increases in almost all the vertebral cancellous architecture parameters examined, including BV/TV (bone volume/tissue volume), Tb.Th, Tb.N (trabecular number), and material density miR21$^{\Delta ot}$ compared to miR21$^{f/f}$ mice (Fig. 4-4H). Similar alterations in cancellous architecture of the distal femur were also detected in female and male miR21$^{\Delta ot}$ compared to miR21$^{f/f}$ mice (Fig. 4-12).

Sex-divergent miR21 regulation of osteocyte cytokine production and release differentially controls osteoclastogenesis. Consistent with the *in vivo* decreases in osteoclast number and surface in the miR21$^{\Delta ot}$ compared to miR21$^{f/f}$ female mice, less mature osteoclasts were generated *in vitro* from female miR21$^{\Delta ot}$ compared to miR21$^{f/f}$ non-adherent BMCs (Fig. 4-5A). On the other hand, *in vitro* generation of mature osteoclasts from male miR21$^{\Delta ot}$ and miR21$^{f/f}$ non-adherent BMCs did not differ (Fig. 4-5B).

To further examine the mechanisms underlying the sex-specific osteoclast effects of osteocytic miR21 removal, we generated osteoclasts from wildtype BMCs cultured with CM from osteocyte-enriched miR21$^{\Delta ot}$ and miR21$^{f/f}$ bone cultures, as illustrated in Fig. 4-5C. Consistent with our *in vivo* results, addition of 50% CM from miR21$^{\Delta ot}$ females led to

0.7-fold less mature osteoclasts (Fig. 4-6D), while addition of only 25% CM was not sufficient to reduce osteoclast number or gene expression (Fig. 4-13A). Conversely, addition of 50% CM from miR21$^{\Delta ot}$ males led to 3.8-fold more osteoclasts that were larger in size (Fig 4-5E), and addition of 25% CM led to a tendency towards increase in osteoclast number and significantly increased osteoclast gene expression (Fig. 4-13B).

Next, we investigated the effects of osteocytic miR21 deficiency on osteocyte cytokine production and release. Consistent with the sex-dimorphic effects on osteoclastogenesis, mRNA levels of several pro-osteoclastogenic cytokines, IL-6, MCP-1, M-CSF, and VEGF-A were reduced in bone lysates from female, but not male miR21$^{\Delta ot}$ compared to miR21$^{f/f}$ mice (Fig. 4-5F,G). Further, osteocytic-miR21 deletion induced sex-specific inflammatory cytokine protein alterations in CM from marrow-flushed osteocyte-enriched bone. In CM from miR21$^{\Delta ot}$ female bones, M-CSF and VEGF protein levels showed tendencies towards decrease, whereas, in CM from miR21$^{\Delta ot}$ male bones, M-CSF and VEGF protein levels were increased, although MCP-1 levels were decreased (Fig. 4-5H,I and Tables 4-5A,B). Interestingly, in serum from these mice, an opposite pattern of expression was observed for several inflammatory cytokines altered in CM from miR21$^{\Delta ot}$ bones (Table 4-6A,B). These pieces of evidence suggest that removal of osteocytic miR21 alters osteoclastogenesis by modifying osteocyte-derived inflammatory cytokine production and release in the local bone microenvironment (Fig. 4-5J).

In addition, we detected sex-dependent decreases in the mRNA levels of several cytokines known to inhibit osteoblast differentiation and activity. Specifically, in bone lysates from miR21$^{\Delta ot}$ females, only SOST mRNA levels were reduced (Fig. 4-14A). On the other hand, in miR21$^{\Delta ot}$ male bones, IL-1β, DKK1, and SOST mRNA expression was significantly decreased compared to miR21$^{f/f}$ mice (Fig. 4-14B).

Moreover, consistent with the sex-divergent effects of osteocytic-miR21 deletion on osteocyte cytokine production, sex-specific changes in several signaling pathways

previously shown to be involved in regulating cytokine production and secretion were detected by Milliplex cell-signaling array analysis in bone lysates (Fig. 4-6A and Tables 4-1,2). Specifically, decreases in phosphorylated/total levels of ERK1/2 (-38%), STAT3 (-26%) and p38 (-28%) were detected in miR21$^{\Delta ot}$ females, but not in males. Moreover, miR21$^{\Delta ot}$ females exhibited a tendency towards increased phosphorylated/total NF-κB (+23%) levels. Further, while miR21$^{\Delta ot}$ males exhibited increased phosphorylated/total p70S6K (+22%) levels, females exhibited a tendency towards decreased p70S6K (-15%) levels. On the other hand, osteocytic miR21 deficiency induced similar decreases in JNK signaling in both females (-35%) and males (-28%), although significance was only reached in female mice.

miR21 has sex-independent effects on bone mechanical properties. Despite the sex-specific effects of osteocytic miR21 deficiency on bone cell activity and architecture, femoral bone mechanical properties were significantly higher in both female and male miR21$^{\Delta Ot}$ mice compared to the respective miR21$^{f/f}$ controls. In particular, in females, femur mechanical testing by 3-point bending detected significantly higher post-yield and total displacement (+35% and +29%), post-yield and total work (+19% and +17%), as well as the post-yield material property total strain (+26%), in miR21$^{\Delta ot}$ compared to miR21$^{f/f}$ mice (Table 4-3). No changes in the pre-yield mechanical properties at either the structural or material levels were detected in the female mice. In males, even greater increases were detected in post-yield and total displacement (+94% and +60%), post-yield and total work (+71% and +56%), as well as the post-yield material properties, total strain and toughness (+56% and +28%) in miR21$^{\Delta ot}$ compared to miR21$^{f/f}$ mice (Table 4-4). On the other hand, decreases in the pre-yield structural property, displacement to yield, and the pre-yield material property, yield stress, were detected in the male miR21$^{\Delta ot}$ compared to miR21$^{f/f}$ mice. Taken together, these findings suggest that bones from

miR21$^{\Delta ot}$ mice are more ductile, providing a potential mechanical advantage since the bones are more tolerant to damage accrual and, thus, less brittle and less susceptible to fracture. Given differences exist both at the structural and material level, it suggests that fundamental differences in the properties of the matrix underlie the enhanced mechanical properties.

Discussion

There is growing evidence that osteocytes are key regulators of bone homeostasis and orchestrators of bone cell activity.[30] In previous studies, we showed that miR21 expression is low in the absence of osteocytic Cx43 and in old female mice, and low miR21 levels are responsible for the increase in osteocyte apoptosis in the Cx43-deficient cells.[119] Additionally, we demonstrated that osteocyte apoptosis directly promotes osteocyte cytokine production and stimulates osteoclast differentiation.

Here we offer additional insights into the role of miR21 in osteocytes. We now provide evidence that the miR21 locus exerts a sex-divergent role in osteocytes controlling osteocyte viability and regulating bone mass/geometry through paracrine actions on osteoblasts and osteoclasts. Further, we reveal a potential mechanism by which miR21 removal from osteocytes differentially alters bone turnover by sex-specific regulation of key signaling pathways in osteocytes as well as cytokine production/secretion. Interesting, we also demonstrate that despite these sex-divergent effects on osteocyte viability and bone turnover, osteocytic miR21 negatively influences bone mechanical properties in a sex-independent manner.

First, we demonstrate that miR21 differentially controls osteocyte viability in females and males. Consistent with our previous findings examining the role of miR21 in Cx43 deficiency and aging,[119] in females, removal of osteocytic miR21 increased osteocyte apoptosis and suppressed mitochondrial gene transcription. These anti-apoptotic effects of miR21 are consistent with numerous studies showing that miR21 promotes cell survival by directly targeting and inhibiting FasL and PTEN.[123-125] In particular, we previously demonstrated that increases in osteocyte apoptosis in Cx43-deficient osteocytic cells and bones from old female mice, are due to low miR21 levels which increase PTEN levels and consequently reduce Akt signaling.[119] In cardiac tissue, miR21 has been shown to directly promote mitochondrial cytochrome B translation and

reduce reactive oxygen species (ROS) production.[126] Additionally, miR21 promotes mitochondrial homeostasis and adaptation in mTORc1-activated cells.[127] Further, miR21 promotes cancer cell-survival by down-regulating PTEN and consequently activating the PI3K/AKT/mTOR pathway.[128] Consistent with these pieces of evidence as well as our current findings showing that miR21 exerts sex-divergent effects on osteocyte viability and mitochondria function, we detected sex-dependent alterations in phosphorylated levels of the mTOR substrate, p70S6K. Specifically, miR21$^{\Delta ot}$ males exhibited significantly higher p70S6K levels, whereas, miR21$^{\Delta ot}$ females showed trends towards lower Akt and p70S6K levels. Interestingly, consistent with our findings in miR21$^{\Delta ot}$ males, several other studies have found that inhibition of miR21 protects against fibrosis by improving mitochondrial function.[129, 130] Taken together these pieces of evidence highlight the possibility that miR21 regulation of mTORc1 signaling in osteocytes may underlie these sex-divergent effects on osteocyte viability and mitochondrial function, however, additional studies are needed to clearly elucidate the specific mechanisms by which osteocytic miR21 exerts these sex-divergent effects. Nevertheless, our findings highlight a novel sex-divergent role of miR21 in osteocytes and raise the possibility that similar sex-divergent miR21 regulation exists in other tissues.

Further, consistent with the effects of osteocytic miR21 removal on osteocyte viability, RANKL/OPG mRNA levels were only increased in bones from miR21$^{\Delta ot}$ females. Surprisingly, despite the RANKL/OPG ratio changes osteoclast differentiation and resorption were attenuated in miR21$^{\Delta ot}$ females, but elevated in miR21$^{\Delta ot}$ males. Similar to our findings in miR21$^{\Delta ot}$ females, Hu et. al, found that osteoclast function was inhibited in global miR21 deficient (miR21$^{-/-}$) mice in spite of the fact that RANKL production and secretion were increased.[131] However, since mice were not separated by gender and because miR21, which is known to regulate osteoclast differentiation and survival,[112, 124] was globally deleted, it is unclear if the inhibitory effects on osteoclasts in this study were

due to a lack of miR21 regulation in osteocytes or a direct result of miR21 deficiency in osteoclasts. In our study, we found that addition of osteocyte-enriched bone culture CM from miR21$^{\Delta ot}$ females suppressed osteoclasts, whereas CM from miR21$^{\Delta ot}$ males stimulated osteoclasts, suggesting that these effects are due to the lack of miR21 in osteocytes. Furthermore, the fact that these results occurred independently of whether female or male BMCs were used, suggests that the sex-specific effects of osteocytic miR21 removal on osteoclasts are due to miR21 regulation in osteocytes rather than direct effects on osteoclasts.

In addition, miR21 regulation in osteoblasts has been shown to promote differentiation and mineralization, by targeting/inhibiting the expression of SMAD7, a negative regulator of osteoblast proliferation, differentiation, and mineralization.[132] Consistent with this, osteoblast differentiation and activity were altered in miR21$^{-/-}$ mice.[131] When cultured *ex vivo* osteogenic differentiation potential of miR21$^{-/-}$ BMCs was decreased, while colony forming efficiency and proliferation rates were increased. Interestingly, despite these changes, osteoblast number and activity were unaltered *in vivo*, possibly because mice of both sexes were combined in the *in vivo* study. In the current study, we found that osteocytic miR21 deletion also altered osteoblast number and activity in a sex- and site-dependent manner. Further, consistent with the effects on bone cell differentiation and activity, osteocytic miR21 deficiency induced sex- and compartment-specific effects on bone mass and architecture. Future studies will be performed to determine whether the mild effect of miR21 deletion on bone mass and architecture is exacerbated with aging.

Based on the non-cell autonomous effects on osteoclasts and osteoblasts detected in the miR21$^{\Delta ot}$ mice, we next investigated the effects of miR21 regulation on osteocyte cytokine production and release. Consistent with the sex-dimorphic effects on osteoclasts and osteoblasts we found that mRNA levels of several cytokines were reduced

in bones from female, but not male miR21$^{\Delta ot}$ mice. On the other hand, we detected decreases in the mRNA levels of IL-1β and DKK1, which negatively regulate osteoblast differentiation and activity, in bones from miR21$^{\Delta ot}$ males, but not females. Further, in CM from miR21$^{\Delta ot}$ bones, M-CSF and VEGF protein levels were increased in males, but showed tendencies towards decrease in females. Additionally, given the changes in IL-6 expression detected at the mRNA level it is also possible that IL-6 levels are altered in the miR21$^{\Delta ot}$ CM, however because the levels were greater than the standard use in the multiplex assays we were unable to measure them. Interestingly, we also found several cytokines exhibited an opposite pattern of expression in serum compared to CM from miR21$^{\Delta ot}$ bones, suggesting that that removal of osteocytic miR21 exerts non-cell autonomous effects on osteoclasts and osteoblasts by locally rather than systemically altering osteocyte-derived cytokine levels.

In addition to these sex-specific alterations in cytokine production and secretion in the miR21$^{\Delta ot}$ mice, we found osteocytic miR21 deficiency altered osteocyte signaling pathways in a sex-dependent manner. Interestingly, several signaling pathways that are regulated by previously identified miR21 target genes were downregulated in miR21$^{\Delta ot}$ females, but not males, as illustrated in Fig. 4-6A. In particular, phosphorylated ERK1/2, p38, and STAT3 levels were significantly reduced, whereas, phosphorylated NF-κB levels showed tendencies towards increase in miR21$^{\Delta ot}$ female bones. Consistent with these findings, previous studies have shown that miR21 directly targets inhibitors of ERK1/2 (Spry1/2), p38 (SMAD7) and STAT3 (PIAS3).[132-134] Additionally, miR21 targets PDCD4, which in turn activates NF-κB signaling.[131, 135]

Further, consistent with the reduced cytokine levels detected in the miR21$^{\Delta ot}$ females, several studies demonstrated that ERK1/2, p38, and STAT3 pathways regulate VEGF and IL-6 secretion.[136-138] Notably, in MLO-Y4 osteocytic cells, advanced glycation end products (AGEs) induce apoptosis and stimulate IL-6 and VEGF production and

secretion, and conversely, inhibition of the ERK1/2, p38, and STAT3 signaling pathways attenuates these effects of AGEs on osteocyte viability and cytokine production.[139] Further, under mechanical loading, STAT3 and ERK1/2 signaling pathways stimulate osteoblast differentiation and osteoclast activity by inducing IL-6.[140] Taken together these findings highlight the possibility that downregulation of the ERK1/2, p38, and STAT3 signaling pathways may contribute to the reduced IL-6 and VEGF production in miR21$^{\Delta ot}$ females. Further, our findings that STAT3 signaling and mitochondrial metabolism are both reduced in the miR21$^{\Delta ot}$ females, are consistent with the previously established role STAT3 in regulating cellular respiration and mitochondrial metabolism.[141] Nevertheless, while these findings suggest that miR21 regulates osteocyte signaling pathways and cytokine production/secretion in sex-specific manner, additional studies are required to clearly elucidate the molecular events mediating these autocrine and paracrine effects of osteocytic miR21 on bone metabolism.

Alterations in miR21 expression have been detected in numerous diseases. However, the tissue-specific roles of miR21 under physiological and pathological conditions remains unclear. In some cases miR21 has been shown to promote disease progression, while in others miR21 is protective.[142, 143] While there are several potential explanations for the varying results regarding the role of miR21 in different tissues under normal and disease conditions, given the findings of our present study, it is possible that the differential effects of miR21 are due to differential sex-dependent roles of miR21. Consistent with this notion, work by Queirós et. al, detected sex differences in the expression of several miRs including miR21, as well as, miR24, miR27a, miR27b, miR106a and miR-106b that negatively regulate MAPK/ERK signaling in the heart.[144] Additionally, the latter study showed that estrogen modulates the expression of these miRs in a sex-specific manner via estrogen receptor (ER) β. Further, in bone, studies have shown induction of miR21 during osteoclastogenesis preserves survival through negative

regulation of FasL and estrogen stimulates osteoclast apoptosis by antagonizing miR21.[124] Taken together these pieces of evidence highlight the possibility that sex-divergent effects of miR21 in osteocytes are due to estrogen mediated regulation of miR21. Thus, given the increasing number of pharmaceutical companies working to develop miR-based drugs combined with the growing number of studies identifying gender-dependent adverse drug reactions,[145] our findings highlight the importance of considering sex-dependent miR roles when developing therapeutics.

Interestingly, despite these sex-specific effects of osteocytic miR21 deficiency, both female and male miR21$^{\Delta Ot}$ mice exhibited markedly higher femoral cortical bone mechanical properties compared to the respective miR21$^{f/f}$ controls. In particular, our findings that osteocytic miR21 deficiency enhanced the femur post-yield mechanical properties, suggest that bones from miR21$^{\Delta ot}$ mice are more ductile, providing a potential mechanical advantage since the bones are more tolerant to damage accrual and, thus, less brittle and less susceptible to fracture. As improvements in mechanical properties cannot be accounted for by the alterations observed at the cellular and structural level, it is likely that they result from differences in the matrix itself. Traditionally, alterations in post-yield properties are due to collagen structure/cross-linking. Consistent with having changes in collagen, JNK signaling, which is increased with aging[146] and shown here to be decreased in both female and male miR21$^{\Delta ot}$ mice, has previously been shown to impair collagen synthesis in osteoblasts and inversely correlate with the expression of collagen genes (Col2A1, Col5A1, Col5A3, Col8A1, and Col8A2) which are decreased in osteoblasts from old animals.[146] These pieces of evidence highlight a possible mechanism by which osteocytic miR21 deficiency improves bone mechanical properties by stimulating collagen synthesis via downregulation of JNK signaling. However, extensive additional studies are required to uncover the molecular and tissue-level mechanisms by which osteocytic miR21 negatively influences bone mechanical integrity.

Moreover, consistent with these negative sex-independent effects of miR21 on bone mechanical properties, several studies have found that miR21 levels are upregulated in serum, bone tissue, and bone cells (osteoblasts and osteoclasts) of osteoporotic patients compared to controls.[147] Additionally, miR21 levels were strongly inversely correlated with BMD and fracture incidence in osteoporotic patients. Thus, our findings that removal of osteocytic miR21 enhances bone biomechanical properties in both sexes, suggest a therapeutic potential of miR21 antagomir treatment to prevent bone fragility in aging in females and males. Further, given the fact that altered miR21 expression is most commonly seen under pathological conditions, our results provide a basis for future studies to test whether osteocytic miR21 deficiency protects against bone loss induced under pathological conditions i.e. sex-steroid deficiency, unloading, or aging.

Collectively, our findings provide evidence that the miR21 locus exerts a sex-divergent role in osteocytes, directly regulating cell viability/mitochondrial function in osteocytes and subsequently altering bone metabolism and architecture through paracrine actions on osteoblasts and osteoclasts. Further, despite these sex-dependent effects, removal of osteocytic miR21 enhances bone mechanical properties in both sexes. Overall, our findings provide novel insights into the sex-dependent and -independent mechanisms by which miR21 regulation in osteocytes alters bone, summarized in Fig. 4-6B, which offer a basis for future studies that could eventually lead to new therapeutic targets to treat bone fragility.

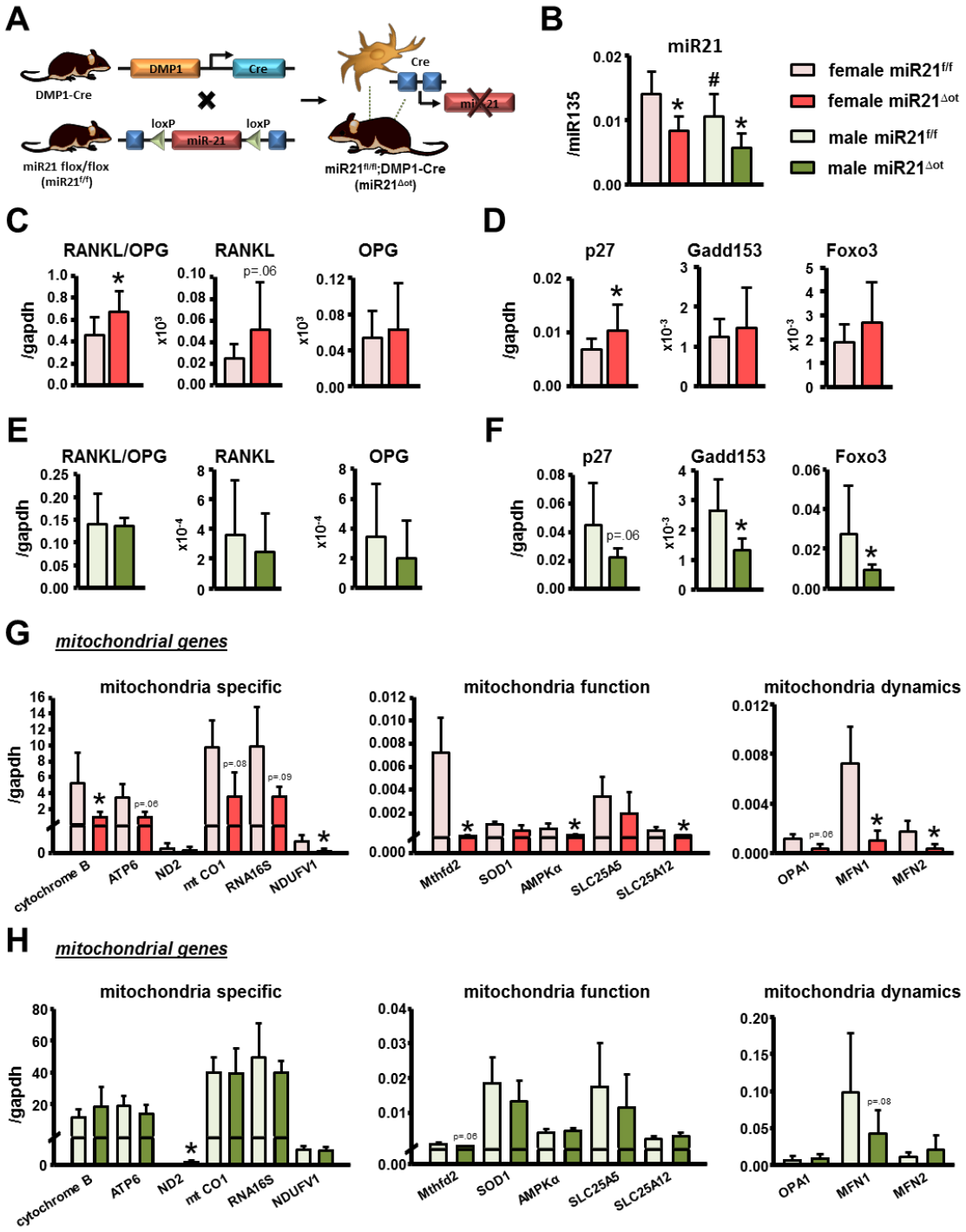

Figure 4-1. Sex-dependent miR21 regulation of osteocyte viability and mitochondrial function. (A) Scheme illustrating generation of mouse model with osteocyte-targeted miR21 deletion. (B) miR-21 levels in calvaria bones from female and male miR21$^{f/f}$ and

miR21$^{\Delta ot}$ mice by qPCR and corrected by miR135 (n= 10-14). Bars represent mean ± s.d., *p<0.05 versus miR21$^{f/f}$ mice, $^{\#}$p<0.05 versus miR21$^{f/f}$ females, by two-way ANOVA. (C) RANKL and OPG levels and (D) mRNA expression of apoptosis-associated genes measured in calvaria bones from female miR21$^{f/f}$ and miR21$^{\Delta ot}$ mice (n= 10-14). (E) RANKL and OPG levels and (F) mRNA expression of apoptosis-associated genes measured in calvaria bones from male miR21$^{f/f}$ and miR21$^{\Delta ot}$ mice (n= 10). mRNA expression of mitochondrial genes in calvaria bones from (G) female and (H) male miR21$^{f/f}$ and miR21$^{\Delta ot}$ mice (n= 10). Bars represent mean ± s.d., *p<0.05 versus miR21$^{f/f}$, by t-test.

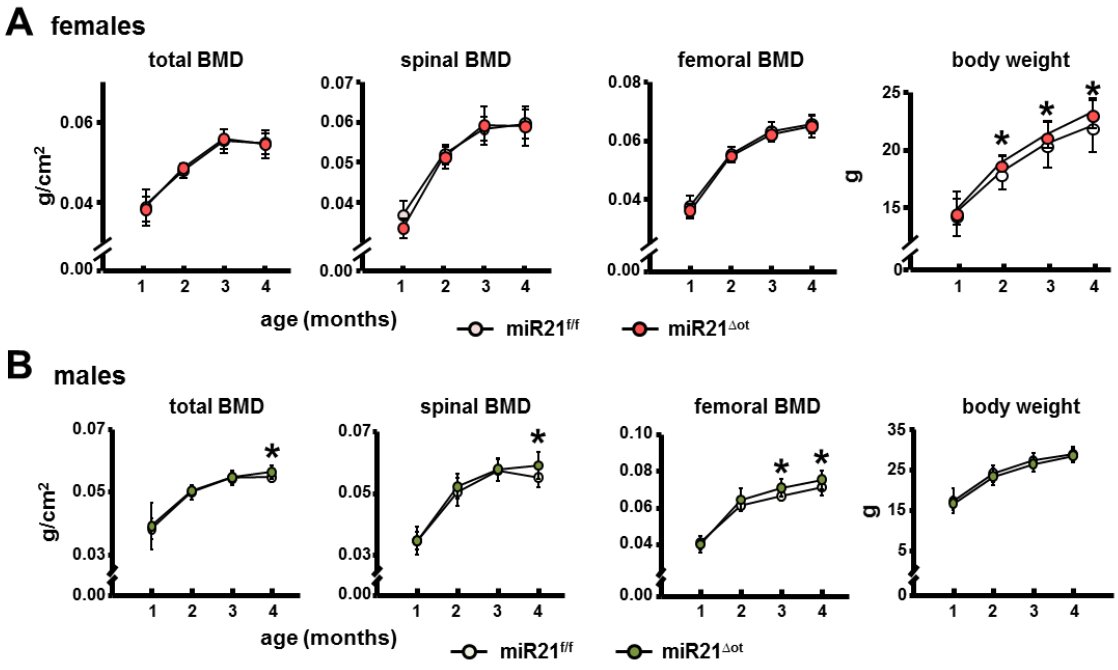

Figure 4-2. Removal of osteocytic miR21 regulates body weight and bone mass accrual in a sex-dependent manner. Body weight, and total, spinal and femoral BMD (DXA) were assessed monthly from 1 to 4 months of age in (A) female and (B) male miR21$^{f/f}$ and miR21$^{\Delta ot}$ mice (n=12-16). Bars represent mean ± s.d., *p<0.05 versus miR21$^{f/f}$ at the same age, by t-test.

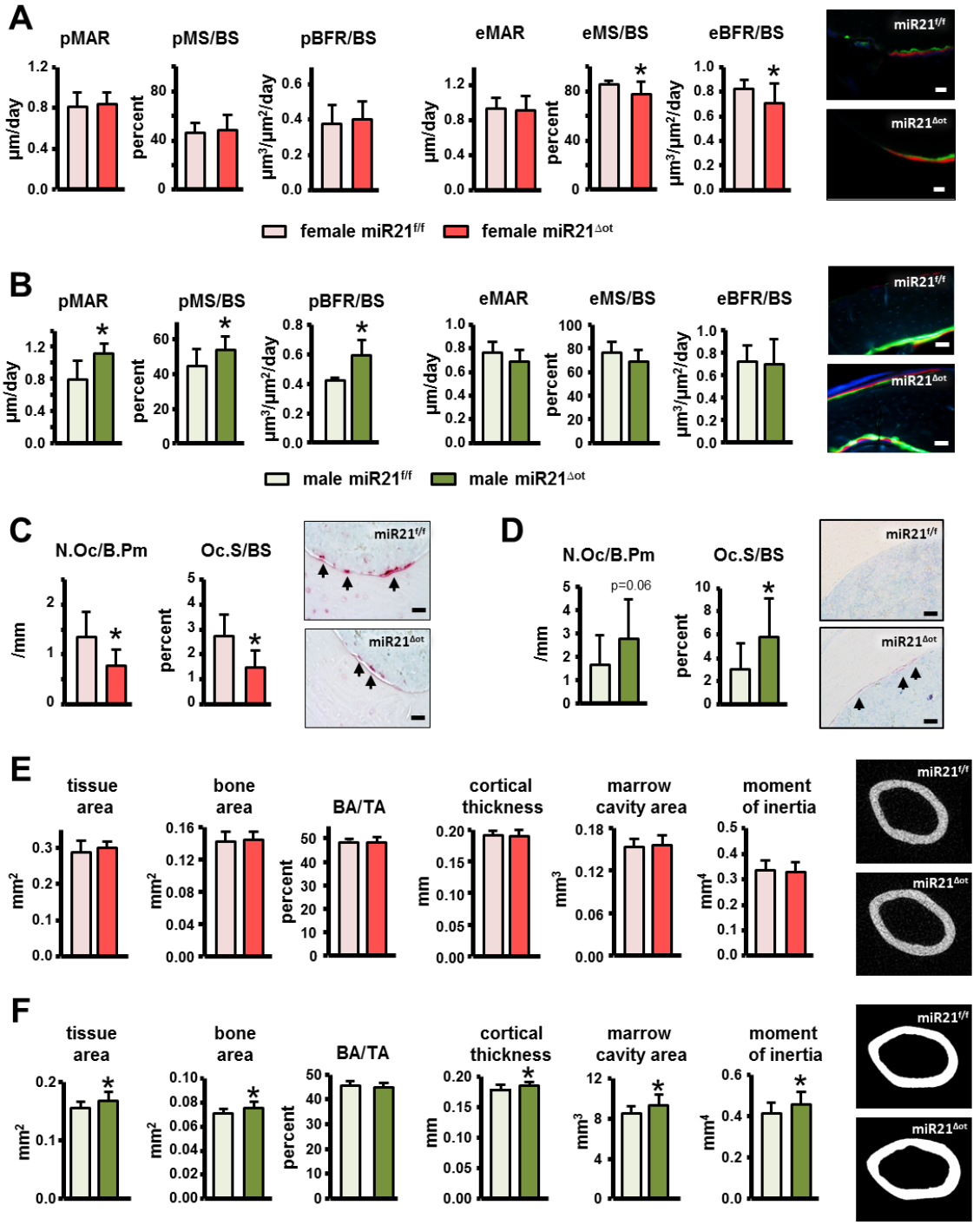

Figure 4-3. Osteocytic-miR21 deletion leads to sex-specific changes in femoral cortical bone turnover and architecture. (A-B) Mineral apposition rate (MAR), mineralizing surface (MS)/BS, and bone formation rate (BFR)/BS were measured in unstained cross-sections

of the femoral mid-diaphysis on the endosteal and periosteal surfaces of (A) female and (B) male miR21$^{f/f}$ and miR21$^{\Delta ot}$ mice (n=9-10). Representative fluorescent images are shown, scale bar indicates 25μm. (C-D) Osteoclast number (N.Oc)/BS and surface covered by osteoclasts (Oc.S)/BS were scored on the endosteal surface of femoral mid-diaphysis bone sections stained for TRAPase/T. blue of (C) female and (D) male miR21$^{f/f}$ and miR21$^{\Delta ot}$ mice (n=10). Representative images from osteoclasts on the bone surface (magenta, arrow) are shown, scale bar indicates 25μm. (E-F) Cortical bone geometry in the femoral mid-diaphysis of (E) female and (F) male miR21$^{f/f}$ and miR21$^{\Delta ot}$ mice was assessed by μCT (n=12). Representative reconstructed images are shown. Bars represent mean ± s.d., *$p<0.05$ versus miR21$^{f/f}$, by t-test.

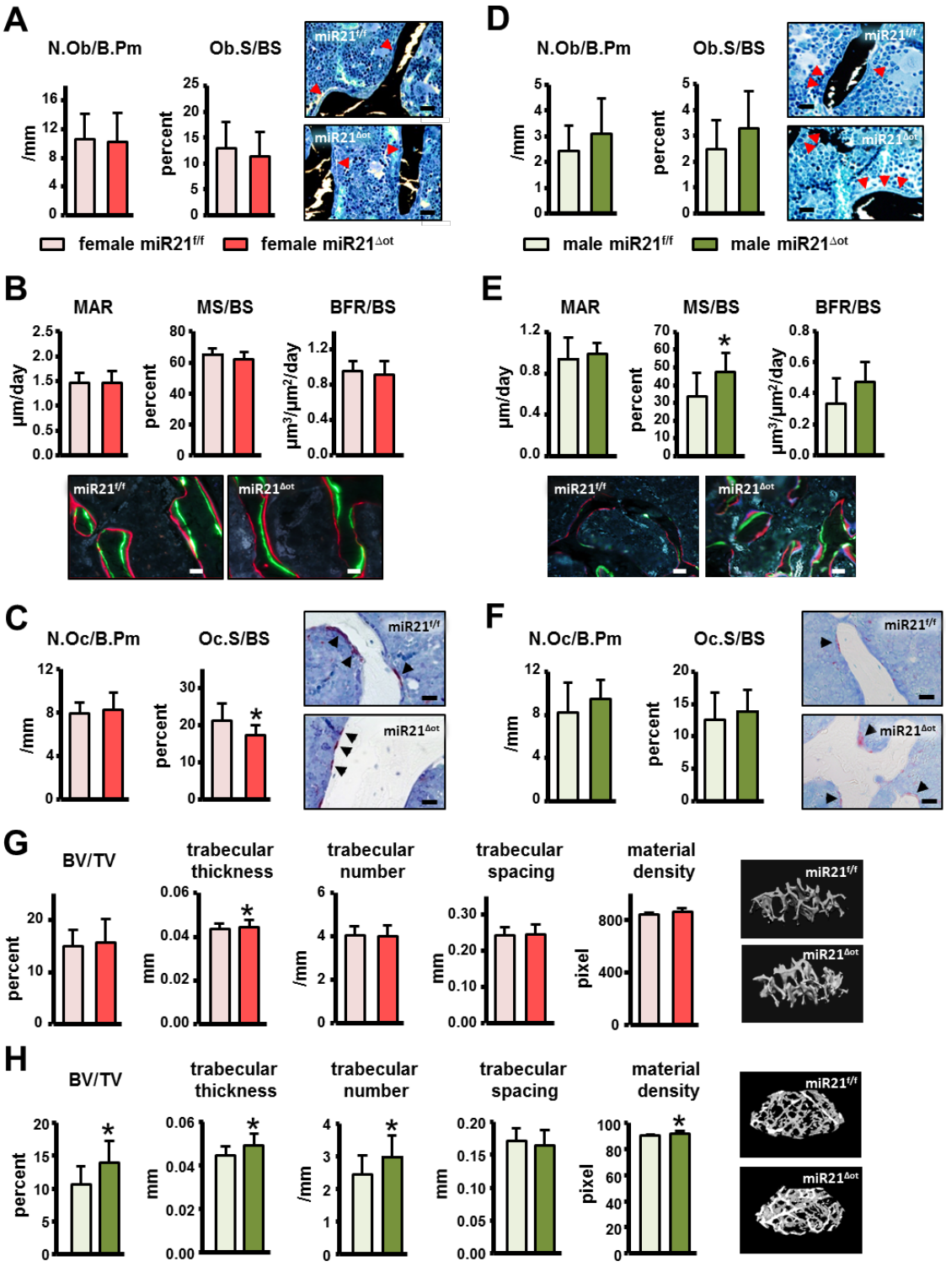
A
N.Ob/B.Pm
/mm
Ob.S/BS
percent
miR21f/f
miR21Δot
female miR21f/f
female miR21Δot
D
N.Ob/B.Pm
/mm
Ob.S/BS
percent
miR21f/f
miR21Δot
male miR21f/f
male miR21Δot
B
MAR
µm/day
MS/BS
percent
BFR/BS
µm³/µm²/day
miR21f/f
miR21Δot
E
MAR
µm/day
MS/BS
percent
*
BFR/BS
µm³/µm²/day
miR21f/f
miR21Δot
C
N.Oc/B.Pm
/mm
Oc.S/BS
percent
*
miR21f/f
miR21Δot
F
N.Oc/B.Pm
/mm
Oc.S/BS
percent
miR21f/f
miR21Δot
G
BV/TV
percent
trabecular thickness
mm
*
trabecular number
/mm
trabecular spacing
mm
material density
pixel
miR21f/f
miR21Δot
H
BV/TV
percent
*
trabecular thickness
mm
*
trabecular number
/mm
*
trabecular spacing
mm
material density
pixel
*
miR21f/f
miR21Δot

Figure 4-4. Sex-dependent alterations in vertebral cancellous bone turnover and architecture induced with removal of osteocytic-miR21. (A-F) Number of osteoblasts (N.Ob)/BS and bone surface covered by osteoblasts (Ob.S)/BS were scored in lumbar vertebra from (A) female and (D) male miR21$^{f/f}$ and miR21$^{\Delta ot}$ mice bone sections stained with von Kossa/McNeal (n=7-10). Representative images of osteoblasts are shown, scale bar indicates 25μm. Mineral apposition rate (MAR), mineralizing surface (MS)/BS, and bone formation rate (BFR)/BS measured in unstained sections of the lumbar vertebra from (B) female and (E) male miR21$^{f/f}$ and miR21$^{\Delta ot}$ mice (n=8-10). Representative fluorescent images are shown, scale bar indicates 25μm. Osteoclast number (N.Oc)/BS and surface covered by osteoclasts (Oc.S)/BS were scored on the cancellous bone surface of the lumbar vertebra from (C) female and (F) male miR21$^{f/f}$ and miR21$^{\Delta ot}$ mice stained for TRAPase/T. blue (n=9-10). Representative images from osteoclasts on the bone surface (magenta, arrow) are shown, scale bar indicates 25μm. (G-H) Analysis of cancellous bone microarchitecture in L4 vertebra from (G) female and (H) male miR21$^{f/f}$ and miR21$^{\Delta ot}$ mice assessed by μCT (n=12-14). Representative 3D images of vertebral cancellous bone are shown. Bars represent mean ± s.d., *$p<0.05$ versus miR21$^{f/f}$, by t-test.

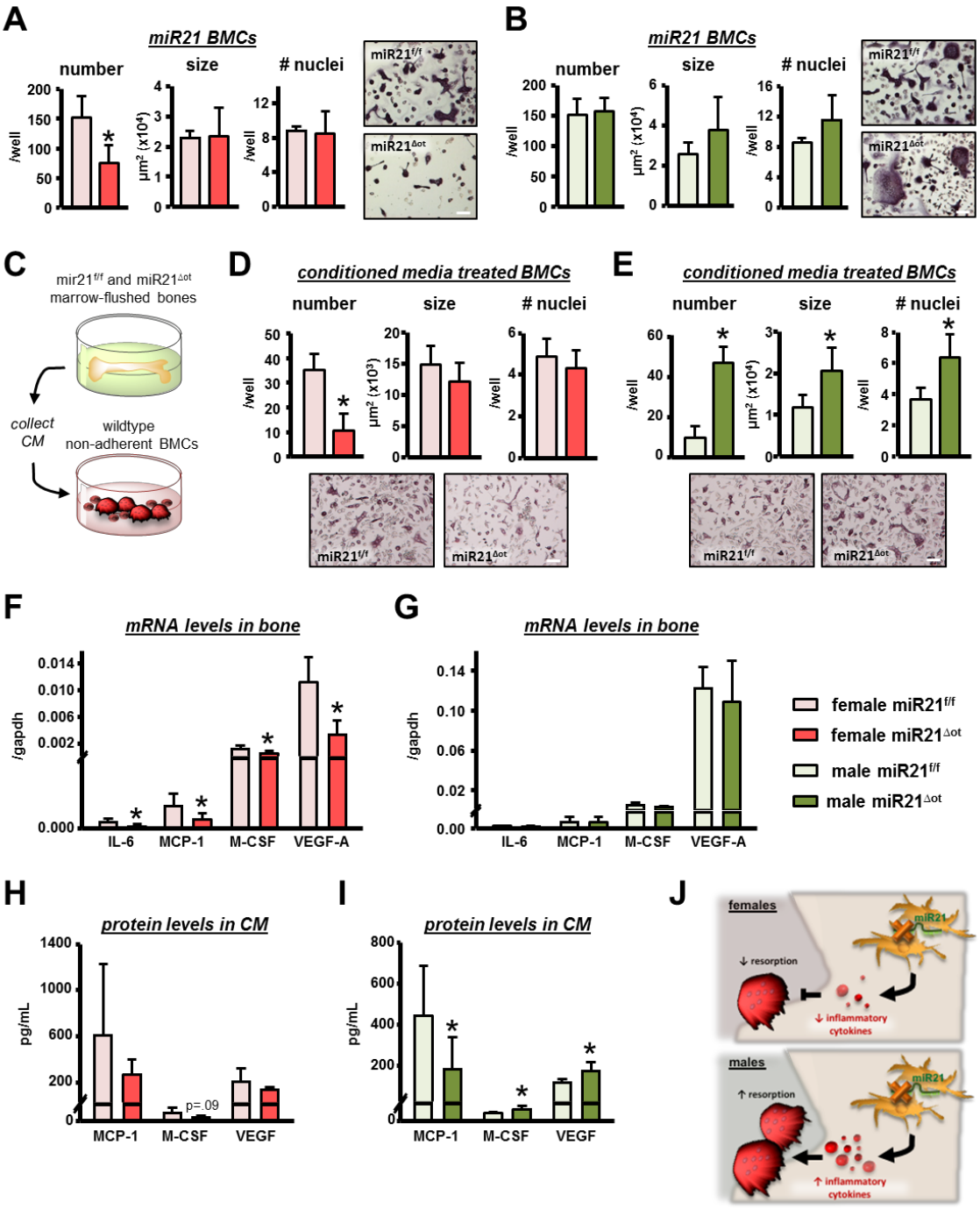

Figure 4-5. Sex-specific regulation of osteoclast differentiation following osteocytic-miR21 removal. (A-B) Non-adherent BMCs harvested from female and male miR21$^{f/f}$ and miR21$^{\Delta ot}$ were differentiated into osteoclasts with RANKL/M-CSF for 7 days. Osteoclast

number per well, average osteoclast size and number of nuclei per osteoclast were scored for (A) female and (B) male miR21$^{f/f}$ and miR21$^{\Delta ot}$ non-adherent BMCs (n=4). Representative images from mature osteoclasts stained for TRAPase are shown, scale bar indicates 100μm. (C) Illustration of experimental design in which non-adherent BMCs isolated from wild-type C57BL/6 mice were treated with CM from *ex vivo* cultures of long bones from female and male miR21$^{f/f}$ and miR21$^{\Delta ot}$ and supplemented with RANKL/M-CSF for 7 days. (D-E) Osteoclast number per well, average osteoclast size and number of nuclei per osteoclast were scored for female non-adherent BMCs treated with CM from (D) female and (E) male miR21$^{f/f}$ and miR21$^{\Delta ot}$ (n=6). Representative images from mature osteoclasts stained for TRAPase are shown, scale bar indicates 100μm. (F-G) mRNA expression of pro-inflammatory cytokine genes in calvaria bones from (F) female and (G) male miR21$^{f/f}$ and miR21$^{\Delta ot}$ mice. (H-I) Pro-inflammatory cytokine protein levels in CM from *ex vivo* marrow-flushed osteocyte enriched bone cultures from (H) female and (I) male miR21$^{f/f}$ and miR21$^{\Delta ot}$ mice, measured by Milliplex cytokine array. Bars represent mean ± s.d., *$p<0.05$ versus miR21$^{f/f}$, by t-test. (J) Illustration of the proposed model by which removal of osteocytic miR21 modulates pro-inflammatory cytokine production and osteoclast differentiation.

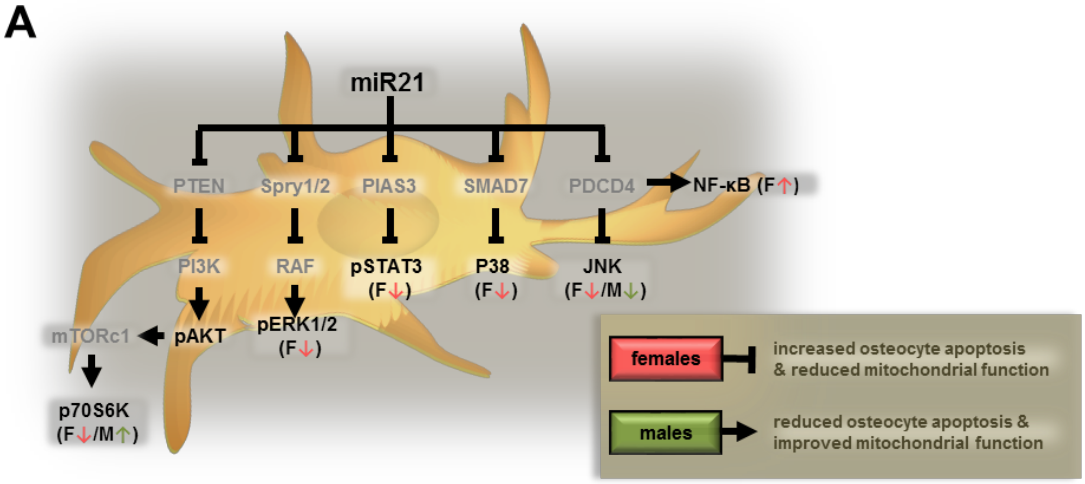
A
miR21
PTEN
Spry1/2
PIAS3
SMAD7
PDCD4
NF-κB (F↑)
PI3K
RAF
pSTAT3 (F↓)
P38 (F↓)
JNK (F↓/M↓)
mTORc1
pAKT
pERK1/2 (F↓)
p70S6K (F↓/M↑)
females
increased osteocyte apoptosis & reduced mitochondrial function
males
reduced osteocyte apoptosis & improved mitochondrial function

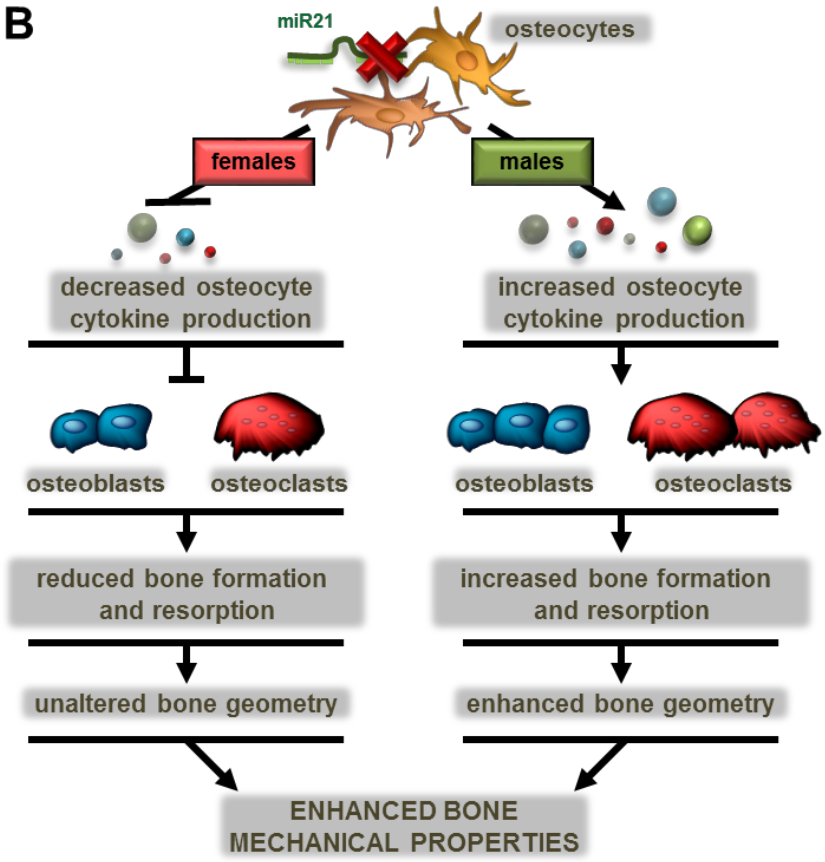
B
miR21
osteocytes
females
males
decreased osteocyte cytokine production
increased osteocyte cytokine production
osteoblasts
osteoclasts
osteoblasts
osteoclasts
reduced bone formation and resorption
increased bone formation and resorption
unaltered bone geometry
enhanced bone geometry
ENHANCED BONE MECHANICAL PROPERTIES

Figure 4-6. Working models illustrating the proposed autocrine and paracrine effects of osteocytic miR21 removal. (A) Figure illustrating the sex-specific regulation of key cell-signaling pathways in osteocytes by miR21, in turn, leads to sex-dependent alterations in osteocyte viability and mitochondrial function. Previously identified miR21 targets are shown in grey and proteins altered in the current study are shown in black. Direction of changes in protein levels are indicated using arrows for miR21$^{\Delta ot}$ female (pink) and male (green) mice. (B) Working model showing the proposed sex-dependent mechanisms by which miR21 regulation in osteocytes alters bone metabolism and geometry through paracrine actions on osteoblasts and osteoclasts. At the same time, removal of osteocytic miR21 enhances bone mechanical properties in a sex-independent manner.

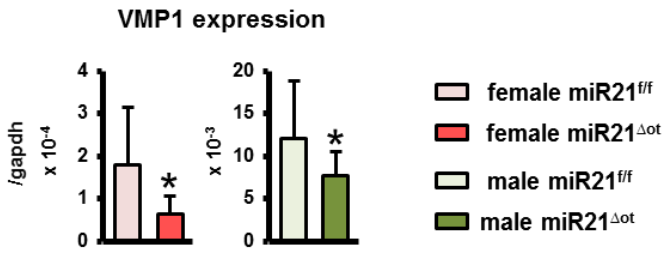

Figure 4-7. VMP1 mRNA levels are decreased in both female and male miR21$^{\Delta ot}$ compared to control miR21$^{fl/fl}$ mice. mRNA levels of vacuole membrane protein-1 (VMP1) measured in calvaria bones from female and male miR21$^{fl/fl}$ and miR21$^{\Delta ot}$ mice. Bars represent mean ± s.d., *$p<0.05$ versus miR21$^{fl/fl}$, by t-test.

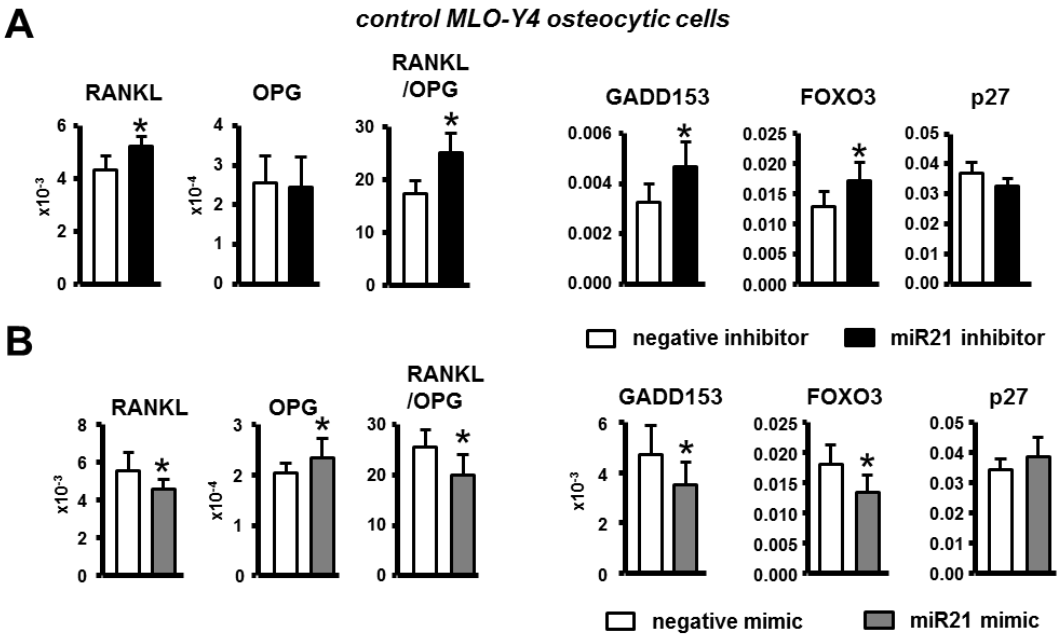

Figure 4-8. miR21 maintains osteocyte viability and regulates RANKL/OPG levels in control MLO-Y4 osteocytic cells. RANKL and OPG levels and apoptosis-associated gene expression (Gadd153, Foxo3, and P27) in miR-21 (A) antagomir and (B) mimic transfected MLO-Y4 osteoctyic cells. Bars represent mean ± s.d., *p<0.05 versus negative control, by t-test.

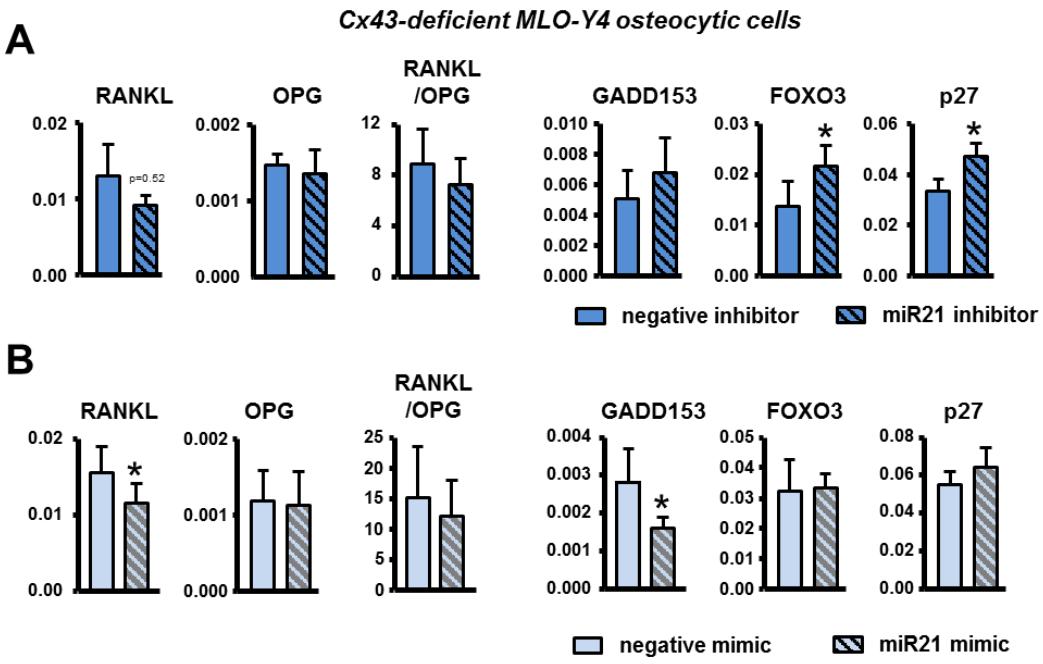

Figure 4-9. miR21 has similar effects on osteocyte viability and RANKL/OPG levels in Cx43-deficient MLO-Y4 osteocytic cells. RANKL and OPG levels and apoptosis-associated gene expression (Gadd153, Foxo3, and P27) in miR-21 (A) antagomir and (B) mimic transfected Cx43-deficient MLO-Y4 cells. Bars represent mean ± s.d., *p<0.05 versus negative control, by t-test.

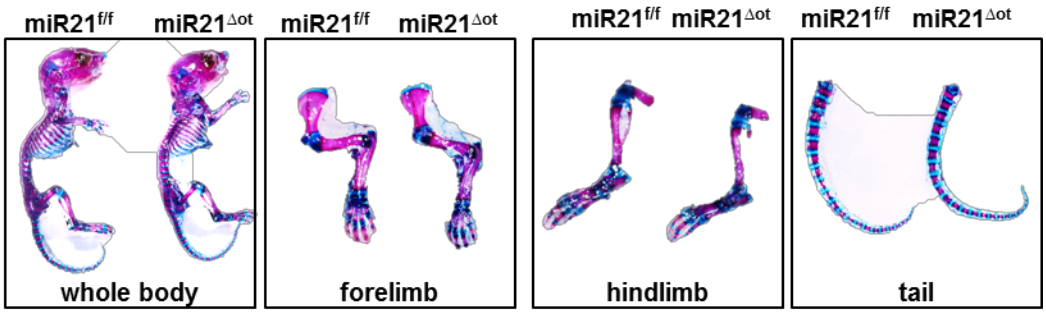

Figure 4-10. Deletion of miR21 from osteocytes did not alter the distribution of cartilage and mineralized bone in newborn mice. Representative images of whole body preparations (n=3/genotype) stained by Alcian blue/alizarin red in 7-day-old mice for evaluation of cartilage (blue) and calcified tissue (magenta).

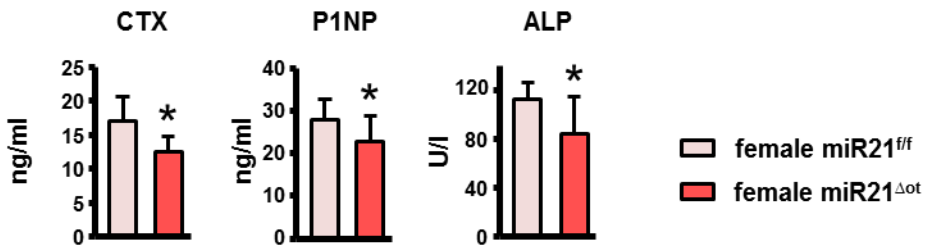

Figure 4-11. Osteocytic miR21 deficiency suppresses bone turnover in female mice. Circulating markers of bone resorption (CTX, n=10-15) and formation (P1NP, 10-14 and ALP, n=10-12) measured in serum of 4-month-old female miR21$^{f/f}$ and miR21$^{\Delta ot}$ mice by ELISA.

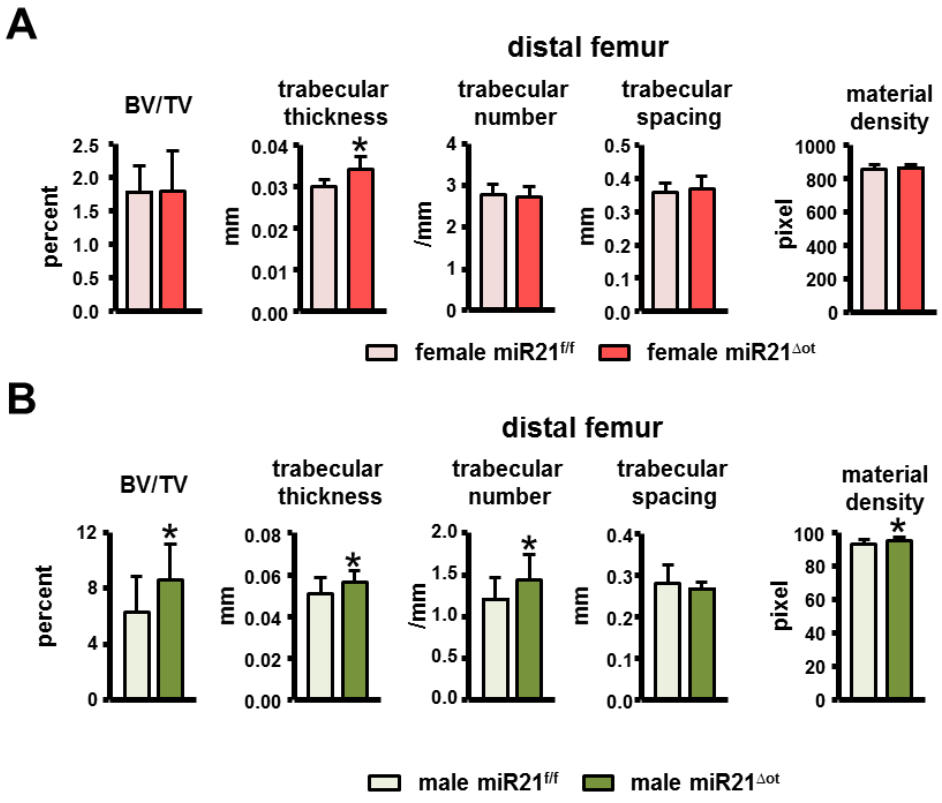

Figure 4-12. Removal of osteocytic alters distal femur cancellous architecture in a sex-dependent manner. Analysis of the distal femur cancellous bone microarchitecture of female and male miR21$^{f/f}$ and miR21$^{\Delta ot}$ mice was assessed by μCT (n=12-14). Bars represent mean ± s.d., *p<0.05 versus miR21$^{f/f}$, by t-test.

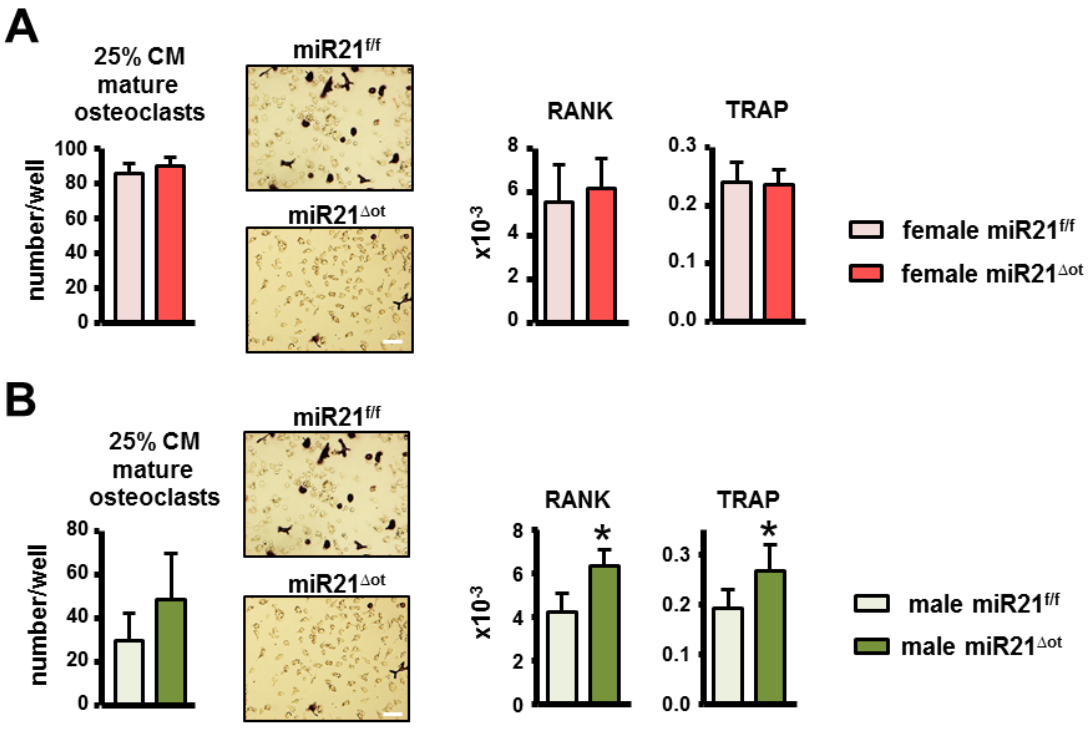

Figure 4-13. Sex-specific regulation of osteoclast differentiation following osteocytic-miR21 removal. Osteoclast number per well and gene expression levels were measured in non-adherent BMCs treated with 25% conditioned media from (A) female and (B) male miR21$^{f/f}$ and miR21$^{\Delta ot}$ (n=6). Representative images from mature osteoclasts stained for TRAPase are shown, scale bar indicates 100μm.

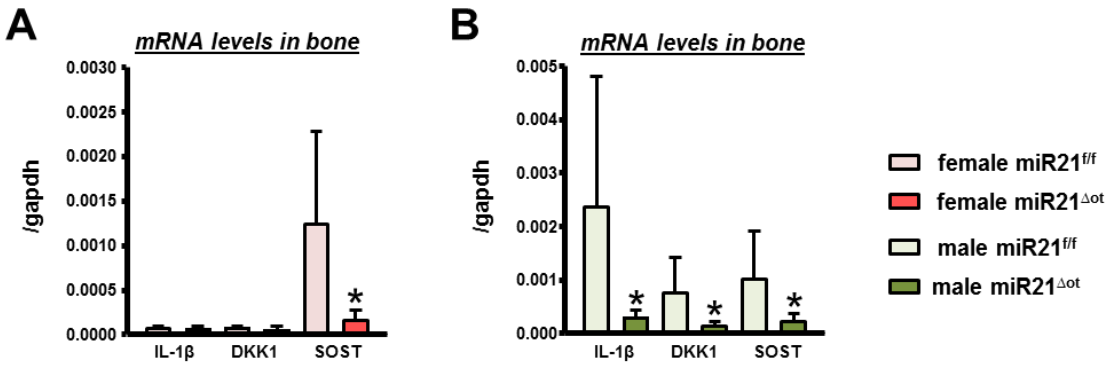

Figure 4-14. Sex-dependent decreases in anti-osteoblastic cytokine mRNA levels in the absence of osteocytic miR21. mRNA levels of IL-1β, DKK1, and SOST measured in calvaria bones from (A) female and (B) male miR21$^{f/f}$ and miR21$^{\Delta ot}$ mice (n=10). Bars represent mean ± s.d., *p<0.05 versus miR21$^{f/f}$, by t-test.

Table 4-1. 9-Plex cell-signaling array results in bones from female miR21$^{\Delta ot}$ mice.

	miR21$^{f/f}$	**miR21$^{\Delta ot}$**	**% change**	**p-value**
CREB	0.012 ± 0.002	0.012 ± 0.005	0.56	0.98
JNK	**0.390 ± 0.123**	**0.298 ± 0.04**	**-35.44**	**0.03**
NF-κB	0.024 ± 0.002	0.030 ± 0.005	22.68	0.06
ERK 1/2	**0.034 ± 0.009**	**0.021 ± 0.006**	**-37.81**	**0.03**
AKT	0.851 ± 0.297	0.745 ± 0.158	-12.54	0.49
P70S6K	0.245 ± 0.054	0.209 ± 0.041	-14.52	0.23
STAT3	**0.055 ± 0.013**	**0.040 ± 0.011**	**-27.65**	**0.05**
STAT5	0.577 ± 0.121	0.576 ± 0.086	-0.253	0.98
P38	**0.533 ± 0.071**	**0.392 ± 0.113**	**-26.48**	**0.03**

*p<0.05 versus miR-21$^{f/f}$ mice, by t-test (n=5-6)

Table 4-2. 9-Plex cell-signaling array results in bones from male miR21$^{\Delta ot}$ mice.

	miR21$^{f/f}$	**miR21$^{\Delta ot}$**	**% change**	**p-value**
CREB	0.011 ± 0.005	0.011 ± 0.002	-0.76	0.97
JNK	0.424 ± 0.128	0.295 ± 0.089	-27.58	0.11
NF-κB	0.028 ± 0.006	0.028 ± 0.006	-1.29	0.92
ERK 1/2	0.037 ± 0.017	0.031 ± 0.009	-16.22	0.46
AKT	0.610 ± 0.085	0.605 ± 0.088	-0.79	0.93
P70S6K	**0.241 ± 0.045**	**0.294 ± 0.028**	**21.87**	**0.04**
STAT3	0.046 ± 0.018	0.050 ± 0.010	8.08	0.67
STAT5	0.585 ± 0.155	0.526 ± 0.041	-10.02	0.39
P38	0.540 ± 0.127	0.575 ± 0.122	6.37	0.64

*p<0.05 versus miR-21$^{f/f}$ mice, by t-test (n=5-6)

Table 4-3. Mechanical strength in cortical bone in female miR21$^{\Delta ot}$ mice.

	miR21$^{f/f}$	**miR21$^{\Delta ot}$**	**% change**
Yield Force (N)	8.978 ± 0.602	8.66 ± 0.486	-3.53
Ultimate Force (N)	11.662 ± 1.013	11.628 ± 1.168	-0.29
Pre-Yield Displacement (μm)	215.073 ± 22.801	221.153 ± 23.920	2.83
Post-yield Displacement (μm)	981.928 ± 380.192	**1328.576 ± 292.795***	35.30
Total Displacement (μm)	1197.002 ± 376.015	**1549.729 ± 285.952***	29.47
Stiffness (N/mm)	47.874 ± 6.39	45.632 ± 4.105	-4.68
Pre-yield Work (mJ)	1.049 ± 0.171	1.019 ± 0.1349	-2.82
Post-yield Work (mJ)	8.200 ± 1.991	**9.791 ± 1.303***	19.40
Total Work (mJ)	9.249 ± 1.910	**10.811 ± 1.298***	16.88
Yield Stress (MPa)	36.905 ± 4.038	35.253 ± 4.983	-4.48
Ultimate Stress (MPa)	47.798 ± 4.570	47.076 ± 5.806	-1.51
Pre-yield Strain (με)	19432.98 ± 1646.98	19533.12 ± 2215.71	0.52
Total Strain (με)	108546.8 ± 34714.9	**137001.5 ± 27440.5***	26.21
Modulus (GPa)	2.156 ± 0.195	2.094 ± 0.239	-2.89
Resilience (MPa)	0.391 ± 0.077	0.368 ± 0.080	-5.74
Toughness (MPa)	3.449 ± 0.818	3.875 ± 0.660	12.33

*$p<0.05$ versus miR-21$^{f/f}$ mice, by t-test (n=10-12)

Table 4-4. Mechanical strength in cortical bone in male miR21$^{\Delta ot}$ mice.

	miR21$^{f/f}$	**miR21$^{\Delta ot}$**	**% change**
Yield Force (N)	11.086 ± 1.858	10.032 ± 2.292	-9.51
Ultimate Force (N)	13.039 ± 1.500	13.507 ± 1.276	3.59
Pre-Yield Displacement (μm)	306.050 ± 57.920	**257.687 ± 50.334***	-15.80
Post-yield Displacement (μm)	511.277 ± 191.202	**992.232 ± 372.887***	94.07
Total Displacement (μm)	786.897 ± 124.494	**1260.106 ± 366.007***	60.14
Stiffness (N/mm)	42.591 ± 4.177	44.465 ± 4.182	4.40
Pre-yield Work (mJ)	1.654 ± 0.533	1.249 ± 0.538	-24.49
Post-yield Work (mJ)	5.563 ± 1.693	**9.537 ± 2.676***	71.43
Total Work (mJ)	6.981 ± 1.325	**10.879 ± 2.793***	55.83
Yield Stress (MPa)	84.042 ± 14.228	**70.200 ± 17.563***	-16.47
Ultimate Stress (MPa)	98.449 ± 7.539	94.338 ± 7.406	-4.18
Pre-yield Strain (με)	44489.068 ± 8781.447	38232.606 ± 7489.234	-14.06
Total Strain (με)	119759.5 ± 24724.3	**186827.1 ± 56494.9***	56.00
Modulus (GPa)	2.237 ± 0.163	2.067 ± 0.299	-7.62
Resilience (MPa)	1.813 ± 0.545	**1.037 ± 0.272***	-42.78
Toughness (MPa)	9.095 ± 3.038	**11.635 ± 2.375***	27.92

*$p<0.05$ versus miR-21$^{f/f}$ mice, by t-test (n=10-12).

Table 4-5A. Conditioned media cytokines in female miR21$^{\Delta ot}$ mice.

	miR21$^{f/f}$	**miR21$^{\Delta ot}$**	**% change**	**p-value**
IL-6	OOR>	OOR>		
Eotaxin	16.63 ± 14.14	6.81 ± 1.52	-59.05	0.12
IFN-g	2.78 ± 0.60	1.88 ± 1.40	-32.43	0.27
IL-1a	19.86 ± 9.73	4.67 ± 4.89	-26.16	0.27
IL-2	OOR<	OOR<		
IL-3	OOR<	OOR<		
IL-4	1.15 ± 0.41	1.00 ± 0.25	-12.88	0.47
IL-5	13.99 ± 6.58	9.66 ± 2.73	-30.94	0.17
IL-7	OOR<	OOR<		
IL-9	133.69 ± 41.57	126.19 ± 22.48	-5.61	0.71
IL-10	5.11 ± 2.24	3.55 ± 1.06	-30.60	0.15
IL-12(p40)	OOR<	OOR<		
IL-12(p70)	13.48 ± 6.96	13.34 ± 4.45	-1.03	0.97
IL-13	OOR<	OOR<		
IL-15	4.05 ± 2.50	6.00 ± 3.53	47.96	0.46
IP-10	117.55 ± 48.07	70.89 ± 49.31	-39.69	0.15
LIF	358.56 ± 202.19	326.44 ± 127.57	-8.96	0.75
LIX	63.85 ± 58.73	40.30 ± 19.16	-36.88	0.37
M-CSF	12.70 ± 8.09	6.7 ± 2.54	-51.44	0.09
MIG	109.53 ± 38.44	86.11 ± 18.64	-21.38	0.21
MIP-1β	48.52 ± 31.58	26.94 ± 5.81	-44.47	0.13
MIP-2	45.33 ± 14.96	44.95 ± 13.45	-0.84	0.97
G-CSF	1127.08 ± 931.54	1026.83 ± 595.91	-8.89	0.83
IL-1β	9.52 ± 6.59	8.66 ± 2.21	-9.15	0.77
IL-17	1.00 ± 0.60	0.91 ± 0.43	-9.47	0.76
KC	379.31 ± 656.65	269.09 ± 302.65	-29.06	0.72
MCP-1	607.36 ± 615.80	264.68 ± 130.32	-56.42	0.21
MIP-1α	36.17 ± 13.52	29.95 ± 6.53	-17.21	0.34
RANTES	OOR<	OOR<		
TNF-α	7.84 ± 6.71	4.28 ± 1.03	-45.39	0.23
GM-CSF	23.13 ± 12.14	19.84 ± 6.10	-14.21	0.57
VEGF	204.67 ± 110.32	132.28 ± 25.83	-35.37	0.15

*$p<0.05$ versus miR-21$^{f/f}$ mice, by t-test (n=3-6). Values outside the standard curve are denoted by “OOR<” or “OOR>” (Out of Range).

Table 4-5B. Conditioned media cytokines in male miR21$^{\Delta ot}$ mice.

	miR21$^{f/f}$	**miR21$^{\Delta ot}$**	**% change**	**p-value**
IL-6	OOR>	OOR>		
Eotaxin	8.22 ± 6.34	6.43 ± 4.13	-21.81	0.57
IFN-g	2.70 ± 0.58	2.54 ± 1.05	-6.06	0.75
IL-1a	15.90 ± 2.24	13.06 ± 4.64	-17.88	0.21
IL-2	OOR<	OOR<		
IL-3	OOR<	OOR<		
IL-4	0.94 ± 0.20	0.82 ± 0.13	-13.25	0.23
IL-5	8.55 ± 2.52	6.01 ± 1.69	-29.77	0.07
IL-7	OOR<	OOR<		
IL-9	122.17 ± 18.99	142.73 ± 18.89	16.84	0.09
IL-10	4.88 ± 3.10	3.37 ± 0.82	-30.94	0.28
IL-12(p40)	OOR<	OOR<		
IL-12(p70)	16.24 ± 3.16	14.74 ± 4.05	-9.29	0.49
IL-13	OOR<	OOR<		
IL-15	3.78 ± 2.44	5.80 ± 6.45	53.63	0.53
IP-10	46.00 ± 17.06	76.65 ± 57.81	64.44	0.26
LIF	432.25 ± 99.60	422.48 ± 178.49	-2.26	0.91
LIX	61.89 ± 14.19	41.35 ± 20.70	-33.19	0.07
M-CSF	**4.45 ± 0.97**	**7.11 ± 1.81**	**59.64***	**0.01**
MIG	75.46 ± 18.73	83.83 ± 26.69	11.10	0.54
MIP-1β	27.84 ± 5.88	23.54 ± 1.77	-15.44	0.12
MIP-2	56.2 ± 16.81	38.11 ± 12.07	-32.19	0.06
G-CSF	1576.48 ± 377.85	1029.03 ± 1013.82	-34.73	0.24
IL-1β	9.56 ± 3.46	9.75 ± 2.73	1.99	0.92
IL-17	1.14 ± 0.23	1.04 ± 0.48	-9.20	0.64
KC	269.79 ± 160.04	97.42 ± 99.26	-63.89	0.06
MCP-1	**443.16 ± 243.87**	**184.39 ± 154.34**	**-58.39**	**0.05**
MIP-1α	29.1 ± 3.34	28.18 ± 3.75	-53.15	0.66
RANTES	OOR<	OOR<		
TNF-α	4.48 ± 0.34	4.29 ± 0.57	-4.17	0.50
GM-CSF	24.80 ± 3.05	21.60 ± 6.18	-12.88	0.28
VEGF	**117.78 ± 15.83**	**176.17 ± 42.68**	**49.58***	**0.01**

*p<0.05 versus miR-21$^{f/f}$ mice, by t-test (n=5-6). Values outside the standard curve are denoted by “OOR<” or “OOR>” (Out of Range).

Table 4-6A. Circulating serum cytokines in female miR21$^{\Delta ot}$ mice.

	miR21$^{f/f}$	**miR21$^{\Delta ot}$**	**% change**	**p-value**
IL-6	3.05 ± 0.81	2.72 ± 1.73	-10.93	0.69
Eotaxin	352.56 ± 78.76	456.28 ± 28.73	29.42	0.07
IFN-g	2.36 ± 1.12	3.50 ± 2.50	48.52	0.36
IL-1a	485.87 ± 142.59	570.13 ± 242.07	17.34	0.52
IL-2	OOR<	OOR<		
IL-3	OOR<	OOR<		
IL-4	1.29 ± 0.08	1.27 ± 0.12	-1.43	0.78
IL-5	6.02 ± 5.17	4.37 ± 0.69	-27.42	0.61
IL-7	0.52 ± 0.58	0.73 ± 0.35	39.96	0.67
IL-9	**150.02 ± 45.49**	**242.73 ± 47.33**	**61.80***	**0.02**
IL-10	1.92 ± 1.26	1.36 ± 0.99	-29.31	0.60
IL-12(p40)	8.26 ± 3.66	11.2 ± 5.95	35.62	0.38
IL-13	49.86 ± 6.71	54.72 ± 13.06	9.74	0.47
IL-15	OOR<	OOR<		
IP-10	94.59 ± 17.53	89.72 ± 11.15	-5.15	0.68
LIF	0.53 ± 0.24	0.73 ± 0.40	36.25	0.38
LIX	5412.89 ± 507.07	4805.08 ± 789.90	-11.23	0.20
M-CSF	1.74 ± 1.13	4.29 ± 2.68	146.74	0.22
MIG	28.21 ± 9.26	20.64 ± 8.43	-26.81	0.28
MIP-1β	31.82 ± 5.11	30.24 ± 11.00	-4.96	0.77
MIP-2	143.02 ± 23.73	161.64 ± 125.87	13.02	0.32
G-CSF	266.61 ± 127.57	334.97 ± 96.01	25.64	0.44
IL-1β	OOR<	OOR<		
IL-17	2.40 ± 0.40	2.16 ± 0.39	-10.13	0.42
KC	63.79 ± 25.20	38.54 ± 10.70	-39.58	0.16
MCP-1	OOR<	OOR<		
MIP-1α	53.21 ± 10.17	54.71 ± 3.97	2.83	0.82
RANTES	17.32 ± 3.39	19.06 ± 1.51	10.04	0.44
TNF-α	OOR<	OOR<		
GM-CSF	OOR<	OOR<		
VEGF	2.04 ± 0.13	1.99 ± 0.33	-2.29	0.76

*$p<0.05$ versus miR-21$^{f/f}$ mice, by t-test (n=5-6). Values outside the standard curve are denoted by “OOR<” or “OOR>” (Out of Range).

Table 4-6B. Circulating serum cytokines in male miR21$^{\Delta ot}$ mice.

	miR21$^{f/f}$	**miR21$^{\Delta ot}$**	**% change**	**p-value**
IL-6	**5.10 ± 1.67**	**2.89 ± 0.61**	**-43.36***	**0.03**
Eotaxin	383.39 ± 96.47	362.02 ± 29.98	-5.57	0.65
IFN-g	3.56 ± 2.27	3.26 ± 0.87	-8.95	0.77
IL-1a	461.29 ± 152.52	555.22 ± 168.37	20.36	0.36
IL-2	OOR<	OOR<		
IL-3	OOR<	OOR<		
IL-4	1.33 ± 0.16	1.23 ± 0.05	-7.33	0.23
IL-5	4.63 ± 2.23	3.76 ± 31.73	-18.71	0.51
IL-7	**1.93 ± 0.75**	**1.08 ± 0.42**	**-43.90**	**0.05**
IL-9	199.95 ± 59.46	306.70 ± 166.10	53.39	0.17
IL-10	4.06 ± 2.38	1.71 ± 1.34	-57.84	0.11
IL-12(p40)	19.23 ± 12.26	10.49 ± 3.90	-45.42	0.16
IL-13	**58.91 ± 6.97**	**39.62 ± 8.74**	**-32.74***	**0.003**
IL-15	OOR<	OOR<		
IP-10	**93.45 ± 19.30**	**72.30 ± 2.60**	**-22.64**	**0.04**
LIF	1.36 ± 0.94	1.59 ± 1.71	16.47	0.79
LIX	4533.92 ± 612.33	5945.02 ± 417.71	31.12	0.003
M-CSF	3.52 ± 2.19	1.60 ± 1.73	-54.66	0.16
MIG	26.31 ± 10.45	19.02 ± 13.81	-27.71	0.34
MIP-1β	42.28 ± 6.52	37.51 ± 6.23	-11.29	0.25
MIP-2	160.42 ± 51.29	158.60 ± 34.38	-1.13	0.95
G-CSF	260.20 ± 39.29	273.27 ± 52.75	5.02	0.65
IL-1β	OOR<	OOR<		
IL-17	**2.77 ± 0.45**	**2.16 ± 0.10**	**-22.17***	**0.02**
KC	147.50 ± 1694.10	48.51 ± 19.63	-67.12	0.22
MCP-1	OOR<	OOR<		
MIP-1α	56.25 ± 12.62	50.33 ± 12.57	-10.53	0.46
RANTES	20.56 ± 5.59	16.25 ± 3.80	-20.94	0.18
TNF-α	OOR<	OOR<		
GM-CSF	OOR<	OOR<		
VEGF	**2.17 ± 0.21**	**1.93 ± 0.84**	**-10.90***	**0.04**

*p<0.05 versus miR-21f/f mice, by t-test (n=5-6). Values outside the standard curve are denoted by “OOR<” or “OOR>” (Out of Range).

Chapter 5

Short-term pharmacologic inhibition of RAGE suppresses bone turnover and muscle atrophy in aging

Rationale

Osteoporosis and sarcopenia are two major clinical complications among the growing list of chronic diseases that primarily affect elderly individuals. Persistent low-grade inflammation, one of the major drivers of aging, is also associated with both bone and muscle dysfunction in aging. Particularly, chronic activation of the receptor for advanced glycation end products (RAGE) and elevated levels of its ligands HMGB1, AGEs, S100 proteins and Aβ fibrils have been linked to bone and muscle loss in various pathologies. Further, genetic or pharmacologic RAGE inhibition has been shown to preserve both bone and muscle mass. However, whether short-term pharmacologic RAGE inhibition can prevent bone and muscle loss in early aging is unknown. To address this question, we treated young (4-mo) and middle-aged (15-mo) C57BL/6 female mice with vehicle or Azeliragon, a small-molecule RAGE inhibitor initially developed to treat Alzheimer's disease.

Introduction

Due to the advances in healthcare over the last several decades, people are now living longer than ever before. Paradoxically, this has created a new clinical challenge, i.e. a vast array of chronic degenerative diseases, including heart disease, cancer, diabetes, neurodegeneration, often accompanied by the development of debilitating conditions, such as sarcopenia and osteoporosis.[1-3] To combat these pathologies of aging, there has been growing interest in geroscience, a research field focused on identifying/targeting common biological mechanisms that drive aging and underlie aging-related pathologies.[3,

[148] Recent advancements in this field have identified several common key risk factors, such as chronic-low grade inflammation, cellular senescence, metabolic dysfunction, macromolecular damage, genomic instability, reduced responsiveness to stress and altered proteostasis, associated with numerous of these 'comorbidities of aging'.[1, 2, 148-150]

However, to date, most work has focused primarily on the mechanisms underlying cardiovascular disease, cancer and neurodegeneration; whereas, the mechanisms underlying debilitating aging-related conditions, such as sarcopenia and osteoporosis, have been less studied. Given the skyrocketing number of individuals with osteoporosis [affecting ~1:2 women of all ages, and ~1:4 men over age 50 and costing the US ~$25.3 billion a year in healthcare expenses[4, 5]] and the increasing incidence of sarcopenia [affecting ~13% of Americans over age 55 and costing the US ~$18.5 billion a year in related-health expenses[151, 152]], there is an essential need to better understand the mechanisms leading to musculoskeletal pathology.

Further, considering the growing evidence showing the interconnected relationship between bone and skeletal muscle[153-155], and the fact that most elderly patients with bone and muscle loss are also affected by other aging-related comorbidities[3, 156], there is a crucial need to identify therapeutics capable of simultaneously targeting and treating multiple pathologies.

Low-grade chronic inflammation is one factor identified as a key driver of numerous aging-related pathologies.[157, 158] Various cell types release inflammatory cytokines, which not only regulate immune response, but also modulate key cellular processes: differentiation, proliferation, apoptosis, and autophagy throughout the organism.[157-159] In particular, emerging evidence suggests that inflammatory cytokine signaling plays a role in regulating bone and skeletal muscle metabolism under both physiological and pathological conditions.[160, 161] Consistently, chronic low-grade inflammation has been

identified as a major contributor of dysfunction in both musculoskeletal tissues in aging.[162-164]

Particularly, elevated RAGE [receptor for advanced glycation end-products] signaling has been shown to contribute to the onset/progression of various aging-related pathologies.[158, 165] RAGE is a multi-ligand pattern recognition receptor, which binds and mediates the cellular response to a range of endogenous damage-associated molecular pattern molecules (DAMPs) including advance glycation end-products (AGEs), HMGB1, S100 proteins, Aβ fibrils, and DNA/RNA.[166, 167] Under physiological conditions, RAGE is expressed at low levels, but during conditions of chronic inflammation RAGE is constitutively activated due to the accumulation of its ligands.[158, 166]

Numerous studies have demonstrated beneficial effects with RAGE inhibition [genetic and pharmacological] in various aging-related pathologies including diabetes, cardiovascular disease, neurodegeneration, and cancer.[168] Further, inhibition of RAGE signaling has been shown to protect against disease-induced bone and muscle loss. Particularly, in bone, genetic RAGE deficiency prevented against OVX induced bone loss; and consistently, blockade of cellular RAGE using soluble RAGE diminished alveolar bone loss in a murine model of diabetic periodontal disease.[169, 170] Additionally, in skeletal muscle, young mice fed a diet high in AGEs exhibited impaired skeletal muscle growth and contractile function.[171] Interestingly, AGEs were found to induce skeletal muscle atrophy by stimulating RAGE-mediated AMPK down-regulation, an effect that was attenuated in RAGE deficient mice.[172] Moreover, high intracellular levels of RAGE ligand, S100B, known to inhibit myogenic differentiation by repressing the myogenic regulatory factors MyoD and myogenin, were detected in muscle satellite cells isolated from aged subjects.[173] Taken together, these pieces of evidence highlight the potential involvement and the therapeutic opportunity to target/inhibit RAGE signaling during the onset/progression of bone and muscle pathology in aging.

Small-molecule RAGE inhibitors have been developed and their therapeutic utility has been evaluated in pre-clinical and clinical studies over the last decade.[174] For example, TTP488 (Azeliragon, AZ), a small-molecule compound that prevents RAGE from binding to AGEs, HMGB1, S100 proteins, and Aβ fibrils (Fig. 5-1A), has been evaluated for the treatment of Alzheimer's disease in pre-clinical and clinical studies.[175-177] However, whether pharmacological inhibition of RAGE affects bone and muscle in young individuals, and whether it attenuates the loss of bone and muscle mass in aging is not known. In this study we examined the possibility of repurposing the Alzheimer's drug, AZ, to prevent aging-induced osteoporosis and sarcopenia. Here we report that while RAGE inhibition does not attenuate the effects of aging on bone, it attenuates the effects of aging on skeletal muscle.

Materials and Methods

Osteoclastogenesis assay. Non-adherent BMCs ($6x10^4$ cells/cm^2) were plated on a 96-well plate with α-minimal essential medium (MEM) supplemented with 10% FBS and 1% penicillin/streptomycin (P/S) plus recombinant murine M-CSF (20 ng/ml) and soluble RANKL (80 ng/ml) (PeproTech Inc., Rocky Hill, NJ, USA) with either 100ng/mL AZ or veh. Media was changed every 2 days for 7 days.[119] Mature osteoclasts (>3 or more nuclei) were quantified after staining for TRAPase using a commercial kit (Sigma-Aldrich, Saint Louis, MO, USA, cat.#387A). Images were acquired using a Zeiss Axiovert 35 microscope equipped with a digital camera (Carl Zeiss, Thronwood, NY, USA). mRNA was isolated from parallel cultures and gene expression was measured by qPCR (Applied Biosystems, Foster City, CA, USA).

RNA extraction and qPCR. Total RNA was isolated using TRIzol (Invitrogen, Grand Island, NY, USA), as published.[83, 119] Reverse transcription was performed using a high-capacity cDNA kit (Applied Biosystems, Foster City, CA, USA). qPCR was performed using the Gene Expression Assay Mix TaqMan Universal Master Mix with an ABI 7900HT real-time PCR system. The house-keeping gene glyceraldehyde 3-phosphate dehydrogenase (GAPDH) was used. Primers and probes were commercially available (Applied Biosystems, Foster City, CA, USA) or were designed using the Assay Design Center (Roche Applied Science, Indianapolis, IN, USA). Relative expression was calculated using the ΔCt method.[178]

Mice and treatment. 4- (young, n=10) and 15-month-old mice (middle-aged, n=10) C57BL/6 female mice were obtained from National Institute on Aging (NIA) and received daily intraperitoneal injection of veh (1.7% DMSO) or 100μg/day (young mice) and 110μg/day (middle-aged mice) of AZ (DC Chemicals, Shanghai, P.R., China, cat.#

DC8338), to account for body weight differences, for 28 days. Mice were assigned an ID number and the age/treatment were recorded in a database. Investigators performing endpoint measurements were only given the mouse ID. Mice were randomized and assigned to each experimental group based on spinal BMD. Mice (4-5/cage) were fed a regular diet (Envigo, Indianapolis, IN) and water *ad libitum*, and maintained on a 12h light/dark cycle. Animals were sacrificed between 3-5 hours after last injection. All experiments were carried out as planned. No mortality was recorded throughout the experiment, although 2 mice exhibited signs of infections near the injection sites. In addition, AZ administration induced splenomegaly (Fig. 5-13), but no other signs of distress were recorded. Young mice received IP injections of calcein (30 mg/kg; Sigma-Aldrich, Saint Louis, MO, USA) and alizarin red (50 mg/kg; Sigma) 7 and 2 days before sacrifice, respectively and aged mice received IP injections of calcein (30 mg/kg; Sigma-Aldrich, Saint Louis, MO, USA) and alizarin red (50 mg/kg; Sigma) 10 and 3 days before sacrifice, respectively, to allow for dynamic histomorphometric measurements.[90] The longer duration between labels in aged mice was done to help facilitate the differentiation of the two labels given the slower bone formation rate.

Bone histomorphometry. Femora and lumbar vertebrae (L1–L3) were dissected and fixed in 10% neutral buffered formalin as previously published.[90] Static histomorphometric analysis was performed on the cancellous surface of sequential methyl methacrylate embedded lumbar vertebrae sections stained with von Kossa/McNeal [osteoblasts] and TRAPase/Toludine blue [osteoclasts]. Additionally, osteoclasts were quantified on the endocortical surface paraffin embedded TRAPase/Toludine blue stained femur cortical bone cross-sections. Dynamic histomorphometric measurements were performed in unstained plastic embedded femoral mid-diaphysis and lumbar vertebrae bone sections.[83] Histomorphometric analysis was performed using OsteoMeasure high-

resolution digital video system (OsteoMetrics Inc., Decatur, GA, USA).[90] The terminology and units used are those recommended by the Histomorphometry Nomenclature Committee of the American Society for Bone and Mineral Research.[85]

Serum biochemistry. Blood was collected by cheek bleeding after 3 h of fasting. Plasma was separated, aliquoted, and stored at − 80°C.[49] N-terminal propeptide of type I procollagen (P1NP) (Immunodiagnostic Systems Inc., Fountain Hill, AZ, USA, cat.#AC-33F1) and C-telopeptide fragments (CTX) (RatLaps, Immunodiagnostic Systems Inc., Fountain Hill, AZ, USA, cat.#AC-06F1) were measured as previously published.[90]

Osteoblast mineralization assay. Adherent-BMCs were cultured for 10 days in α-MEM supplemented with 10% FBS and 1% penicillin/streptomycin in the presence of 50 μM ascorbic acid and 10 mM β-glycerol phosphate, as previously described.[179] Cells were fixed with 3.7% paraformaldehyde in PBS for 1 hour, rinsed twice with distilled water, and stained for 10 min with 40 mM Alizarin Red S (pH 4.2) at room temperature under shaking. Cells were then washed 5 times with water, followed by a 15 min-wash with PBS. Alizarin Red S was extracted by adding 1% cetylpyridinium chloride for 15 min at room temperature with shaking. OD was measured at 490 nm.

Apoptosis. Osteocyte apoptosis was detected in paraffin-embedded femur cross-sections using previously published protocols.[46] Briefly, femora were deparaffinized, treated with 3% H_2O_2 to inhibit endogenous peroxidase activity, blocked and then incubated with rabbit monoclonal anti-active caspase-3 antibody (1:75; Thermo Fisher Scientific In., Rockford, IL, USA, cat.#PA5-23921).[180] Sections were then incubated with anti-rabbit biotinylated secondary antibody followed by avidin conjugated peroxidase (Vectastain Elite ABC Kit; Vector Laboratories Inc., Burlingame, CA, USA). Color was

developed with a diaminobenzidine substrate chromogen system (Acros Organics, New Jersey, USA). Cells expressing the protein of interest are stained in brown, whereas negative cells are green-blue. Nonimmune IgG was used as negative control.

Ex vivo bone organ cultures. Long bones were isolated from 4- and 16-month-old female C57BL/6 mice and BMCs were flushed out with α-MEM. Osteocyte-enriched marrow-flushed long bones were cultured *ex vivo* in α-MEM supplemented with 10% FBS and 1% P/S with veh or AZ (100ng/mL) and cultured for 24 hours. Following treatment, bones were collected, frozen in liquid nitrogen, and stored at − 80°C. Gene expression was measured by qPCR (Applied Biosystems, Foster City, CA, USA).

Bone mineral density (BMD) and body composition (fat and lean mass) by dual energy x-ray absorptiometry (DXA). Bone mineral density (BMD) and body composition were measured monthly by dual X-ray absorptiometry (DXA) using a PIXImus densitometer (G.E. Medical Systems, Lunar Division, Madison, WI, USA).[181] BMD measurements included total BMD (excluding the head and tail), entire femur (femoral BMD) and L1–L6 vertebra (spinal BMD).[90] Body composition included body weight, fat mass, and lean mass. Calibration was performed before scanning with a standard phantom, as recommended by the manufacturer.

Micro-computed tomography (μCT) analysis. Femora and L4 vertebrae were dissected, wrapped in saline-soaked gauze and frozen at − 20°C.[90] Vertebra and femora, 6 bones per scan, were scanned using a 65kV source, 0.5mm Al filter, 0.7 degree rotation and two-image averaging with an isotropic voxel size of 9μm using a SkyScan 1176 system (SkyScan, Kontich, Belgium). Scans were reconstructed and analyzed using

manufacturer software. Nomenclature is reported in accordance with the guidelines for μCT.[84]

Biomechanical testing. Femoral three-point bending testing was performed following previously published protocols.[90] Structural mechanical properties, ultimate load, stiffness, displacement and work were determined from the load–deformation curves using standard definitions while material-level estimations of properties were calculated using standard equations. Cross-sectional moment of inertia and anterior–posterior diameter were determined by μCT and were used to calculate material-level properties, as previously described.[90]

Muscle weight. Skeletal muscles gastrocnemius, tibialis anterior, quadriceps and soleus, were harvested and weighed immediately following dissection. Muscle weight was corrected by total body weight and reported as the percentage of muscle per body weight. After weighing, muscles were snap frozen and store at -80°C until used for gene expression analysis.

Muscle histology and morphometric analysis. The forearms of mice were removed and fixed in 10% neutral buffered formalin. Forearms were cross-sectioned, demineralized and embedded in paraffin and then sectioned on a microtome. Tissue morphology was assessed on 4 μm–thick cross-sections of muscles sections stained with hematoxylin and eosin (H&E) dye. Myofiber cross-sectional area (CSA) was analyzed on H&E-stained forearm muscle section images using image J analysis software and tablet input device.[182]

C2C12 cell culture and myotube diameter measurement. C2C12 myoblasts were grown and seeded onto 12-well plates (7,500 cells/cm^2). The cells were then exposed to DMEM supplemented with horse serum for five days, then subsequently treated for 48 hrs with 5% serum from young or aged animals treated with veh or AZ. Myotubes were fixed using chilled acetone/methanol (1:1) and washed with PBS, stained using a primary antibody against myosin heavy chain (#MF-20, Developmental Studies Hybridoma Bank, Iowa City, IA) overnight at 4ºC, then stained with Alexaflour 594-labeled secondary antibody (Invitrogen, Grand Island, NY) at room temperature for one hour. Myotubes were imaged using an Axio Observer.Z1 motorized microscope (Zeiss, Oberchoken, Germany). Average myotube diameter was measured per field of view using Image J analysis software[183] and a Cintiq pen tablet input device (Wacom, Vancouver, WA).

Western blot analysis. Ubiquitin-conjugated protein levels were evaluated in protein lysates isolated from the quadriceps of young and aged veh- and AZ-treated mice. Protein lysates were separated on 10% SDS–PAGE gels (BioRad) and electrotransferred to nitrocellulose membranes (Millipore, Billerica, MA, USA). Membranes were then incubated in blocking solution (SEABlock) for 60 min and probed with primary antibodies diluted 1:1000 in SeaBLOCK + 0.2% Tween against a monoclonal anti-Ubiqutin (#3933, Cell Signaling Technologies, Danvers, MA) overnight at 4°C, followed by corresponding secondary fluorescent antibodies diluted 1:10,000 in SEABlock + 0.2% Tween for 1 h at room temperature. After rinsing with PBS-T, the membranes were developed using LICOR imaging. Bands were detected using an Odyssey Infrared Imaging System (LI-COR Biosciences, Lincoln, NE, USA), and their intensity was quantified using ImageJ.

Statistical analysis. Data were analyzed by using SigmaPlot (Systat Software Inc., San Jose, CA, USA). All values are reported as the mean ± standard deviation. Differences were evaluated either by two-way ANOVA with post-hoc analysis using Tukey Method or by Student's t-test, as appropriate. Differences were considered significant when $p<0.05$.

Results

AZ differentially alters bone metabolism through direct and indirect actions. To test the effects of pharmacological RAGE inhibition using the small-molecule inhibitor, AZ (Fig. 5-1A), on osteoclast differentiation, we first treated wildtype non-adherent bone marrow cells (BMC) isolated from 4-month-old (young) or 16-month-old (middle-aged) C57BL/6 female mice with vehicle (veh) or AZ *in vitro.* Consistent with previous findings in global genetic RAGE knockout mice,[184] a lower number of mature osteoclasts (≥3 nuclei) developed from young or middle-aged BMCs treated with AZ (Fig. 5-1B). Further, more osteoclast were developed when cells were isolated from middle-aged mice. Based on these findings, we next investigated the effects *in vivo* of systemic AZ administration on osteoclast differentiation/activity and whether it prevents bone loss in aging. To this end we treated female wild type C57BL/6 4-month-old (young) and 15-month-old (middle-aged) mice daily with AZ 100μg/d (young), 110μg/d (middle-aged), or veh for 28 days (Fig. 5-1C).

Bone histomorphometric analysis of veh-treated mice revealed no alterations in osteoclast number (N.Oc/BS) or surface (Oc.S/BS) per bone surface on the femur endocortical or vertebral cancellous bone surfaces (Fig. 5-1D,E) with aging, although, vertebral cancellous osteoclast number per tissue area (N.Oc/T.Ar) was lower in middle-aged compared to young veh-treated mice. Further, vertebral cancellous bone perimeter (B.Pm) was decreased in the middle-aged compared to young mice (Fig. 5-1E). Vertebral cancellous osteoclast number per tissue area (N.Oc/T.Ar) was lower in middle-aged compared to young veh-treated mice. Consistently, serum bone resorption marker, C-terminal telopeptide (CTX), levels were lower (Fig. 5-1F) and osteoclast gene expression was significantly decreased in middle-aged compared to young veh-treated mice (Fig. 5-7).

Consistent with the *in vitro* findings, static histomorphometric analysis revealed that AZ treatment in young and middle-aged mice significantly reduced the number of osteoclasts on the vertebral cancellous and femoral endocortical bone surfaces (Fig. 5-1D,E). However, AZ treatment did not alter the expression of any osteoclast-related genes in the tibia, aside from an increase in calcitonin receptor (Fig. 5-7). Further, we were surprised to find that serum CTX levels were higher in the AZ-treated mice at both ages (Fig. 5-1F), suggesting that more bone surfaces are being resorbed in the presence of AZ.

We next examined the effects of aging and AZ treatment on osteoblast differentiation and function. Histomorphometric analysis revealed that vertebral cancellous osteoblast number per tissue area (N.Ob/T.Ar) was significantly decreased in middle-aged compared to young veh-treated mice, although due the decreased vertebral cancellous B.Pm in the middle-aged mice osteoblast number and surface per bone surface (N.Ob/BS and Ob.S/BS) were unchanged (Fig. 5-1G). Further, veh-treated middle-aged mice exhibited lower serum bone formation marker, pro-collagen type 1 N-terminal propeptide (P1NP) levels (Fig. 5-1H), and gene expression analysis detected similar decreases in mRNA levels for osteoblastic genes with aging (Fig. 5-8). However, no aging-related changes in mineral apposition rate (MAR), mineralizing surface (MS)/BS, or bone formation rate (BFR)/BS were detected by dynamic histomorphometric analysis of the vertebral cancellous bone of young and middle-aged veh-treated mice (Fig. 5-1I). On the other hand, age-related alterations in bone formation were detected on the surfaces of the femur mid-diaphysis (Fig. 5-9), suggesting that in the middle-aged veh-treated control mice only cortical bone formation was altered.

In contrast to the effects of AZ on osteoclasts, the effects on osteoblasts were age-dependent. Specifically, while vertebral cancellous osteoblast parameters, N.Ob/T.Ar, N.Ob/BS and Ob.S/BS were lower with AZ treatment in mice at both ages, uncorrected N.Ob was only lower in the middle-aged AZ-treated mice (Fig. 5-1G). Consistently,

dynamic histomorphometric analysis only detected decreases in bone formation in the vertebral cancellous and femur mid-diaphysis endocortical bone in the middle-aged, but not young AZ-treated mice (Fig. 5-1I,5-8). Additionally, *in vitro* treatment of young and middle-aged primary adherent BMCs had age-dependent effects, increasing mineralization in young cells, but attenuating mineralization in aged cells (Fig. 5-1J). On the other hand, systemic *in vivo* AZ treatment decreased serum P1NP levels in both young and aged mice (Fig. 5-1H). Further, osteoblast gene expression was decreased in the tibia with AZ treatment in both ages (Fig. 5-7). Taken together these results suggest that inhibition of RAGE signaling may differentially affect osteoblast differentiation/activity, at least on the vertebral cancellous surface, in an age-dependent manner.

Inhibition of RAGE signaling increases osteocyte apoptosis and pro-inflammatory cytokine production. Based on the notion that osteocytes are key regulators of bone turnover and to the idea that aging-related reductions in osteocyte viability contribute to bone loss,[7] we next sought to test the effects of AZ treatment on osteocytes. We first measured osteocyte apoptosis in active capase3-stained femur cortical bone cross-sections. Aging did not alter the proportion of active capase3 positive apoptotic osteocytes, as found before by TUNEL staining,[8] but the number of empty lacunae (an indication of dying osteocytes) was increased in middle-aged compared to young veh-treated mice (Fig. 5-2A). Additionally, osteocyte gene expression was decreased with aging (Fig. 5-2B), and consistent with the decreased osteoclast parameters observed in the middle-aged mice, RANKL/OPG gene expression was lower in middle-aged mice compared to young animals (Fig. 5-2C).

AZ treatment did not alter the proportion of active capase3-positive apoptotic osteocytes, but significantly increased empty lacunae prevalence in young and middle-aged mice (Fig. 5-2A). Consistently, the expression of the osteocyte genes Sost and

DMP1 was decreased with AZ treatment in both ages (Fig. 5-2B), whereas, AZ treatment increased the RANKL/OPG ratio in bones from middle-aged mice and led to higher inflammatory cytokine IL-6 and MCP-1 gene expression in bones from young and middle-aged mice (Fig. 5-2C). Further, gene expression analysis detected tendencies towards increase in the expression of the apoptosis-associated genes p27 and Foxo3, and a significant increase in the RANKL/OPG mRNA ratio, and in the levels of IL-6 and MCP-1 in *ex vivo* AZ treated osteocyte-enriched bone organ cultures (Fig. 5-2D-F). Taken together these findings highlight the possibility that the *in vivo* alterations in osteoclast activity induced with AZ treatment may be a combination of the direct and indirect effects associated with RAGE inhibition in osteoclasts and osteocytes, as illustrated in Fig. 5-2G.

Short-term systemic RAGE inhibition with AZ treatment does not significantly alter bone architecture or mechanical properties. Dual energy x-ray absorptiometry (DXA) analysis showed that spinal bone mineral density (BMD) was significantly decreased with aging, whereas, total and femoral BMD were unchanged in the middle-aged compared to young veh-treated mice (Fig. 5-3A). On the other hand, micro-computed tomography (μCT) analysis and 3-point femoral biomechanical testing detected the expected changes in bone geometry and mechanics, respectively. Specifically, lumbar vertebra and distal femur trabecular BV/TV (bone volume/tissue volume) and trabecular number (Tb.N) were decreased, whereas trabecular spacing (Tb.S) was increased in the middle-aged mice compared to young veh-treated mice (Fig. 5-3B,C). In addition, femur cortical BA/TA (bone area/ tissue area) was decreased, whereas, polar mean moment of inertia (MMI), a measurement of resistance to bending, marrow cavity widening, and bone tissue porosity were increased with aging (Fig. 5-3D). Further, the biomechanical properties at the structural and material levels were all

decreased in the middle-aged compared to young veh-treated mice, with the exception of stiffness, which was increased with aging (Table 5-1).

Consistent with the changes in bone cell differentiation/activity, DXA analysis revealed that AZ treatment decreased total and femoral BMD in young and middle-aged mice, without affecting spinal BMD (Fig. 5-3A). However, despite the effects on BMD, no changes in bone geometry (trabecular and cortical) or biomechanical properties following systemic short-term AZ treatment in mice at either age were detected by μCT analysis or 3-point femoral biomechanical testing, respectively (Fig. 5-3B-D and Table 5-1).

Systemic RAGE inhibition prevents the loss of lean muscle mass and preserves the function of cellular processes required to maintain skeletal muscle homeostasis in aging. Based on the previous reports that both aging and RAGE signaling alter adipose and skeletal muscle mass,[171] we next tested the effects of systemic AZ treatment on these tissues. As expected, body weight of middle-aged compared to young veh-treated mice was increased (Fig. 5-4A), and body composition was altered, with greater fat mass and lower lean mass compared to young veh-treated mice (Fig. 5-4B). Consistently, gastrocnemius, tibialis anterior, and quadriceps mass corrected by body weight were all decreased in the middle-aged veh-treated mice (Fig. 5-4C). Further, gene expression analysis detected decreases in the expression of MyoD with aging (Fig. 5-4D). Moreover, histomorphometric analysis of H&E-stained forearm skeletal muscle revealed decreases in the average myofiber cross-sectional area (CSA) in middle-aged compared to young veh-treated mice (Fig. 5-5A,B). Interestingly, *in vitro* treatment of C2C12 myotubes with 5% serum from middle-aged compared to young veh-treated mice also reduced average myotube diameter and led to a leftward shift in the representative histograms of the distribution of myotube diameter (Fig. 5-5C,D), suggesting that circulating serum factors may contribute to aging-induced muscle atrophy. Consistent with

the increased muscle atrophy, ubiquitinated protein levels and expression of the E3 ubiquitin ligases Atrogin-1 and MuRF-1, generally overexpressed in conditions associated with muscle atrophy,[185, 186] were increased in the skeletal muscles of middle-aged compared to young veh-treated mice (Fig. 5-5E,F).

In young mice, AZ decreased body weight (Fig. 5-4A), and altered body composition reducing the fat mass and increasing lean mass (Fig. 5-4B). Consistently, gastrocnemius and tibialis anterior muscle mass (Fig. 5-4C), as well as myogenin and MyoD expression, measured in the tibialis anterior muscle (Fig. 5-4D), were increased with AZ treatment. However, quadriceps muscle weight was decreased (Fig. 5-4C) and the level of ubiquitinated proteins appear to increase with treatment in the young mice (Fig. 5-5E). Notably, addition of serum from the young AZ-treated mice to C2C12 myotubes also significantly reduced myofiber size and histomorphometric analysis of H&E-stained forearm muscle revealed decreases in the average myofiber CSA in young AZ-treated mice (Fig. 5-5B,C).

In middle-aged mice, AZ had similar effects on body composition, reversing the aging-associated increases in body weight (Fig. 4-4A), as well as, the alterations in body composition by reducing the fat mass and increasing lean mass (Fig. 5-4B). Further, AZ reversed the aging-induced loss of the gastrocnemius, tibialis anterior, and quadriceps muscle mass in the middle-aged treated mice (Fig. 5-4C). Consistently, RAGE inhibition increased myogenin expression at both ages, and restored MyoD levels in the middle-aged mice (Fig. 5-4D). Moreover, while AZ did not completely reverse the aging-induced decreases in myofiber CSA (Fig. 5-5B), *in vitro* treatment of C2C12 myoblasts with serum from the middle-aged AZ-treated mice did not result in the decreased myotube diameter that was induced by serum from the middle-aged veh-treated mice (Fig. 5-5C,D).

Consistent with these findings, AZ attenuated the aging-induced increases in ubiquitinated protein levels and the mRNA levels of Atrogin-1 (Fig. 5-5E,F). Further, AZ

treatment reversed the aging-associated alterations in the expression of genes involved in the regulation of skeletal muscle cellular processes. Particularly, autophagy- and mitochondria-related gene expression was decreased with aging, and AZ treatment increased expression of these genes in young and middle-aged mice (Fig. 5-10), suggesting that *in vivo* AZ treatment may protect against aging-induced muscle atrophy, in part, by preserving the proper functioning of cellular processes normally required to maintain skeletal muscle homeostasis and metabolism. On the other hand, while aging increased Atrogin-1 and MuRF-1 levels in bone, as previously shown with glucocorticoid administration,[187] AZ did not block these increases (Fig. 5-11).

AZ treatment reverses the aging-induced metabolic alterations in skeletal muscle but not in bone. Despite the similar aging-induced loss of bone and muscle mass, the findings from the present study reveal that aging differentially alters skeletal muscle and bone metabolism. Particularly, gene expression analysis of skeletal muscles from young and middle-aged veh-treated mice demonstrated that aging decreased glucose transporter (Glut1-4) gene expression (Fig. 5-6A). Further, gene expression of glycolytic enzymes (PGK1, LDHA, PDK1) was decreased with aging, whereas the levels of enzymes involved in the regulation of oxidative metabolism (PGC-1α and PPAR-α) were unchanged or showed tendencies towards increase with aging in the veh-treated mice (Fig. 5-6B,C). In contrast, in bone, Glut3 gene expression was decreased with aging, whereas, Glut1 and Glut2 expression was significantly increased and Glut4 was not changed with aging (Fig. 5-6D). Further, LDHA and PGK1 expression was increased with aging, whereas PGC-1α and PPAR-α expression was unaltered in bone samples from middle-aged compared to young veh-treated mice (Fig. 5-6E,F).

We next examined the metabolic effects of AZ treatment in skeletal muscle and bone. In skeletal muscle, AZ increased glucose transporter, Glut1, Glut3, and Glut4, gene

expression, and led to a tendency towards increase in Glut2 gene expression in mice at both ages (Fig. 5-6A). Further, in skeletal muscle PGK1 and LDHA expression was increased, while the PGC-1α and PPAR-α expression was unchanged with AZ treatment in young and middle-aged mice (Fig. 5-6B,C). In bone, AZ treatment increased Glut1 and Glut3 gene expression and led to a tendency towards increase in Glut2 gene expression, while Glut4 was not changed (Fig. 5-6D). Similarly, LDHA, PGK1, and PGC1α expression was increased in bone lysates from AZ-treated mice at both ages (Fig. 5-6E,F). Interestingly, we also found that the mRNA expression of leptin and IGF-1, factors known to alter cell metabolism, were also differentially altered with aging in skeletal muscle and bone tissue lysates (Fig. 5-12). However, AZ led to similar decreases in leptin levels in both tissues at both ages.

Discussion

Inflammation is a complex biological process initiated in many cell types in response to various stimuli, which stimulates the secretion of numerous factors and subsequently mediates processes such as protective immunity, tissue repair and damage resolution.[149] Further, while acute inflammation stimulates repair, chronic-sustained inflammation leads to progressive damage.[162] Particularly, chronic low-grade inflammation has been associated with numerous age-related degenerative diseases and with related debilitating conditions, such as sarcopenia and osteoporosis.[158, 165] Several potential mechanisms of age-associated chronic inflammation have been proposed, including the accumulation senescent cells, impaired mitochondrial function, reduced levels of autophagy, and altered NF-κB signaling,[149, 162] which are also seen in bone and skeletal muscle with aging.[188, 189]

Consistently, sustained RAGE signaling, a known regulator of NF-κB, has been shown to contribute to the onset/progression of various aging-related pathologies.[158, 165] Particularly, several pieces of evidence have highlighted the potential involvement of elevated RAGE signaling in the onset/progression of bone and muscle pathology in aging.[169-171] However, given the physiological importance of inflammation, whether blocking RAGE can reverse aging-related pathologies, particularly, osteoporosis and sarcopenia, remains unknown.

In this study, we tested the effects of short-term systemic administration of the small-molecule RAGE inhibitor, AZ, on bone and skeletal muscle in aging using a series of *in vitro* and *in vivo* experiments. Overall, our findings provide evidence that short-term pharmacologic RAGE inhibition has effects on bone and muscle metabolism in young and middle-aged mice.

Consistent with previous findings in global genetic RAGE knockout mice,[170, 190, 191] RAGE inhibition by AZ treatment decreased osteoclast differentiation *in vitro.* However, *in*

vivo AZ administration suppressed bone remodeling and led to a small but significant decrease in BMD in young and middle-aged mice. These findings are consistent with previous studies showing that femoral cancellous bone accrual and architecture were decreased, and femur osteoblast gene (ALP, Cola1, Runx2, and Osterix) expression was lower in 4-month-old RAGE knockout compared to control wildtype mice.[192] Interestingly, despite these cellular changes, bone geometry and strength were maintained. Nevertheless, our findings provide further support for the important physiological role of RAGE signaling in bone. However, opposed to previous findings in RAGE knockout mice, our results suggest that direct versus indirect effects of RAGE inhibition in bone cells differentially regulates bone metabolism.

Particularly, the differential direct versus indirect effects of AZ on osteoclasts may be due to the increases in cell death and inflammatory cytokine production in osteocytes both *in vitro* and *in vivo*. Hence, despite the direct inhibitory effects of AZ treatment on osteoclasts, the effects of RAGE inhibition in osteocytes may indirectly promote bone resorption. Considering previous reports that NF-κB signaling is required for proper osteoclast function and that AGE-RAGE mediated activation NF-κB signaling induces osteoclastogenesis[184, 193] coupled with the known anti-apoptotic effects of NF-κB signaling,[194] inhibition of NF-κB signaling may mediate the differential effects of AZ.

Given the cell type specific effects of AZ, future studies will be designed to examine whether administering a different dose or altering the treatment regimen [intermittent vs chronic], previously seen with other therapeutics, could optimize the beneficial effects of AZ on bone. For example, depending on the mode of administration, intermittent vs chronic, parathyroid hormone (PTH), has anabolic or catabolic actions on the skeleton.[195] Notably, the catabolic actions of PTH have been shown to result from indirect actions on osteoclasts mediated through direct actions on osteoblasts and osteocytes, by modulating RANKL and MCP-1 levels,[196-198] both of which were increased by AZ.

In addition to the skeletal effects of AZ, we found that treatment reversed the aging-induced alterations in body composition, leading to lower fat and higher lean body mass compared to veh-treated control mice at both ages. These findings are consistent with recent studies demonstrating that RAGE signaling regulates the metabolic and inflammatory response to high fat feeding in mice.[199] In this study, genetic RAGE deficiency and administration of systemic soluble RAGE, a decoy receptor RAGE isoform, reduced fat mass in high fat diet fed mice. Although, despite the beneficial effects of AZ administration on the skeletal muscle of middle-aged mice, AZ had differential effects on skeletal muscles of young animals. Specifically, while several similar positive effects were detected in the tibialis anterior muscle, quadriceps mass was decreased and ubiquitin-mediated protein degradation was increased in young AZ-treated mice.

Nevertheless, consistent with the beneficial effects on lean body mass, we found that AZ treatment reversed the aging-induced decreases in skeletal muscle mass and attenuated several aging-induced changes known to be associated with chronic inflammation, including NF-κB signaling, mitochondrial function and autophagy. Specifically, AZ preserved the expression of known myogenic regulatory factors, such as myogenin and MyoD, and attenuated ubiquitin-mediated protein degradation in the aged mice. Consistently, it has been suggested that activation of NF-κB post-transcriptionally reduces the cellular levels of MyoD.[200] Further, deletion of the β subunit of the inhibitor of NF-κB kinase, IKKβ, reduces inflammation, leading to improved skeletal muscle strength, maintained mass, and enhanced regeneration.[201]

In addition, AGEs induce skeletal muscle atrophy and dysfunction in diabetic mice via RAGE-mediated AMPK-induced downregulation of the Akt pathway.[172] In this study, Atrogin-1 levels were attenuated following RAGE inhibition and consistent with this, Atrogin-1 has been previously shown to directly suppress MyoD expression, inhibiting protein synthesis and inducing aging-related skeletal muscle atrophy.[202] Consistently,

reports suggest that the association between Atrogin-1 and skeletal muscle atrophy may be more related to its inhibitory effects on protein synthesis.[203, 204] Taken together these pieces of evidence suggest that in middle-aged mice AZ treatment may restore key cellular processes normally involved in the maintenance of skeletal muscle mass by directly inhibiting AGE-RAGE signaling or by downregulating NF-κB signaling in the skeletal muscle.

However, given the increased myotube diameter in C2C12 cultures exposed to serum from middle-aged AZ-treated mice, it is also possible that the observed beneficial effects are due to systemic alterations rather than direct effect of AZ in skeletal muscle. Thus, additional studies are needed to understand the mechanisms underlying the beneficial effects of systemic AZ treatment on skeletal muscle in middle-aged mice. Additionally, whether AZ administration also improves muscle function remains to be elucidated.

Nevertheless, our findings suggest that systemic AZ treatment in middle-aged mice might contribute to reverse the derangements observed in the skeletal muscle primarily by correcting the aging-associated metabolic defects and by preventing the effects of AGEs and potentially other RAGE ligands. Indeed, our findings that AZ treatment prevents against the aging-related decreases in skeletal muscle glucose transporter gene expression, are consistent with reports that AGEs inhibit insulin actions in skeletal muscle and induce interference of glucose uptake.[205] In particular, AGE-RAGE binding induces inflammation, triggering ER-stress and initiating the unfolded protein response (UPR), which subsequently promotes nuclear translocation of NF-κB.[206, 207] Further, recent work demonstrated that nuclear NF-κB directly binds and represses Slc2a4 gene transcription, suppressing GLUT4 expression and disrupting glucose uptake.[208] Thus, our findings that aging decreased skeletal muscle GLUT4 gene expression, an effect reversed by AZ administration, suggest that systemic RAGE inhibition reverses the aging-induced

alterations in skeletal muscle glucose uptake, potentially by blocking AGE actions on skeletal muscle.

Further, AZ treatment reversed the aging-induced declines in the expression of skeletal muscle glycolytic, but not oxidative metabolism enzymes, which is consistent with reports that NF-κβ activation primarily induces fast-twitch, glycolytic muscle fiber atrophy.[209] However, despite the findings that AZ treatment had similar effects on glucose transporter and glycolytic enzyme gene expression in bone, aging had opposite effects on their expression in bone and skeletal muscle. Altogether, these findings suggest that aging differentially effects glucose uptake and metabolism in the different tissues, which highlights a potential mechanism underlying the differential effects of AZ treatment on bone and skeletal muscle in aging.

In conclusion, our study suggests that short-term pharmacologic RAGE inhibition has distinct effects on bone and muscle metabolism. Thus, while AZ treatment did not attenuate the aging-induced alterations in bone, it did rescue some of the changes in skeletal muscle. In particular, our data conclusively validate the role of RAGE signaling in promoting musculoskeletal derangements associated with aging, thus making it an interesting therapeutic target. Altogether, our findings strongly support that idea that AZ may represent a novel therapeutic option for the treatment of aging-induced sarcopenia.

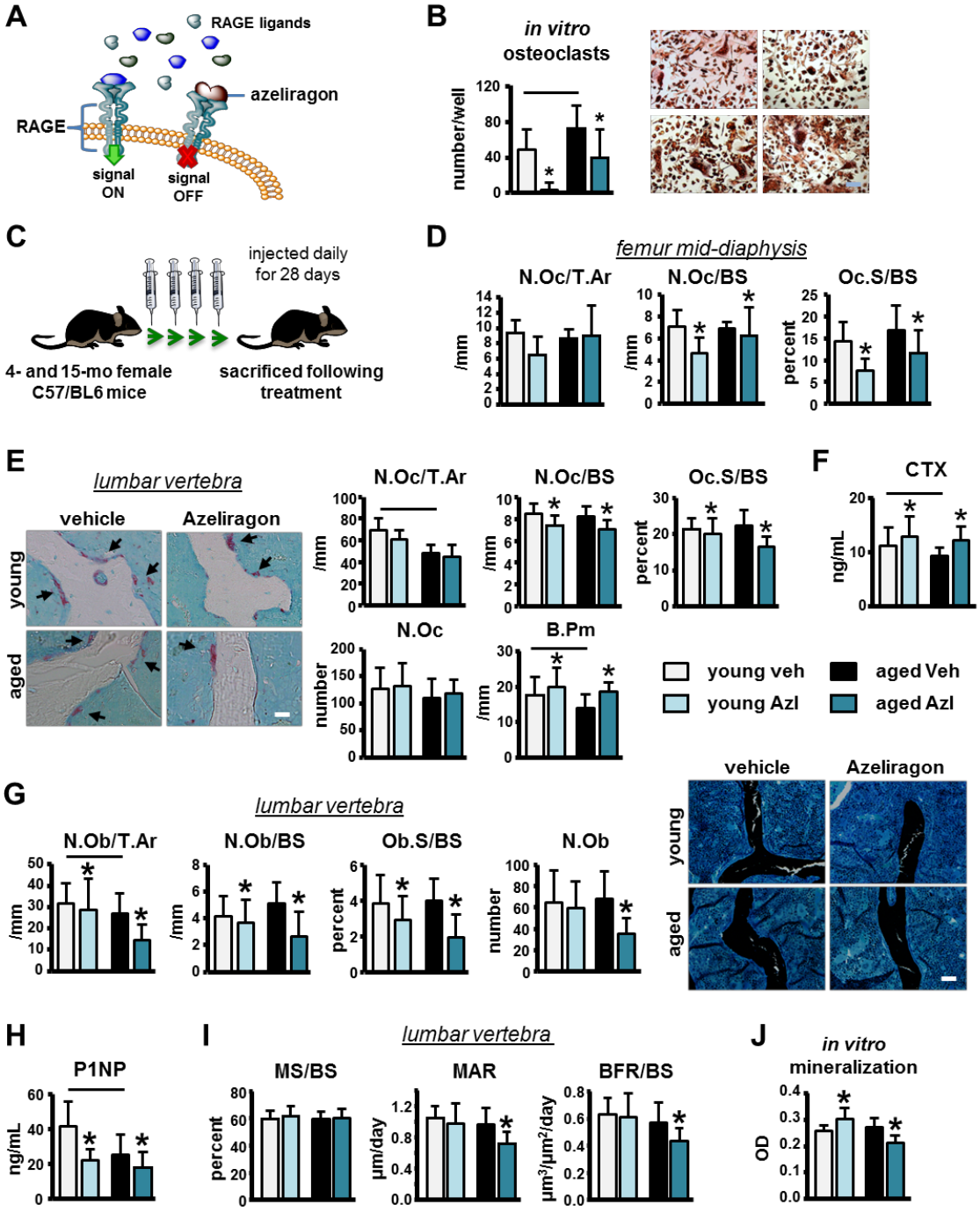

Figure 5-1. AZ differentially alters bone metabolism through direct and indirect actions. A) Illustration of AZ mechanism of action. B) Mature osteoclasts/well generated *in vitro* from non-adherent BMCs from young and middle-aged WT female mice (n=6). Representative images are shown, scale bar indicates 50µm. C) Illustration of *in vivo* experimental design.

Osteoclasts on D) femoral cortical mid-diaphysis and E) vertebral cancellous TRAP/T.blue stained sections (n=8-9). Representative images are shown (black arrows point at osteoclasts), scale bar indicates 25μm. F) Serum CTX levels in young and aged veh and AZ-treated mice (n=10). G) Osteoblasts on von Kossa/McNeal stained vertebra sections (n=7-10). Representative images are shown, scale bar indicates 25μm. H) Circulating serum PINP levels in young and middle-aged veh- and AZ-treated mice (n=8-10). I) Dynamic histomorphometric parameters in unstained vertebra sections (n=8-10). J) Mineralization assay of primary osteoblasts generated *in vitro* from adherent-BMCs from young and aged WT mice (n=5). Bars represent mean ± SD, black line: $p<0.05$, vs young mice and *$p<0.05$, vs veh-treated mice by two-way ANOVA, Tukey.

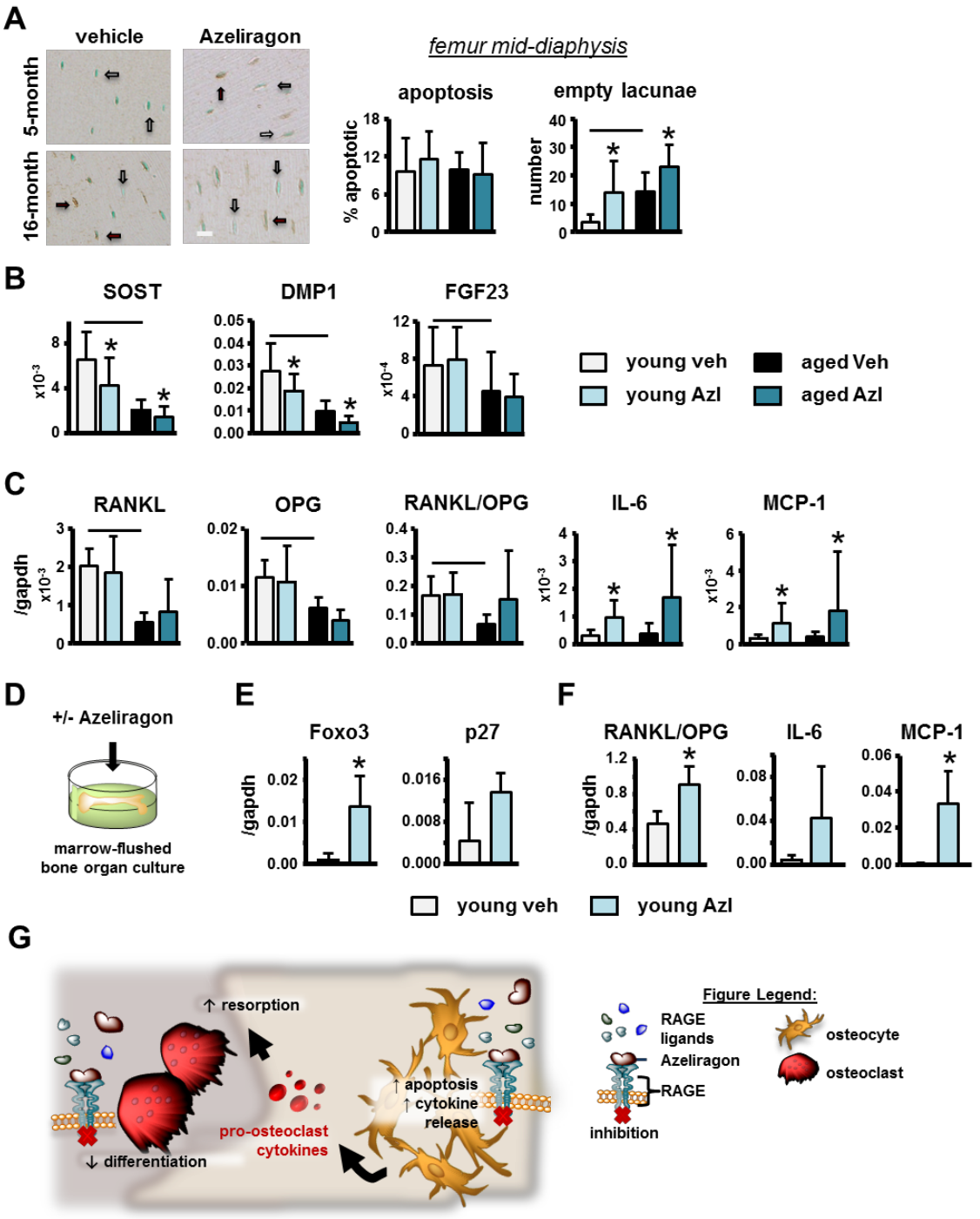

Figure 5-2. Systemic RAGE inhibition with AZ treatment increases osteocyte apoptosis and pro-inflammatory cytokine production. A) Active-caspase3 positive apoptotic osteocytes and number of empty lacunae scored in active caspase3 stained bone sections (n=8-10). Representative images of active caspase3-positive osteocytes (arrow, black),

scale bar indicates 10μm. B) Osteocytic gene and C) cytokine mRNA levels in tibia from young and middle-aged veh and AZ-treated mice (n=7-10). D) Illustration of bone organ culture experimental design. mRNA expression of E) apoptosis-associated and F) pro-inflammatory cytokines in marrow-flushed bone cultures (n=3-5). Bars represent mean ± SD, black line: $p<0.05$, vs young mice and *$p<0.05$, vs veh-treated mice by two-way ANOVA, Tukey. G) Illustration of proposed AZ direct and indirect effects on bone cells.

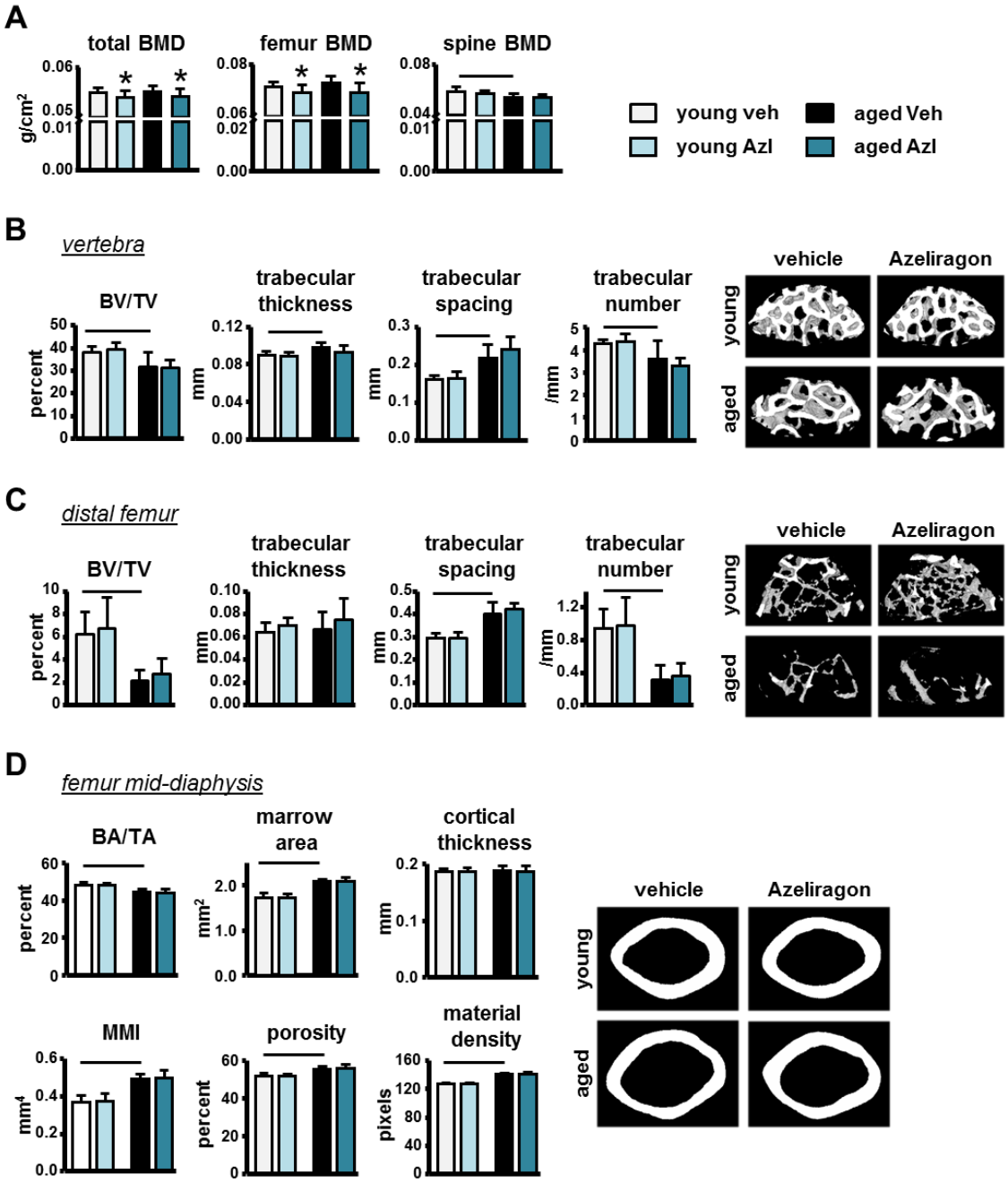

Figure 5-3. Short-term AZ treatment decreases bone mass accrual, but not bone architecture in young or middle-aged mice. A) BMD of young and middle-aged mice following veh- or AZ-treatment (n=8-10). Cancellous microarchitecture evaluated by μCT in the B) L4 vertebra and C) distal femur (n=8-9). Representative images are shown. D) Cortical bone geometry evaluated by μCT in the femoral mid-diaphysis (n=8-9).

Representative images are shown. Bars represent mean ± SD, black line: $p<0.05$, vs young mice and *$p<0.05$, vs veh-treated mice by two-way ANOVA, Tukey.

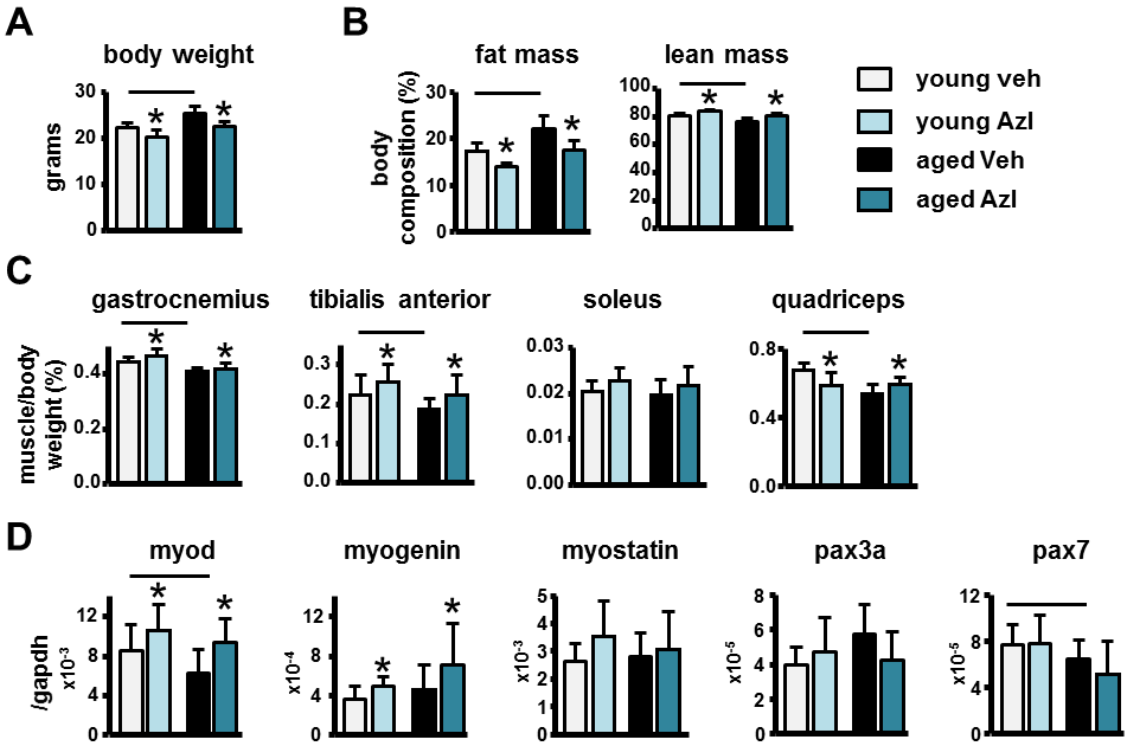

Figure 5-4. AZ treatment reverses the loss of skeletal muscle mass induced with aging. A) Body weight, B) fat and lean mass indicated as percentage of body weight (n=8-10), C) muscle weights (n=8-9), D) myogenesis and satellite cell marker mRNA expression in tibialis anterior muscle (n=7-9) of young and aged mice. Bars represent mean±SD, black line: $p<0.05$, vs young mice and *$p<0.05$, vs veh-treated mice by two-way ANOVA, Tukey.

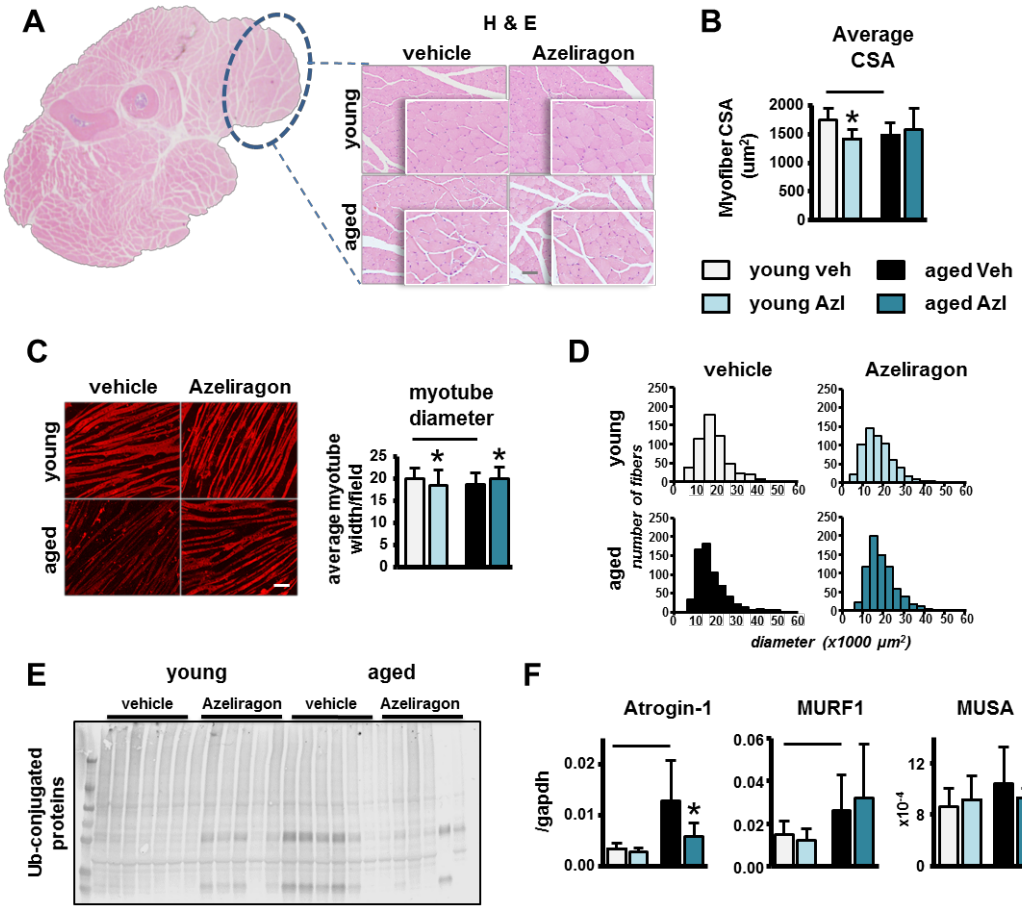

Figure 5-5. AZ treatment restores the function of cellular processes required to maintain skeletal muscle homeostasis in aging. A) low- and high-magnification images of forearm muscle cross-sections, muscle of interest is circled in black, scale bar indicates 50μm, and B) average myofiber cross-sectional area (CSA) (n=6-8). C) Average myotube diameter per field and D) distribution of myotube diameter of serum-treated C2C12 cells (n=10). Representative images are shown, scale bar indicates 50μm. E) Ubiquitin-conjugated and GAPDH protein patterns in skeletal muscle (n=6). F) mRNA levels of atrophy-related genes in tibialis anterior muscle (n=7-9). Bars represent mean ± SD, black line: $p<0.05$, vs young mice and *$p<0.05$, vs veh-treated mice by two-way ANOVA, Tukey.

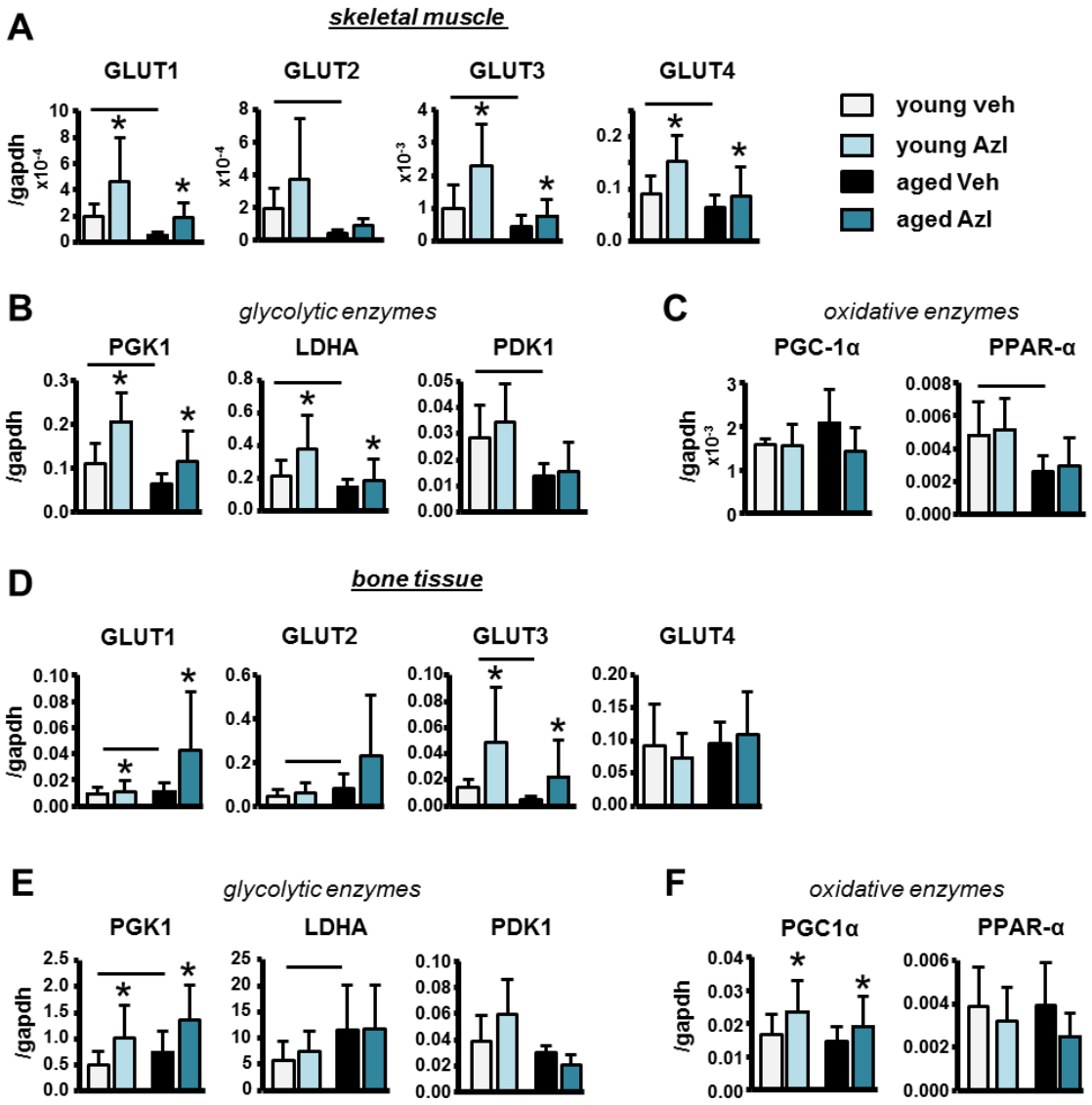

Figure 5-6. Systemic inhibition of RAGE signaling reverses the aging-induced metabolic alterations in skeletal muscle, but not in bone. Glucose transporter GLUT1-4, and glycolytic and oxidative enzyme mRNA levels in tibialis anterior muscle (A-C) and in tibia (D-F) (n=7-9). Bars represent mean ± SD, black line: $p<0.05$, vs young mice and *$p<0.05$, vs veh-treated mice by two-way ANOVA, Tukey.

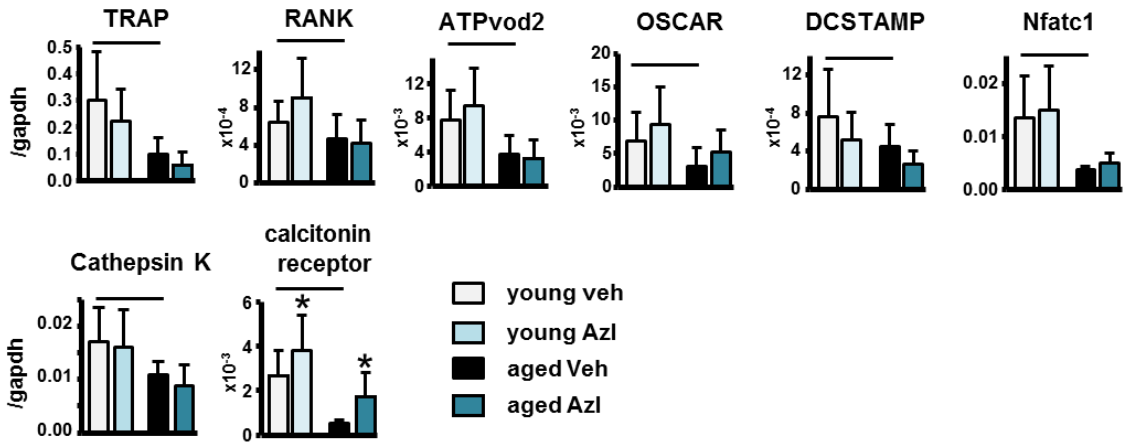

Figure 5-7. Osteoclast gene expression was decreased in aged mice and Azeliragon treatment did not significantly alter osteoclast genes at either age. Osteoclast-related gene mRNA expression in whole tibia samples isolated from young and middle-aged vehicle- and Azeliragon-treated mice. Bars represent mean ± SD, black line: $p<0.05$, versus young mice by two-way ANOVA, Tukey, *$p<0.05$, versus vehicle-treated mice by two-way ANOVA, Tukey.

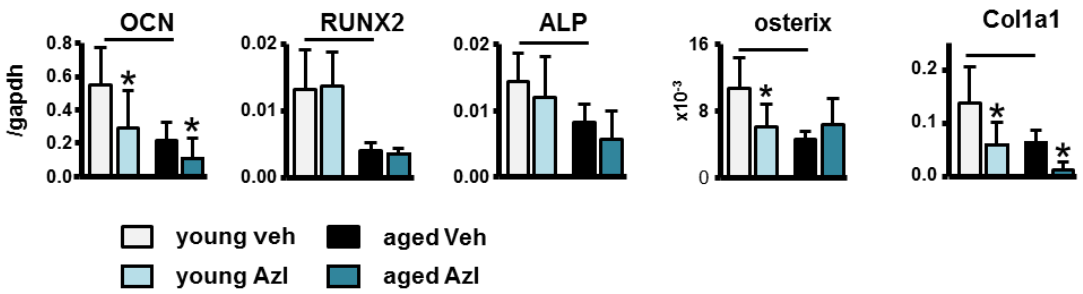

Figure 5-8. Aging and Azeliragon treatment decreased osteoblast gene expression. mRNA expression of osteoblast-related genes in whole tibia samples isolated from young and aged vehicle- and Azeliragon-treated mice. Bars represent mean ± SD, black line: $p<0.05$, versus young mice by two-way ANOVA, Tukey, *$p<0.05$, versus vehicle-treated mice by two-way ANOVA, Tukey.

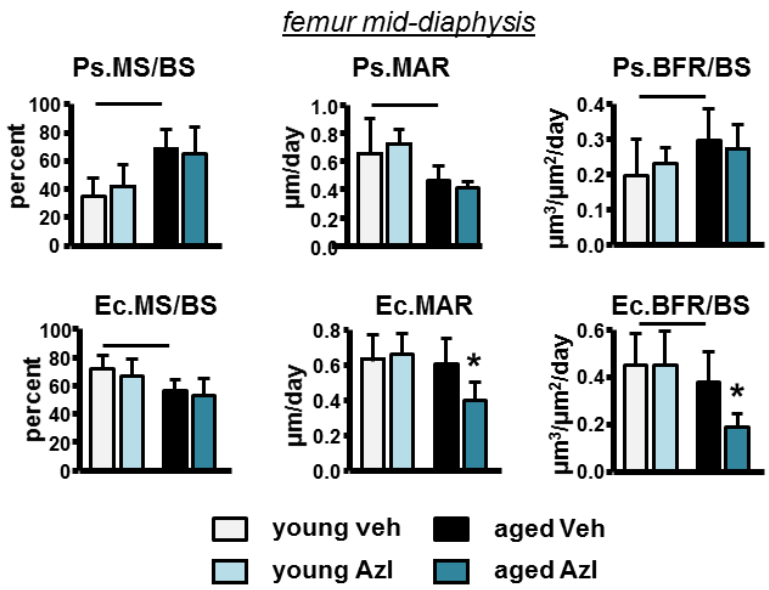

Figure 5-9. Azeliragon decreased bone formation in middle-aged, but not young mice. Mineral apposition rate (MAR), mineralizing surface (MS)/BS, and bone formation rate (BFR)/BS measured in unstained sections of the femoral mid-diaphysis from young and aged vehicle- and Azeliragon-treated mice. Bars represent mean ± SD, black line: $p<0.05$, versus young mice by two-way ANOVA, Tukey, *$p<0.05$, versus vehicle-treated mice by two-way ANOVA, Tukey.

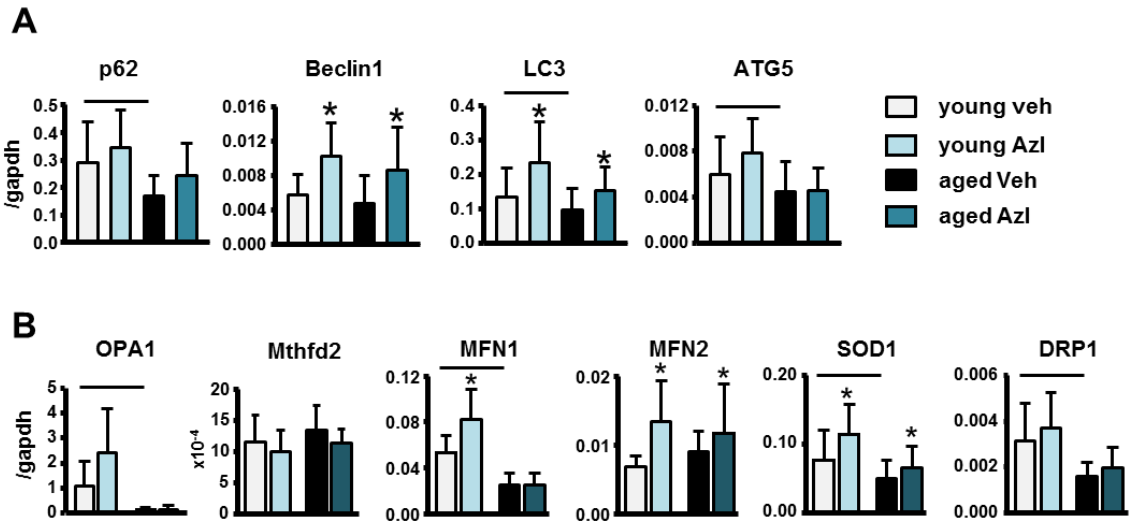

Figure 5-10. Azeliragon treatment restored mRNA levels of several autophagy- and mitochondria-related genes decreased with aging. mRNA levels of A) autophagy- and B) mitochondria-related genes measured in tibialis anterior muscle samples isolated from young and middle-aged vehicle- and Azeliragon-treated mice. Bars represent mean ± SD, black line: $p<0.05$, versus young mice by two-way ANOVA, Tukey, *$p<0.05$, versus vehicle-treated mice by two-way ANOVA, Tukey.

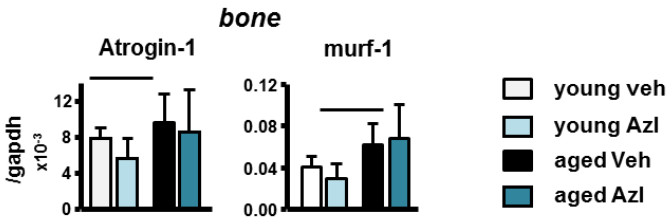

Figure 5-11. In bone, Azeliragon treatment did not alter E3 ubiquitin ligase expression. mRNA levels of Atrogin-1 and Murf1 measured in whole-tibia bones from young and middle-aged vehicle- and Azeliragon-treated mice. Bars represent mean SD, black line: $p<0.05$, versus aged mice by two-way ANOVA, Tukey, *$p<0.05$, versus vehicle-treated mice by two-way ANOVA, Tukey (n=7-9).

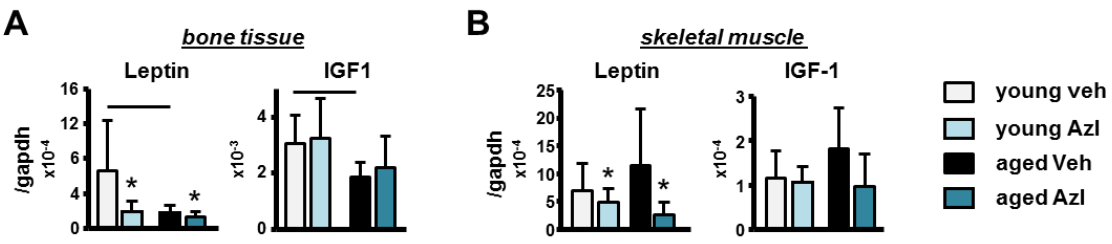

Figure 5-12. Aging differentially alters hormone-related gene, Leptin and IGF1, expression in bone and skeletal muscle. mRNA levels of Leptin and IGF1, measured in A) tibialis anterior muscle and B) whole-tibia bones from young and middle-aged vehicle- and Azeliragon-treated mice. Bars represent mean ± SD, black line: $p<0.05$, versus young mice by two-way ANOVA, Tukey, *$p<0.05$, versus vehicle-treated mice by two-way ANOVA, Tukey.

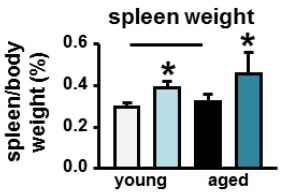

Figure 5-13. Azeliragon administration induced splenomegaly**.** Spleen weight of young and middle-aged mice expressed as percentage of body weight (n=8-9). Bars represent mean SD, black line: $p<0.05$, versus aged mice by two-way ANOVA, Tukey, *$p<0.05$, versus vehicle-treated mice by two-way ANOVA, Tukey.

Table 5-1. Biomechanical properties measured in the femoral mid-diaphysis by 3-point bending test.

	vehicle 5-month-old	**RAGE inhibitor 5-month-old**	**vehicle 16-month-old**	**RAGE inhibitor 16-month-old**
Yield Force (N)	12.67 ± 2.38	14.81± 2.26	9.08 ± 3.37#	9.23 ± 4.16
Ultimate Force (N)	15.09 ± 0.93	15.70 ± 1.31	16.86 ± 1.52	15.69 ± 2.87
Displacement to Yield (μm)	372.58 ± 37.86	419.13 ± 51.66	256.65 ± 122.07#	280.42 ± 137.34
Postyield Displacement (μm)	642.63 ± 344.32	439.93 ± 147.15	332.56 ± 150.72#	394.35 ± 70.29
Total Displacement (μm)	991.91 ± 327.71	773.72 ± 172.42	584.99 ± 92.72#	633.75 ± 119.06
Stiffness (N/mm)	34.27 ± 3.79	36.11 ± 2.88	44.02 ± 8.09#	43.81 ± 7.84
Work to Yield (mJ)	2.64 ± 0.76	3.35 ± 0.80	1.47 ± 1.27#	1.66 ± 1.25
Postyield Work (mJ)	6.85 ± 3.20	5.55 ± 1.48	4.25 ± 1.84#	4.56 ± 0.73
Total Work (mJ)	9.23 ± 3.19	8.39 ± 2.47	6.16 ± 1.77#	5.52 ± 1.26
Yield Stress (MPa)	75.51 ± 19.78	71.99 ± 21.16	48.16 ± 18.39#	49.46 ± 22.18
Ultimate Stress (MPa)	91.83 ± 11.62	86.58 ± 9.87	89.98 ± 10.44	84.14 ± 12.12
Strain to Yield (mε)	365.29 ± 56.95	341.73± 111.10	307.97 ± 152.87	301.48 ± 147.93
Total Strain (mε)	933.81 ± 322.76	713.88 ± 165.82*	630.26 ± 106.21#	687.64 ± 113.83
Modulus (GPa)	2.16 ± 0.38	2.12 ± 0.15	2.20 ± 0.34	2.18 ± 0.47
Resilience (MPa)	1.50 ± 0.54	1.69 ± 0.47	0.85 ± 0.75#	0.95 ± 0.72
Toughness (MPa)	5.20 ± 2.14	4.03 ± 1.05	3.56 ± 1.10#	3.53 ± 1.01

#p<0.05, versus aged mice by two-way ANOVA, Tukey, *p<0.05, versus vehicle-treated mice by two-way ANOVA, Tukey.

Chapter 6

High mobility group box1 (HMGB1) protein regulates osteoclastogenesis through direct actions on osteocytes and osteoclasts *in vitro*

Rationale

Old age and Cx43 deletion in osteocytes are associated with increased osteocyte apoptosis and osteoclastogenesis. We previously demonstrated that apoptotic osteocytes release elevated concentrations of the pro-inflammatory cytokine, high mobility group box1 protein (HMGB1) and apoptotic osteocyte conditioned media (CM) promotes osteoclast differentiation. Further, prevention of osteocyte apoptosis blocks osteoclast differentiation and attenuates the extracellular release of HMGB1 and RANKL. Moreover, sequestration of HMGB1, in turn, reduces RANKL production/release by MLO-Y4 osteocytic cells silenced for Cx43 ($Cx43^{def}$), highlighting the possibility that HMGB1 promotes apoptotic osteocyte-induced osteoclastogenesis. However, the role of HMGB1 signaling in osteocytes has not been well studied. Additionally, the mechanisms underlying its release and the receptor(s) responsible for its actions are not clear. Here, we assessed the effects of HMGB1 signaling in osteoclasts and osteocytes. Further, we tested whether RAGE signaling in osteoclasts regulates the stimulatory effects of apoptotic osteocytes on osteoclastogenesis.

Introduction

Over the last decade the interconnected bidirectional link between the skeleton and immune system has been extensively demonstrated, leading to creation of the osteoimmunology field.[211, 212] In particular, numerous studies have reported that inflammatory conditions increase the risk of developing osteoporosis.[189, 213] Consistent

with this, emerging evidence suggests that inflammatory cytokines function as local regulators of bone cell function under physiological conditions and in disease states.[184, 213]

In particular, cytokines and growth factors produced and released by osteocytes control osteoblast and osteoclast differentiation and activity, thereby regulating bone remodeling. It has long been proposed that maintenance of osteocyte viability is a key process by which osteocytes control bone remodeling.[30] Osteocyte viability is reduced in conditions of increased bone fragility,[26, 32-34, 51] and, conversely, agents that preserve bone strength prevent osteocyte apoptosis.[32, 40, 42, 43] Moreover, osteocyte apoptosis and the prevalence of empty lacunae are increased in old mice and humans.[8, 45]

In previous work, we demonstrated that deletion of the gap junction protein, connexin (Cx) 43 from osteocytes increases osteocyte apoptosis and leads to the accumulation of osteoclasts on the adjacent bone surfaces.[46] Consistent with these findings, Cx43-deficient mice exhibit a skeletal phenotype resembling that of bones from old mice and humans, with bone marrow cavity widening, periosteal expansion, and defective bone material properties.[38, 46] Further, more osteoclasts developed from bone marrow cells (BMCs) cultured in the presence of MLO-Y4 osteocytic cells silenced for Cx43 ($Cx43^{def}$), or treated with conditioned media (CM) from $Cx43^{def}$ cells, compared to scramble (scr) control cells.[119] Consistent with this, $Cx43^{def}$ osteocytic cells undergo accelerated apoptosis and release increased concentrations of soluble (s)RANKL and high mobility group box 1 (HMGB1), which promote osteoclast resorption.[119]

The pro-inflammatory cytokine HMGB1 is a multifunctional redox sensitive protein expressed and released by most cell types including bone cells (osteoclasts, osteoblasts, osteocytes), which exerts various cellular compartment-specific functions.[191] Additionally, following its extracellular secretion, HMGB1 operates as a damage associated molecular pattern (DAMP) protein, and mediates a variety of cellular processes by interacting with

two receptors, the receptor for advanced glycation end products (RAGE) and the toll-like receptor 4 (TLR4).[52]

In bone cells, HMGB1 signaling has been shown to modulate key cellular processes including differentiation, proliferation, apoptosis, and autophagy, and subsequently regulate bone tissue homeostasis, turnover, and repair.[50, 51, 53, 54, 119, 214, 215] For example, in mesenchymal stem cells (MSCs) and osteoblasts, HMGB1 signaling stimulates the release of cytokines and osteogenic MSC differentiation.[215, 216] Consistent with these findings, HMGB1 has beneficial effects on bone repair and promotes facture healing.[53, 217, 218] In osteoclasts, HMGB1-RAGE signaling regulates RANKL-induced osteoclast differentiation and activity.[54] Further, epidermal growth factor-mediated HMGB1 release induces RANK expression via CD68 in patients with autoimmune disease, suggesting that extracellular HMGB1 promotes osteoclast differentiation in human diseases.[219] In osteocytes, aside from the reports by our groups,[50, 119] showing that HMGB1 is secreted from dying osteocytes, the role of HMGB1 signaling in osteocytes has not been well studied. Further, the mechanisms underlying its release and the receptor(s) responsible for its actions is not clear.

In the current study, we assessed the effects of HMGB1 signaling in osteoclasts and osteocytes. Further, we tested whether RAGE signaling in osteoclasts regulates the stimulatory effects of apoptotic osteocytes on osteoclastogenesis. Overall our results suggest that, in osteoclasts, direct HMGB1 actions affect early stages of osteoclast differentiation through TLR4 activation in bone marrow macrophages (BMMs), followed by RAGE activation in pre-osteoclasts. Further, in osteocytes, direct HMGB1 actions stimulate pro-osteoclastogenic signal release from $Cx43^{def}$ osteocytes. These findings demonstrate that HMGB1 exerts dual effects on bone cells, stimulating osteoclast differentiation through RAGE and TLR4 activation in osteoclasts and inducing pro-osteoclastogenic cytokine secretion from osteocytes. Thus, direct actions of HMGB1

signaling in osteoclasts and osteocytes, rather than indirect effects of apoptotic osteocyte-derived extracellular HMGB1 appear to underlie the stimulatory effects of apoptotic osteocytes on osteoclasts.

Materials and Methods

Cell culture. MLO-Y4 osteocytic cells stably silenced for Cx43 ($Cx43^{def}$) or scramble shRNA controls were produced using lentivial shRNA transfection, as previously published.[119, 220] 2 x 10^4 cells/cm^2 MLO-Y4 osteocytic cells were seeded on collagen-coated 48-well plates and and cultured for 12 hours. RAGE-deficient non-adherent BMCs were isolated from two global RAGE knockout mouse models. BMCs isolated from global RAGE knockout mice, previous reported by Philip et al.,[192] were co-cultured with MLO-Y4 osteocytic cells. Additionally, BMCs were isolated from RAGE knockout mice generated by CRISPR/Cas9 as detailed in the supplemental information (Fig. 6-5). The efficiency of the knock out was determined in genomic DNA by PCR and in lung lysates by Western blotting (Fig. 6-6). BMCs were cultured with conditioned media from *ex vivo* long bone cultures of young and old female C57BL/6 mice.

RNA extraction and real-time PCR (qPCR). RNA was isolated and purified using TRIzol, as published.[119] Briefly, a high-capacity cDNA kit was used to perform reverse transcription and then Gene Expression Assay Mix TaqMan Universal Master Mix with an ABI 7900HT real-time PCR system was used to perform qPCR. Glyceraldehyde 3-phosphate dehydrogenase (GAPDH) was used as the house-keeping gene. Primers and

probes were already available at the vendor site, or designed with the Assay Design Center (Roche Applied Science, Indianapolis, IN, USA).

HMGB1 receptor inhibitors. The small molecular RAGE inhibitor, Azeliragon (DC Chemicals, cat.# DC8338) and LPS-RS ultrapure (InvivoGen, cat.# tlrl-prslps) were used at a concentration of 100ng/mL to inhibit RAGE and TLR4, respectively.

In vitro HMGB1 neutralization. Following overnight culture, Cx43 or scramble control silenced MLO-Y4 osteocytic cells were exposed to 0.5μg/ml non-immune (ni) rabbit IgG or neutralizing rabbit anti-HMGB1 antibodies for 24h and CM was collected then concentrated 4x using centricon, as published.[119] For cultures with immunoglobulins, CM was cultured with 10μl/ml Protein A agarose (Sigma-Aldrich, cat.#11134515001) overnight to remove the immunoglobulins. IgG-depleted CM was then collected, 1M HEPES was added and CM was stored at -20°C until used for the osteoclastogenesis assays.

Ex vivo bone organ cultures. Long bones were isolated from young (4-month-old) and old (21-month-old) female C57BL/6 mice obtained from National Institute on Aging (NIA). BMCs were flushed out with α-minimal essential medium (MEM). Osteocyte-enriched marrow-flushed long bones were then cultured ex vivo in α-MEM containing 10% FBS and 1% penicillin/streptomycin (P/S) for 48h. Conditioned media was collected 1M HEPES was added and stored at -20°C until used for the osteoclastogenesis assays.

Osteoclastogenesis assays: HMGB1 receptor inhibitor treatment. BMCs were collected from wildtype C57BL/6 mice and cultured for 48h with α-MEM supplemented with 10% FBS and 1% P/S.[119] Next, non-adherent BMCs were collected and seeded at a density of $2x10^4$ cells/cm^2 on 96-well plates and cultured with sub-optimal levels of RANKL

(40 ng/ml) and M-CSF (20 ng/ml). Inhibitors of the HMGB1 receptors RAGE (Azeliragon) or TLR4 (LPS-RS) were added at 100ng/ml in BMMs (added during day 1-3) and pre-osteoclasts (added during day 3-5).

Osteoclastogenesis assays: in co-culture and with osteocytic conditioned medium. BMCs were collected from wildtype C57BL/6 mice and cultured for 48h with α-MEM supplemented with 10% FBS and 1% P/S.[119] Next, non-adherent BMCs, wildtype or RAGE-deficient, were collected and 2x104 cells/cm2 were plated on 96-well plates and exposed to conditioned media collected from scramble control and Cx43-deficient MLO-Y4 osteocytic cells or ex vivo cultures of osteocyte-enriched marrow-flushed long bones isolated from 4- and 21-month old female C57BL/6 mice. RANKL (80 ng/ml) and M-CSF (20 ng/ml) were added to facilitate osteoclast differentiation and media was changed at day 3. For the co-culturing assays BMCs were isolated from C57BL/6 mice and cultured for 24–48 h. Non-adherent BMCs ($2x10^5$ cells/cm^2) were seeded onto Cx43 and scramble control silenced MLO-Y4 osteocytic cells and treated with 10nM 1.25(OH)2 vitamin D3 and 1M PGE2. Medium was changed every 2 days for 5 days, as previously published.[97] Cells were stained using a commercially available TRAPase kit (Sigma-Aldrich) and mature osteoclasts with ≥ 3 or more nuclei were quantified. A Zeiss Axiovert 35 microscope with a digital camera was used to obtain images.

Generation of RAGE knockout mice. A CRISPR/Cas9 approach was employed to generate RAGE (*Ager*; MGI: 893592) knockout mice, using methods described by Low et al.[221] A guide RNA protospacer sequence was selected using a combination of the MIT CRISPR Design tool developed by Hsu et. al.[222] (crispr.mit.edu/; tool no longer available) and a second design tool develo.ped by Doench et. al.[223] (http://www.broadinstitute.org/rnai/public/analysis-tools/sgrna-design). The 19 nucleotide

(nt) guide sequence selected (shown in blue) was predicted to create a double-strand cleavage 3 bp downstream of the translational start site. The biologically active sgRNA was generated as described,[221] using forward and reverse RNA templates from Integrated DNA Technologies (IDT). Homology-directed repair at the cleavage site utilized a 200-base single-stranded oligodeoxynucleotide (ssODN) with homology to RAGE exon 1 and flanking regions (Fig. 6-5A). The ssODN contained a single-base insertion immediately following the start codon that induces a translational frame-shift, as well as six additional mutations that create an optimized Kozak sequence for efficient translational initiation, eliminate the Cas9 PAM sequence to prevent retargeting, and create a Bgl I site for screening purposes Fig. 6-5B KO shows a partial sequence of the ssODN). A mix containing 50 ng/μl Cas9 protein (PNABio), 25 ng/μl sgRNA, and 20 ng/μl ssODN were microinjected into the pronuclei of fertilized C57BL/6J mouse eggs by the VCU Transgenic/Knockout Mouse Core using standard methods. Microinjected eggs were implanted into the oviducts of ICR pseudopregnant females, and pups were screened for the desired knockout allele by two alternative PCR protocols. The first protocol employed KO and WT allele-specific reverse primers (KO: 5'-GACGCTGGCCATGGTGGCGG-3'), with mutations in red, and (WT: 5'-CCCCGCTGGCATGGTGCTTC-3') in separate reactions with a common forward primer (5'-TTACAAAGCTCCAACAGGTTTGGG-3'), yielding allele-specific 408-bp PCR products (Fig. 6A). *Cerk* gene primers (5'-GGTGGGAGAGAAATCTCCTAGTTC-3') and (5'-AAAGCCACTTGCTGTCCCTCTGTG-3') were included in both reactions, generating a 630-bp internal control. The second PCR protocol primers flanked the targeted region, (5'-GAACTCGGTGGGTTGAAGGAAGTG-3') and (5'- AAGGGTAACTCCTGAGGTTGAGTG-3'), and yielded 676-bp (WT) or 677-bp (KO) products. Subsequent digestion of the KO product with Bgl I produced 405-bp and 272-bp fragments (not shown). Three potential founders were selected for breeding and further characterization, including DNA sequencing. One line (line 7) carrying the desired

sequence changes was ultimately selected for study. Heterozygotes were bred to each other, yielding homozygous offspring with the expected frequency. A 442-bp PCR product flanking the targeted region from a RAGE KO homozygote was sequenced to verify that the gene was correctly targeted (Fig. 6-5C).

Western Blot Analysis. Lungs were collected, frozen immediately with liquid nitrogen, and stored at −80°C. Pulmonary tissue was homogenized in RIPA buffer with protease/phosphatase inhibitors and protein concentration was determined using the BCA protein assay (Thermoscientific). Samples (40μg/lane) were separated by 10% SDS-PAGE and transferred to a nitrocellulose membrane. After incubation in 10% non-fat milk blocking solution overnight at 4°C, the membrane was incubated with rabbit anti-RAGE (1:1,000; Sigma–Aldrich) followed by incubation with horseradish peroxidase-conjugated secondary antibodies (Jackson ImmunoResearch). The membrane was probed again with a polyclonal anti-β actin antibody (1:5,000; Sigma– Aldrich, St. Louis, MO), followed by the corresponding secondary antibody. Immunopositive bands were detected by enhanced chemiluminescence (ECL).

Statistical analysis. Data were analyzed with SigmaPlot (Systat Software Inc., San Jose, CA, USA). All results are presented as the mean ± standard deviation. Differences were assessed using two-way ANOVA, and Tukey Method for post-hoc analysis or Student's t-test, as appropriate. Differences of $p<0.05$ were regarded as significant.

Results

Inhibition of HMGB1 and its receptors alters osteoclast differentiation. Consistent with previous reports,[54] direct inhibition of HMGB1 signaling during the process of osteoclast differentiation with anti-HMGB1 neutralizing antibodies reduced the number of mature osteoclasts generated *in vitro* from non-adherent BMCs compared to cells treated with control rabbit non-immune IgG antibodies (Fig. 6-1A). Therefore, we tested effects of the HMGB1 receptors, RAGE and TLR4, on different stages of the osteoclast differentiation process. For this, the inhibitors for the receptors were supplemented at early stages of differentiation (day 1-3), later in differentiation (day 3-5), or throughout the experiment (day 1-5) (Fig. 6-1B). We found that in osteoclasts precursors, inhibition of TLR4, but not RAGE, reduced osteoclast number; whereas, in later stages of differentiation, RAGE, but not TLR4 inhibition, decreased osteoclast formation (Fig. 6-1C). Further, when added throughout differentiation (day 1-5), osteoclast number was reduced by the individual inhibitors and additively suppressed with a combination of both Azeliragon and LPS-RS. Taken together, these data stress the critical function of HMGB1 signaling at different stages of the osteoclast maturation process, and suggest that HGMB1 produced by osteoclasts has direct effects on differentiation via TLR4 activation in BMMs and RAGE activation in pre-osteoclasts.

Apoptotic osteocyte induced increases in osteoclast differentiation are not mediated through RAGE-signaling in osteoclasts. Consistent with our previous findings that conditioned media from apoptotic $Cx43^{def}$ MLO-Y4 osteocytic cells induces osteoclastogenesis,[119] more osteoclasts were produced when conditioned media from osteocyte-enriched long bone cultures of old (21-mo) compared to young (4-mo) mice was added to wildtype BMCs; an effect that was attenuated by pre-treatment with the apoptosis inhibitor, DEVD-CHO (Fig. 6-2A,B).

Based on our previous findings that apoptotic osteocytes release elevated levels of HMGB1, we next evaluated whether RAGE signaling in osteoclasts facilitates the stimulatory effects of apoptotic osteocyte conditioned media on osteoclastogenesis. Similar to previous reports,[184, 213] both genetic and pharmacological RAGE inhibition in BMCs decreased osteoclast number (Fig. 6-2C-E). However, despite the inhibitory effects of RAGE inhibition in osteoclasts with control media, the addition of conditioned media from old bones to BMCs from wildtype or global RAGE-knockout mice enhanced osteoclast number by 1.3- and 1.7-fold, respectively, vs. conditioned media from young bones (Fig. 6-2C). Moreover, co-culturing $Cx43^{def}$ osteocytic cells with wildtype or RAGE-knockout BMCs increased osteoclast number 2- and 4-fold, respectively compared to cells co-cultured with scramble control osteocytic cells (Fig. 6-2D). Additionally, $Cx43^{def}$ conditioned media induced 1.6-fold more osteoclasts than conditioned media from scramble control osteocytic cells, when cultured with or without the small-molecule RAGE inhibitor, Azeliragon (Fig. 6-2E). Taken together, our findings suggest that even though RAGE deficiency/inhibition reduces osteoclast differentiation, apoptotic osteocyte conditioned media-induced increases in osteoclastogenesis are not mediated through HMGB1/RAGE activation in osteoclasts.

Autocrine actions of apoptotic osteocyte-derived HMGB1 in osteocytes, rather than direct signaling in osteoclasts promotes osteoclastogenesis. We next tested whether HMGB1 released by osteocytes has autocrine effects on the osteocytic cells and/or mediates the effect of the osteocytic cells on osteoclasts. We first cultured MLO-Y4 osteocytic cells silenced for Cx43 or scramble controls with an anti-HMGB1 antibody to block the autocrine effects of secreted HMGB1 on osteocytes. The conditioned media was collected and then anti-HMGB1 antibody was removed by immunoprecipitation. Alternatively, conditioned media from MLO-Y4 cells was

immunodepleted with an anti-HMGB1 antibody after collection. Both conditioned media preparations were then used in osteoclastogenesis assays. We found that conditioned media prepared from MLO-Y4 cells that had been cultured in HMGB1-deficient conditions yielded fewer osteoclasts than control media (Fig. 6-3A). Conversely, and consistent with the results included in Fig. 6-2, immunodepletion of HMGB1 from $Cx43^{def}$ CM after collecting the media, did not prevent osteoclast formation (Fig. 6-3B). Together, these data suggest that direct HMGB1 actions in osteocytes stimulates osteoclast differentiation.

Discussion

Numerous reports have shown that inflammatory cytokines function as local signals that influence bone cell function under both physiological and pathological conditions.[160, 161] In particular, HMGB1 has been shown to be involved in mediating various cellular processes in bone. [191] In the current study, we demonstrate that HMGB1 effects on both osteocytes and osteoclasts alter osteoclast differentiation (Fig. 6-4).

Our current findings provide additional evidence that HMGB1 receptor signaling regulates osteoclastogenesis. As predicted by Zhou et. at., our findings demonstrate that during osteoclast differentiation TLR4 is required for early HMGB1 signaling, whereas RAGE is required for later HMGB1 signaling.[54] These studies showed that HMGB1-TLR4 signaling is required for early osteoclast differentiation stages including ERK and NF-κB activation, whereas, HMGB1-RAGE signaling is required for integrin signaling and proper actin ring formation during later osteoclast differentiation signaling events.

Based on our previous findings that apoptotic osteocytes release elevated levels of extracellular HMGB1, we next tested whether RAGE signaling in osteoclasts mediates the stimulatory effects of apoptotic osteocyte conditioned media on osteoclastogenesis. However, while osteoclastogenesis was decreased with RAGE deficiency, neither genetic nor pharmacological RAGE inhibition blocked the apoptotic osteocyte-induced increases in osteoclastogenesis. Taken together, these pieces of evidence suggest that apoptotic osteocytes do not increase osteoclastogenesis by directly activating RAGE signaling in osteoclasts.

In support of this notion, we also found that while HMGB1 immunodepletion from $Cx43^{def}$ conditioned media did not inhibit osteoclast formation, treatment of $Cx43^{def}$ osteocytes with HMGB1 neutralizing antibody followed by HMGB1 immunodepletion, prevented osteoclast differentiation stimulated by $Cx43^{def}$ conditioned media, suggesting direct HMGB1 actions in osteocytes, rather than indirect actions on osteoclasts, stimulates

osteoclast differentiation induced by apoptotic osteocytes. This idea is consistent with our previously published findings showing that HMGB1 neutralizing antibody treatment in Cx43^{def} osteocytes attenuates the release of the pro-osteoclastogenic cytokine RANKL from Cx43^{def} osteocytes.[119]

Additionally, other inflammatory cytokines known to activate RAGE have also been shown to have similar effects on cell viability and cytokine production/release in osteoblasts and osteocytes.[224, 225] For example, MLO-Y4 osteocytic cell apoptosis is stimulated by advanced glycation end products (AGEs)[226] and promote pro-inflammatory cytokine release (IL-6, TNFα, RANKL, VEGFA) from both osteoblasts and osteocytes,[50, 139, 227] which may subsequently increase osteoclastogenesis. Further, high levels of AGEs in bone are associated with increased osteoclast activity in humans, despite a lack of effect of AGEs on osteoclast activity *in vitro.*[228] In addition, S100A9, another ligand for RAGE, has similar effects on cell viability and cytokine secretion in osteoblasts and osteocytes.[119, 224, 225] Specifically, S100A9 treatment in osteoblasts stimulates RAGE expression and promotes cytokine release; and S100A9-treated osteoblast CM increases osteoclast differentiation/activity, whereas when added directly to osteoclasts S100A9 inhibits osteoclastogenesis.[224]

Overall, these data suggest that in bone HMGB1 signaling in osteocytes stimulates pro-inflammatory cytokine release, which subsequently induces osteoclastogenesis. Future studies will be carried out aiming to elucidate the specific effects of HMGB1 signaling in osteocytes and identify the receptor responsible for these effects.

In summary, our findings demonstrate that HMGB1 directly promotes osteoclastogenesis through RAGE and TLR4 stimulation in osteoclasts, and increases pro-osteoclastogenic cytokine release from apoptotic osteocytes (Fig. 6-4). Thus, direct actions of HMGB1 signaling in osteoclasts and osteocytes, rather than indirect effects of

apoptotic osteocyte-derived extracellular HMGB1 appear to underlie the stimulatory effects of apoptotic osteocytes on osteoclasts.

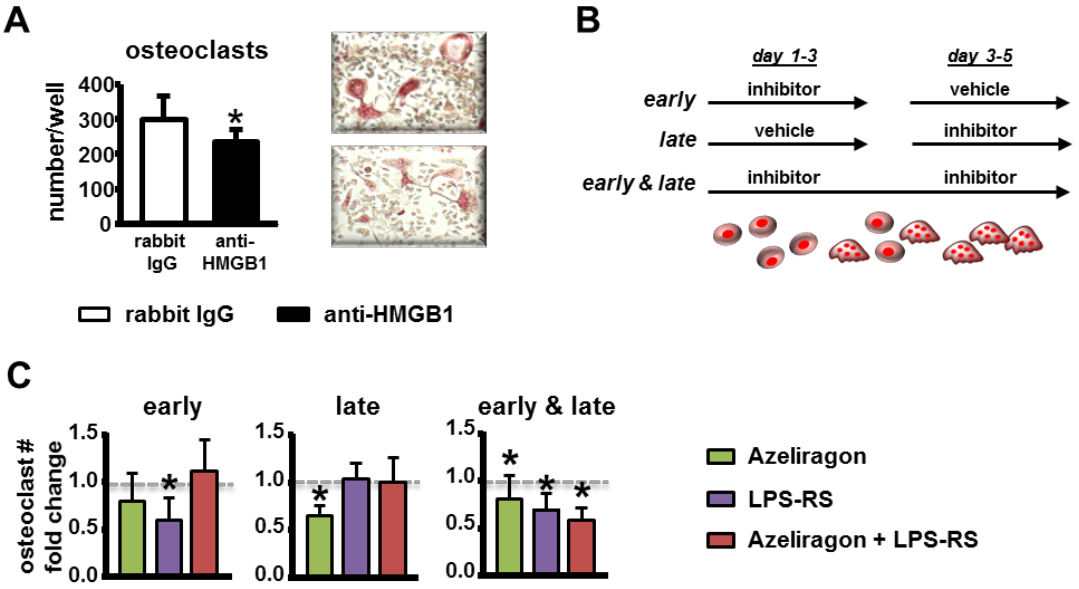

Figure 6-1. Inhibition of HMGB1 and its receptors alters osteoclast differentiation in a stage-dependent manner. (A) Non-adherent BMCs treated with rabbit IgG control or anti-HMGB1 antibodies. Bars represent mean ± S.D. (n=6). *p<0.05 vs vehicle rabbit IgG control treated cells by t-test. Representative osteoclast images are shown. (B) Illustration of the experimental design testing the effects of inhibitor treatment at different stages of osteoclast differentiation and (C) osteoclast numbers reported as fold changes. Inhibitors or vehicle were added to BMMs (day 1-3) or pre-osteoclasts (day 3-5) HMGB1 receptor inhibitor- (Azeliragon and LPS-Rs) treated non-adherent BMCs at different stages of differentiation. *p<0.05 vs vehicle control treated non-adherent BMCs by one-way ANOVA. Bars represent mean ± S.D. (n=6).

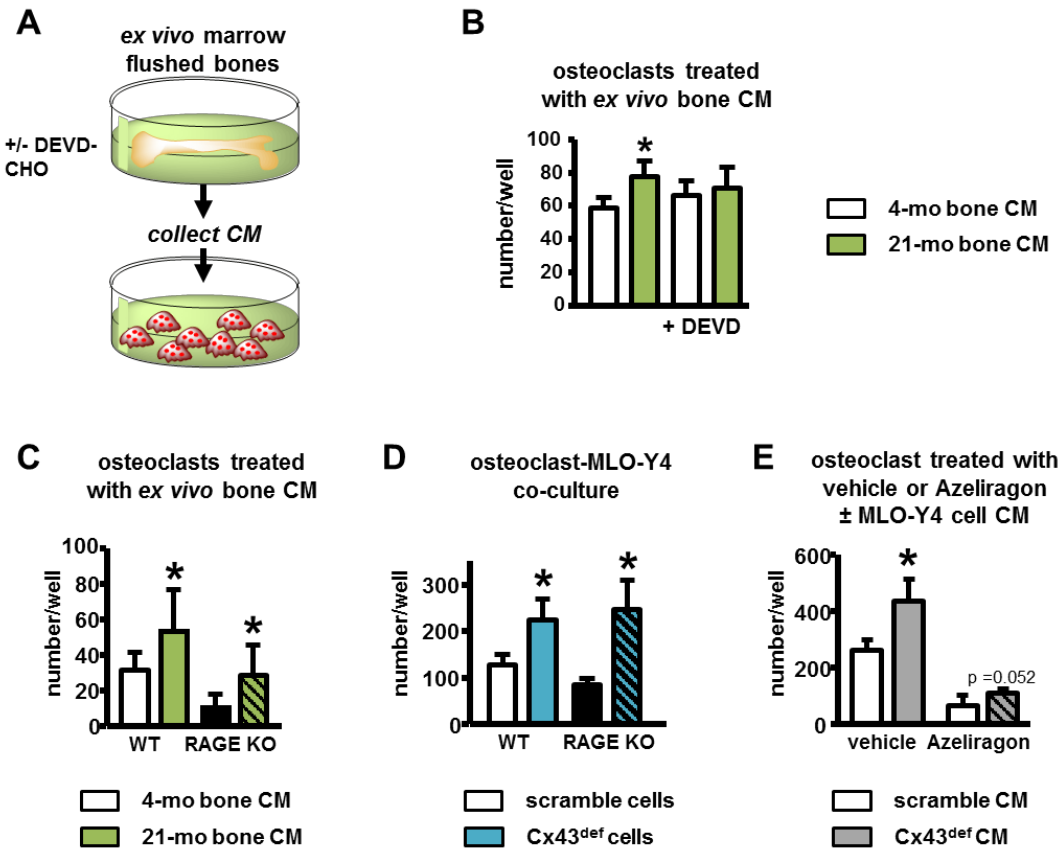

Figure 6-2. Apoptotic osteocyte induced increases in osteoclast differentiation are not mediated through RAGE signaling in osteoclasts. (A) Scheme illustrating experimental design. (B) Non-adherent BMCs treated with conditioned media (CM) collected from *ex vivo* osteocyte-enriched bone cultures of young (4-month-old) and old (21-month-old) female mice treated with vehicle or DEVD-CHO. *p<0.05 vs young bone culture CM-treated osteoclasts by two-way ANOVA, n=6. (C-E) Osteoclast differentiation was induced in non-adherent BMCs (C) Wildtype and RAGE-deficient BMCs treated with CM from *ex vivo* osteocyte-enriched bone cultures of young and old female mice. Bars represent mean ± S.D. *p<0.05 versus young bone culture CM-treated osteoclasts by two-way ANOVA, n=6. (D) Wildtype and RAGE-deficient BMCs co-cultured with scramble or $Cx43^{def}$ MLO-Y4 osteocytic cells. Bars represent mean ± S.D. *p<0.05 versus osteoclasts co-cultured with scramble MLO-Y4 cells by two-way ANOVA, n=6. (n=6). (E) Wildtype BMCs treated

with CM from scramble or Cx43^{def} MLO-Y4 osteocytic cells in the presence of vehicle or Azeliragon (100ng/mL). Bars represent mean ± S.D. *$p<0.05$ versus scramble CM treated osteoclasts precursors +/- Azeliragon by two-way ANOVA, n=6.

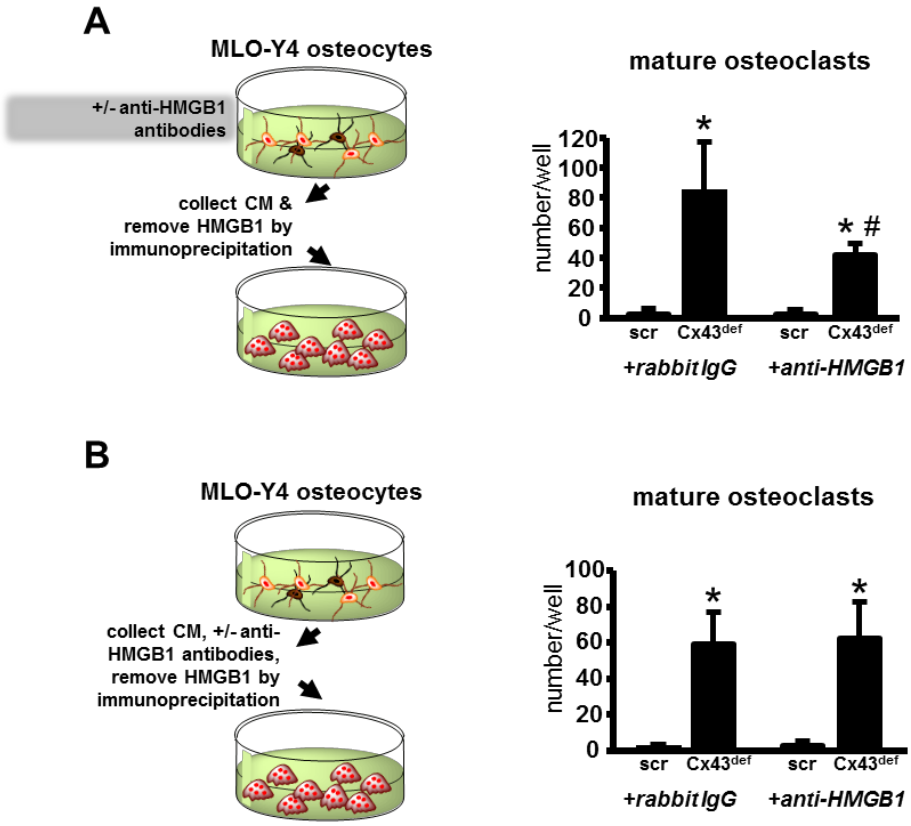

Figure 6-3. Direct actions of apoptotic osteocyte-derived HMGB1 in osteocytes, rather than indirect signaling in osteoclasts promotes osteoclastogenesis. Mature osteoclasts generated *in vitro* from non-adherent BMCs treated with conditioned media from (A) scramble and Cx43-deficient MLO-Y4 osteocytic cells or (B) conditioned media from scramble and $Cx43^{def}$ MLO-Y4 osteocytic cells treated with rabbit IgG or anti-HMGB1 neutralizing antibodies, then removed by immunoprecipitation. Bars represent mean ± S.D. *$p<0.05$ versus scramble cells, $^{\#}<0.05$ versus corresponding IgG-treated cells by two-way ANOVA, n=4.

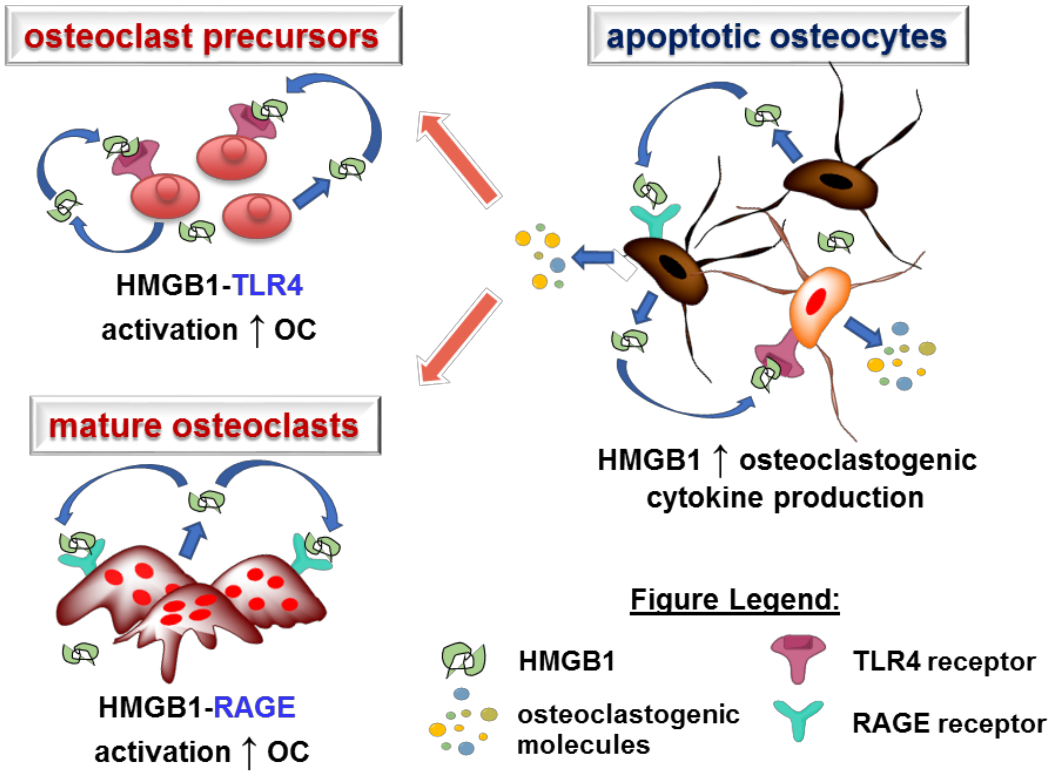

Figure 6-4. Schematic Summary. Dual effects exerted by HMGB1 on bone cells, resulting in increased osteoclastogenesis, directly by promoting osteoclast differentiation via activation of TLR4 and RAGE in osteoclasts and indirectly by increasing the release of pro-osteoclastogenic cytokine from osteocytes.

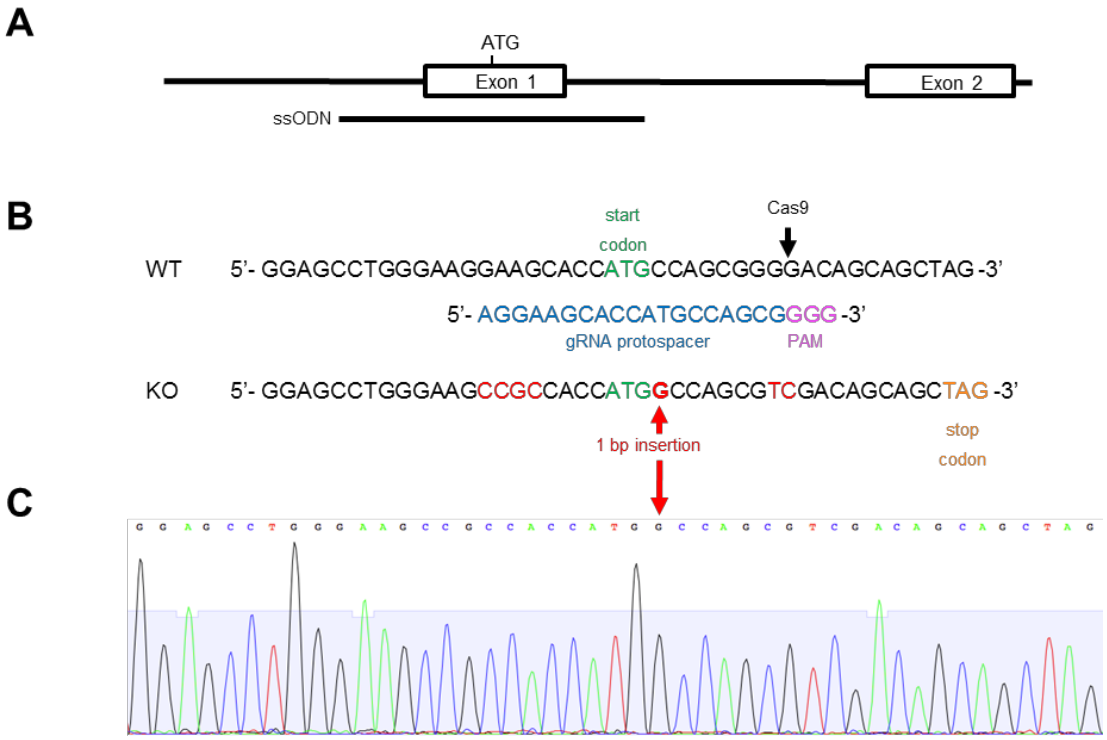

Figure 6-5. RAGE knockout mouse targeting strategy using CRISPR/Cas9. (A) Diagram of RAGE exon 1 and flanking sequences, indicating the locations of the translational start codon and 200-base ssODN repair template carrying seven mutations. (B) Sequences of the WT and KO RAGE alleles. Indicated in the WT sequence is the translational start codon (green), and Cas9 cleavage site (arrow). Indicated in the KO sequence is the translational start codon (green), and the 1-bp insertion (bold red) that creates both a translational frame-shift and an early translational termination site (orange). Six additional mutations (red) in the KO sequence create an optimized Kozak sequence (GCCGCCACC) for efficient translational initiation, eliminate the Cas9 PAM sequence to prevent retargeting, and create a Bgl I site (GCCACCATGGC) for screening purposes. Also shown are the Cas9 gRNA protospacer (blue) and PAM (pink) sequences. (C) Partial sequencing chromatogram from a homozygous RAGE KO mouse corresponding to the same region shown for the KO allele in (B).

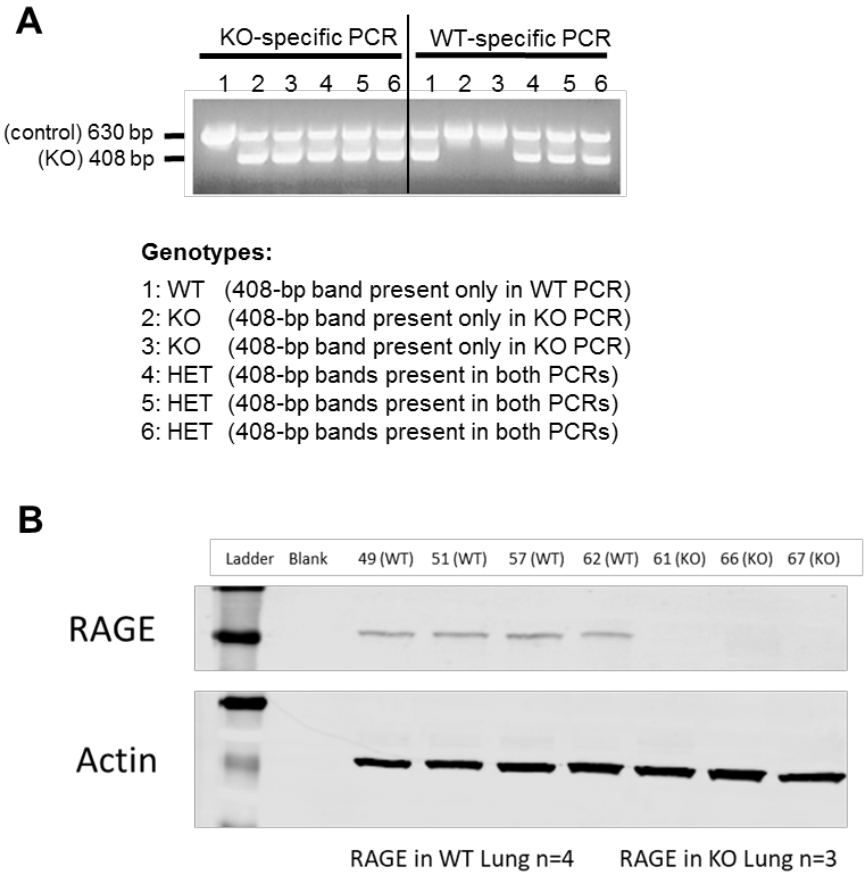

Figure 6-6. Allele-specific PCR genotyping and western blot confirmation of RAGE KO mice generation. (A) Six pups from a RAGE KO heterozygote x heterozygote mating were genotyped using KO and WT allele-specific protocols. Both protocols employed a common forward primer, but the reverse primers were specific for either the KO or WT allele. Both KO and WT PCR products are 408 bp. *Cerk* gene primers were included in both reactions, generating a 630-bp internal control. (B) RAGE protein levels measured in lung lysates from RAGE KO and WT littermate mice (n=3-4).

Chapter 7

Summary of Findings and Future Directions

The current series of studies were conducted in order to better understand the mechanisms underlying the increases in osteocyte apoptosis seen in aging and to identify the apoptotic osteocyte-derived signaling factors responsible for the subsequent increases in osteoclastogenesis. Gaining a better understanding of these events is an important step towards the discovery of new therapeutic targets to treat bone fragility in aging. Overall, the findings from these studies provide further insights into the mechanisms underlying osteocyte apoptosis as well as the signaling molecules linking osteocyte apoptosis to osteoclast activation in aging.

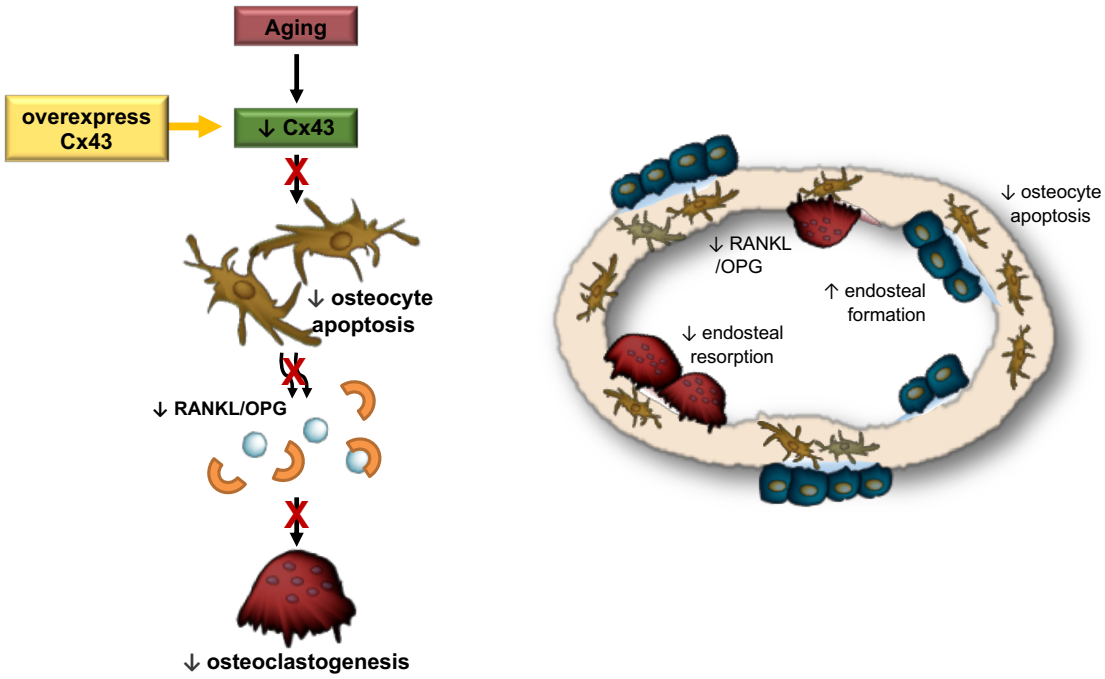

Figure 7-1. Cx43 expression in osteocytes ameliorates age-induced cortical bone changes by preserving osteocyte viability, decreasing bone resorption, and maintaining bone formation, leading to improved bone strength.

Previous work from our laboratory demonstrated that Cx43 is critical for osteocyte survival, and that removal of osteocytic Cx43 leads a skeletal phenotype similar to that observed in aging.[38, 46] Based on this evidence, we first examined the contribution of osteocytic Cx43 to the skeletal phenotype of aged mice, using $Cx43^{OT}$ mice expressing a Cx43 transgene targeted to DMP1-8kb-expressing cells.[90] As illustrated in Fig. 7-1, in these studies we showed overexpression of osteocytic Cx43 in aging attenuated the prevalence of apoptotic osteocytes in cortical bone, and to a lesser extent in the cancellous bone. In addition, we found that in aged $Cx43^{OT}$ mice these reductions in osteocyte apoptosis were accompanied by changes in bone remodeling with increased formation and decreased resorption along the endocortical bone surface. Further, consistent with the reductions in bone resorption, the RANKL/OPG gene expression ratio was lower in cortical bone lysates of 14-month-old $Cx43^{OT}$ compared to WT mice. Thus, these findings further demonstrate the critical role of Cx43 in maintaining osteocyte viability as well as the direct link between osteocyte apoptosis and osteoclastogenesis.

Although, given the fact that we did not detect differences in cortical bone mass or geometry between the two genotypes at 14 months of age, it is reasonable to speculate that the increases in the structural and material properties in the 14-month-old $Cx43^{OT}$ mice were not due to changes in bone architecture, but are likely due to other factors at the level of the collagen/mineral. Thus, further studies are needed to better understand the mechanisms underlying the changes in the material properties of the bone of mice expressing DMP1-Cx43. In addition, whether the improved ability of the bone to resist damage is due to prevention of microdamage accumulation or direct preservation of the bone material by living osteocytes or a combination of both, remains to be determined.

Interestingly, our findings that osteocyte-targeted Cx43 transgene expression was sufficient to reduce osteocyte apoptosis in both bone compartments, whereas changes in bone turnover and improvements in the bone mechanical properties were only observed

in cortical bone, further demonstrate the differential bone compartment-specific actions of Cx43. Additionally, these findings raise the possibility Cx43-dependent regulation of osteocyte viability is a critical regulator of bone turnover in cortical, but not trabecular bone. Therefore, future studies are also needed to better understand the mechanisms underlying these bone compartment specific effects of Cx43, and to identify whether Cx43 contributes to the divergent effects that aging has on bone remodeling in the trabecular and cortical bone compartments.

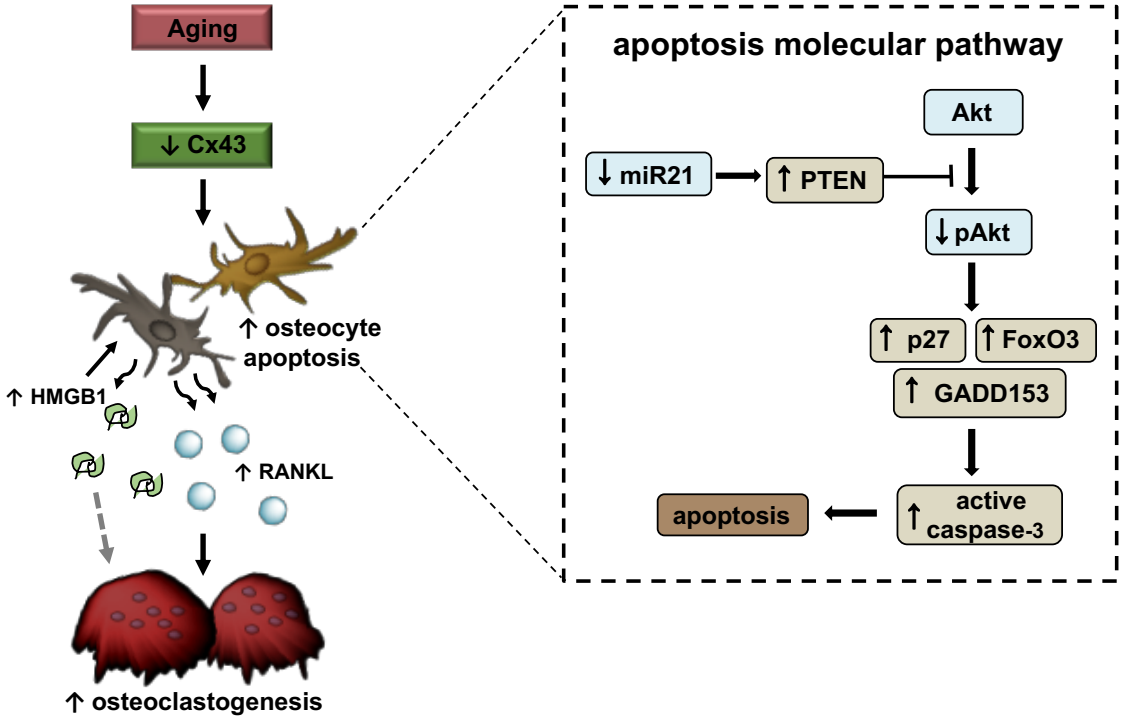

Figure 7-2. Working model showing decreased osteocytic Cx43 leads to a reduction in miR21 levels which, in turn, leads to an increase in PTEN levels and consequently a reduction in Akt activation. Decreased Akt activity leads to increased expression of the apoptosis-related genes p27, FoxO3 and GADD153 resulting in caspase-3-mediated apoptosis. At the same time, apoptotic osteocytes release RANKL and HMGB1, which induce osteoclast differentiation and recruitment.[119]

In the next series of studies we worked to dissect the molecular signaling pathway underlying osteocyte apoptosis triggered in the absence of osteocytic Cx43 and by aging, illustrated in Fig. 7-2.[119] In addition, we sought to unveil the molecular link between osteocyte apoptosis and targeted osteoclastic bone resorption. Overall, our findings provide evidence that, at least in female mice, osteocyte apoptosis in old age and the absence of osteocytic Cx43 is a result of decreased miR21 levels, which subsequently lead to increased PTEN protein levels and decreased Akt activation. Further, we found that apoptotic osteocytes release more HMGB1, which in turn induces osteoclast precursor differentiation, highlighting osteocyte-derived HMGB1 as a possible factor linking osteocyte apoptosis and targeted osteoclastogenesis.

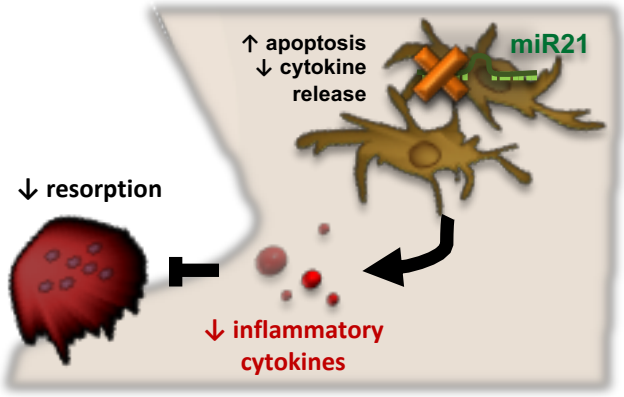

Figure 7-3. In females osteocytic miR21 deletion led to high levels of osteocyte apoptosis that were accompanied by decreases in bone resorption.

Given these findings regarding the role of osteocytic miR21 *in vitro*, we next investigated the role of osteocytic miR21 locus *in vivo*, using a mouse model in which miR21 was deleted from osteocytes. Surprisingly, in females, we found that osteocytic miR21 deletion led to high levels of osteocyte apoptosis that were accompanied by decreases in bone resorption (and formation) compared to miR21$^{f/f}$ littermates (Fig. 7-3). Taken together, these unexpected findings suggest that in addition to the role of osteocytic

miR21 in maintaining osteocyte viability, miR21 also appears to regulate osteocyte inflammatory-cytokine production/release. Consistently, recent studies in other tissues, have identified miR21 as a key switch in the control of inflammatory responses.[230] In particular, miR21 has been shown to be involved in mediating both the initial pro-inflammatory and later anti-inflammatory responses, and dysregulation of miR21 expression contributes to the onset and progression of various inflammatory diseases.[230] Additionally, miR21 has been shown to be secreted in extracellular vesicles (EV), and increased exosomal-miR21 is a biomarker of several inflammatory diseases and has also been shown to mediate inflammatory responses.[231, 232]

Following their release exosomes contribute to disease onset and progression by enhancing the release of pro-inflammatory proteins and miRs.[232] Further, caspase3 activation stimulates EV release[233, 234] and coincides with extracellular HMGB1 release.[50, 160] Moreover, miR21 is increased in pancreatic βcell-derived EV in response to inflammatory cytokines.[235] Additionally, miR21 regulates osteoclast survival and function,[236] and promotes RANKL-induced osteoclastogenesis,[237] and estrogen induces osteoclast apoptosis by repressing miR21.[124] In osteoporotic patients, miR21 is elevated in serum and bone samples,[147] and global miR21 deficiency inhibits osteoclast activity and prevents ovariectomy-induced bone loss.[131] Taken together these pieces of evidence raise the possibility that in old age and Cx43 deficiency, low osteocytic miR21 and HMGB1 levels result from enhanced EV release mediated by caspase3 activation in apoptotic osteocytes; with subsequent osteoclast activation facilitated through HMGB1 receptor activation and/or by osteoclast uptake of miR21-containing EV. Thus, future studies are needed to determine if EV, through cytokine and miR transfer, mediate osteoclast recruitment, which will provide insights into the mechanisms underlying the release of osteoclastogenic signals by apoptotic osteocytes in old age and Cx43 deficiency.

In addition to these findings, in this study we showed that the miR21 locus exerts a sex-divergent role in osteocytes controlling osteocyte viability and regulating bone mass/geometry through paracrine actions on osteoblasts and osteoclasts (Fig. 4-6B). Further, we revealed a potential mechanism by which miR21 removal from osteocytes differentially alters bone turnover by sex-specific regulation of key signaling pathways in osteocytes as well as cytokine production/secretion (Fig. 4-6A). However, additional studies are needed to clearly elucidate the specific mechanisms by which osteocytic miR21 exerts these sex-divergent effects. Further, future studies will be performed to determine whether the mild effect of miR21 deletion on bone mass and architecture is exacerbated with aging. Nevertheless, given the increasing interest of pharmaceutical companies in the development of miR-based drugs combined with the growing number of studies identifying gender-dependent adverse drug reactions,[145] our findings highlight the importance of considering possible sex-dependent roles of miRs when developing therapeutics.

Interestingly, despite these sex-specific effects of osteocytic miR21 deficiency in this study, both female and male miR21$^{\Delta Ot}$ mice exhibited markedly higher femoral cortical bone mechanical properties compared to the respective miR21$^{f/f}$ controls. While our findings highlight a possible mechanism by which osteocytic miR21 deficiency improves bone mechanical properties by stimulating collagen synthesis via downregulation of JNK signaling, extensive additional studies are required. Thus, in future studies we will also work to uncover the molecular and tissue-level mechanisms by which osteocytic miR21 negatively influences bone mechanical integrity. Overall, our findings from this study provide novel insights into the sex-dependent and -independent mechanisms by which miR21 regulation in osteocytes alters bone, which offer a basis for future studies that could eventually lead to new therapeutic targets to treat bone fragility.

Based on our findings that apoptotic osteocytes release more HMGB1, and that inhibition of HMGB1-RAGE activation with HMGB1 BoxA treatment, blocks the increases in osteoclast differentiation induced by conditioned media from apoptotic osteocytes,[119] we next tested the skeletal effects of short-term systemic administration of the small-molecule RAGE inhibitor, Azeliragon (AZ). Overall, our findings from this study showed that AZ did not prevent the aging-induced alterations in bone geometry or mechanics, likely due to its differential effects [direct vs. indirect] on bone cell viability/function, as illustrated in Fig. 7-4. Particularly, we found that AZ had differential effects on osteoclast differentiation and activity, which may have been due to the increases in cell death and inflammatory cytokine production in osteocytes we detected with AZ treatment both *in vitro* and *in vivo*. Hence, in addition to the direct inhibitory effects of AZ treatment on osteoclasts, the effects of RAGE inhibition in osteocytes may have indirectly stimulated bone resorption.

Thus, given the cell type specific effects of AZ, future studies will be designed to examine whether administering a different dose or altering the treatment regimen [intermittent vs chronic], previously seen with other therapeutics, could optimize the beneficial effects of AZ on bone. However, since these pro-apoptotic effects of RAGE inhibition in osteocytes are consistent with previous studies in other cell types showing the HMGB1-RAGE signaling promotes autophagy and protects against apoptosis,[238-240] it is also possible that an osteoclast targeted-RAGE inhibitor may be needed to obtain beneficial skeletal effects with aging. Additionally, given the previous findings showing that HMGB1-TLR4 signaling induces apoptosis and stimulates inflammatory responses,[241, 242] it is possible that treatment with the TLR4 inhibitor, Lps-Rs,[243] rather than the RAGE inhibitor, AZ, may be more successful at attenuating the negative skeletal effects in aging mice. Thus, in order to better understand the skeletal effects of HMGB1 signaling in aging, future studies using the TLR4 inhibitor, Lps-Rs,[243] in aged mice could also be performed.

Interestingly, despite the lack of effect of AZ in bone, our findings suggest that short-term pharmacologic RAGE inhibition has distinct effects on skeletal muscle. In particular, our data validate the role of RAGE signaling in promoting musculoskeletal derangements associated with aging, thus making it an interesting therapeutic target. Altogether, our findings strongly support that idea that AZ may represent a novel therapeutic option for the treatment of aging-induced sarcopenia, which will be further tested in future studies.

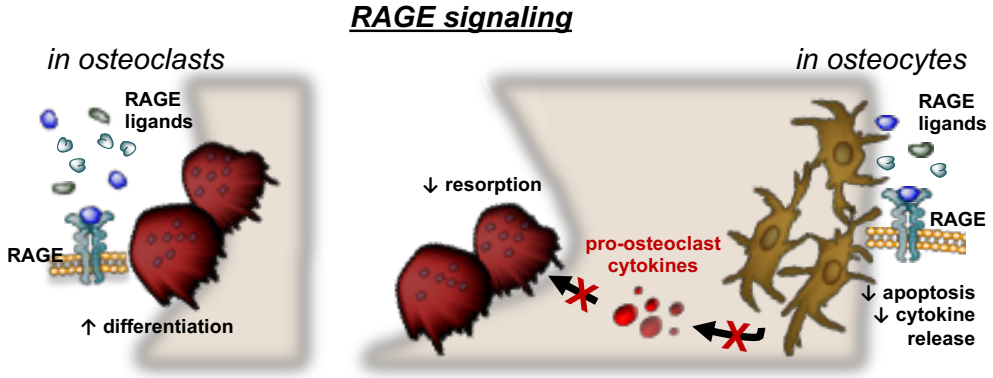

Figure 7-4. Model of the proposed effects of RAGE signaling in osteocytes and osteoclasts.

We also tested whether RAGE signaling in osteoclasts mediates the stimulatory effects of apoptotic osteocyte conditioned media on osteoclastogenesis. However, consistent with the *in vivo* effects of AZ treatment on osteoclasts, while osteoclastogenesis was decreased with RAGE deficiency, neither genetic nor pharmacological RAGE inhibition blocked the apoptotic osteocyte-induced increases in osteoclastogenesis. Taken together these pieces of evidence suggest that apoptotic osteocytes do not increase osteoclastogenesis by directly activating RAGE signaling in osteoclasts**.** Conversely, our data suggest that, HMGB1 signaling in osteocytes stimulates pro-inflammatory cytokine release, which subsequently induces osteoclastogenesis. Thus, direct actions of HMGB1 signaling in osteoclasts and osteocytes, rather than indirect effects of apoptotic osteocyte-

derived extracellular HMGB1 appear to underlie the stimulatory effects of apoptotic osteocytes on osteoclasts (Fig. 7-5). Additionally, given our findings that RAGE inhibition with AZ treatment stimulated osteocyte cell death and inflammatory cytokine production, and the previous studies showing that HMGB1-RAGE signaling is anti-apoptotic while HMGB1-TLR4 signaling is pro-apoptotic,[238, 241, 242, 244] one could speculate that HMGB1 signaling through TLR4 rather than RAGE mediates these effects in osteocytes. Thus, future studies will be carried out in order to elucidate the specific effects of HMGB1 signaling in osteocytes and clearly identify the receptor responsible for these effects.

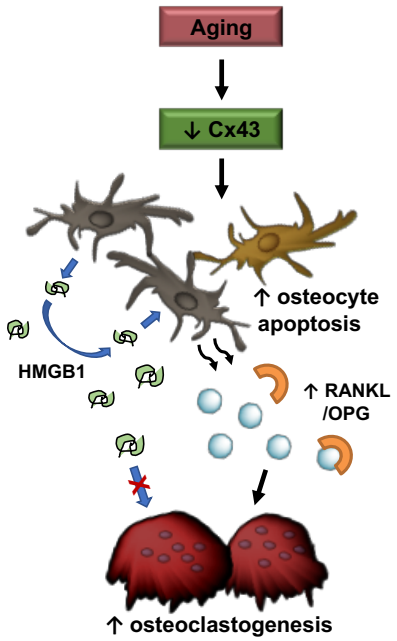

Figure 7-5. Autocrine actions of HMGB1 signaling in osteocytes, rather than paracrine effects of apoptotic osteocyte-derived extracellular HMGB1 signaling in osteoclasts appear to underlie the stimulatory effects of apoptotic osteocytes on osteoclasts.

In summary, the findings from this current series of studies using a combination of several *in vitro* and *in vivo* models, summarized in Fig. 7-6, further highlight the critical role osteocytes play in the maintenance of cortical bone structure and mechanical properties

in aging. We demonstrated the requirement of Cx43-mediated actions in osteocytes for the preservation of osteocyte viability and cortical bone quality in aging. Additionally, our findings support a model where reduced Cx43 levels in osteocytes in old animals leads to apoptosis and the release of RANKL and HMGB1, which signal osteoclasts to increase resorption along associated bone surfaces. However, our findings also suggest that HMGB1 exerts dual effects on osteoclasts, directly by inducing differentiation through TLR4 and RAGE activation and indirectly by increasing pro-osteoclastogenic cytokine secretion from osteocytes. Interestingly, our findings also provide evidence that the miR21 locus in osteocytes exerts sex-dependent and -independent skeletal effects. Thus, while these studies answered many important questions, they also uncovered several key questions that need to be further investigated in future studies. Overall, these pieces of evidence provide a foundation for a variety of future studies to further examine the effects of preventing osteocyte viability and/or blocking apoptotic osteocyte-derived signaling molecules to prevent bone fragility in aging.

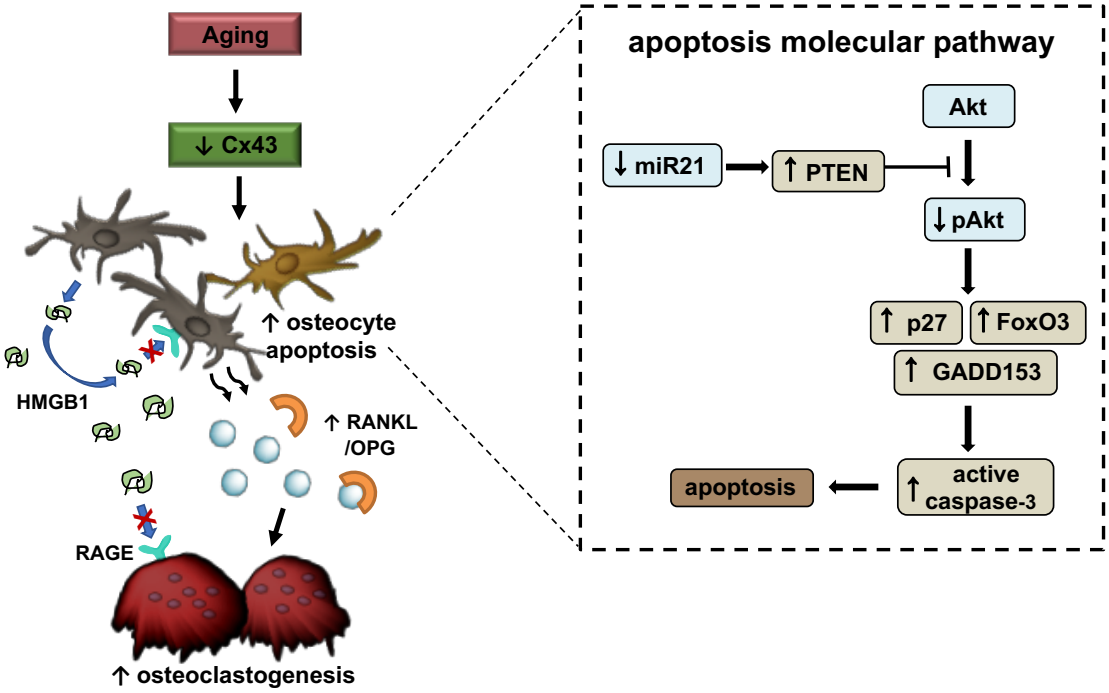

Figure 7-6. Working model summarizing the findings of the current series of studies.

Bibliography

1. Khosla, S., Farr, J.N. & Kirkland, J.L. Inhibiting Cellular Senescence: A New Therapeutic Paradigm for Age-Related Osteoporosis. *J Clin Endocrinol Metab* **103**, 1282-1290 (2018).
2. Rodier, F., Zhou, D. & Ferbeyre, G. Cellular senescence, geroscience, cancer and beyond. *Aging (Albany NY)* **10**, 2233-2242 (2018).
3. Franceschi, C. *et al.* The Continuum of Aging and Age-Related Diseases: Common Mechanisms but Different Rates. *Front Med (Lausanne)* **5**, 61 (2018).
4. Fischer, S. *et al.* Estimating the long-term functional burden of osteoporosis-related fractures. *Osteoporos Int* **28**, 2843-2851 (2017).
5. Abrahamsen, B., van Staa, T., Ariely, R., Olson, M. & Cooper, C. Excess mortality following hip fracture: a systematic epidemiological review. *Osteoporos Int* **20**, 1633-1650 (2009).
6. Shuler, F.D., Conjeski, J., Kendall, D. & Salava, J. Understanding the burden of osteoporosis and use of the World Health Organization FRAX. *Orthopedics* **35**, 798-805 (2012).
7. Jilka, R.L. & O'Brien, C.A. The Role of Osteocytes in Age-Related Bone Loss. *Curr. Osteoporos. Rep* **14**, 16-25 (2016).
8. Almeida, M. *et al.* Skeletal involution by age-associated oxidative stress and its acceleration by loss of sex steroids. *J. Biol. Chem* **282**, 27285-27297 (2007).
9. Almeida, M. Aging mechanisms in bone. *Bonekey. Rep* **1** (2012).
10. Zebaze, R.M. *et al.* Intracortical remodelling and porosity in the distal radius and post-mortem femurs of women: a cross-sectional study. *Lancet* **375**, 1729-1736 (2010).
11. Parfitt, A.M. Age-related structural changes in trabecular and cortical bone: cellular mechanisms and biomechanical consequences. *Calcif Tissue Int* **36 Suppl 1**, S123-128 (1984).
12. Riggs, B.L. *et al.* A population-based assessment of rates of bone loss at multiple skeletal sites: evidence for substantial trabecular bone loss in young adult women and men. *J Bone Miner Res* **23**, 205-214 (2008).
13. Syed, F.A. *et al.* Effects of chronic estrogen treatment on modulating age-related bone loss in female mice. *J. Bone Miner. Res* **25**, 2438-2446 (2010).
14. Halloran, B.P. *et al.* Changes in bone structure and mass with advancing age in the male C57BL/6J mouse. *J Bone Miner. Res* **17**, 1044-1050 (2002).
15. Iida, H. & Fukuda, S. Age-related changes in bone mineral density, cross-sectional area and strength at different skeletal sites in male rats. *J Vet Med Sci* **64**, 29-34 (2002).
16. Silbermann, M. *et al.* Age-related trend for osteopenia in femurs of female C57BL/6 mice. *Compr Gerontol A* **1**, 45-51 (1987).
17. Ferguson, V.L., Ayers, R.A., Bateman, T.A. & Simske, S.J. Bone development and age-related bone loss in male C57BL/6J mice. *Bone* **33**, 387-398 (2003).
18. Shahnazari, M. *et al.* Bone turnover markers in peripheral blood and marrow plasma reflect trabecular bone loss but not endocortical expansion in aging mice. *Bone* **50**, 628-637 (2012).
19. Langdahl, B., Ferrari, S. & Dempster, D.W. Bone modeling and remodeling: potential as therapeutic targets for the treatment of osteoporosis. *Ther Adv Musculoskelet Dis* **8**, 225-235 (2016).
20. Okman-Kilic, T. Estrogen Deficiency and Osteoporosis. *Advances in Osteoporosis* (2015).

21. Chen, H., Zhou, X., Fujita, H., Onozuka, M. & Kubo, K.Y. Age-related changes in trabecular and cortical bone microstructure. *Int. J. Endocrinol* **2013**, 213234 (2013).
22. Zimmermann, E.A. *et al.* Age-related changes in the plasticity and toughness of human cortical bone at multiple length scales. *Proc. Natl. Acad. Sci. U. S. A* **108**, 14416-14421 (2011).
23. Jilka, R.L., Noble, B. & Weinstein, R.S. Osteocyte apoptosis. *Bone* **54**, 264-271 (2012).
24. Plotkin, L.I. Apoptotic osteocytes and the control of targeted bone resorption. *Curr. Osteoporos. Rep* **12**, 121-126 (2014).
25. Kassem, M. & Marie, P.J. Senescence-associated intrinsic mechanisms of osteoblast dysfunctions. *Aging Cell* **10**, 191-197 (2011).
26. Aguirre, J.I. *et al.* Osteocyte apoptosis is induced by weightlessness in mice and precedes osteoclast recruitment and bone loss. *J. Bone Min. Res* **21**, 605-615 (2006).
27. Cardoso, L. *et al.* Osteocyte apoptosis controls activation of intracortical resorption in response to bone fatigue. *J. Bone Miner. Res* **24**, 597-605 (2009).
28. Emerton, K.B. *et al.* Osteocyte apoptosis and control of bone resorption following ovariectomy in mice. *Bone* **46**, 577-583 (2009).
29. Tatsumi, S. *et al.* Targeted ablation of osteocytes induces osteoporosis with defective mechanotransduction. *Cell Metab* **5**, 464-475 (2007).
30. Bonewald, L.F. The Amazing Osteocyte. *J. Bone Miner. Res* **26**, 229-238 (2011).
31. Dallas, S.L., Prideaux, M. & Bonewald, L.F. The osteocyte: an endocrine cell ... and more. *Endocr. Rev* **34**, 658-690 (2013).
32. Kousteni, S. *et al.* Nongenotropic, sex-nonspecific signaling through the estrogen or androgen receptors: dissociation from transcriptional activity. *Cell* **104**, 719-730 (2001).
33. Tomkinson, A., Reeve, J., Shaw, R.W. & Noble, B.S. The death of osteocytes via apoptosis accompanies estrogen withdrawal in human bone. *J. Clin. Endocrinol. Metab* **82**, 3128-3135 (1997).
34. Weinstein, R.S., Jilka, R.L., Parfitt, A.M. & Manolagas, S.C. Inhibition of osteoblastogenesis and promotion of apoptosis of osteoblasts and osteocytes by glucocorticoids: potential mechanisms of their deleterious effects on bone. *J. Clin. Invest* **102**, 274-282 (1998).
35. Civitelli, R. *et al.* Connexin43 mediates direct intercellular communication in human osteoblastic cell networks. *J. Clin. Invest* **91**, 1888-1896 (1993).
36. Kato, Y., Windle, J.J., Koop, B.A., Mundy, G.R. & Bonewald, L.F. Establishment of an osteocyte-like cell line, MLO-Y4. *J. Bone Miner. Res* **12**, 2014-2023 (1997).
37. Plotkin, L.I. & Bellido, T. Beyond gap junctions: Connexin43 and bone cell signaling. *Bone* **52**, 157-166 (2013).
38. Bivi, N. *et al.* Deletion of Cx43 from osteocytes results in defective bone material properties but does not decrease extrinsic strength in cortical bone. *Calcif. Tissue Int* **91**, 215-224 (2012).
39. Lloyd, S.A., Loiselle, A.E., Zhang, Y. & Donahue, H.J. Connexin 43 deficiency desensitizes bone to the effects of mechanical unloading through modulation of both arms of bone remodeling. *Bone* **57**, 76-83 (2013).
40. Plotkin, L.I. *et al.* Connexin 43 is required for the anti-apoptotic effect of bisphosphonates on osteocytes and osteoblasts in vivo. *J. Bone Miner. Res* **23**, 1712-1721 (2008).
41. Burr, D.B. & Allen, M.R. *Basic and Applied Bone Biology*, Edn. 1. (Elsevier, 2013).

42. Jilka, R.L. *et al.* Increased bone formation by prevention of osteoblast apoptosis with parathyroid hormone. *J. Clin. Invest* **104**, 439-446 (1999).
43. Plotkin, L.I. *et al.* Prevention of osteocyte and osteoblast apoptosis by bisphosphonates and calcitonin. *J. Clin. Invest* **104**, 1363-1374 (1999).
44. Tiede-Lewis, L.M. *et al.* Degeneration of the osteocyte network in the C57BL/6 mouse model of aging. *Aging (Albany. NY)* (2017).
45. Qiu, S., Rao, D.S., Palnitkar, S. & Parfitt, A.M. Age and distance from the surface but not menopause reduce osteocyte density in human cancellous bone. *Bone* **31**, 313-318 (2002).
46. Bivi, N. *et al.* Cell autonomous requirement of connexin 43 for osteocyte survival: consequences for endocortical resorption and periosteal bone formation. *J. Bone Min. Res* **27**, 374-389 (2012).
47. Bivi, N. *et al.* Cx43 in osteocytes, but not in osteoblasts, is required to preserve osteocyte viability, bone geometry and material stiffness. *J. Bone Miner. Res* **25**, S112 (2010).
48. Buo, A.M., Tomlinson, R.E., Eidelman, E.R., Chason, M. & Stains, J.P. Connexin43 and Runx2 Interact to Affect Cortical Bone Geometry, Skeletal Development, and Osteoblast and Osteoclast Function. *J. Bone Miner. Res* **32**, 1727-1738 (2017).
49. Pacheco-Costa, R. *et al.* Defective cancellous bone structure and abnormal response to PTH in cortical bone of mice lacking Cx43 cytoplasmic C-terminus domain. *Bone* **81**, 632-643 (2015).
50. Yang, J. *et al.* HMGB1 is a bone-active cytokine. *J. Cell Physiol* **214**, 730-739 (2008).
51. Charoonpatrapong, K. *et al.* HMGB1 expression and release by bone cells. *J Cell Physiol* **207**, 480-490 (2006).
52. Scaffidi, P., Misteli, T. & Bianchi, M.E. Release of chromatin protein HMGB1 by necrotic cells triggers inflammation. *Nature* **418**, 191-195 (2002).
53. Taniguchi, N. *et al.* Stage-specific secretion of HMGB1 in cartilage regulates endochondral ossification. *Mol. Cell Biol* **27**, 5650-5663 (2007).
54. Zhou, Z. *et al.* HMGB1 regulates RANKL-induced osteoclastogenesis in a manner dependent on RAGE. *J. Bone Miner. Res* **23**, 1084-1096 (2008).
55. Yang, H., Antoine, D.J., Andersson, U. & Tracey, K.J. The many faces of HMGB1: molecular structure-functional activity in inflammation, apoptosis, and chemotaxis. *J. Leukoc. Biol* **93**, 865-873 (2013).
56. Milovanovic, P. *et al.* Osteocytic Canalicular Networks: Morphological Implications for Altered Mechanosensitivity. *ACS Nano* (2013).
57. Fyhrie, D.P. & Christiansen, B.A. Bone Material Properties and Skeletal Fragility. *Calcif. Tissue Int* **97**, 213-228 (2015).
58. Peng, S. *et al.* MicroRNAs regulate signaling pathways in osteogenic differentiation of mesenchymal stem cells (Review). *Mol. Med. Rep* (2016).
59. Garzon, R., Calin, G.A. & Croce, C.M. MicroRNAs in Cancer. *Annu. Rev. Med* **60**, 167-179 (2009).
60. He, X., Eberhart, J.K. & Postlethwait, J.H. MicroRNAs and micromanaging the skeleton in disease, development and evolution. *J. Cell Mol. Med* **13**, 606-618 (2009).
61. Tu, K.N. *et al.* Osteoporosis: A Review of Treatment Options. *P T* **43**, 92-104 (2018).
62. Migliaccio, S., Brama, M. & Spera, G. The differential effects of bisphosphonates, SERMS (selective estrogen receptor modulators), and parathyroid hormone on bone remodeling in osteoporosis. *Clin Interv Aging* **2**, 55-64 (2007).

63. Drieling, R.L. *et al.* Long-Term Oral Bisphosphonate Therapy and Fractures in Older Women: The Women's Health Initiative. *J Am Geriatr Soc* **65**, 1924-1931 (2017).
64. Smith, E.R. & Allen, M.R. Bisphosphonate-induced reductions in rat femoral bone energy absorption and toughness are testing rate-dependent. *J Orthop Res* **31**, 1317-1322 (2013).
65. Lloyd, A.A. *et al.* Atypical fracture with long-term bisphosphonate therapy is associated with altered cortical composition and reduced fracture resistance. *Proc Natl Acad Sci U S A* **114**, 8722-8727 (2017).
66. Ma, S. *et al.* Long-term effects of bisphosphonate therapy: perforations, microcracks and mechanical properties. *Sci Rep* **7**, 43399 (2017).
67. Yue, B., Ng, A., Tang, H., Joseph, S. & Richardson, M. Delayed healing of lower limb fractures with bisphosphonate therapy. *Ann R Coll Surg Engl* **97**, 333-338 (2015).
68. Isaacs, J.D., Shidiak, L., Harris, I.A. & Szomor, Z.L. Femoral insufficiency fractures associated with prolonged bisphosphonate therapy. *Clin Orthop Relat Res* **468**, 3384-3392 (2010).
69. Coe, L.M., Tekalur, S.A., Shu, Y., Baumann, M.J. & McCabe, L.R. Bisphosphonate treatment of type I diabetic mice prevents early bone loss but accentuates suppression of bone formation. *J Cell Physiol* **230**, 1944-1953 (2015).
70. Tang, S.Y., Allen, M.R., Phipps, R., Burr, D.B. & Vashishth, D. Changes in non-enzymatic glycation and its association with altered mechanical properties following 1-year treatment with risedronate or alendronate. *Osteoporos Int* **20**, 887-894 (2009).
71. Follet, H. *et al.* Risedronate and alendronate suppress osteocyte apoptosis following cyclic fatigue loading. *Bone* **40**, 1172-1177 (2007).
72. Kogianni, G. *et al.* Fas/CD95 is associated with glucocorticoid-induced osteocyte apoptosis. *Life Sci* **75**, 2879-2895 (2004).
73. Plotkin, L.I., Manolagas, S.C. & Bellido, T. Dissociation of the pro-apoptotic effects of bisphosphonates on osteoclasts from their anti-apoptotic effects on osteoblasts/osteocytes with novel analogs. *Bone* **39**, 443-452 (2006).
74. Plotkin, L.I., Bivi, N. & Bellido, T. A bisphosphonate that does not affect osteoclasts prevents osteoblast and osteocyte apoptosis and the loss of bone strength induced by glucocorticoids in mice. *Bone* **49**, 122-127 (2011).
75. Plotkin, L.I. & Bellido, T. Osteocytic signalling pathways as therapeutic targets for bone fragility. *Nat. Rev. Endocrinol* **12**, 593-605 (2016).
76. Kalajzic, I. *et al.* Dentin matrix protein 1 expression during osteoblastic differentiation, generation of an osteocyte GFP-transgene. *Bone* **35**, 74-82 (2004).
77. Tong, D., Li, T.Y., Naus, K.E., Bai, D. & Kidder, G.M. In vivo analysis of undocked connexin43 gap junction hemichannels in ovarian granulosa cells. *J. Cell Sci* **120**, 4016-4024 (2007).
78. Bivi, N. *et al.* Absence of Cx43 selectively from osteocytes enhances responsiveness to mechanical force in mice. *J. Orthop. Res* **31**, 1075-1081 (2013).
79. Dutta, S. & Sengupta, P. Men and mice: Relating their ages. *Life Sci* **152**, 244-248 (2016).
80. Tu, X. *et al.* Osteocytes mediate the anabolic actions of canonical Wnt/b-catenin signaling in bone. *Proc. Natl. Acad. Sci U. S. A* **112**, E478-E486 (2015).
81. O'Brien, C.A. *et al.* Control of bone mass and remodeling by PTH receptor signaling in osteocytes. *PLoS ONE* **3**, e2942 (2008).

82. Bellido, T. *et al.* Chronic elevation of PTH in mice reduces expression of sclerostin by osteocytes: a novel mechanism for hormonal control of osteoblastogenesis. *Endocrinology* **146**, 4577-4583 (2005).
83. Pacheco-Costa, R. *et al.* High Bone Mass in Mice Lacking Cx37 Due to Defective Osteoclast Differentiation. *J. Biol. Chem* **289**, 8508-8520 (2014).
84. Bouxsein, M.L. *et al.* Guidelines for assessment of bone microstructure in rodents using micro-computed tomography. *J. Bone Miner. Res* **25**, 1468-1486 (2010).
85. Dempster, D.W. *et al.* Standardized nomenclature, symbols, and units for bone histomorphometry: A 2012 update of the report of the ASBMR Histomorphometry Nomenclature Committee. *J. Bone Miner. Res* **28**, 2-17 (2013).
86. Allen, M.R., Reinwald, S. & Burr, D.B. Alendronate reduces bone toughness of ribs without significantly increasing microdamage accumulation in dogs following 3 years of daily treatment. *Calcif. Tissue Int* **82**, 354-360 (2008).
87. Sato, A.Y. *et al.* Protection from glucocorticoid-induced osteoporosis by anti-catabolic signaling in the absence of Sost/sclerostin. *J. Bone Miner. Res* **31**, 1791-1802 (2016).
88. Weinstein, R.S. & Manolagas, S.C. Apoptosis and osteoporosis. *Am. J. Med* **108**, 153-164 (2000).
89. Nakashima, T. *et al.* Evidence for osteocyte regulation of bone homeostasis through RANKL expression. *Nat. Med* **17**, 1231-1234 (2011).
90. Davis, H.M. *et al.* Cx43 overexpression in osteocytes prevents osteocyte apoptosis and preserves cortical bone quality in aging mice. *JBMR Plus* **4**, 206-216 (2018).
91. Kar, R., Riquelme, M.A., Werner, S. & Jiang, J.X. Connexin 43 channels protect osteocytes against oxidative stress-induced cell death. *J. Bone Miner. Res* **28**, 1611-1621 (2013).
92. Bivi, N., Lezcano, V., Romanello, M., Bellido, T. & Plotkin, L.I. Connexin43 interacts with barrestin: a pre-requisite for osteoblast survival induced by parathyroid hormone. *J. Cell. Biochem* **112**, 2920-2930 (2011).
93. Lecanda, F. *et al.* Gap junctional communication modulates gene expression in osteoblastic cells. *Mol. Biol. Cell* **9**, 2249-2258 (1998).
94. Zhou, L., Kasperek, E.M. & Nicholson, B.J. Dissection of the molecular basis of pp60(v-src) induced gating of connexin 43 gap junction channels. *J. Cell Biol* **144**, 1033-1045 (1999).
95. Krutovskikh, V.A., Yamasaki, H., Tsuda, H. & Asamoto, M. Inhibition of intrinsic gap-junction intercellular communication and enhancement of tumorigenicity of the rat bladder carcinoma cell line BC31 by a dominant-negative connexin 43 mutant. *Mol. Carcinog* **23**, 254-261 (1998).
96. Plotkin, L.I., Manolagas, S.C. & Bellido, T. Transduction of cell survival signals by connexin-43 hemichannels. *J. Biol. Chem* **277**, 8648-8657 (2002).
97. Miyazaki, T., Neff, L., Tanaka, S., Horne, W.C. & Baron, R. Regulation of cytochrome c oxidase activity by c-Src in osteoclasts. *J. Cell Biol* **160**, 709-718 (2003).
98. Zhang, Q.Y., Wu, L.Q., Zhang, T., Han, Y.F. & Lin, X. Autophagy-mediated HMGB1 release promotes gastric cancer cell survival via RAGE activation of extracellular signal-regulated kinases 1/2. *Oncol Rep* **33**, 1630-1638 (2015).
99. Zhang, X., Tang, N., Hadden, T.J. & Rishi, A.K. Akt, FoxO and regulation of apoptosis. *Biochim. Biophys. Acta* **1813**, 1978-1986 (2011).
100. Hoshi, T., Zagotta, W.N. & Aldrich, R.W. Biophysical and molecular mechanisms of Shaker potassium channel inactivation. *Science* **250**, 533-538 (1990).
101. Dahl, G., Levine, E., Rabadan-Diehl, C. & Werner, R. Cell/cell channel formation involves disulfide exchange. *Eur. J Biochem* **197**, 141-144 (1991).

102. Bao, X., Chen, Y., Reuss, L. & Altenberg, G.A. Functional expression in xenopus oocytes of gap-junctional hemichannels formed by a cysteine-less connexin 43. *J. Biol. Chem* **279**, 9689-9692 (2004).
103. Plotkin, L.I., Manolagas, S.C. & Bellido, T. Glucocorticoids induce osteocyte apoptosis by blocking focal adhesion kinase-mediated survival: evidence for inside-out signaling leading to anoikis. *J. Biol. Chem* **282**, 24120-24130 (2007).
104. Almeida, M., Han, L., Martin-Millan, M., O'Brien, C.A. & Manolagas, S.C. Oxidative stress antagonizes Wnt signaling in osteoblast precursors by diverting beta-catenin from T cell factor- to forkhead box O-mediated transcription. *J. Biol. Chem* **282**, 27298-27305 (2007).
105. Cao, J., Venton, L., Sakata, T. & Halloran, B.P. Expression of RANKL and OPG correlates with age-related bone loss in male C57BL/6 mice. *J Bone Miner. Res* **18**, 270-277 (2003).
106. Fonken, L.K. *et al.* The Alarmin HMGB1 Mediates Age-Induced Neuroinflammatory Priming. *J. Neurosci* **36**, 7946-7956 (2016).
107. Terrando, N. *et al.* Systemic HMGB1 Neutralization Prevents Postoperative Neurocognitive Dysfunction in Aged Rats. *Front Immunol* **7**, 441 (2016).
108. Mollica, L. *et al.* Glycyrrhizin binds to high-mobility group box 1 protein and inhibits its cytokine activities. *Chem. Biol* **14**, 431-441 (2007).
109. Yang, H. *et al.* Reversing established sepsis with antagonists of endogenous high-mobility group box 1. *Proc. Natl. Acad. Sci. U. S. A* **101**, 296-301 (2004).
110. Genetos, D.C., Zhou, Z., Li, Z. & Donahue, H.J. Age-related changes in gap junctional intercellular communication in osteoblastic cells. *J. Orthop. Res* **30**, 1979-1984 (2012).
111. Kozomara, A. & Griffiths-Jones, S. miRBase: annotating high confidence microRNAs using deep sequencing data. *Nucleic Acids Res* **42**, D68-D73 (2014).
112. Pitari, M.R. *et al.* Inhibition of miR-21 restores RANKL/OPG ratio in multiple myeloma-derived bone marrow stromal cells and impairs the resorbing activity of mature osteoclasts. *Oncotarget* **6**, 27343-27358 (2015).
113. Cao, J.J. *et al.* Aging impairs IGF-I receptor activation and induces skeletal resistance to IGF-I. *J. Bone Miner. Res* **22**, 1271-1279 (2007).
114. Ma, X., Becker Buscaglia, L.E., Barker, J.R. & Li, Y. MicroRNAs in NF-kappaB signaling. *J. Mol. Cell Biol* **3**, 159-166 (2011).
115. Grey, A., Chen, Q., Xu, X., Callon, K. & Cornish, J. Parallel phosphatidylinositol-3 kinase and p42/44 mitogen-activated protein kinase signaling pathways subserve the mitogenic and antiapoptotic actions of insulin-like growth factor I in osteoblastic cells. *Endocrinology* **144**, 4886-4893 (2003).
116. Hill, P.A., Tumber, A. & Meikle, M.C. Multiple extracellular signals promote osteoblast survival and apoptosis. *Endocrinology* **138**, 3849-3858 (1997).
117. Lu, G., Haider, H.K., Jiang, S. & Ashraf, M. Sca-1+ stem cell survival and engraftment in the infarcted heart: dual role for preconditioning-induced connexin-43. *Circulation* **119**, 2587-2596 (2009).
118. Klune, J.R., Dhupar, R., Cardinal, J., Billiar, T.R. & Tsung, A. HMGB1: endogenous danger signaling. *Mol. Med* **14**, 476-484 (2008).
119. Davis, H.M. *et al.* Disruption of the Cx43/miR21 pathway leads to osteocyte apoptosis and increased osteoclastogenesis with aging. *Aging Cell* **16**, 551-563 (2017).
120. Smith-Vikos, T. & Slack, F.J. MicroRNAs and their roles in aging. *J. Cell Sci* **125**, 7-17 (2012).

121. Taipaleenmaki, H., Bjerre, L., Chen, L., Kauppinen, S. & Kassem, M. MicroRNAs: Targets for enhancing osteoblast differentiation and bone formation. *Eur. J. Endocrinol* (2011).
122. Tu, X. *et al.* Noncanonical Wnt signaling through G protein-linked PKCdelta activation promotes bone formation. *Dev. Cell* **12**, 113-127 (2007).
123. Francis, H. *et al.* Regulation of the extrinsic apoptotic pathway by microRNA-21 in alcoholic liver injury. *J. Biol. Chem* (2014).
124. Sugatani, T. & Hruska, K.A. Down-regulation of miR-21 biogenesis by estrogen action contributes to osteoclastic apoptosis. *J. Cell Biochem* **114**, 1217-1222 (2013).
125. Ma, X. *et al.* The oncogenic microRNA miR-21 promotes regulated necrosis in mice. *Nat Commun* **6**, 7151 (2015).
126. Li, H. *et al.* MicroRNA-21 Lowers Blood Pressure in Spontaneous Hypertensive Rats by Upregulating Mitochondrial Translation. *Circulation* **134**, 734-751 (2016).
127. Lam, H.C. *et al.* Rapamycin-induced miR-21 promotes mitochondrial homeostasis and adaptation in mTORC1 activated cells. *Oncotarget* **8**, 64714-64727 (2017).
128. Go, H. *et al.* MicroRNA-21 plays an oncogenic role by targeting FOXO1 and activating the PI3K/AKT pathway in diffuse large B-cell lymphoma. *Oncotarget* **6**, 15035-15049 (2015).
129. Gomez, I.G. *et al.* Anti-microRNA-21 oligonucleotides prevent Alport nephropathy progression by stimulating metabolic pathways. *J. Clin. Invest* **125**, 141-156 (2015).
130. Chau, B.N. *et al.* MicroRNA-21 Promotes Fibrosis of the Kidney by Silencing Metabolic Pathways. *Sci. Transl. Med* **4**, 121ra118 (2012).
131. Hu, C.H. *et al.* miR-21 deficiency inhibits osteoclast function and prevents bone loss in mice. *Sci. Rep* **7**, 43191 (2017).
132. Li, H., Yang, F., Wang, Z., Fu, Q. & Liang, A. MicroRNA-21 promotes osteogenic differentiation by targeting small mothers against decapentaplegic 7. *Mol Med Rep* **12**, 1561-1567 (2015).
133. Liu, L.Z. *et al.* MiR-21 induced angiogenesis through AKT and ERK activation and HIF-1alpha expression. *PLoS One* **6**, e19139 (2011).
134. Ma, X. *et al.* Loss of the miR-21 allele elevates the expression of its target genes and reduces tumorigenesis. *Proc. Natl. Acad. Sci. U. S. A* **108**, 10144-10149 (2011).
135. Merline, R. *et al.* Signaling by the Matrix Proteoglycan Decorin Controls Inflammation and Cancer Through PDCD4 and MicroRNA-21. *Sci. Signal* **4**, ra75 (2011).
136. Cho, Y.C., Kim, Y.R., Kim, B.R., Bach, T.T. & Cho, S. Thunbergia alata inhibits inflammatory responses through the inactivation of ERK and STAT3 in macrophages. *Int J Mol Med* **38**, 1596-1604 (2016).
137. Wu, X. *et al.* IL-17 promotes tumor angiogenesis through Stat3 pathway mediated upregulation of VEGF in gastric cancer. *Tumour Biol* **37**, 5493-5501 (2016).
138. Hong, F.Y., Bao, J.F., Hao, J., Yu, Q. & Liu, J. Methylglyoxal and advanced glycation end-products promote cytokines expression in peritoneal mesothelial cells via MAPK signaling. *Am J Med Sci* **349**, 105-109 (2015).
139. Chen, H. *et al.* Advanced glycation end products induced IL-6 and VEGF-A production and apoptosis in osteocyte-like MLO-Y4 cells by activating RAGE and ERK1/2, P38 and STAT3 signalling pathways. *Int Immunopharmacol* **52**, 143-149 (2017).

140. Zhichao Hao, Y.M., Jun Wu, Xianxian Li, Helin Chen, Jiefei Shen and Hang Wang Osteocytes regulate osteoblast differentiation and osteoclast activity through Interleukin-6 under mechanical loading. *RSC Advances* **7**, 50200–50209 (2017).
141. Wegrzyn, J. *et al.* Function of mitochondrial Stat3 in cellular respiration. *Science* **323**, 793-797 (2009).
142. Rodrigues, P.M. *et al.* miR-21 ablation and obeticholic acid ameliorate nonalcoholic steatohepatitis in mice. *Cell Death. Dis* **8**, e2825 (2017).
143. Jia, Z. *et al.* Ischemic Postconditioning Protects Against Intestinal Ischemia/Reperfusion Injury via the HIF-1alpha/miR-21 Axis. *Sci. Rep* **7**, 16190 (2017).
144. Queiros, A.M. *et al.* Sex- and estrogen-dependent regulation of a miRNA network in the healthy and hypertrophied heart. *Int J Cardiol* **169**, 331-338 (2013).
145. Rademaker, M. Do women have more adverse drug reactions? *Am. J. Clin. Dermatol* **2**, 349-351 (2001).
146. Zhang, X. *et al.* Activation of JNK signaling in osteoblasts is inversely correlated with collagen synthesis in age-related osteoporosis. *Biochem Biophys Res Commun* **504**, 771-776 (2018).
147. Seeliger, C. *et al.* Five Freely Circulating miRNAs and Bone Tissue miRNAs Are Associated With Osteoporotic Fractures. *J. Bone Miner. Res* **29**, 1718-1728 (2014).
148. Seals, D.R., Justice, J.N. & LaRocca, T.J. Physiological geroscience: targeting function to increase healthspan and achieve optimal longevity. *J Physiol* **594**, 2001-2024 (2016).
149. Howcroft, T.K. *et al.* The role of inflammation in age-related disease. *Aging (Albany NY)* **5**, 84-93 (2013).
150. Gerakis, Y. & Hetz, C. A decay of the adaptive capacity of the unfolded protein response exacerbates Alzheimer's disease. *Neurobiol Aging* **63**, 162-164 (2018).
151. Sousa, A.S. *et al.* Financial impact of sarcopenia on hospitalization costs. *Eur J Clin Nutr* **70**, 1046-1051 (2016).
152. Tournadre, A., Vial, G., Capel, F., Soubrier, M. & Boirie, Y. Sarcopenia. *Joint Bone Spine* (2018).
153. Karsenty, G. & Mera, P. Molecular bases of the crosstalk between bone and muscle. *Bone* **115**, 43-49 (2018).
154. Collins, K.H. *et al.* Obesity, Metabolic Syndrome, and Musculoskeletal Disease: Common Inflammatory Pathways Suggest a Central Role for Loss of Muscle Integrity. *Front Physiol* **9**, 112 (2018).
155. Reginster, J.Y., Beaudart, C., Buckinx, F. & Bruyere, O. Osteoporosis and sarcopenia: two diseases or one? *Curr Opin Clin Nutr Metab Care* **19**, 31-36 (2016).
156. Agostini, D. *et al.* Muscle and Bone Health in Postmenopausal Women: Role of Protein and Vitamin D Supplementation Combined with Exercise Training. *Nutrients* **10** (2018).
157. Amarasekara, D.S., Yu, J. & Rho, J. Bone Loss Triggered by the Cytokine Network in Inflammatory Autoimmune Diseases. *J Immunol Res* **2015**, 832127 (2015).
158. Ramasamy, R., Shekhtman, A. & Schmidt, A.M. The multiple faces of RAGE--opportunities for therapeutic intervention in aging and chronic disease. *Expert Opin Ther Targets* **20**, 431-446 (2016).
159. Heneka, M.T. *et al.* Neuroinflammation in Alzheimer's disease. *Lancet Neurol* **14**, 388-405 (2015).
160. Bidwell, J.P., Yang, J. & Robling, A.G. Is HMGB1 an osteocyte alarmin? *J. Cell Biochem* **103**, 1671-1680 (2008).

161. Karsenty, G. & Mera, P. Molecular bases of the crosstalk between bone and muscle. *Bone* (2017).
162. Fougere, B., Boulanger, E., Nourhashemi, F., Guyonnet, S. & Cesari, M. Chronic Inflammation: Accelerator of Biological Aging. *J Gerontol A Biol Sci Med Sci* **72**, 1218-1225 (2017).
163. Picca, A. *et al.* Bone-Muscle Crosstalk: Unraveling New Therapeutic Targets for Osteoporosis. *Curr Pharm Des* **23**, 6256-6263 (2017).
164. Andersson, U., Yang, H. & Harris, H. Extracellular HMGB1 as a therapeutic target in inflammatory diseases. *Expert Opin Ther Targets* **22**, 263-277 (2018).
165. Cardoso, A.L. *et al.* Towards frailty biomarkers: Candidates from genes and pathways regulated in aging and age-related diseases. *Ageing Res Rev* (2018).
166. Sorci, G., Riuzzi, F., Giambanco, I. & Donato, R. RAGE in tissue homeostasis, repair and regeneration. *Biochim Biophys Acta* **1833**, 101-109 (2013).
167. Lee, E.J. & Park, J.H. Receptor for Advanced Glycation Endproducts (RAGE), Its Ligands, and Soluble RAGE: Potential Biomarkers for Diagnosis and Therapeutic Targets for Human Renal Diseases. *Genomics Inform* **11**, 224-229 (2013).
168. Schmidt, A.M. Soluble RAGEs - Prospects for treating & tracking metabolic and inflammatory disease. *Vascul Pharmacol* **72**, 1-8 (2015).
169. Lalla, E. *et al.* Blockade of RAGE suppresses periodontitis-associated bone loss in diabetic mice. *J Clin Invest* **105**, 1117-1124 (2000).
170. Ding, K.H. *et al.* Disordered osteoclast formation in RAGE-deficient mouse establishes an essential role for RAGE in diabetes related bone loss. *Biochem Biophys Res Commun* **340**, 1091-1097 (2006).
171. Egawa, T. *et al.* Potential involvement of dietary advanced glycation end products in impairment of skeletal muscle growth and muscle contractile function in mice. *Br J Nutr* **117**, 21-29 (2017).
172. Chiu, C.Y. *et al.* Advanced glycation end-products induce skeletal muscle atrophy and dysfunction in diabetic mice via a RAGE-mediated, AMPK-down-regulated, Akt pathway. *J Pathol* **238**, 470-482 (2016).
173. Tubaro, C., Arcuri, C., Giambanco, I. & Donato, R. S100B protein in myoblasts modulates myogenic differentiation via NF-kappaB-dependent inhibition of MyoD expression. *J Cell Physiol* **223**, 270-282 (2010).
174. Bongarzone, S., Savickas, V., Luzi, F. & Gee, A.D. Targeting the Receptor for Advanced Glycation Endproducts (RAGE): A Medicinal Chemistry Perspective. *J Med Chem* **60**, 7213-7232 (2017).
175. Walker, D., Lue, L.F., Paul, G., Patel, A. & Sabbagh, M.N. Receptor for advanced glycation endproduct modulators: a new therapeutic target in Alzheimer's disease. *Expert Opin Investig Drugs* **24**, 393-399 (2015).
176. Panza, F. *et al.* Emerging drugs to reduce abnormal beta-amyloid protein in Alzheimer's disease patients. *Expert. Opin. Emerg. Drugs* **21**, 377-391 (2016).
177. Galasko, D. *et al.* Clinical trial of an inhibitor of RAGE-Abeta interactions in Alzheimer disease. *Neurology* **82**, 1536-1542 (2014).
178. Livak, K.J. & Schmittgen, T.D. Analysis of relative gene expression data using real-time quantitative PCR and the 2^{-DDC_T} method. *Methods* **25**, 402-408 (2001).
179. Posritong, S. *et al.* Pyk2 deficiency potentiates osteoblast differentiation and mineralizing activity in response to estrogen or raloxifene. *Mol Cell Endocrinol* **474**, 35-47 (2018).
180. Delgado-Calle, J. *et al.* Bidirectional Notch signaling and osteocyte-derived factors in the bone marrow microenvironment promote tumor cell proliferation and bone destruction in multiple myeloma. *Cancer Res* **76**, 1089-1100 (2016).

181. Zhang, Y. *et al.* Enhanced osteoclastic resorption and responsiveness to mechanical load in gap junction deficient bone. *PLoS ONE* **6**, e23516 (2011).
182. Bonetto, A., Rupert, J.E., Barreto, R. & Zimmers, T.A. The Colon-26 Carcinoma Tumor-bearing Mouse as a Model for the Study of Cancer Cachexia. *J. Vis. Exp* (2016).
183. Schneider, C.A., Rasband, W.S. & Eliceiri, K.W. NIH Image to ImageJ: 25 years of image analysis. *Nat Methods* **9**, 671-675 (2012).
184. Zhou, Z. & Xiong, W.C. RAGE and its ligands in bone metabolism. *Front Biosci (Schol Ed)* **3**, 768-776 (2011).
185. Lecker, S.H. *et al.* Multiple types of skeletal muscle atrophy involve a common program of changes in gene expression. *FASEB J* **18**, 39-51 (2004).
186. Sandri, M. *et al.* Foxo transcription factors induce the atrophy-related ubiquitin ligase atrogin-1 and cause skeletal muscle atrophy. *Cell* **117**, 399-412 (2004).
187. Sato, A.Y. *et al.* Glucocorticoids induce bone and muscle atrophy by tissue-specific mechanisms upstream of E3 ubiquitin ligases. *Endocrinology* **158**, 664-677 (2017).
188. Bonaldo, P. & Sandri, M. Cellular and molecular mechanisms of muscle atrophy. *Dis. Model. Mech* **6**, 25-39 (2013).
189. Lin, T.H. *et al.* NF-kappaB as a Therapeutic Target in Inflammatory-Associated Bone Diseases. *Adv Protein Chem Struct Biol* **107**, 117-154 (2017).
190. Zhou, Z. *et al.* Regulation of osteoclast function and bone mass by RAGE. *J. Exp. Med* **203**, 1067-1080 (2006).
191. Charoonpatrapong, K. *et al.* HMGB1 expression and release by bone cells. *J Cell Physiol* **207**, 480-490 (2006).
192. Philip, B.K. *et al.* RAGE supports parathyroid hormone-induced gains in femoral trabecular bone. *Am. J Physiol Endocrinol. Metab* **298**, E714-E725 (2010).
193. Boyce, B.F., Xiu, Y., Li, J., Xing, L. & Yao, Z. NF-kappaB-Mediated Regulation of Osteoclastogenesis. *Endocrinol Metab (Seoul)* **30**, 35-44 (2015).
194. Novack, D.V. Role of NF-kappaB in the skeleton. *Cell Res* **21**, 169-182 (2011).
195. Silva, B.C. & Bilezikian, J.P. Parathyroid hormone: anabolic and catabolic actions on the skeleton. *Curr. Opin. Pharmacol* **22**, 41-50 (2015).
196. Li, X. *et al.* Parathyroid hormone stimulates osteoblastic expression of MCP-1 to recruit and increase the fusion of pre/osteoclasts. *J. Biol. Chem* **282**, 33098-33106 (2007).
197. Wein, M.N. & Kronenberg, H.M. Regulation of Bone Remodeling by Parathyroid Hormone. *Cold Spring Harb. Perspect. Med* **8**, pii: a031237 (2018).
198. Murrills, R. Parathyroid hormone and bone cells. *Clinical Reviews in Bone & Mineral Metabolism* **4**, 233-257 (2008).
199. Song, F. *et al.* RAGE regulates the metabolic and inflammatory response to high-fat feeding in mice. *Diabetes* **63**, 1948-1965 (2014).
200. Li, H., Malhotra, S. & Kumar, A. Nuclear factor-kappa B signaling in skeletal muscle atrophy. *J Mol Med (Berl)* **86**, 1113-1126 (2008).
201. Van Gammeren, D., Damrauer, J.S., Jackman, R.W. & Kandarian, S.C. The IkappaB kinases IKKalpha and IKKbeta are necessary and sufficient for skeletal muscle atrophy. *FASEB J* **23**, 362-370 (2009).
202. Fanzani, A., Conraads, V.M., Penna, F. & Martinet, W. Molecular and cellular mechanisms of skeletal muscle atrophy: an update. *J Cachexia Sarcopenia Muscle* **3**, 163-179 (2012).
203. Senf, S.M., Dodd, S.L. & Judge, A.R. FOXO signaling is required for disuse muscle atrophy and is directly regulated by Hsp70. *Am. J. Physiol Cell Physiol* **298**, C38-C45 (2010).

204. McLoughlin, T.J. *et al.* FoxO1 induces apoptosis in skeletal myotubes in a DNA-binding-dependent manner. *Am J Physiol Cell Physiol* **297**, C548-555 (2009).
205. Koopman, R., Ly, C.H. & Ryall, J.G. A metabolic link to skeletal muscle wasting and regeneration. *Front Physiol* **5**, 32 (2014).
206. Piperi, C., Adamopoulos, C., Dalagiorgou, G., Diamanti-Kandarakis, E. & Papavassiliou, A.G. Crosstalk between advanced glycation and endoplasmic reticulum stress: emerging therapeutic targeting for metabolic diseases. *J Clin Endocrinol Metab* **97**, 2231-2242 (2012).
207. Anelli, T. & Sitia, R. Protein quality control in the early secretory pathway. *EMBO J* **27**, 315-327 (2008).
208. Furuya, D.T. *et al.* Identification of nuclear factor-kappaB sites in the Slc2a4 gene promoter. *Mol Cell Endocrinol* **370**, 87-95 (2013).
209. Wang, Y. & Pessin, J.E. Mechanisms for fiber-type specificity of skeletal muscle atrophy. *Curr Opin Clin Nutr Metab Care* **16**, 243-250 (2013).
210. Davis, H.M. *et al.* Short-term pharmacologic RAGE inhibition differentially affects bone and skeletal muscle in middle-aged mice. **124**, 89-102 *Bone* (2019).
211. Mori, G., D'Amelio, P., Faccio, R. & Brunetti, G. The Interplay between the bone and the immune system. *Clin Dev Immunol* **2013**, 720504 (2013).
212. Terashima, A. & Takayanagi, H. Overview of Osteoimmunology. *Calcif Tissue Int* **102**, 503-511 (2018).
213. Souza, P.P. & Lerner, U.H. The role of cytokines in inflammatory bone loss. *Immunol. Invest* **42**, 555-622 (2013).
214. Meng, E. *et al.* High mobility group box 1 protein inhibits the proliferation of human mesenchymal stem cells and promotes their migration and differentiation along osteoblastic pathway. *Stem Cells Dev* **17**, 805-813 (2008).
215. Feng, L. *et al.* HMGB1 promotes the secretion of multiple cytokines and potentiates the osteogenic differentiation of mesenchymal stem cells through the Ras/MAPK signaling pathway. *Exp Ther Med* **12**, 3941-3947 (2016).
216. Li, Q., Yu, B. & Yang, P. Hypoxia-induced HMGB1 in would tissues promotes the osteoblast cell proliferation via activating ERK/JNK signaling. *Int J Clin Exp Med* **8**, 15087-15097 (2015).
217. Palumbo, R. *et al.* Extracellular HMGB1, a signal of tissue damage, induces mesoangioblast migration and proliferation. *The Journal of Cell Biology* **164**, 441-449 (2004).
218. Hurtgen, B.J. *et al.* Autologous minced muscle grafts improve endogenous fracture healing and muscle strength after musculoskeletal trauma. *Physiol Rep* **5** (2017).
219. Hou, C., Luan, L. & Ren, C. Oxidized low-density lipoprotein promotes osteoclast differentiation from CD68 positive mononuclear cells by regulating HMGB1 release. *Biochemical and Biophysical Research Communications* **495**, 1356-1362 (2018).
220. Plotkin, L.I., Vyas, K., Gortazar, A.R., Manolagas, S.C. & Bellido, T. barrestin complexes with connexin (Cx) 43 and anchors ERKs outside the nucleus: a requirement for the Cx43/ERK-mediated anti-apoptotic effect of bisphosphonates in osteocytes. *J. Bone Miner. Res* **21**, S65 (2006).
221. Low, B.E., Kutny, P.M. & Wiles, M.V. Simple, Efficient CRISPR-Cas9-Mediated Gene Editing in Mice: Strategies and Methods. *Methods Mol Biol* **1438**, 19-53 (2016).
222. Hsu, P.D. *et al.* DNA targeting specificity of RNA-guided Cas9 nucleases. *Nat Biotechnol* **31**, 827-832 (2013).
223. Doench, J.G. *et al.* Rational design of highly active sgRNAs for CRISPR-Cas9-mediated gene inactivation. *Nat Biotechnol* **32**, 1262-1267 (2014).

224. Yoshida, T., Flegler, A., Kozlov, A. & Stern, P.H. Direct inhibitory and indirect stimulatory effects of RAGE ligand S100 on sRANKL-induced osteoclastogenesis. *J Cell Biochem* **107**, 917-925 (2009).
225. Kim, H. *et al.* Extracellular S100A4 negatively regulates osteoblast function by activating the NF-kappaB pathway. *BMB Rep* **50**, 97-102 (2017).
226. Notsu, M. *et al.* Advanced Glycation End Product 3 (AGE3) Increases Apoptosis and the Expression of Sclerostin by Stimulating TGF-beta Expression and Secretion in Osteocyte-Like MLO-Y4-A2 Cells. *Calcif. Tissue Int* (2017).
227. Tanaka, K., Yamaguchi, T., Kanazawa, I. & Sugimoto, T. Effects of high glucose and advanced glycation end products on the expressions of sclerostin and RANKL as well as apoptosis in osteocyte-like MLO-Y4-A2 cells. *Biochem. Biophys. Res. Commun* **461**, 193-199 (2015).
228. Dong, X.N., Qin, A., Xu, J. & Wang, X. In situ accumulation of advanced glycation endproducts (AGEs) in bone matrix and its correlation with osteoclastic bone resorption. *Bone* **49**, 174-183 (2011).
229. Davis, H.M. *et al.* High mobility group box1 (HMGB1) protein regulates osteoclastogenesis through direct actions on osteocytes and osteoclasts *in vitro*. *J Cell Biochem* **in press** (2019).
230. Sheedy, F.J. Turning 21: Induction of miR-21 as a Key Switch in the Inflammatory Response. *Front Immunol* **6**, 19 (2015).
231. Tian, T. *et al.* Exosome uptake through clathrin-mediated endocytosis and macropinocytosis and mediating miR-21 delivery. *J. Biol. Chem* **289**, 22258-22267 (2014).
232. Lo Cicero, A., Stahl, P.D. & Raposo, G. Extracellular vesicles shuffling intercellular messages: for good or for bad. *Curr. Opin. Cell Biol* **35**, 69-77 (2015).
233. Sirois, I. *et al.* Caspase-3-dependent export of TCTP: a novel pathway for antiapoptotic intercellular communication. *Cell Death. Differ* **18**, 549-562 (2011).
234. Boing, A.N. *et al.* Active caspase-3 is removed from cells by release of caspase-3-enriched vesicles. *Biochim. Biophys. Acta* **1833**, 1844-1852 (2013).
235. Lakhter, A.J. *et al.* Beta cell extracellular vesicle miR-21-5p cargo is increased in response to inflammatory cytokines and serves as a biomarker of type 1 diabetes. *Diabetologia* (2018).
236. Ji, X., Chen, X. & Yu, X. MicroRNAs in Osteoclastogenesis and Function: Potential Therapeutic Targets for Osteoporosis. *Int. J. Mol. Sci* **17** (2016).
237. Sugatani, T., Vacher, J. & Hruska, K.A. A microRNA expression signature of osteoclastogenesis. *Blood* **117**, 3648-3657 (2011).
238. Mou, K., Liu, W., Han, D. & Li, P. HMGB1/RAGE axis promotes autophagy and protects keratinocytes from ultraviolet radiation-induced cell death. *J Dermatol Sci* **85**, 162-169 (2017).
239. Yang, X., Xue, P., Liu, X., Xu, X. & Chen, Z. HMGB1/autophagy pathway mediates the atrophic effect of TGF-beta1 in denervated skeletal muscle. *Cell Commun Signal* **16**, 97 (2018).
240. Sun, X. & Tang, D. HMGB1-dependent and -independent autophagy. *Autophagy* **10**, 1873-1876 (2014).
241. Shao, Y. *et al.* HMGB1/TLR4 signaling induces an inflammatory response following high-pressure renal pelvic perfusion in a porcine model. *Am J Physiol Renal Physiol* **311**, F915-F925 (2016).
242. Magna, M. & Pisetsky, D.S. The role of HMGB1 in the pathogenesis of inflammatory and autoimmune diseases. *Mol. Med* **20**, 138-146 (2014).
243. Maroso, M. *et al.* Toll-like receptor 4 and high-mobility group box-1 are involved in ictogenesis and can be targeted to reduce seizures. *Nat. Med* **16**, 413-419 (2010).

244. Wu, C.Z. *et al.* HMGB1/RAGE axis mediates the apoptosis, invasion, autophagy, and angiogenesis of the renal cell carcinoma. *Onco Targets Ther* **11**, 4501-4510 (2018).

CURRICULUM VITAE

Hannah Marie Davis

Education

2015-2019	Doctor of Philosophy Major: Anatomy and Cell Biology; Minor: Clinical Research Indiana University
2009-2013	Bachelor of Science Major: Biology; Minors: Studio Art and Psychology Indiana University

Research Experience

2013-2015	Research Technician Indiana University School of Medicine Department of Anatomy and Cell Biology
2011-2013	Student Researcher Indiana University Department of Biology
Summer 2012	UROP Summer Fellow Indiana University-Purdue University Indianapolis Department of Biology
Summer 2011	Summer Research Internship Indiana University-Purdue University Indianapolis Department of Biology

Industry Experience

2018-Present	Project Assistant (Part-time) Medical and Scientific Affairs contractor at Roche Diagnostics

Teaching Experience

2016-2018	Teaching Assistant Molecular Cell Systems Processes IBMG core course

Fellowships and Awards

2018	Ruth L. Kirschstein National Research Service Award (NRSA) Individual Predoctoral Fellowship (F31)-awarded and relinquished

2018	Cagiantas Scholarship recipient, Indiana University School of Medicine (IUSM)
2018	Erica M. Daniel Kepner Award for Scientific Achievement recipient, IUSM
2018	Young Investigator Travel Award, Annual ASBMR Meeting
2018	Graduate and Professional Education Grant recipient, IUPUI
2017	Comprehensive Musculoskeletal Training Program (T32) pre-doctoral position recipient, IUSM
2017	Dr. Charles Turner Young Investigator Bone Research Award recipient, IUSM
2017	Young Investigator Travel Award, Annual ASBMR Meeting
2015	Young Investigator Travel Award, Annual ASBMR Meeting
2015	Endocrinology Fellows Foundation Ninth Annual Fellows Forum on Metabolic Bone Disease

Professional Societies and student organizations

2018-Present	Science Outreach Community at IUSM
2018-Present	American Medical Writers Association (AMWA) *2019 Conference Communications Chair*
2018	National Association of Scientific Writers (NASW)
2018	American Society for Cell Biology (ASCB)
2017-2018	International Society for Extracellular Vesicles (ISEV)
2015-Present	American Society for Bone and Mineral Research (ASBMR)

Publications

Davis HM, Deosthale PJ, Valdez S, Gomez L, White F, Subler MA, Windle J, Bidwell JP, Bruzzaniti A, Plotkin LI. Autocrine actions of high mobility group box1 protein (HMGB1) on osteocytes and osteoclasts regulate osteoclastogenesis. J Cell Biochem, in press, 2019.

Davis HM, Essex AL, Valdez S, Deosthale PJ, Aref MW, Allen M, Bonetto A, Plotkin LI. Short-term pharmacologic RAGE inhibition differentially effects bone and skeletal muscle in aging. Bone 124:89-102, 2019.

Plotkin LI, **Davis HM**, Essex AL. RAGE signaling in musculoskeletal biology. Skeletal Biology and Regulation Section in Current Osteoporosis Reports section, Current Osteoporosis Reports (M Forwood and A Robling, Section Editors, D Burr, Editor in Chief) 17:16-25, 2019.

Plotkin LI, **Davis HM**. Role of connexins and pannexins in bone and muscle mass and function. Osteosarcopenia – Translational Research in Bone, Muscle and Fat Interactions (G. Luque, editor), Springer, in press, 2019.

Davis HM, Aref MW, Aguilar-Perez A, Pacheco-Costa R, Allen K, Valdez S, Herrera C, Atkinson EG, Mohammad A, Lopez D, Harris MA, Harris SE, Allen MR, Bellido T, Plotkin LI. Cx43 overexpression in osteocytes prevents osteocyte apoptosis and preserves cortical bone quality in aging mice. Journal of Bone and Mineral Research Plus 2:206-216, 2018.

Pacheco-Costa R*, **Davis HM***, Atkinson EG, Dilley JE, Byiringiro I, Aref MW, Allen MR, Bellido T, Plotkin LI. Reversal of loss of bone mass in old mice treated with mefloquine. Bone 114:22-31, 2018. *co-first authors

Davis HM, Pacheco-Costa R, Plotkin LI. Response to R. L. Nevin “Considerations in the repurposing of mefloquine for prevention and treatment of osteoporosis”. Bone 146:306, 2018.

Plotkin LI, **Davis HM**. MicroRNA regulation in osteocytes. MicroRNAs in Skeletal Development section, Current Molecular Biology Reports (A Delany, Editor, A van Wijnen, Editor in Chief) 4:191-197, 2018.

Davis HM*, Pacheco-Costa R*, Atkinson EG, Brun LR, Gortazar AR, Harris J, Hiasa M, Bolarinwa SA, Yoneda T, Ivan M, Bruzzaniti A, Bellido T, Plotkin LI. Disruption of the Cx43/miR21 pathway leads to osteocyte apoptosis and increased osteoclastogenesis with aging. Aging Cell 16:551-563, 2017. *co-first authors

Sato AY, Richardson D, Cregor M, **Davis HM**, Au ED, McAndrews K, Zimmers TA, Organ JM, Peacock M, Plotkin LI, Bellido T. Glucocorticoids induce bone and muscle atrophy by tissue-specific mechanisms upstream of E3 ubiquitin ligases. Endocrinology 158(3):664-77, 2017.

Shao Y, Hernandez-Buquer S, Childress P, Stayrook KR, Alvarez MB, **Davis H**, Plotkin L, He Y, Condon KW, Burr DB, Warden SJ, Robling AG, Yang FC, Wek RC, Allen MR, Bidwell JP. Improving Combination Osteoporosis Therapy In a Preclinical Model of Heightened Osteoanabolism. Endocrinology 158(9):2722-40, 2017.

Eaton MS, Weinstein N, Newby JB, Plattes MM, Foster HE, Arthur JW, Ward TD, Shively SR, Shor R, Nathan J, **Davis HM**, Plotkin LI, Wauson EM, Dewar BJ, Broege A, Lowery JW. Loss of the nutrient sensor TAS1R3 leads to reduced bone resorption. J.Physiol Biochem 74(1):3-8. PM:29019082, 2017.

Plotkin LI, Pacheco-Costa R, **Davis HM**. microRNAs and connexins in bone: interaction and mechanisms of delivery. Current Molecular Biology Reports 3:63-70, 2017.

Plotkin LI, **Davis HM**, Cisterna BA, Saez JC. Connexins and pannexins in bone and skeletal muscle. Current Osteoporosis Reports 15:326-334, 2017.

Pacheco-Costa R and **Davis HM**. The role of under-investigated connexins in musculoskeletal tissues: A Brief Review with emphasis on bone tissue. Actualizaciones en Osteología 13(1):58-66, 2017.

Hammond MA, Bernam AG, Pacheco-Costa R, **Davis HM**, Plotkin LI, Wallace JM. Removing or truncating connexin 43 in murine osteocytes alters cortical geometry, nanoscale morphology, and tissue mechanics in the tibia. Bone88:85-91, 2016.

Pacheco-Costa R, **Davis HM**, Katchburian E, Atkinson EG, Plotkin LI, Reginato RD. Osteocytic connexin 43 is not required for the increase in bone mass induced by intermittent PTH administration in male mice. Journal of Musculoskeletal and Neuronal Interactions 16:47-57, 2016.

Plotkin LI, Gortazar AR, **Davis HM**, Condon KW, Gabilondo H, Maycas M, Allen MR, Bellido T. Inhibition of osteocyte apoptosis prevents the increase in osteocytic RANKL but it does not stop bone resorption or the loss of bone induced by unloading. Journal of Biological Chemistry. 290:18934-18942, 2015.

Pacheco-Costa R, **Davis HM**, Sorenson C, Hon MC, Hassan I, Reginato RD, Allen MR, Bellido T, Plotkin LI. Defective cancellous bone structure and abnormal response to PTH in cortical bone of mice lacking Cx43 cytoplasmic C-terminus domain. Bone 81:632-643, 2015.

Davis HM and Plotkin LI. MicroRNAs and bone biology: summary of microRNA-related abstracts presented at the 2015 Annual Meeting of the American Society for Bone and Mineral Research. Actualizaciones en Osteología 11:251-256, 2015.

Pacheco-Costa R, Hassan I, Reginato RD, **Davis HM**, Bruzzaniti A, Allen MR, Plotkin LI. High Bone Mass in Mice Lacking Cx37 Due to Defective Osteoclast Differentiation. Journal of Biological Chemistry 289:8508-8520, 2014.

Manuscripts-submitted/under-review

Davis HM, Deosthale PJ, Essex AL, Pacheco-Costa R, Atkinson EG, Aref MW, Dilley J, Bellido T, Ivan M, Allen M, Plotkin LI. Osteocytic miR21 deficiency improves bone strength independent of sex despite having sex divergent effects on osteocyte viability and bone turnover.

Aguilar-Perez A, Pacheco-Costa R, Atkinson EG, Deosthale PJ, **Davis HM**, Essex AL, Dilley JE, Gomez L, Rupert J, Zimmers T, Thompson RJ, Allen MR, Plotkin LI. Age- and sex-dependent role of osteocytic pannexin1 on bone and muscle mass and strength.

Conference Presentations and Abstracts

Davis HM, Valdez S, Aguilar-Perez A, Aref MW, Deosthale P, Essex A, Allen MR, White F, Windle J, and Plotkin LI. Short-term pharmacologic inhibition of RAGE suppresses

bone turnover and muscle atrophy in aging. Plenary poster presentation at the Annual Meeting of the American Society for Bone and Mineral Research (ASBMR), Montreal, Quebec, Canada, September, 2018.

Davis HM, Pacheco-Costa R, Aref MW, Valdez S, Essex A, Atkinson EG, Dilley JE, Herrera C, Deosthale P, Ivan M, Allen MR, Bellido T, Plotkin LI. Sex divergent role of osteocytic miR21 in the maintenance of osteocyte viability and regulation of bone turnover. Plenary poster at the Annual Meeting of the ASBMR, Montreal, Quebec, Canada, September, 2018.

Davis HM, Valdez S, Gomez LJ, Bruzzaniti A, Plotkin LI. Autocrine actions of high mobility group box1 protein (HMGB1) on osteocytes and osteoclasts regulate osteoclastogenesis. Plenary poster presentation at the Annual Meeting of the ASBMR, Montreal, Quebec, Canada, September, 2018.

Nelson JH, **Davis HM**, McAndrews K, Cregor MD, Thompson WR, Plotkin LI, Robling AG, Bellido T, Delgado-Calle J. Sclerostin regulates adipocyte fate and mediates paracrine and endocrine signaling between osteocytes and fat. Presentation at the Annual Meeting of the ASBMR, Montreal, Quebec, Canada, September, 2018.

Aguilar-Perez A, Pacheco-Costa R, Atkinson EG, Deosthale P, Gomez LJ, Dilley JE, **Davis HM**, Herrera C, Thompson R, Allen MR, Liu Z, Bruzzaniti A, Zimmers T, Plotkin LI. Critical sex- and age-dependent role of osteocytic pannexin1 on bone and muscle mass and strength. Poster presentation at the Annual Meeting of the ASBMR, Montreal, Quebec, Canada, September, 2018.

Essex A, **Davis HM**, Valdez S, Pin F, Bonnetto A, Plotkin LI. Systemic RAGE inhibition reverses the aging-induced alterations of skeletal muscle mass and metabolism. Poster presentation at the Annual Meeting of the ASBMR, Montreal, Quebec, Canada, September, 2018.

Davis HM, Aref MW, Aguilar-Perez A, Pacheco-Costa R, Allen K, Valdez S, Herrera C, Atkinson EG, Mohammad A, Lopez D, Harris MA, Harris SE, Alen M, Bellido T, Plotkin LI. Cx43 overexpression in osteocytes prevents osteocyte apoptosis and preserves cortical bone quality in aging mice. Oral presentation at the Advances in Mineral Metabolism meeting, Snowmass, Colorado, April, 2018.

Davis HM, Pacheco-Costa R, Herrera C, Aguilar-Perez A, Lugo J, Plotkin LI. Similar increase in bone resorption and decrease in bone mass but opposite effects in osteocytic gene expression in female versus male mice with FMR1 deletion, a model of fragile X syndrome. Plenary poster presentation at the Annual Meeting of the ASBMR, Denver, Colorado, September, 2017.

Davis HM, Schartz ND, Herrera C, Pacheco-Costa R, Wyatt SK, Brewster AL, Plotkin LI. Status epilepticus leads to reduced bone mass and strength in juvenile rats. Poster presentation at the Annual Meeting of the ASBMR, Denver, Colorado, September, 2017.

Pacheco-Costa R, **Davis HM,** Atkinson EG, Dilley J, Herrera C, Condon K, Ivan M, Bellido T, Plotkin LI. Unexpected decrease in osteoclast number and bone resorption with increased osteocyte apoptosis in the absence of osteocytic miR21. Plenary poster

presentation at the Annual Meeting of the ASBMR, Denver, Colorado, September, 2017.

Pacheco-Costa R, Atkinson EG, Dilley J, **Davis HM,** Herrera C, Thompson R, Bellido T, Plotkin LI. Absence of pannexin-1 in osteocytes leads to high bone mass due to distinct cellular mechanisms in cancellous versus cortical bone, and in young versus old mice. Oral presentation at the Annual Meeting of the ASBMR, Denver, Colorado, September, 2017.

Pacheco-Costa R, Atkinson EG, Dilley JE, **Davis HM,** Herrera C, Byiringiro I, Thompson RJ, Bellido T, Plotkin LI. Distinct cellular and age-related mechanisms of genetic and pharmacologic pannexin1 inhibition resulting in high bone mass. Oral presentation at the International Gap Junction Meeting Glasgow, UK. 2017.

Davis HM, Atkinson EG, Pacheco-Costa R, Lopez D, Aref M, Brown D, Harris MA, Harris SE, Allen MR, Bellido T, Plotkin LI. Osteocyte specific Cx43 overexpression improves cortical bone mass and strength, but reduces cancellous bone in old mice. Poster presentation at the Annual Meeting of the ASBMR, Atlanta, Georgia, September, 2016.

Davis HM, Atkinson EG, Harris J, Pacheco-Costa R, Gortazar AR, Ivan M, Bruzzaniti A, Bellido T, Plotkin LI. Reduced microRNA21 and enhanced HMGB1 release: a mechanistic explanation for increased osteocyte apoptosis and resorption in the absence of Cx43 and with aging. Poster presentation at the Annual Meeting of the ASBMR, Atlanta, Georgia, September, 2016.

Davis HM, Atkinson EG, Harris J, Pacheco-Costa R, Gortazar AR, Ivan M, Bruzzaniti A, Bellido T, Plotkin LI. (2015). Reduction in microRNA21 promotes apoptosis and increases RANKL in osteocytes: a mechanistic explanation for the enhanced resorption in the absence of Cx43 and with aging. Plenary poster presentation at the Annual Meeting of the ASBMR, Seattle, Washington, October, 2015.

Davis HM, Atkinson EG, Harris J, Pacheco-Costa R, Gortazar AR, Ivan M, Bruzzaniti A, Bellido T, Plotkin LI. (2015). Reduction in microRNA21 promotes apoptosis and increases RANKL in osteocytes: a mechanistic explanation for the enhanced resorption in the absence of Cx43 and with aging. Poster presentation at the Endocrinology Fellows Foundation Ninth Annual Fellows Forum on Metabolic Bone Disease, Seattle, Washington, October, 2015.

Pacheco-Costa R, Sorenson C, Hon MC, **Davis HM,** Hassan I, Reginato RD, Katchburian E, Allen MR, Bellido T, Plotkin LI. (2015). Cx43 scaffolding CT intracellular domain is required for achieving proper bone architecture and for some, but not all, anabolic actions of intermittent PTH administration. Oral presentation at the 2015 International Gap Junction Conference, Valparaiso, Chile, March, 2015.

Hammond MA, Pacheco-Costa R, **Davis HM,** Plotkin LI, Wallace JM. (2014). Removing or Truncating Cx-43 in Osteocytes Alters Nanoscale Composition and Microscale Mechanics. Poster presentation at the 2015 ORS meeting, March, 2015.

Pacheco-Costa R, Hassan I, Sorenson C, **Davis HM,** Hammond MA, Reginato RD, Katchburian E, Wallace JM, Bellido T, Plotkin LI. (2014). Cx43 scaffolding C-terminus

intracellular domain is required for achieving proper bone architecture and strength, but is not involved in osteocytic Cx43-dependent cortical bone homeostasis. Poster presentation at the 36th Annual Meeting of the ASBMR, Houston, TX, USA. Journal of Bone and Mineral Research 29 (Supl.1):S378. 2014.